UC Riverside

UC Riverside Electronic Theses and Dissertations

Title

Beyond Traditional Four-Connected Zeolitic Frameworks: Design, Syntheses and Characterization of Porous Zeolitic Imidazolate Frameworks and Open-Framework Metal Chalcogenides

Permalink

https://escholarship.org/uc/item/2jd9v81v

Author

Wu, Tao

Publication Date

2011

Peer reviewed|Thesis/dissertation

eScholarship.org Powered by the California Digital Library
University of California

UNIVERSITY OF CALIFORNIA
RIVERSIDE

Beyond Traditional Four-Connected Zeolitic Frameworks: Design, Syntheses and Characterization of Porous Zeolitic Imidazolate Frameworks and Open-Framework Metal Chalcogenides

A Dissertation submitted in partial satisfaction
of the requirements for the degree of

Doctor of Philosophy

in

Chemistry

by

Tao Wu

August 2011

Dissertation Committee:
Dr. Pingyun Feng, Chairperson
Dr. Christopher A. Reed
Dr. Michael Marsella

Copyright by
Tao Wu
2011

This Dissertation of Tao Wu is approved:

_____

_____

_____

Committee Chairperson

University of California, Riverside

Acknowledgements

Though only my name appears on the cover of this dissertation, I could never have reached the heights and explored the depths and finished my Ph. D. study smoothly without the help, support, guidance and efforts of a lot of people.

First, my deepest gratitude is to my mentor Dr. Pingyun Feng for her careful guidance and infectious enthusiasm. Her endless patience and strong support helped me overcome many crisis situations in both my scientific research and daily life. Her insightful and knowledgeable guidance made my graduate period much more productive. I hope that one day I would become as good an advisor to my students as Ping has been to me.

I am also grateful to Prof. Xianhui Bu at CSULB for his valuable discussions that helped me sort out lots of technical details of my work. It is my pleasure to collaborate with him. I also warmly appreciate Dr. Jian Zhang and Dr. Shoutian Zheng in Bu's lab for their enthusiastic help in collecting data.

I am greatly indebted to many past and current members in Feng's group for their providing a rich working experience, intellectual stimulation and friendship: Dr. Xiqing Wang, Dr. Zhien Lin, Dr. Yang Liu, Dr. Zhenyu Zhang, Dr. Puhong Liang, Dr. Qipu Lin, Dr. Rui Liu, Dong Zhao, Xiang Zhao, Shan Wang, Fan Zuo, Le Wang, Cong Zhou, Jikai Liu, and Fei Bu. I would also like to thank several undergraduate students for their help: Ripsime Khazhakyan, Victoria Chau, and Richard Ma.

I am also thankful to my committee members Professor Christopher A. Reed and Professor Michael Marsella for their valuable comments on my dissertation.

I would like to take this opportunity to thank Dr. Fook Tham for the collection and analysis of some data.

Most importantly, none of this would have been possible without the love and patience of my family. I would like to express my heart-felt gratitude to my mother Yinfeng Jiang, my wife Rui Zhou, my daughters Siyu and Sarah, and my sisters for everything they have done for me.

Finally, I would like to take the opportunity to thank all persons who have ever helped me before.

Dedication

To my mother Yinfeng Jiang, my wife Rui Zhou, my two daughters Siyu and Sarah.

ABSTRACT OF THE DISSERTATION

Beyond Traditional Four-Connected Zeolitic Frameworks:
Design, Syntheses and Characterization of Porous Zeolitic Imidazolate Frameworks and Open-Framework Metal Chalcogenides

by

Tao Wu

Doctor of Philosophy, Graduate Program in Chemistry
University of California, Riverside, August 2011
Dr. Pingyun Feng, Chairperson

Zeolites have played essential roles in a number of industrial processes and technological applications. The intensive research in crystalline microporous materials has successfully extended such traditional inorganic zeolites to semiconducting open-framework metal chalcogenides and hybrid porous coordination polymers. Our research group has made a number of key advances in the development of metal chalcogenide clusters and their self-assembled open frameworks. Some of these key advances resulted from this thesis work and are described here. This dissertation also deals with the synthesis of some unique families of porous frameworks based on coordination polymers.

Porous zeolitic metal imidazolate frameworks can be considered as integrating features of both traditional inorganic zeolites and porous coordination polymers because the Si-O-Si angle in zeolites is coincident with that of the bridging angle formed by the Metal-Imidazolate-Metal unit. In this thesis work, two different strategies are employed. The first is the use of mixed, sterically tuned and complementary imidazole ligands,

which results in several novel zeolitic topologies with both 3-ring and large rings (>12). The second is the use of novel tetrahedral nodes (e.g., Li and B), which leads to a new family of boron imidazolate open-framework materials.

Open-framework metal chalcogenides are a new generation of inorganic porous materials because their semiconducting properties could expand the utility of inorganic porous materials into areas in which traditional insulating inorganic zeolite materials have had little impact. Key synthetic discoveries made in this thesis work include (1) synthesis of a family of Sn- and/or S-doped Zn-Ga-Se clusters and frameworks and demonstration of site-selective doping chemistry controlled by the interplay of multiple fundamental chemical and geometrical factors, (2) synthesis of two selenide 3D superlattices based on dual-sized supertetrahedral clusters and demonstration of charge density tuning of chalcogenide clusters using three types of charge-complementary and yet geometry-matching metal cations (di-, tri-, and tetravalent ions), (3) synthesis of the largest discrete chalcogenide clusters with tunable band gaps, which further blurs the boundary between molecular clusters and colloidal nanoparticles, and (4) the synthesis of a new family of 3D covalent arrays of supertetrahedral clusters and negatively-charged imidazolate ligands.

Table of Contents

Acknowledgements iv

Dedication vi

Abstract vii

List of Tables xv

List of Figures xvi

List of Schemes xxiii

Chapter 1 Overview of Crystalline Microporous Zeolitic Materials 1

1.1 Crystalline Microporous Materials 1

1.1.1 Inorganic Zeolites 2

1.1.2 Porous Coordination Polymers (PCPs) 4

1.2 Porous Zeolitic Metal Imidazolate Frameworks (PZMIFs) 7

1.2.1 Basic Design Concept on the Construction of PZMIFs 8

1.2.2 Framework Compositions and Topologies 9

1.2.3 Synthetic Methods and Strategies 12

1.2.4 Porosity and Stability and Potential Applications 14

1.3 Open-framework Metal Chalcogenides Based on Supertetrahedral Clusters 15

1.3.1 Basic Design Concept and Construction of Open-Framework Metal Chalcogenides 16

1.3.2 Structure and Composition of Supertetrahedral Clusters 19

1.3.3 Connectivity and Framework Topology Based on Tn Clusters 22

1.3.4 Selected Properties and Potential Applications of Chalcogenide Supperlattices 23

1.4 Contribution from This Work 26

1.5 References 30

Chapter 2 Porous Zeolitic Metal Imidazolate Frameworks 38

2.1 Introduction 38

2.2 Experimental Section 43

2.2.1 Materials and General Methods 43

2.2.2 Solvothermal Syntheses 43

2.2.3 Single-crystal X-ray Structure Determination 45

2.2.4 Gas Adsorption Measurement 46

2.3 Results and Discussion 47

2.3.1 A New Zeolitic Topology with Sixteen-membered Ring and Multidimensional Large Pore Channels in TIF-1 47

2.3.2 Unprecedented Organization of d4R Units in TIF-2 51

2.3.3 Organization of Cubic Double 4-Ring Units into 3-D Distorted Body-Centered Cubic Framework 55

2.3.4 Ordered Cooperative Assembly of Two Different Pairs of Complementary Ligands 57

2.3.5 Thermal Stability 59

2.3.6 Gas Sorption 60

2.4 Conclusion 63

2.5 References 64

Chapter 3 Zeolitic Boron Imidazolate Frameworks 67

3.1 Introduction 67

3.2 Experimental Section 71

3.2.1 Materials and General Methods 71

3.2.2 Syntheses 71

3.2.3 Gas Adsorption Measurement 77

3.2.4 Single-crystal X-ray Structure Determination 78

3.3 Results and Discussion 79

3.3.1 Two-Step Synthesis Strategy and Importance of Lithium Precursors 79

3.3.2 Stucture 81

3.3.3 Gas Sorption 88

3.3.4 Effect of Substituted Group on Framework Topology and Pore Size 91

3.4 Conclusion 95

3.5 References 96

Chapter 4 Synthetic Control of Selenide Supertetrahedral Clusters and Three-Dimensional Co-Assembly by Charge-Complementary Metal Cations 101

4.1 Introduction 101

4.2 Experimental Section 105

4.2.1 Solvothermal Syntheses 105

4.2.2 Structure Determination 105

4.2.3 Powder X-ray Diffraction 106

4.2.4 Optical Properties 106

4.2.5 Thermal Analysis 107

4.3 Results and Discussion 107

4.3.1 Synthesis 107

4.3.2 Stucture 109

4.3.3 Thermal Analysis 114

4.3.4 Optical Properties 114

4.4 Conclusion 120

4.5 References 121

Chapter 5 Isolated Inorganic Supertetrahedral T4 Clusters 124

5.1 Introduction 124

5.2 Experimental Section 131

5.2.1 Materials and General Methods 131

5.2.2 Solvothermal Syntheses 131

5.2.3 Single-crystal X-ray Structure Determination 138

5.3 Results and Discussion 140

5.3.1 Transformation from 3D Covalent Framework to Discrete T4 Clusters 140

5.3.2 Geometric and Charge-density Matching Between T4 Clusters and Organic Templates 142

5.3.3 Solubility Behaviors and Stabilization of T4 Clusters with Surface Organic Cations 147

5.3.4 Tunable Optical Properties in Solution and Solid State 149

5.3.5 Effects of Organic Templates on the Competing Crystallization of OCF-5 vs. OCF-40 and on Properties of OCF-40 152

5.4 Conclusion 157

5.5 References 158

Chapter 6 Phase Selection and Site-Selective Distribution by Tin and Sulfur in Supertetrahedral Zinc Gallium Selenides 161

6.1 Introduction 161

6.2 Experimental Section 165

6.2.1 Materials and General Methods 165

6.2.2 Solvothermal Syntheses 165

6.2.3 Single-crystal X-ray Structure Determination 167

6.3 Results and Discussion 170

6.3.1 Determination and Selection of Optimum Synthesis Parameters 170

6.3.2 Cluster and Crystal Structures 172

6.3.3 Site Selective Distribution of S and Sn in Zn-Ga-Se-based T4 Cluster 178

6.3.4 Effects of Amine-Type on Sn- and S-Doping and on Size and Charge of T4 cluster 180

6.3.5 Phase Selectivity Controlled by Amine-Type, Sn- and S-Doping 182

6.3.6 Effects of Cluster Size and Charge on the Phase Selectivity 184

6.3.7 Optical Properties 187

6.4 Conclusion 191

6.5 References 192

Chapter 7 Three-Dimensional Covalent Co-Assembly between Inorganic Supertetrahedral Clusters and Imidazolates 195

7.1 Introduction 195

7.2 Experimental Section 197

7.2.1 Solvothermal Syntheses 197

7.2.2 Structure Determination 202

7.2.3 Powder X-ray Diffraction 202

7.2.4 Optical Property 202

7.2.5 Thermal Analysis 203

7.2.6 Gas Adsorption 203

7.2.7 Quantum Chemical Calculations for Frontier Orbital of the Fragment of the Crystal Lattice 204

7.3 Results and Discussion 204

7.3.1 Synthesis 204

7.3.2 Structures 205

7.3.3 Optical Properties 211

7.3.4 Quantum Chemical Calculations 213

7.3.5 Gas Adsorption 213

7.4 Conclusion 216

7.5 References 217

List of Tables

Table 1.1 Composition, structure, and framework density of some reported zeolitic imidazolate frameworks arranged in decreasing framework density.

Table 1.2 A summary of compositions of isolated supertetrahedral clusters (Tn).

Table 2.1 A Summary of Crystal Data and Refinement Results.

Table 2.2 Coordination sequences and vertex symbols of TIF-1.

Table 2.3 Coordination sequences and vertex symbols of TIF-2.

Table 3.1 A Summary of Crystal Data and Refinement Results.

Table 5.1 A Summary of Crystal Data and Refinement Parameters for OCF-5s and OCF-40s.

Table 5.2 Syntheses of OCF-5s and OCF-40s.

Table 5.3 Effects of different amine templates on the competing crystallization of OCF-5s and OCF-40s.

Table 6.1 Summary of crystal data and refinement results.

Table 6.2 The refined occupancy factors of Ga/Sn and Se/S in OCF-5-ZnGaSnSeS-TMDP and OCF-5-ZnGaSnSeS-DAMP at various crystallographic sites with T4 clusters.

Table 6.3 The refined occupancy factors of Se/S and Ga/Sn in select OCF-n at various crystallographic sites with T4 clusters.

Table 6.4 Summary of M-Q (M = Zn, Ga, Sn; Q = S, Se) bond lengths.

Table 7.1 Summary of crystal data and refinement results.

List of Figures

Figure 1.1 The IUPAC classification of porous materials on the basis of pore diameter.

Figure 1.2 Basic structure of inorganic zeolite and three representative zeolite topologies.

Figure 1.3 Two representative porous coordination polymers.

Figure 1.4 Selected crystal structures of porous zeolitic metal imidazolate frameworks with several main topologies.

Figure 1.5 The functionalization of one PZMIF with aldehyde group.

Figure 1.6 Ball-and-stick representation of T2, T3, T4 and T5 supertetrahedral clusters. Green ball stands for cation site, orange for anion site.

Figure 1.7 The 3D diamond-type superlattice of ICF-5CuInS-Na serving as photocatalysts for water splitting.

Figure 2.1 The asymmetric unit of TIF-1Zn (green balls for Zn atoms, blue balls for N atoms and black balls for C atoms; the disordered part of ligands are represented by pale grey sticks).

Figure 2.2 The loop configurations of four kinds of T-atoms (a, b, and c) in secondary building unit (d) in TIF-1.

Figure 2.3 Connectivity of adjacent SBUs at the same layer (a) and neighboring layers (b).

Figure 2.4 Left: the topological network of TIF-1 viewed along [001]. Right: cross-sectional view of multi-dimensional channels.

Figure 2.5 The frameworks of TIF-1 shown as natural tilings. The large cage is shown in purple (right) or blue (left).

Figure 2.6 The asymmetric unit of TIF-2 (a), TIF-3 (b), TIF-4 (c), TIF-5 (d) (green balls for Zn atoms, blue balls for N atoms, grey balls for C atoms, black balls for H atoms and red ball for O atoms).

Figure 2.7 (a) The novel topology of TIF-2 viewed along [001] direction; (b) 2-D layer viewed along [100], containing special double four-rings (*d4R*); (c) double crankshaft chain (*dcc*).

Figure 2.8 TIF-2: (a) Connectivity of adjacent *d4r* at the same layer; (b) connectivity of adjacent *d4r* and *dcc*.

Figure 2.9 The frameworks of TIF-2 shown as natural tilings.

Figure 2.10 (a) GME topology viewed along [001] direction; (b) each double 6-rings (*d6r*) is joined to adjacent six *d6r*; (c) a basic double crankshaft chain (*dcc*) contained in GME framework.

Figure 2.11 (a) ACO zeolite framework in TIF-3 viewed along [001] direction; (b) each *d4R* is connected to 8 adjacent *d4R*.

Figure 2.12 (a) Cag topology of TIF-4 viewed along [001] direction (the space filling is C_6H_6, green atom for Zn atom, orange bar for imidazolate, purple bar for 5-methylbenzimidazolate), containing $Zn_4(Im)_4$ four-ring (b), $Zn_6(Im)_4(5\text{-MBim})_2$ six-ring (c), and $Zn_8(Im)_4(5\text{-MBim})_4$ eight-ring (d).

Figure 2.13 (a) GIS Topology of TIF-5 viewed along [100] (green atom for Zn^{2+} or Co^{2+}, orange bar for imidazolate, purple bar for 5, 6-dimethylbenzimidazolate), containing $Zn_4(Im)_4$ four-ring (b), $Zn_4(Im)_2(5,6\text{-DMBim})_2$ four-ring (c), and $Zn_8(Im)_2(5\text{-MBim})_6$ eight-ring (d).

Figure 2.14 Nitrogen gas adsorption isotherm at 77K for TIF-1. P/P_0 is the ratio of gas pressure (P) to saturation pressure (P_0), with P_0=740 torr.

Figure 2.15 Nitrogen gas adsorption isotherm at 77K for TIF-2. P/P_0 is the ratio of gas pressure (P) to saturation pressure (P_0), with P_0=740 torr. Inset is the corresponding pore size distribution curves.

Figure 3.1 View of the coordination environment in BIF-1-Li showing the connectivity between the Li and B tetrahedral (a) and its 3-D framework structure (b) with zni net (c) and three different ring sizes (d-f).

Figure 3.2 (a) View of the coordination environment and (b) the diamondoid unit in BIF-2-Li.

Figure 3.3 Top: diagram of SOD topology in $MB(Mim)_4$ ($M=Li^+$ or Cu^+); BN_4 tetrahedra are shown in orange, MN_4 tetrahedra in green, N in blue, and C in black; the big yellow sphere represents the void space in β cage. Bottom: SOD topology with natural tiling [$4^6.6^8$].

Figure 3.4 Top: diagram of RHO topology in $MB(Mim)_4$ ($M=Li^+$ or Cu^+); BN_4 tetrahedra are shown in orange, MN_4 tetrahedra in green, N in blue, and C

in black; the big yellow sphere represents the void space in α cage. Bottom: RHO topology with natural tiling $[4^{12}.6^8.8^6]+3[4^8.8^2]$.

Figure 3.5 Space filling diagrams of 4-ring $M_2B_2(4\text{-Mim})_4$ (left), 6-ring $M_3B_3(4\text{-Mim})_6$ (middle) and 8-ring $M_4B_4(4\text{-Mim})_8$ (right) in RHO (M=Li or Cu, B in orange, N in blue, M in green, C in black, and H in grey). Obviously, the pore aperture size of 8-ring is larger than that of 6-ring and 4-ring.

Figure 3.6 Left: The view of 2-D layer in BIF-12 viewed along *a* axis, the big spheres represent (±)-2-amino-1-butanol molecules. Right: 2-D (4.8^2) *fes* topology of BIF-12 (orange ball stands for boron, purple for lithium).

Figure 3.7 2-D structure of [MB(benzimidazolate)$_4$] (M = Li or Cu) in BIF-13 viewed from *c* axis.

Figure 3.8 N_2 gas sorption isotherm of BIF-3-Li (top) and BIF-3-Cu (bottom) at 77K. P/P_0 is the ratio of gas pressure (P) to saturation pressure (P_0), with P_0=769 torr.

Figure 3.9 CO_2 adsorption isotherms of BIF-3-Li and BIF-3-Cu at 273 K.

Figure 3.10 Nitrogen gas sorption isotherm at 77K for BIF-9-Li and BIF-9-Cu. P/P_0 is the ratio of gas pressure (P) to saturation pressure (P_0), with P_0=770 torr.

Figure 3.11 Gas sorption isotherm of BIF-9-Li and BIF-9-Cu for H_2 at 77K, and for CO_2 at 273K.

Figure 4.1 The powder X-ray diffraction (PXRD) pattern of OCF-42.

Figure 4.2 The energy dispersive X-ray (EDAX) spectroscopy of OCF-42-ZnGaGeSe-TMDP (left) and OCF-42-ZnGaSnSe-TMDP (right).

Figure 4.3 The 3-D open frameworks of OCF-42 viewed along *b* axis. The red sites highlight the location of T2 clusters and blue sites highlight the location of T4 clusters, and green sites highlight the location of Zn in T4 clusters. Note that the ratio between T4 and T2 clusters is 4, which is unprecedented for this type of materials.

Figure 4.4 The connectivity of T2 and T4 clusters in OCF-42. Each T2 cluster is connected to four T4 clusters (left), and each T4 cluster is corner-shared to one T2 and three T4 clusters (right).

Figure 4.5 Because T2 clusters can be treated as a single pseudo-tetrahedral site or a zeolite-type secondary building unit with four tetrahedral sites, two

different topological nets can be derived depending on the treatment of T2 clusters. Top: a new non-interpenetrated zeolitic topology in OCF-42 when only the T4 clusters are considered as the artificial 4-connected atom; Bottom: a new topological framework when both supertetrahedral T2 and T4 clusters are treated as 4-connected nodes.

Figure 4.6 Natural tilling framework with the symbol $[4^2.6^2]+2[6.8^2]+3[8^4]$ (…*mn*…means *n* kind of *m* face in each separate tilling) in OCF-42 when T2 and T4 supertetrahedral clusters were treated as artifical tetrahedral atoms. The net is in the RCSR database (http://rcsr.anu.edu.au) as "wut".

Figure 4.7 Thermogravimetric analysis of OCF-42-ZnGaGeSe-TMDP (top) and OCF-42-ZnGaSnSe-TMDP (bottom) in static air and flowing N_2 atmosphere.

Figure 4.8 PXRD of OCF-42-ZnGaGeSe-TMDP (left) and OCF-42-ZnGaSnSe-TMDP (bottom).

Figure 4.9 PXRD of the residue of OCF-42-ZnGaGeSe-TMDP heated at 1000^{o}C in air. The residue of OCF-42-ZnGaGeSe is identified as the mixture of cubic $ZnGa_2O_4$, monoclinic Ga_2O_3, and cubic Zn_2GeO_4 phase.

Figure 4.10 PXRD of residue of OCF-42-ZnGaSnSe-TMDP heated at 1000^{o}C in air. The residue of OCF-42-ZnGaSnSe treated in air at 1000^{o}C is composed of the mixture of cubic $ZnGa_2O_4$, monoclinic Ga_2O_3, and tetragonal SnO_2 phase.

Figure 4.11 Solid-state UV/Vis absorption spectra of OCF-42s.

Figure 4.12 Photoluminescent emission spectra of OCF-42 excited at wavelength 420nm.

Figure 5.1 The SEM picture of OCF-40-CuGaSnSe-PR: (a) rhombic dodecahedron shape. The rhombic dodecahedron shape is in agreement with the predicated crystal morphology (b) from the internal crystal structure according to Bravais Friedel Donnay Harker (BFDH) method.

Figure 5.2 The energy dispersive X-ray (EDAX) spectroscopy of OCF-5-CuGaSnSe-DPM (a), OCF-40-CuGaSnSe-PR (b), OCF-40-ZnGaSnSe-PR (c), OCF-40-CuGaSnS-PR d), OCF-40-ZnGaSnS-PR (e), OCF-40-MnGaSnSe-PR (f), OCF-40-ZnMnGaSnSe-PR (g), OCF-40-CuMnGaSnSe-PR (h), OCF-40-CuZnGaSnSe-PR (i) and OCF-40-CuZnMnGaSnSe-PR (j).

Figure 5.3 The powder X-ray diffraction (PXRD) patterns: (a) pure OCF-40-CuGaSnSe-PR; (b) pure OCF-40-ZnGaSnSe-PR; (c) pure OCF-40-CuGaSnS-PR; (d) pure OCF-40-ZnGaSnS-PR.

Figure 5.4 Possible transformation from OCF-5-CuGaSnSe-DPM to OCF-40-CuGaSnSe-PR triggered by gradual dissociation of DPM into piperidine.

Figure 5.5 (a) The two-fold interpenetrated (red and yellow) 3D framework constructed by corner-sharing supertetrahedral T4 clusters in OCF-5-MGaSnSe (M=Cu, Zn); (b) The isolated supertetrahedral T4 cluster surrounded by twenty-four protonated piperidine molecules in OCF-40s (red ball stands for Ga, orange for Se/S, yellow for Sn, green for Zn or Mn or mixed Cu/Ga, blue for N, grey for C, white for H).

Figure 5.6 (a) The body-centered cubic (BCC) packing pattern in one unit cell; (b) the spatial orientation of three adjacent piperidinium cations.

Figure 5.7 The Mulliken charge distribution of Se^{2-} at the four corners and six edge-centers by RB3LYP/LANL2DZ theoretical calculation on OCF-40-CuGaSnSe-PR (Pink ball stands for Ga, orange for Se, blue for Sn, red for Cu.)

Figure 5.8 The strong N-H···Se hydrogen bond formed between corner Se^{2-} and protonated piperidine viewed along one side of the cluster (a), down C_3 axis (b), edged Se^{2-} and protonated piperidine cations viewed down C_3 axis (c).

Figure 5.9 Effects of Cu^{+} vs. Zn^{2+} and Se^{2-} vs. S^{2-} on band structures in solution. The UV-Vis adsorption spectra of the filtrate of crystalline OCF-40s (15mg) immersed and stirred in 5ml DMSO, respectively, at room temperature.

Figure 5.10 Effects of Cu^{+} vs. Zn^{2+} and Se^{2-} vs. S^{2-} on band structures in solid state. Normalized solid-state UV-Vis absorption spectra of OCF-40s. The inset gives the photos of the as-synthesized crystalline materials.

Figure 5.11 Effects of different metal ions (Mn^{2+}, Cu^{+}/Mn^{2+}, Zn^{2+}/Mn^{2+}, Cu^{+}/Zn^{2+}, and $Cu^{+}/Zn^{2+}/Mn^{2+}$) on band structures. Normalized solid-state UV-Vis absorption spectra of OCF-40-MnGaSnSe-PR, OCF-40-CuMnGaSnSe-PR, OCF-40-ZnMnGaSnSe-PR, OCF-CuZnGaSnSe-PR and OCF-40-CuZnMnGaSnSe-PR.

Figure 5.12 The XRPD patterns of as-synthesized samples containing several different amine templates with OCF-5s (a) and OCF-40s (b) structures.

Figure 5.13 Effects of surface organic templates on band structures. Normalized solid-state UV-Vis absorption spectra of OCF-40-CuGaSnSe-4-MPR (band gap 1.80eV) and OCF-40-ZnGaSnSe-4-MPR (band gap 2.60eV), compared to OCF-40-CuGaSnSe-PR and OCF-40-ZnGaSnSe-PR.

Figure 6.1 The energy dispersive X-ray (EDAX) spectroscopy of OCF-n.

Figure 6.2 The powder X-ray diffraction patterns on OCF-1, OCF-5s and OCF-40.

Figure 6.3 The structures of OCF-1 (a), OCF-5 (b) and OCF-40 (c). The disordered amine template molecules in OCF-1 and OCF-5 are omitted for clarity. Red spheres stand for Ga, yellow for S, green for Zn, purple for Sn/Ga, orange for Se/S.

Figure 6.4 The labelling scheme for various Se^{2-} or S^{2-} sites in the T4 supertetrahedral cluster. The green spheres stand for Zn^{2+}, red for Ga^{3+}/Sn^{4+}, yellow for S^{2-}, orange for Se^{2-}/S^{2-}. L1 and L2 indicate the edge distance.

Figure 6.5 Illustration of selective elemental distribution in pentanary T4-ZnGaSnSeS cluster in OCF-5-ZnGaSnSeS-TMDP.

Figure 6.6 The size of five types of T4 clusters in OCF-5. The definition of L1 and L2 is shown in figure 6.4.

Figure 6.7 Normalized solid-state Uv-vis adsorption spectra of OCF-5-ZnGaSe-AEP and OCF-5-ZnGaSnSe-AEP, showing the red shift caused by Sn-doping.

Figure 6.8 Normalized solid-state Uv-vis adsorption spectra of OCF-1-ZnGaSeS-TMDP, OCF-5-ZnGaSnSeS-TMDP and OCF-42-ZnGaSnSe-TMDP.

Figure 6.9 Normalized solid-state Uv-vis adsorption spectra of OCF-5-ZnGaSnSe-ECHA and OCF-5-ZnGaSnSeS-ECHA, showing the blue shift caused by S-doping.

Figure 6.10 Normalized solid-state Uv-vis adsorption spectra of OCF-5-ZnGaSnSeS-TMDP, OCF-5-ZnGaSnSeS-DAMP and OCF-5-ZnGaSnSeS-ECHA.

Figure 7.1 Single network (left) with diamond topology (right) when P1 clusters in OCF-31 are treated as tetrahedral nodes. Tetrahedron in yellow is the sulfur atom in central anti-T1.

Figure 7.2 Connectivity of supertetrahedral chalcogenide cluster T3 (a) and T4 (b) crosslinked by imidazolate. Classical adamantane-like unit based on T3 cluster (c) and T4 cluster (d) in SCIFs. 3-D single net and two-fold

interpenetrated frameworks with diamond topology in SCIF-3 (e, f); single net and three-fold interpenetrated frameworks with diamond topology in SCIF-8 (g, h) viewed down the *b* axis, with ethyl group omitted for clarity. 3-D single and two-fold interpenetrated frameworks with diamond topology in SCIF-7 (i, j) and SCIF-9 (k, l), viewed down the *b* axis.

Figure 7.3 3-D single (a, c) and two-fold interpenetrated (b, d) frameworks with diamond topology in SCIF-1 and SCIF-2, respectively, viewed through *b* axis.

Figure 7.4 The normalized solid-state Uv-Vis absorption spectra of SCIF-3, -7, -8, -9.

Figure 7.5 The HOMO of T3-EIM-T3 molecular moiety in the perfect aligned (a, 0 degree distortion) and most distorted (b, 30 degree distortion) orientation, showing the p-π conjugation system between cluster and imidazolate.

Figure 7.6 Thermogravimetric analysis (TGA) for complex SCIF-3 under nitrogen atmosphere.

Figure 7.7 Powder X-ray diffraction patterns of SCIF-3.

Figure 7.8 CO_2 gas sorption isotherms of SCIF-3 at 273.15K.

List of Schemes

Scheme 1.1 Analogous geometrical configuration in metal imdazolate framework and silicate zeolite.

Scheme 1.2 Imidazolate and it derivatives used in PZMIFs.

Scheme 1.3 The extension of four-connected zeolitic frameworks.

Scheme 2.1 Schematic display of the relative orientation of imidazolate rings which is strongly affected by the steric hindrance of substituted groups, size of template molecules, and the interactions between the substituted groups and template molecules (top); Schematic display of the relative position of adjacent 8 nodes, such as M-M-M angle and M-M-M-M torsion angle tuned by different orientation of imidaozlate, which induce the different zeolitic topology and porosity (bottom).

Scheme 3.1 The charge distribution of all components in several neutral zeolitic frameworks.

Scheme 3.2 The syntheses of B-Im system ligands.

Scheme 4.1 Four different strategies to create supertetrahedral clusters and their co-assemblies through charge-complementary metal cations with different oxidization states. H^+-TMDP is protonated 4, 4'-trimethylenedipiperidine.

Scheme 5.1 Molecular structures and names of eight similar amine templates including their abbreviations.

Scheme 6.1 The structure of thiourea and sulfone molecules with different substituent groups used as sulfur sources.

Scheme 6.2 The name (including abbreviation) and structure of amine templates.

Scheme 6.3 Schematic of reactions in presence of different amine templates and auxiliary reactants. X means no crystalline products are obtained.

Scheme 7.1 Imidazole and its derivatives and template amine.

Scheme 7.2 Comparison on synthetic procedure of several chalcogenide superlattices with or without adding imidazole or its derivatives.

Chapter 1

Overview of Crystalline Microporous Zeolitic Materials

1.1 Crystalline Microporous Materials

Porous materials are of particular interest due to their various industrial applications that arise from their inherent uniform porosity and high surface area. Porous materials are regarded as solids or matrixes with an inter-connected network and confined pores or channels, which could be utilized as chambers for trapping small gas or liquid molecules, or as substrates for various size-and-shape-selective chemical catalytic reactions.

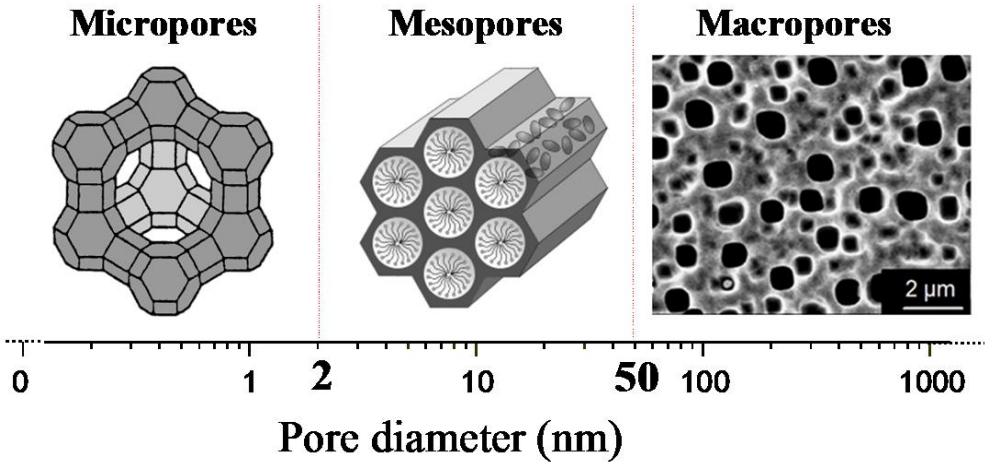


Figure 1.1 The IUPAC classification of porous materials on the basis of pore diameter.

There are a variety of porous materials differing in chemical composition, pore geometry and size, and degree of crystallinity. According to IUPAC notation,[1] materials with pore diameter greater than 50 nm are called macroporous materials, materials with pore diameter greater than 2 nm and less than 50 nm are called mesoporous materials,

and materials with pore diameter smaller than 2 nm are called microporous materials (Figure 1.1). Based on the difference in their chemical compositions, porous materials can be classified into pure inorganic porous materials (such as aluminosilicates) and carbon-based materials (such as activated carbons).[2-5] Porous materials can also be divided as crystalline materials (such as inorganic zeolites materials) and amorphous materials (such as activated carbons) based on degree of crystallinity. Different from non-crystalline materials, crystalline porous materials possess well-defined framework structure and pore size.

In this chapter, I would like to focus on the recent progress in the field of crystalline microporous materials, especially the materials with zeolitic frameworks which are composed of four-connected metal ions or metal clusters as nodes and bi-bridged inorganic anions or negatively-charged/neutral organic ligands as linkers. These materials show rich compositional diversity with tunable microporosity and interesting optical properties, which demonstrate their potential application in gas adsorption and separation, photocatalytic activity, etc.

1.1.1 Inorganic Zeolites

Zeolites, also called molecular sieves, are crystalline, highly porous solids with pore size below 20Å.[6] In general, these crystals consist of a three-dimensional pore system with interconnected tunnels, cages, or pores with precisely defined diameters. They are constructed by corner-sharing SiO_4 and AlO_4 tetrahedras. (Figure 1.2) These tetrahedras are the basic building blocks for various zeolite structures, such as zeolites A and X (the most common commercial adsorbents).[7] Due to the presence of trivalent

aluminium, zeolites usually exhibit a negatively-charged framework, which is balanced by positive cations (such as alkali metal ions or alkaline earth metal ions or protonated amines) and generates a strong electrostatic field distributing on the internal surface.

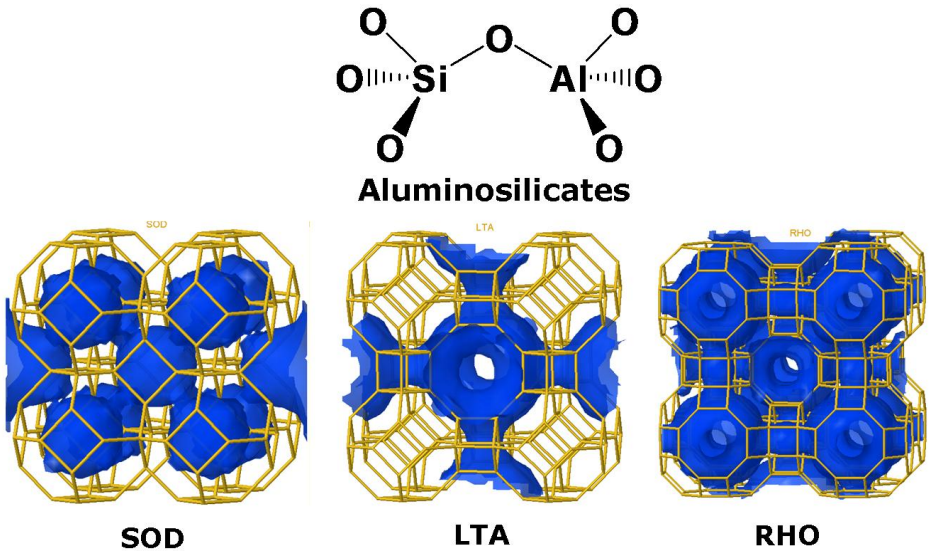


Figure 1.2. Basic structure of inorganic zeolite and three representative zeolite topologies.

Because of the typical structural features, zeolites exhibit adsorption, ion exchange, and catalysis properties, which make them useful in gas separation, detergent, and petroleum industry. Firstly, zeolites can act as a sponge to adsorb and trap small molecules in their crystal structures. This makes it useful as dry agents. Secondly, the embedded cations in zeolites can be exchanged with other cations to fine tune the pore size or the adsorption characteristics. The cations in the channels can also go through ion-exchange. For instance, zeolites with sodium ions can be used as water softening agent for processing hard water by exchanging Ca^{2+} or Mg^{2+} with Na^{+}. Their ability to soften water makes them widely used in the global laundry detergent market. In addition, many synthetic zeolites (such as ZSM-5) can also be used as catalysts in the petrochemical

industry, for instance in fluid catalytic cracking and hydro-cracking.[8] The protonated zeolites, prepared by ion-exchange, can be used as catalysts to facilitate acid-catalyzed reactions, such as isomerisation, alkylation, and cracking.

Following the great success made in zeolite molecular sieves, in 1982, Flanigen et al. reported the synthesis of aluminophosphate molecular sieves that extended crystalline aluminosilicate microporous materials to non-aluminosilicate compositions.[9] Inspired by this discovery, many research groups made considerable efforts in synthesizing open-framework materials by replacing framework cations (i.e. Al^{3+} or Si^{4+}) in zeolites with other cations (such as Ga^{3+}, Ge^{4+}, and P^{5+}), even transition metal cations (such as Co^{2+}, Fe^{3+}, and Mn^{2+}) were introduced.[10] In addition, the usage of structure-directing agents with various charge, size, and shape played an effective role in facilitating the formation of different zeolite frameworks. A large number of new porous materials, especially those containing extra-large pores, chiral frameworks, helical pores, and multidirectional intersecting channels have been synthesized. In comparison with the traditional aluminosilicate zeolites, the new family of crystalline oxide open-framework materials exhibited a wider range of chemical and physical properties.[11]

1.1.2 Porous Coordination Polymers (PCPs)

Increasing demands for various applications of porous materials have stimulated great research interests in creating inorganic-organic hybrid porous materials in order to overcome some of the limitations of pure inorganic metal oxide zeolite materials, such as low surface area and small pore size. Since 1990s, a new class of crystalline microporous hybrid materials, porous coordination polymers (PCPs, also called metal-organic

frameworks, MOFs), have undergone a rapid development and explosive growth.[12-18] PCPs represent an important and new type of inorganic-organic hybrid materials, and also represent a new development on the interface between molecular coordination chemistry and materials science.

Like its name as embodied, PCPs consist of metal ions or metal ion clusters coordinated to rigid or flexible organic molecules to form three-dimensional structures. Unlike oxygen bridges in inorganic zeolites, abundant organic linkers in PCPs, ranging from organic acids with di- or multi-carboxylate or phosphonate functional groups to N-containing heterocyclic ligands, extensively enrich their pore types and framework structures. Beside large amount of optional and easily-tailorable organic linkers, metal ions in PCPs can also be chosen from light-weight alkaline and alkaline earth metal ions to p-block main-group metal ions, and from transition metal ions to lanthanides, even actinides. Many stable secondary building units (SBUs) composed of metal oxide cluster have been created in PCPs, and are further used as tectons for rational design of PCPs with specific structure topology and pore size. [19]

Compared to conventionally microporous inorganic materials, such as zeolites, PCPs have exceptionally high porosity, extraordinary low density, high surface area, and uniform and tunable pore size, which seems to take advantage of the properties of both organic and inorganic porous materials. To be noticed, among PCPs' frameworks, organic ligands serving as linkers play an important role in controlling their pore size and shape, and make it possible to further functionalize their pore surfaces. So far, the surface area of some PCPs can be extended into many times of those of inorganic porous

materials through using long and large organic ligands as linkers.[20] Morever, some strategies, such as post-synthetic modification, have also been developed to obtain new functional materials. Such stable and tunable pores in a range of novel structures give rise to a great number of potential applications, such as gas separations and storage (hydrogen, methane and carbon dioxide), catalysis, as well as drug delivery. [21-29]

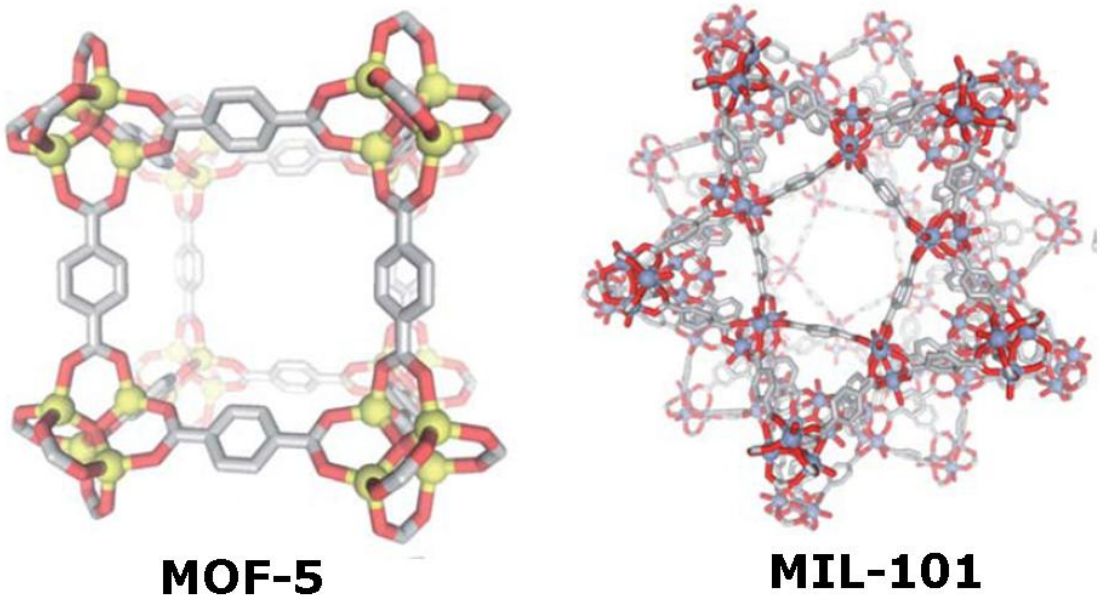


Figure 1.3. Two representative porous coordination polymers. (Reproduced with permission from ref. 37 copyright 2011 Royal Society of Chemistry)

Many reviews have been published which summarized the recent development of PCPs and their extensive applications in materials science.[30-37] There are two important PCPs that need to be mentioned here, MOF-5 and MIL-101, because the two representative PCPs have induced wide research interest in terms of their own structural characteristics and properties. (Figure 1.3) In 1999, Yaghi reported the first exceptionally stable and highly porous metal-organic framework, named MOF-5.[38] This material was obtained through the reaction of zinc nitrate with 1, 4-benzenedicarboxylate acid in the

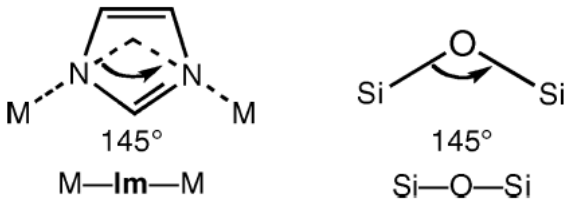
presence of hydrogen peroxide and DMF/chlorobenzene. Structure analysis shows that this material has primary cubic space group. Each oxide-centered metal cluster is connected to six organic linkers. The nitrogen gas sorption reveals a reversible type I isotherm. The surface area is as high as 2900 m^2/g. Later, in 2005, Férey created a crystal structure based on chromium terephthalate, MIL-101,[39] which has large pore sizes and high surface area. The material is assembled by corner-sharing supertetrahedra, which consist of Cr_3O trimers and 1, 4-benzenedicarboxylic acids. The supertetrahedra are microporous with an 8.6 Å free aperture. MIL-101 has an augmented three-dimensional MTN zeolite topology with a very large cell volume (702000 $Å^3$). MIL-101 is highly porous with BET and Langmuir surface areas of about 4100 ± 200 and 5900 ± 300m^2/g, respectively.

1.2 Porous Zeolitic Metal Imidazolate Frameworks (PZMIFs)

Although both inorganic zeolites and porous coordination polymers, as two important crystalline microporous materials, have attracted extensive attention for their practical or potential applications, these porous materials still have their own limitations. For example, small pore size and low surface area of zeolite have thus far restricted their applications only to small molecules, and PCPs have relatively lower thermal stability and hydro(solvo)thermal stability. In order to combine their respective advantages of these two important porous materials, much increasing interest is focused on the syntheses of porous zeolitic coordination polymers (PZCPs). Along this line, exploration on porous zeolitic metal imidazolate frameworks (PZMIFs) catches much more attention than other PZCPs.

1.2.1 Basic Design Concept on the Construction of PZMIFs

Coordination polymers constructed from tetrahedral building units and having zeolitic topologies are scarce.[40] Many attempts to construct PCPs with zeolitic topology based on the assembly of tetrahedral building units with linear rigid or flexible bidentate ligands have constantly led to the formation of a cubic diamond-like topology, which is regarded as the default structure for the assembly of extended frameworks from simple four-connected nodes, particularly single metal ions connected by flexible linkers. [41]



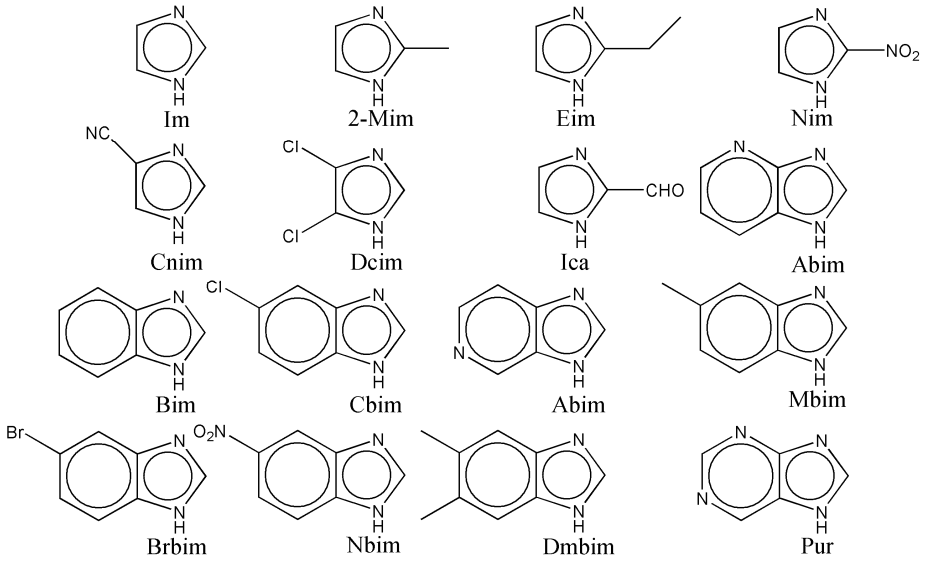
Scheme 1.1. Analogous geometrical configuration in metal imdazolate framework and silicate zeolite.

In 2002, You and co-authors reported a novel four-connected metal imidazolate framework, $[Co_5(Im)_{10}]$.[42] Although this framework has no pore opening, it exhibits neither the diamond topology nor the conventional zeolite structure, which is regarded as pioneering work on creating zeolitic coordination polymers with novel structure by using imidazolate as bridging ligands. The strategy for creating such metal imidazolate frameworks is based on expanding the zeolite topologies by construction of a tetrahedral building block, TX_4, in which the T-X-T angle is about 145. Imidazole was chosen as the linker X since the two-coordinate N atoms of this bidentate ligand are oriented at an angle of about 144, which is very close to the Si-O-Si angle of 145 in zeolites. (Scheme 1.1)

Based on above synthetic strategy, You et al continue exploring their idea to construct new porous zeolitic metal imidazolate frameworks,[43-45] however, all of these show no porosity until Huang and co-authors reported two PZMIFs in 2006.[46] Among these, Zn(2-methyl-imidazolate)$_2$ is a open framework with SOD topology, which is coded as ZIF-8 by Yaghi.[47] Notice that it is Yaghi's significant and fruitful work that stimulated a widespread interests in this area.

1.2.2 Framework Compositions and Topologies

As embodied by its name, zeolitic metal imidazolate frameworks (ZMIFs) are constructed from tetrahedrally-coordinated divalent metal ions (e.g., Zn^{2+}, Co^{2+}, Cu^{2+}, Cd^{2+}) bridged by imidazolate (Im^-) or its derivatives. Scheme 1.2 lists all imidazolate derivatives that have been used in the construction of PZMIFs. The substituted groups, some hydrophilic and some hydrophobic, can be used to effectively tune the properties of pore surface and its functionalization.



Scheme 1.2. Imidazolate and it derivatives used in PZMIFs.

Table 1.1. Composition, structure, and framework density of some reported zeolitic imidazolate frameworks arranged in decreasing framework density.

Composition	**Net** [a]	**Zeolite** [b]	**Cage Face**	***T*/*V*, nm^{-3}** [c]	**Ref.**
Zn(im)(mIm)	zni	—	$[6^3.12^2]$	4.62	[47]
$Zn(im)_2$	cag	—	$[4^2.6^8]$	3.68	[47]
$Zn(im)_2$	cag	—	$[4^2.6^8]$	3.66	[52]
$Zn(im)_2$	crb	BCT	$[6^2.8^2]$	3.64	[47,52]
$Co(im)_2$	nog	—	$[5^4.6^2.8^4]$	3.50	[42]
$Zn(im)_2$	nog	—	$[5^4.6^2.8^4]$	3.45	[52]
$Zn(abim)_2$	dia	—	$[6^4]$	3.31	[53]
Zn(nim)	frl	—	$[4^4.6^2.8^2]$	3.22	[53]
$Zn(dcim)_2$	lcs	—	$[6^5]$	3.16	[53]
$Zn(im)_2$	crb	BCT	$[6^2.8^2]$	2.80, 2.78	[47,52]
$Zn(im)_2$	dft	DFT	$[6^2.8^4]$	2.66, 2.56	[47,52]
$Zn(phim)_2$	sod	SOD	$[4^6.6^8]$	2.62	[50]
$Zn(eim)_2$	ana	ANA	$[6^2.8^3]$	2.57	[46]
$Zn(phim)_2$	sod	SOD	$[4^6.6^8]$	2.50	[47]
$Co(phim)_2$	sod	SOD	$[4^6.6^8]$	2.51	[47]
$Zn(mim)_2$	sod	SOD	$[4^6.6^8]$	2.47	[47]
$Zn(mim)_2$	sod	SOD	$[4^6.6^8]$	2.44	[46]
$Zn(im)_2$	gis	GIS	$[4^6.8^4]$	2.31, 2.47	[47,52]
$Zn(im)_2$	mer	MER	$[4^{12}.8^6]$	2.25	[47]
Zn(bim)(nim)	gme	GME	$[4^6.8^3.12^2]$	2.09	[47]
$Zn(purinate)_2$	lta	LTA	$[4^{12}.6^8.8^6]$	2.04	[51]
$Zn(phim)_2$	rho	RHO	$[4^{12}.6^8.8^6]$	2.01	[47]
$Co(phim)_2$	rho	RHO	$[4^{12}.6^8.8^6]$	2.01	[47]
$Zn(mim/eim)_2$	rho	RHO	$[4^{12}.6^8.8^6]$	1.92	[46]
$Zn(cbim)_2$	poz	—	$[3^{32}.4^{36}.8^2.10^8.12^4]$	1.51	[54]
$Zn(cbim)_2$	moz	—	$[3^{48}.4^{108}.12^{26}]$	1.29	[54]

[a] For definitions of three-letter abbreviations, see Reticular Chemistry Structure Resource (http://rcsr.anu.edu.au/). [b] See ref. [6]. [c] *T*/*V* is the density of metal atoms per unit volume. The cage face symbol [...n^m...] signifies that the cage has m faces that are n rings).

Based on the general consideration on the charge of frameworks, divalent metal (M^{2+}) ions are usually chosen as tetrahedral building unit to balance the negative charge of imidazolate ligands (Im^{-1}) for achieving neutral TX_2 frameworks. Recently, the Eddaoudi research group created zeolitic metal imidazolate frameworks with negative charge, which is balanced by protonated amine filled in the channels. [48, 49] In such materials, trivalent main-group metal ions (In^{3+}) are used as tetrahedral nodes and the ligand 4, 5-imidazoledicarboxylic acids are used as the bridging linkers. Later on, mono-valent metal ions have been used to build PZMIFs by our groups (see chapter 3).

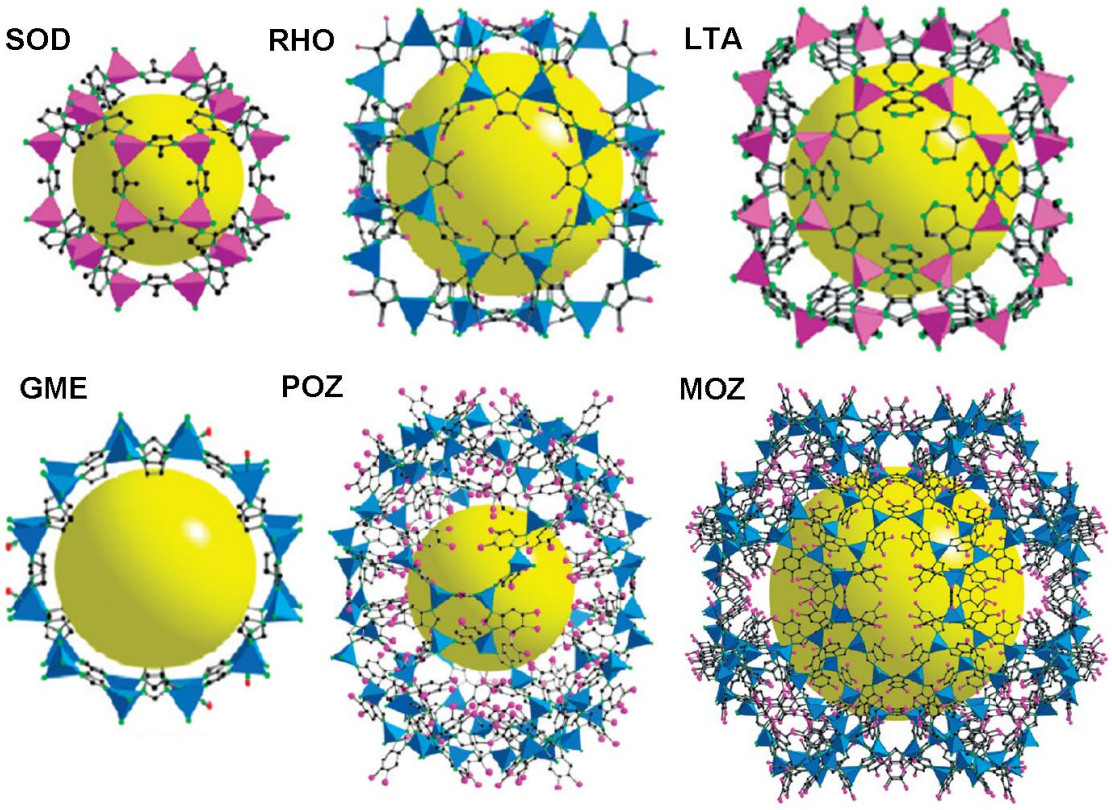


Figure 1.4. Selected crystal structures of porous zeolitic metal imidazolate frameworks with several main topologies. (Reproduced with permission from ref. 55 copyright 2009 American Chemical Society)

During the last six years, over 100 new zeolitic metal imidazolate framework structures have been created with different framework topologies.[55] Some of them possess the zeolite topologies, such as ANA, BCT, DFT, GIS, GME, LTA, MER, RHO and SOD, as shown in Table 1.1 and Figure 1.4. Several new types of topology (frl, lcs, neb, zni, poz and moz) are also found in PZMIFs, which have never been observed in zeolites or in other aluminosilicates or related materials. Two amazing PZMIFs reported by Yaghi's group need to be highlighted here. ZIF-95 and ZIF-100 display unprecedented structural complexity and novel topologies termed as poz and moz, respectively.[54] The most notable aspect of structure of ZIF-100 is a giant moz cage with 264 vertices (Figure 1.4). The outer and inner sphere diameters are around 67.2 and 35.6 Å, respectively, which are far larger than the diameters of the faujasite supercage in zeolite FAU (18.1 and 14.1Å) and the diameter of C60 (10.5Å).

One of the most desirable and intriguing topological features in inorganic zeolites is the 3-ring (i.e., rings with three tetrahedral atoms or T-atoms) because it has been proposed that the 3-ring can lead to low-framework density, large cavity and high pore volume. This discipline is also supported in the construction of PZMIFs. As shown in Table 1.1, the 3-ring is observed in two colossal cage, i.e. poz and moz, which is also accompanied with co-existence of 12-ring.

1.2.3 Synthetic Methods and Strategies

The typical synthesis of PZMIFs involves mixing the desired hydrated divalent transition metal salts and the imidazole units in a base solvent (such as DMF, or containing small amount of organic amine), and heating the mixtures to temperatures

ranging from 80 to 150 °C, followed by cooling reaction vials to room temperature. The molar ratio and concentration of the metal ions and imidazole units, as well as the reaction temperature are important in the formation of crystalline materials.

Extra-framework structure directing agents (e.g. tetraalkylammonium cations) play an important role in determining the framework topology. In the synthesis of inorganic zeolites, the structural diversities of the materials are in largely caused by the effect of various structural directing agents. However, in PZMIFs, while the structure directing effect of extra-framework species (usually solvents) may still be used to promote the crystallization and control the product topology, it is shown that the type of imidazolate ligand played a crucial role in creating novel zeolitic topologies. In addition to the ligand-solvent interaction, the ligand-ligand interaction has been recognized as a variable that can be utilized to control the framework topology. For example, two obvious different zeolite topologies, SOD and RHO, can be formed from 2-methylimidazolate and benzimidazolate, respectively. This indicated that the substitutions at the 4- and 5-positions of the Im unit produced sufficient steric hindrance to prevent the formation of a structure with the RHO topology. Since the ligand-ligand interactions can be tuned by the type, number, and position of substituents on the imidazolate ring, a smart synthetic strategy on mixing two or more complementary imidazolate ligands in the same assembly process has been adopted to achieve many new zeolitic topologies. High-throughput synthetic approach can be a very efficient way to screen the mixtures of different imidazole linkers and create different topologies. [53]

1.2.4 Porosity and Stability and Potential Applications

In comparison with inorganic zeolites, some of PZMIFs have much higher surface area. For example, the Langmuir surface areas of ZIF-8-SOD[47] and ZIF-70-GME [53], prepared in Yaghi's group, are1810 m^2/g and 1970 m^2/g, respectively. Later, Liu et al expand surface area of PZMIFs up to 3010 m^2/g by the approach of elongating the M-N bond (M=Cd), that represents the highest value among the currently discovered PZMIFs.[56]

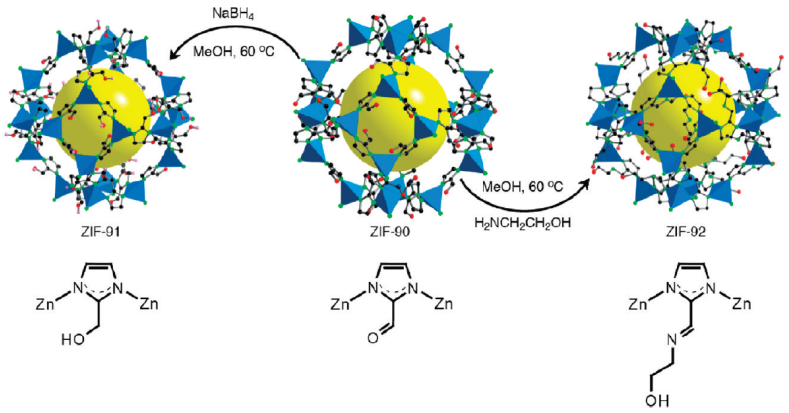


Figure 1.5. The functionalization of one PZMIF with aldehyde group. (Reproduced with permission from ref. 55 copyright 2009 American Chemical Society)

In addition to permanent porosity, many PZMIFs also exhibit remarkably high thermal and chemical stability. For example, ZIF-8 can be boiled in water, alkaline solutions, and refluxed in organic solvents without loss of crystallinity and porosity. The chemical and thermal stabilities of PZMIFs are much better than that of conventional PCPs. In addition, their frameworks also display high thermal stability (up to 500^oC) as anticipated for structures formed from robust linkers. The chemical stability of PZMIFs in both aqueous and organic solvents provides opportunity for the further modifications on the imidazole linkers of the frameworks without alternating their original structures.

For instance, the imidazolate-2-carboxyaldehyde linker in ZIF-90 could be reduced by $NaBH_4$ to the corresponding alcohol derivative, and converted into an imine functionality in refluxing methanol with the presence of corresponding amine reactant (Figure 1.5).[57]

High porosity allying with thermal stability make PZMIFs attractive candidates for many other applications such as gas storage, separation, and substrate for catalytic reaction. Beside certain hydrogen uptake capacity,[58] PZMIFs exhibit exceptional uptake capacities for CO_2 and can selectively separate CO_2 from industrially relevant gas mixtures (such as CH_4, CO, O_2, and N_2). [59-61] Yaghi claimed that 1L of ZIF-69 can store 82.6 L of CO_2 at 273 K, which displays a superior ability to store CO_2 in comparison to the industrially utilized adsorbent BPL carbon.[53] In addition, Xu et al employed ZIF-8 as a support for preparing nanoparticulate (NP) Au catalysts by a simple solid grinding method, which exhibited considerable activity in the gas phase CO oxidation.[62] Later, they also stabilized core-shell structured bimetallic NPs on ZIF-8 by a facile successive deposition-reduction method. This bimetallic Au@Ag NPs synergistically improved the catalytic activity of reduction of 4-nitrophenol (4-NPh) by $NaBH_4$ in water.[63]

1.3 Open-framework Metal Chalcogenides Based on Supertetrahedral Clusters

The intrinsic semiconducting properties of many bulk-phase metal chalcogenide materials endow them with lots of potential applications in material science, such as solar cells,[64] light-emitting diodes (LEDs),[65] thin-film transistors,[66] optical switches,[67] chemical sensors[68]. Since the first open-framework metal chalcogenide was reported by Bedard and co-workers in 1989,[69] research on crystalline porous metal-chalcogenide frameworks

with zeolitic structure has attracted great attention because such materials are capable of integrating porosity with semi-conductivity and inducing some potential applications.

1.3.1 Basic Design Concept and Construction of Open-Framework Chalcogenides

In general, the syntheses of new inorganic zeolite materials involve the replacement of tetrahedral metal ions by others. Resulting metal oxides are usually insulators and have very limited electric and optical applications. To expand microporous materials beyond their traditional applications, some researchers tried to synthesize microporous semiconducting materials. Different from the conventional cation substitution in the process of expanding four-connected inorganic zeolite frameworks, some creative research works were carried out to create microporous metal chalcogenides by replacing framework anions (O^{2-}) with chalcogenides (S^{2-} or Se^{2-}). Such microporous chalcogenides are expected to have potential applications in the areas such as shape- and size-selective sensors, high-surface-area photo-catalysts, and photo-electrodes device.

It is worth noting that, beside the chemically-related discrepancy of oxygen and sulfur atoms in their corresponding materials, these inorganic bridging linkers likewise exhibit difference in the construction of new type of zeolitic structures from the viewpoint of their structural chemistry. First of all, metal sulfides have long T-S bond distance (>2.1Å) and small T-S-T angles (between 105 and 115 degrees), which are much smaller than the typical T-O-T angles in metal oxides that usually range from 140^{o} to 150^{o}. This geometrical feature is desirable for the formation of 3-membered ring, which could lead to highly open frameworks with low framework density. Secondly, rich bridging modes (μ_n-S, n = 2, 3, 4) of sulfur have been found in metal sulfides, which

gives them more opportunity on the formation of new non-zeolitic porous structures than common metal oxide with only μ_2-O linker.

Original efforts to make porous metal chalcogenides began with germanium and tin sulfides with tetravalent metal ions.[70-72] These M(IV)-S (M=Ge or Sn) chalcogenides contain $[M_4S_{10}]^{4-}$ clusters (also called T2 cluster) formed through four MS_4-fused tetrahedras. These single-metal sulfide materials did not show open structure feature until the subsequent incorporation of low valent cations (such as Mn^{2+}, Fe^{2+}, Co^{2+}) into this M(IV)-S system.[73-76] Through combining tetravalent (M^{4+}) cations with trivalent (M^{3+}, such as Ga^{3+} and In^{3+}) cations in metal chalcogenides, our group synthesized a series of open-framework chalcogenides with new zeolitic topologies. Some materials in this series possess porosity and adequate stability toward ion exchange and thermal treatment. For example, UCR-20GaGeS has extended SOD topology with 3-membered rings. Its Cs^+-exchanged product exhibits the type I isotherm with surface area of 807 m^2/g and its pore size is as large as 9.5Å.[77]

Different from germanium or tin chalcogenides, pure indium and gallium chalcogenides could form three-dimensional frameworks balanced by protonated amine or inorganic cations. These M(III)-E (M = Ga or In; E = S or Se) open frameworks are usually composed of $[M_{10}E_{20}]^{10-}$ clusters, instead of $[M_4E_{10}]^{4-}$. such clusters are obviously larger than $M_4E_{10}^{4-}$ clusters, and contain both μ_2-E and μ_3-E coordination chalcogen.[78-82] In order to distinguish them from simple ME_4 unit, these large clusters were described as "supertetrahedral cluster" and denoted as T*n* clusters (*n* is the number of metal sites on each tetrahedral edge) by O'Keeffe and Yaghi *et al* because they have the basic

tetrahedral shape and all metal sites are tetrahedrally coordinated. Although these three-dimensional chalcogenide frameworks do not belong to typical zeolitic topology, they demonstrated four-connected network when "supertetrahedral clusters" were simplified and treated as a simple four-connected nodes or artificial tetrahedral atoms. During the subsequent efforts in enriching the compositions and frameworks of M(III)-E chalcogenides, the incorporation of monovalent (such as Cu^{+}) or divalent (such as Zn^{2+}, Cd^{2+}, Mn^{2+}, Co^{2+}, Fe^{2+}) metal cations into indium or gallium chalcogenide materials has produced many chalcogenides materials with new open framework topologies which are often based on the assembly of large supertetrahedral chalcogenide clusters.[83]

In fact, many years of efforts on preparing crystalline microporous chalcogenides have demonstrated that open-framework metal chalcogenides frequently consist of clusters serving as their structural secondary building units, which is dramatically distinct from single TX4 tetrahedra in most of metal oxide open-framework materials. Among various clusters (e.g. tetrahedron-shaped clusters, cubic clusters and semi-cubic clusters), tetrahedron-shaped clusters, have attracted increasing interest because they possess simple and symmetrical structures and can serve as artificial tetrahedral atoms to readily form zeolite-like porous semiconductors. So far, four different types of tetrahedral clusters have been created and classified as supertetrahedral clusters, penta-supertetrahedral clusters, capped-supertetrahedral clusters, and super-supertetrahedral cluster, which are denoted as T*n*, P*n*, C*n*, and T*p,q* respectively, in terms of their structural characteristics.[84,85] Among these clusters, supertetrahedral T*n* clusters are the most fundamental series and other series of clusters can be geometrically derived from

T*n* clusters. In this section, I just focus on supertetrahedral cluster (T*n*) since it is closely related to my dissertation.

1.3.2 Structure and Composition of Supertetrahedral Clusters

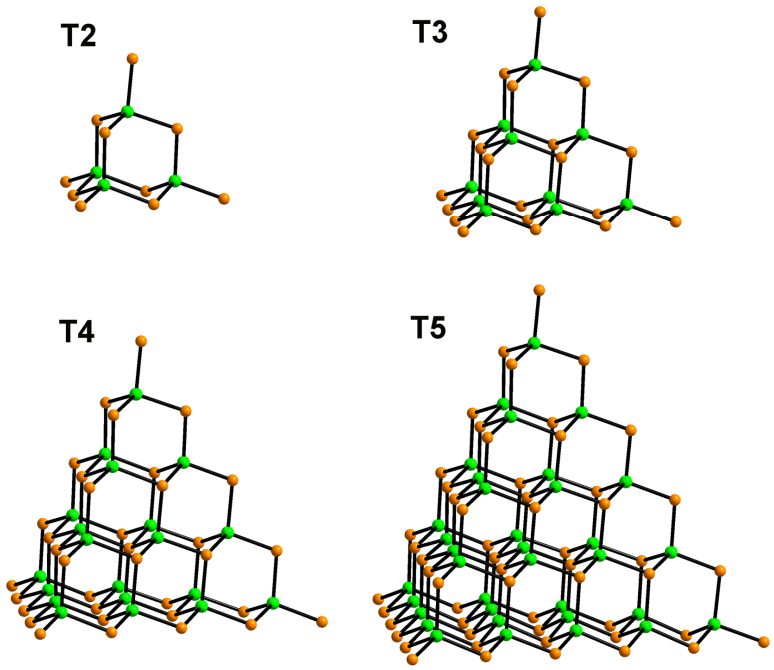


Figure 1.6 Ball-and-stick representation of T2, T3, T4 and T5 supertetrahedral clusters. Green ball stands for cation site, orange for anion site.

Supertetrahedral clusters (denoted as T*n* by Yaghi and O'Keeffe) are regular, tetrahedron-shaped fragments of the cubic ZnS type lattice, as shown in Figure 1.6 and Table 1.2 The number n represents the number of metal layers. The simplest case is T1 and it is just a tetrahedron with the composition of MX_4 (M = metal cation and X = S^{2-}, Se^{2-}, or Te^{2-}). For other isolated or discrete T*n* (n>2) clusters, the mathematical notation for the compositions of T2, T3, T4, T5 and Tn clusters are M_4X_{10}, $M_{10}X_{20}$, $M_{20}X_{35}$, $M_{35}X_{56}$, and M_xX_y (x=[n(n+1)(n+2)]/6; y=[(n+1)(n+2)(n+3)]/6), respectively, where M is a metal cation and X is a chalcogen anion. In general, the number of anions in a Tn

cluster is equal to the number of cations in a T(*n*+1) cluster. When these supertetrahedral clusters covalently connect each other through corner-shared mode, the overall stoichiometry of the framework varies with their pattern of connectivity. In a typical situation, each of four corners of a supertetrahedral cluster is bonded to other four supertetrahedral clusters to form an infinite 3-D framework, and the total number of anions per supertetrahedral cluster will be reduced by 2.

As mentioned before, discrete T2 cluster is the earliest achieved supertetrahedral cluster with a wide range of compositions, including $Ga_4E_{10}^{8-}$(E = S or Se),[86] $In_4E_{10}^{8-}$,[86] $Ge_4E_{10}^{4-}$,[87,88] $Sn_4E'_{10}^{4-}$ (E' = Se or Te)[89-91] and $M_4(ER)_{10}^{2-}$ (M = Zn^{2+}, Cd^{2+}, Mn^{2+}, Fe^{2+}, Co^{2+}, or Hg^{2+}; R = an organic group).[92-95] Some of these have been adopted as artificial atoms or secondary building units (SBU) for the construction of 2-D or 3-D frameworks. In addition to the discrete T3 clusters with capped-organic ligands, such as $M_{10}E_4(ER)_{16}^{4-}$, $M_{10}E_4(ER)_{12}L_4$ (M= Cd^{2+}, Zn^{2+}, or Hg^{2+}; E = S, Se or Te; R = an organic group; L = terminal ligand), [92, 96-97] and $[Ga_{10}S_{16}(L)_4]$ (L=3,5-dimethypyridine),[98] some "naked" T3 clusters ($M_{10}X_{18}^{6-}$, M = Ga, In; X = S or Se) are also found in covalently-connected three-dimensional frameworks.[81,99-101] Prior to this work, no isolated T4 cluster was synthesized. All of these T4 clusters were synthesized as $M_4In_{16}S_{35}^{10-}$ (M = Mn, Fe, Co, Zn, Cd)[83,99] or $Zn_4Ga_{16}S_{35}^{10-}$ (E = S or Se)[101,102] and were involved in 3-D open framework structures. The largest supertetrahedral cluster synthesized so far is the T5 cluster with the composition of $[Zn_{13}In_{22}S_{56}]^{20-}$ or $[Cu_5In_{30}S_{56}]^{17-}$.[103,104] These T5 clusters occur in covalent two- and three-dimensional superlattices and are not yet known in the isolated form.

Table 1.2 A summary of compositions of isolated supertetrahedral clusters (Tn).

n	Stoichiometry	Compositons
1	MX_4	$[ME_4]^{6-}$ (M = Zn, Mn, Co, Fe, Cd); $[ME_4]^{5-}$ (M = In, Ga); $[ME_4]^{4-}$ (M = Sn, Ge; E = S, Se, or Te; $M(SPh)_4^{2-}$ (M = Zn, Cd); $[M(SPh)_4]^-$ (M = Ga, In); $[Sn(SPh)_4]$
2	M_4X_{10}	$[Ge_4E_{10}]^{4-}$ (E = S, Se); $[Sn_4E_{10}]^{4-}$(E = S, Se, Te); $[M_4S_{10}]^{8-}$ (M = Ga, In); $[In_4Se_{10}]^{8-}$, $[M_4(SPh)_{10}]^{2-}$ (M = Zn, Fe, Co, Cd); $[(Ga_x/In_x)(Ge_y/Sn_y)E_{10}]^{(20-3x-4y)-}$ (x+y = 4, E = S or Se)
3	$M_{10}X_{20}$	$[M_{10}S_{20}]^{10-}$ (M = In, Ga); $[M_{10}Se_{20}]^{10-}$ (M = In, Ga); $[M_{10}E_4(SPh)_{16}]^{4-}$ (M = Zn, Cd; E = S, Se; Ph), $[Zn_{10}S_4(SEt)_{12}Et_4]^{4-}$ (Et = ethyl); $[Ga_{10}S_{16}(L)_4]^{2-}$ (L = 3,5-lutidine) ; $[M_5Sn_5S_{20}]^{10-}$ (M = Zn, Co)
4	$M_{20}X_{35}$	$[M_4In_{16}S_{35}]^{14-}$ (M = Mn, Fe, Co, Zn, Cd); $[Zn_4Ga_{16}E_{35}]^{14-}$ (E = S, Se)
5	$M_{35}X_{56}$	$[Cu_5In_{30}S_{56}]^{17-}$; $[Zn_{13}In_{22}S_{56}]^{20-}$
6	$M_{56}X_{84}$	none
7	M_xX_y	none

As concluded in Table 1.2, the number of T*n* clusters with sulfide compositions is dramatically greater than that of selenides and tellurides. Moreover, with the increasing size of T*n* cluster, the total number of metal sites and non-metal sites could go up to one hundred, which provide more possibility to create multi-component supertetrahedral clusters with tunable optical properties. However, prior to this work, no more than two metal cations co-exist in one supertetrahedral cluster, and few open-framework chalcogenides contain sulfide and selenide simultaneously. Especially, for high valent main-group metal ions (such as Sn^{4+}), they frequently occur in T1 and T2 clusters, not in T3 clusters, except one example $[M_5Sn_5S_{20}]^{10-}$ (M=Zn, Co), which was also regarded as the largest isolated naked cluster without any capped or terminal organic ligands.[105]

1.3.3 Connectivity and Framework Topology Based on T*n* Cluster

For most of supertetrahedral T*n* clusters in open-framework chalcogenide superlattices, the metal sites adopt tetrahedral coordination geometry. Chalcogen anions can be tri-coordinated, even tetra-coordinated chalcogenide anions T4 and T5 clusters. So the whole frameworks can not be simply viewed as zeolitic prototype. In order to well understand the structure of chalcogenide frameworks and establish the relationship between these frameworks and structurally-known zeolites, all supertetrahedral clusters in 3-D frameworks are usually simplified as artificial or pseudo tetrahedral atoms by ignoring the internal structure of the clusters. With such simplification, 3-D chalcogenide frameworks can be regarded as four-connected network which is similar to zeolitic topology. There are eight four-connected topologies reported in metal chalcogenide system: single and double diamond, ABW, CrB_4, SOD, UCR-1, ICF-24, and ICF-25. In contrast to metal oxide system, the number of topological frameworks in chalcogenide system is much less, which could be attributed to the fact that the angle of T-X-T (X = S or Se) is not flexible and smaller than that of T-O-T. Therefore, to expand the number of framework types in chalcogenide superlattices, it would be important to overcome this structural disadvantage.

It is worth noting that the above simplification of network takes consideration of the structure geometry only and does not consider the difference in the size of supertetrahedral clusters and bridging ligands between clusters. In fact, even though the same size of Tn clusters prefer assembling into 3-D framework during crystallization, clusters with different sizes can also be assembled into 3-D framework. For instance, the

reaction of discrete T2 cluster $[Ge_4S_{10}]^{4-}$ with divalent transition metal ions leads to three-dimensional frameworks with single-diamond lattice, where tetrahedral nodes sites is alternately occupied by T1 and T2 clusters (i.e., T1-T2 superlattice). The second example is T3-T4 superlattices occurring in UCR-19 with double-diamond lattice.[99, 106] Prior to our work, no other chalcogenide superlattices with dual-size Tn clusters have been reported. It is especially rare with the clusters that have big differences in size ($\triangle n \geq 2$). In addition to the different sized clusters, different types of linkers can also be used to construct extended framework structures. The most common case is the single two-connected corner-sharing S^{2-} or Se^{2-}. A two-connected polysulfide anions (S_3^{2-}) linkers were found in UCR-18.[99] Vaqueiro *et al* successfully developed a method that can replace inorganic linkers with neutral nitrogen-containing heterocyclic ligands. In that case, 1, 2-di(4-pyridyl)ethylene or 4,4'-bipyridine replaced sulfide anions at the corner of T3 $[Ga_{10}S_{20}]$ cluster. Framework materials with zero-, one-, two-dimensions have been obtained[107-109] Unfortunately, no Tn-based 3-D framework containing neutral organic linkers or negatively-charged organic linkers was reported prior to our work.

1.3.4 Selected Properties and Potential Applications of Chalcogenide Supperlattices

Crystalline open-framework chalcogenide materials integrating porosity with semi-conductivity have many interesting properties with potential applications.

First, highly negatively-charged anionic open frameworks make them useful as inorganic ion exchangers. The large amount of protonated organic amines trapped in the cages or channels can be replaced by small sized inorganic cations (such as Li^+, Na^+) to

give materials porosity. For example, organic cations in UCR-20GaGeS-TAEA could be almost completely ion-exchanged by Cs^+ at room temperature, and the resulting product exhibits the type I isotherm characteristic of a microporous system.[77] The exchanges among different inorganic cations are also interesting. An open-framework sulfide material, $K_6Sn[Zn_4Sn_4S_{17}]$, showed highly selective ion-exchange properties for Cs^+ and NH_4^+ ions.[110] In addition, due to the high polarizability of anionic framework and weak interaction with inorganic charge-balanced cations, chalcogenide framework materials exhibited fast-ion conductivity.[77] For example, at 18 ºC, the conductivity of ICF-5CuInS-Na ranges from 1.0×10^{-4} Ω^{-1} cm^{-1} under 0.2% relative humidity to 1.2×10^{-2} Ω^{-1} cm^{-1} under 100% relative humidity. At room temperature, the conductivity of ICF-26 ranges from 0.011 Ω^{-1} cm^{-1} at 29.8% relative humidity to 0.15 Ω^{-1} cm^{-1} under 100% relative humidity, which is the highest specific conductivity achieved among crystalline open framework chalcogenides.

Moreover, different form most of metal oxides with wide band gaps, porous metal chalcogenide materials have relatively narrow band gaps, and have proved to be efficient photo-catalysts for the water splitting in visible region (Figure 1.7). For example, upon irradiation with visible light, about 18 μmol h^{-1} g^{-1} of H_2 gas was produced from an aqueous solution of Na_2S (0.5 M, as sacrificial agent) with the ICF-5CuInS-Na as catalyst.[111] Compared to two anhydrous dense phases with similar compositions ($CuInS_2$ with the cubic ZnS structure and $CuIn_5S_8$ with the spinel structure), the efficiency of ICF-5-CuInS is much higher, which could been understood by the more active sites available in this open framework material. However, the poor stability of metal chalcogenide

catalysts limit their practical application since *in situ* generated holes can oxidize the sulfide atoms in the framework. As a result, sacrificing agents are needed during the water-splitting process.

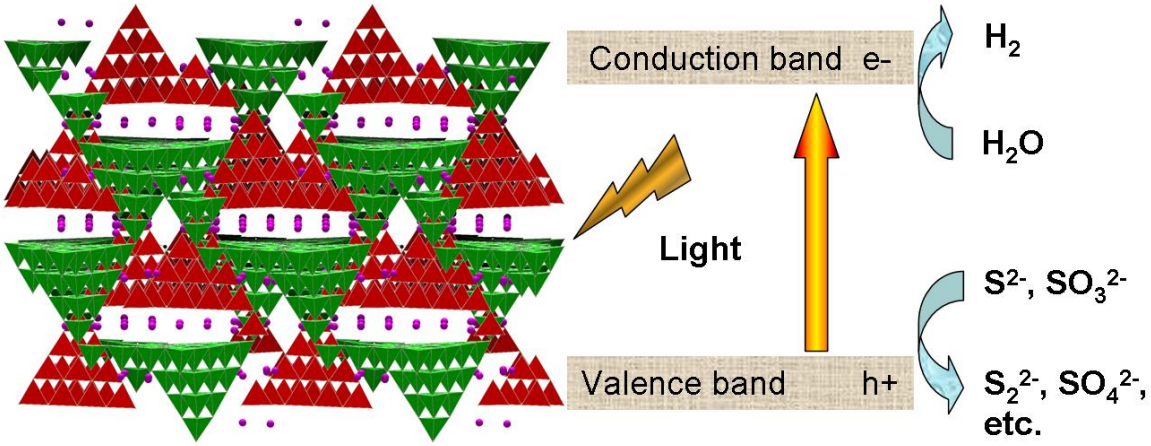
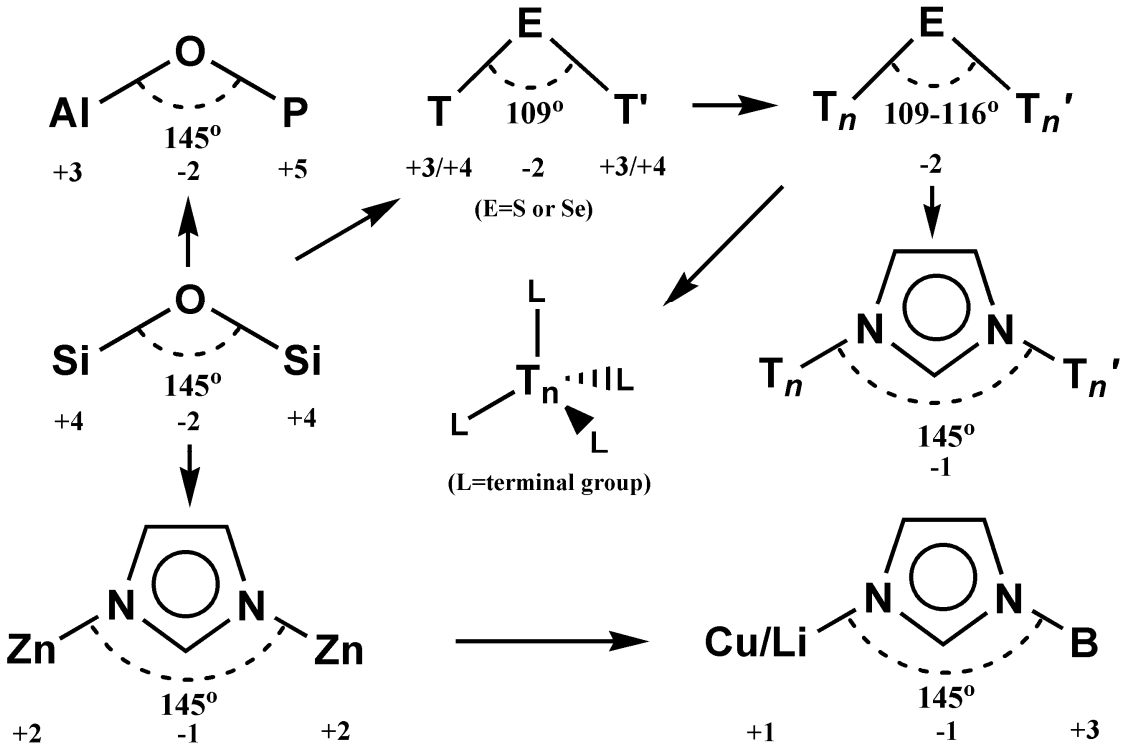


Figure 1.7. The 3D diamond-type superlattice of ICF-5CuInS-Na serving as photocatalysts for water splitting.

The use of doping to tune electronic structures is a well-established method in band gap engineering that has been successfully used for many years in dense phase solid materials. In open framework solids within a given compositional domain, the band gap can also be tuned by controlling pore geometry in addition to adjusting chemical compositions. These cluster-based open framework materials provide an additional level of control over the electronic properties through the porosity and spatial assemblies of clusters. For example, open-framework chalcogenide materials with the same gallium selenides compositions and different structures show band gaps ranging from 1.4 to 1.7 eV. Their corresponding structures with gallium sulfide compositions show smaller band gap ranging from 2.6 to 2.8 eV).[101] It appears that the framework anions have a much more dramatic impact on the band gap than framework cations.

Open-framework metal chalcogenides have also been found to display photoluminescence with tunable emission wavelengths ranging almost continuously from 440 to 600 nm by varying their framework compositions and structures.[99]

1.4 Contribution from This Work



Scheme 1.3. The extension of four-connected zeolitic frameworks with different compositions.

Creation of new crystalline microporous materials is an important topic due to their practical or potential application in chemical industry. Researchers are interested in developing solid porous materials with either novel chemical compositions or new framework topologies because the properties and applications of porous materials are intimately related to their compositional and topological features. During the past decade, our research group has made extraordinary progress in the creation of crystalline open-

framework metal chalcogenides with zeolitic topology. These open-framework chalcogenide materials with semiconducting properties could be regarded as an extension with respect to traditional four-connected inorganic zeolite materials. In this thesis, we continue expanding four-connected crystalline porous materials and enriching their compositions and framework topologies. All of the synthesized materials can be related to traditional inorganic zeolites, as shown in Scheme 1.3.

PZMIF can be considered as the combination of both traditional inorganic zeolites and PCPs because the Si-O-Si angle in zeolites is coincident with that of the bridging angle in the M-Im-M. In chapter 2, by introducing substituted imdazole ligands into PZMIF system together with mix-linker synthetic strategy, several novel zeoltic topologies with 3-ring and large ring have been obtained. These topologies are new and have never been observed in inorganic zeolites.[112,113] The work highlights the significance of framework building units in the control of the framework topology.

Utilizing strategy based on charge separation of node atoms and charge balance principle, a new family of boron imidazolate open-framework materials by cross-linking 4-connected boron imidazolate complexes with 4-connected Li^+ or Cu^+ centers is rationally designed and synthesized. This work is discussed in chapter 3.[114-116] The compositions of these materials are very unique compared to either inorganic zeolites or metal-organic framework materials. It represents a unique family of materials that border between MOFs and covalent frameworks because the tetrahedral vertices (B, Li, and Cu) are joined together by a combination of covalent (B-N) and coordination bonds (Li-N and Cu-N).

In chapter 4, the first quaternary 3-D open-framework selenide superlattices based on T2 and T4 dual-sized supertetrahedral clusters have been synthesized using three types of charge-complementary and yet geometry-matching metal cations. Such charge-complementary metal cations could control the cluster size and co-assembly through differing bond valence requirements of *di*-, *tri*-, and *tetra*-coordinated Se^{2-} sites. The cluster-scale phase separation controlled by charge-complementary metal cations illustrates that a high degree of control is possible even in the complicated quaternary compositions.

When the size of semiconductors becomes smaller and smaller and reaches the extreme situation as is the case in chalcogenide supertetrahedral clusters, different chemically distinct sites occur, which can dramatically affect the doping chemistry at different sites and also spatial assembly of such clusters into covalent superlattices. In chapter 5, we use the Zn-Ga-Se supertetrahedral clusters and their frameworks as the model system to examine the doping chemistry of Sn^{4+} and S^{2-} in the Zn-Ga-Se clusters. The cooperative effect of amine-templating, Sn- and/or S-doping leads to a rich chemical system with tunable framework compositions, topologies, and electronic properties.

Some types of T*n* clusters can also be synthesized in the discrete form, allowing them to exist as soluble species in solution. In addition to their tunable electronic and optical properties, these soluble clusters can be used as unique precursors for the synthesis of novel porous semiconducting and optical materials. In chapter 6, we report a family of discrete chalcogenide T4 clusters. These T4 clusters are the largest molecular

T*n* clusters known to date and can be made in various compositions showing tunable band structures in both solution and solid state.

Chapter 7 displays a family of 3-D covalent arrays of supertetrahedral chalcogenide clusters and imidazolate ligands. These materials represent the first examples of supertetrahedral clusters being assembled with anionic ligands. This work demonstrated the possibility of integrating metal chalcogenides and zeolitic metal imidazolate materials. The work also represents a significant step forward for the metal chalcogenide chemistry because of the demonstrated feasibility to use organic ligands to covalently assemble *larger* supertetrahedral clusters into even *higher* dimensions (3-D).

1.5 References

(1) Sing, K. S. W. *Pure Appl. Chem.*, **1985**, *57*, 603-619.

(2) Breck, D. W. *Zeolite Molecular Sieves: Structure, Chemistry, and Use*, **1974**, Wiley, New York.

(3) Meier, W. M.; Olsen, D. H.; Baerlocher, C. *Atlas of Zeolite Structure Types*, **1996**, Elsevier, London.

(4) Venuto, P. B. *Microporous Mater.*, **1994**, *2*, 297-411.

(5) Kresge, C. T.; Leonowicz, M. E.; Roth, W. J.; Vartuli, J. C.; Beck, J. S. *Nature*, **1992**, *359*, 710-712.

(6) Baerlocher, Ch.; McCusker, L. B.; Olson, D. H. *Atlas of Zeolite Framework Types*, **2007**, 6th revised edition, Elsevier.

(7) Brunner, G. O. *Zeolites*, **1990**, *10*, 612-614.

(8) Dyer, A. *An Introduction to Zeolite Molecular Sieves*, **1988**, John Wiley & Sons.

(9) Wilson, S. T.; Lok, B. M.; Messina, C. A.; Cannan, T. R.; Flanigen, E. M. *J. Am. Chem. Soc.*, **1982**, *104*, 1146-1147.

(10) Cheetham, A. K.; Férey, G.; Loiseau, T. *Angew. Chem. Int. Ed.*, **1999**, *38*, 3282-3292.

(11) Davis, M. E. *Nature* **2002**, *417*, 813-821.

(12) Janiak, C. *Angew. Chem. Int. Ed. Engl.* **1997**, *36*, 1431-1434.

(13) Batten, S. R.; Robson, R. *Angew. Chem. Int. Ed.* **1998**, *37*, 1460-1494.

(14) Blake, A. J.; Champness, N. R.; Hubberstey, P.; Li, W.-S.; Withersby, M. A.; Schröder, M. *Coord. Chem. Rev.* **1999**, *183*, 117-138.

(15) Eddaoudi, M.; Moler, D. B.; Li, H.; Chen, B.; Reineke, T. M.; O'Keeffe, M.; Yaghi, O. M. *Acc. Chem. Res.* **2001**, *34*, 319-330.

(16) Evans, O. R.; Lin, W. *Acc. Chem. Res.* **2002**, *35*, 511-522.

(17) Kitagawa, S.; Kitaura, R.; Noro, S. *Angew. Chem. Int. Ed.* **2004**, *43*, 2334-2375.

(18) Fang, Q.-R.; Makal, T. A.; Young, M. D.; Zhou, H.-C. *Comments on Inorganic Chemistry*, **2010**, *31*, 165-195.

(19) Tranchemontagne, D. J.; Mendoza-Cortés, J. L.; O'Keeffe, M.; Yaghi, O. M. *Chem. Soc. Rev.* **2009**, *38*, 1257-1283.

(20) Furukawa, H.; Ko, N.; Go, Y. B.; Aratani, N.; Choi, S. B.; Choi, E.; Yazaydin, A. O.; Snurr, R. Q.; O'Keeffe, M.; Kim, J.; Yaghi, O. M. *Science* **2010**, *239*, 424-428.

(21) Horcajada, P.; Serre, C.; Maurin, G.; Ramsahye, N. A.; Balas, F.; Vallet-Regi, M.; Sebban, M.; Taulelle, F.; Férey, G. *J. Am. Chem. Soc.* **2008**, *130*, 6774-6780.

(22) Park, Y. K.; Choi, S. B.; Kim, H.; Kim, K.; Won, B. H.; Choi, K.; Choi, J. S.; Ahn, W. S.; Won, N.; Kim, S.; Jung, D. H.; Choi, S. H.; Kim, G. H.; Cha, S. S.; Jhon, Y. H.; Yang, J. K.; J. Kim, *Angew. Chem. Int. Ed.* **2007**, *46*, 8230-3233.

(23) Farrusseng, D.; Aguado, S.; Pinel, C. *Angew. Chem. Int. Ed.* **2009**, *48*, 2-14.

(24) Ma, L. Q.; Abney, C.; Lin, W. B. *Chem. Soc. Rev.* **2009**, 38, 1248-1256.

(25) Murray, L. J.; Dincã, M.; Long, J. R. *Chem. Soc. Rev.* **2009**, *38*, 1294-1314.

(26) Czaja, A. U.; Trukhan, N.; Müller, U. *Chem. Soc. Rev.* **2009**, *38*, 1284-1293.

(27) Spokoyny, A. M.; Kim, D.; Sumrein, A.; Mirkin, C. A. *Chem. Soc. Rev.* **2009**, *38*, 1218-1227.

(28) Lee, J. Y.; Farha, O. K.; Roberts, J.; Scheidt, K. A.; Nguyen, S. T.; Hupp, J. T. *Chem. Soc. Rev*. **2009**, *38*, 1450-1459.

(29) Wang, Z.; Cohen, S. M. *Chem. Soc. Rev.* **2009**, *38*, 1315-1329.

(30) Li, J. R.; Kuppler, R. J.; Zhou, H. C. *Chem. Soc. Rev.* **2009**, *38*, 1477-1504.

(31) Férey, G.; Serre, C. *Chem. Soc. Rev.* **2009**, *38*, 1380-1399.

(32) Chen, B. L.; Xiang, S. C.; Qian, G. D. *Acc. Chem. Res.* **2010**, *43*, 1115-1124.

(33) Kuppler, R. J.; Timmons, D. J.; Fang, Q.-R.; Li, J.-R.; Makal, T. A.; Young, M. D.; Yuan, D.; Zhao, D.; Zhuang, W.; Zhou, H.-C. *Coor. Chem. Rev.* **2009**, *253*, 3042-3066.

(34) Tranchemontagne, D. J.; Ni, Z.; O'Keeffe, M.; Yaghi, O. M. *Angew. Chem. Int. Ed.* **2008**, *47*, 2-14.

(35) Perry IV, J. J.; Perman, J. A.; Zaworotko, M. J. *Chem. Soc. Rev.* **2009**, *38*, 1400-1417.

(36) Allendorf. M. D.; Bauer, C. A.; Bhakta, R. K.; Houk, R. J. T. *Chem. Soc. Rev.* **2009**, *38*, 1330-1352.

(37) Shimomura, S.; Kitagawa, S. *J. Mater. Chem.* **2011**, *21*, 5537-5546.

(38) Li, H.; Eddaoudi, M.; O'Keeffe, M.; Yaghi, O. M *Nature* **1999**, *402*, 276-279.

(39) Férey, G.; Mellot-Draznieks, C.; Serre, C.; Millange, F.; Dutour, J.; Surblé, S.; Margiolaki, I. *Science* **2005**, *309*, 2040-2042.

(40) Fang, Q.-R.; Zhu, G.-S.; Xue, M.; Sun, J.-Y.; Wei, Y.; Qiu, S.-L.; Xu, R.-R. *Angew. Chem. Int. Ed.* **2005**, *44*, 3845-3848.

(41) O'Keeffe, M.; Eddaoudi, M.; Li, H.; Reineke, T.; Yaghi, O. M. *J. Solid State Chem.* **2000**, *152*, 3-20.

(42) Tian, Y. Q.; Cai, C. X.; Ji, Y.; You, X. Z.; Peng, S. M.; Lee, G. S. *Angew. Chem. Int. Ed.* **2002**, *41*, 1384-1386.

(43) Tian, Y. Q.; Cai, C. X.; Ren, X. M.; Duan, C. Y.; Xu, Y.; Gao, S.; You, X. Z. *Chem. Eur. J.* **2003**, *9*, 5673-5685.

(44) Tian, Y.-Q.; Chen, Z. X.; Weng, L.-H.; Guo, H. B.; Gao, S.; Zhao, D. Y. *Inorg. Chem.* **2004**, *43*, 4631-4635.

(45) Tian, Y.-Q.; Xu, L.; Cai, C.-X.; Wei, J.-C.; Li, Y.-Z.; You, X. Z. *Eur. J. Inorg. Chem.* **2004**, 1039-1044.

(46) Huang, X.-C.; Lin, Y.-Y.; Zhang, J. P.; Chen, X.-M. *Angew. Chem. Int. Ed.* **2006**, *45*, 1557-1559.

(47) Park, K. S.; Ni, Z.; Côté, A. P.; Choi, J. Y.; Huang, R.; Uribe-Romo, F. J.; Chae, H. K.; O'Keeffe, M.; Yaghi, O. M. *Proc. Natl Acad. Sci. USA* **2006**, *103*, 10186-10191.

(48) Liu, Y.; Kravtsov, V. Ch.; Larsen, R.; Eddaoudi, M. *Chem. Commun.* **2006**, 1488-1490.

(49) Liu, Y.; Kravtsov, V. Ch.; Eddaoudi, M. *Angew. Chem., Int. Ed.* **2008**, 47, 8446-8449.

(50) Huang, X.-C.; Zhang, J.-P.; Chen, X.-M. *Chin. Sci. Bull.* **2003**, *48*, 1531-1534.

(51) Hayashi, H.; Côté, A. P.; Furukawa, H.; O'Keeffe, M.; Yaghi, O. M. *Nature Materials* **2007**, *6*, 501-506.

(52) Tian, Y.-Q.; Zhao, Y.-M.; Chen, Z.-X.; Zhang, G.-N.; Weng, L.-H.; Zhao, D.-Y. *Chem. Eur. J.* **2007**, *13*, 4146-4154.

(53) Banerjee, R.; Phan, A.; Wang, B.; Knobler, C.; Furukawa, H.; O'Keeffe, M.; Yaghi, O. M. *Science* **2008**, *319*, 939-943.

(54) Wang, B.; Côté, A. P.; Furukawa, H.; O'Keeffe, M.; Yaghi, O. M. *Nature* **2008**, *453*, 207-212.

(55) Phan, A.; Doonan, C. J.; Uribe-Romo, F. J.; Knobler, C. B.; O'Keeffe, M.; Yaghi, O. M. *Acc. Chem. Res*, **2009**, *43*, 58-67.

(56) Tian, Y.-Q.; Yao, S.-Y.; Gu, D.; Cui, K.-H.; Guo, D.-W.; Zhang, G.; Chen, Z.-X.; Zhao, D.-Y. *Chem. Eur. J.* **2010**, *16*, 1137-1141.

(57) Morris, W.; Doonan, C. J.; Furukawa, H.; Banerjee, R.; Yaghi, O. M. *J. Am. Chem. Soc.* **2008**, *130*, 12626-12627.

(58) Wu, H.; Zhou, W.; Yildirim, T. *J. Am. Chem. Soc.* **2007**, *129*, 5314-5315.

(59) Banerjee, R.; Furukawa, H.; Britt, D.; Knobler, C.; O'Keeffe, M.; Yaghi, O. M. *J. Am. Chem. Soc.*, **2009**, *131*, 3875-3877.

(60) Morris, W.; Leung, B.; Furukawa, H.; Yaghi, O. K.; He, N.; Hayashi, H.; Houndonougbo, Asta, Y. M.; Laird, B. B.; Yaghi, O. M. *J. Am. Chem. Soc.*, **2010**, *132*, 11006-11008.

(61) Pérez-Pellitero, J.; Amrouche, H.; Siperstein, F. R.; Pirngruber, G.; Nieto-Draghi, C.; Chaplais, G.; Simon-Masseron, A.; Bazer-Bachi, D.; Peralta, D.; Bats, N. *Chem. Eur. J.* **2010**, 16, 1560-1571.

(62) Jiang, H.-L.; Liu, B.; Akita, T.; Haruta, M.; Sakurai, H.; Xu, Q. *J. Am. Chem. Soc.* **2009**, *131*, 11302-11303.

(63) Jiang, H.-L.; Akita, T.; Ishida, T.; Haruta, M.; Xu, Q. *J. Am. Chem. Soc.* **2011**, *133*, 1304-1306.

(64) Huynh, W. U.; Dittmer, J. J.; Alivisatos, A. P. *Science*, **2002**, *295*, 2425-2427.

(65) Nizamoglu, S.; Ozel, T.; Sari, E.; Demir, H. V. *Nanotechnology*, **2007**, *18*, 1-5.

(66) Ridley, B. A.; NiVi, B. Jacobson, J. M. *Science*, **1999**, *286*, 746-749.

(67) Erlacher, A.; Miller, H.; Ullrich *J. Appl. Phys*. **2004**, *95*, 2927-2929.

(68) Somers, R. C.; Bawend, M. G.; Nocera, D. G. *Chem. Soc. Rev.* **2007**, *36*, 579-590.

(69) Bedard, R. L.; Wilson, S. T.; Vail, L. D.; Bennett, J. M.; Flanigen, E. M. *Stud. Surf. Sci. Catal. A* **1989**, *49*, 375-387.

(70) Nellis, D. M.; Ko, Y; Tan, K.; Koch, S.; Parise, J. B. *Chem. Comm.* **1995,** *541-542*.

(71) MacLachlan, M. J.; Petrov, S.; Bedard, R. L.; Manners, I.; Ozin, G. A. *Angew. Chem. Int. Ed.* **1998,** *37,* 2076-2079.

(72) Cahill, C. L.; Ko, Y; Hanson J. C.; Tan, K.; Parise, J. B. *Chem. Mater.* **1998,** *10,* 1453-1458.

(73) Yaghi, O. M.; Sun, Z.; Richardson, D. A.; Groy, T. L. *J. Am. Chem. Soc.* **1994**, *116,* 807-808.

(74) Bowes, C. L.; Lough, A. J.; Malek, A.; Ozin, G. A.; Petrov, S.; Young, D. *Chem. Ber.* **1996**, *129*, 283-287.

(75) Ahari, H.; Garcia, A.; Kirkby, S.; Ozin, G. A.; Young, D.; Lough, A. J. *J. Chem. Soc., Dalton Trans.* **1998,** 2023-2027.

(76) Cahill, C. L.; Parise, J. B. *Chem. Mater.* **1997**, *9*, 807-811.

(77) Zheng, N.; Bu, X.; Wang, B.; Feng, P. *Science* **2002**, *298*, 2366-2369.

(78) Cahill, C. L.; Ko, Y; Parise, J. B. *Chem. Mater.* **1998,** *10,* 19-21.

(79) Cahill, C. L.; Parise, J. B. *J. Chem. Soc., Dalton Trans.* **2000**, 1475-1482.

(80) Cahill, C. L.; Gugliotta B.; Parise, J. B. *Chem. Comm.* **1998,** 1715-1716.

(81) Li, H.; Laine, A.; O'Keeffe, M.; Yaghi, O. M. *Science* **1999**, *283*, 1145-1147.

(82) Li, H.; Eddaouli, M.; Laine, A.; O'Keeffe, M.; Yaghi, O. M. *J. Am. Chem. Soc*. **1999**, *121*, 6096-6097.

(83) Li, H.; Kim, J.; Groy, T. L.; O'Keeffe, M.; Yaghi, O. M. *J. Am. Chem. Soc*. **2001**, *123*, 4867-6868.

(84) Feng, P.; Bu, X.; Zheng, N. *Acc. Chem. Res.* **2005**, *38*, 293-303.

(85) Bu, X.; Zheng, N.; Feng, P. *Chem. Eur. J.* **2004**, 10, 3356-3362.

(86) Krebs, B.; Voelker, D.; Stiller, K. *Inorg. Chim. Acta* **1982**, *65*, L101-L102.

(87) Krebs, B. *Angew Chem., Int. Ed.* **1983,** *22*, 113-134.

(88) Krebs, B.; Henkel, G. *Angew Chem. Int. Ed.* **1991,** *30*, 769-788.

(89) Ahari, H.; Lough, A.; Petrov, S.; Ozin, G. A.; Bedard, R. L. *J. Mater. Chem.* **1999**, *9*, 1263-1274.

(90) Park, C. W.; Pell, M. A.; Ibers, J. A. *Inorg. Chem.* **1996**, *35*, 4555-4558.

(91) Pirani, A. M.; Mercier, P. A.; Dixon, D. A.; Borrmann, H.; Schrobilgen, G. J. *Inorg. Chem.* **2001**, *40*, 4823-4829.

(92) Dance, I. G.; Choy, A.; Scudder, M. L. *J. Am. Chem. Soc.* **1984**, *106*, 6285-6295.

(93) Dance, I. G. *J. Am. Chem. Soc.* **1979**, *101*, 6264-6273.

(94) Costa, T.; Dorfman, J. R.; Hagen, K. S.; Holm, R. H. *Inorg. Chem.* **1983,** *22*, 4091-4099.

(95) Hagen, K. S.; Berg, J. M.; Holm, R. H. *Inorg. Chim. Acta* **1980,** *45*, L17-L18.

(96) Behrens, S.; Bettenhausen, M.; Eichhofer, A.; Fenske, D. *Angew Chem. Int. Ed.* **1998,** *36*, 2797-2799.

(97) Eichhofer, A.; Deglmann, P. *Eur. J. Inorg. Chem.* **2004,** 349-355.

(98) Vaqueiro, P.; Romero, M. L. *Chem. Commun.* **2007**, 3282-3284.

(99) Zheng, N.; Bu, X.; Feng, P. *J. Am. Chem . Soc .* **2003,** *125*, 1138-1139.

(100) Wang, C.; Bu, X.; Zheng, N.; Feng, P. *Chem. Commun.* **2002**, *13*, 1344-1345.

(101) Bu, X.; Zheng, N.; Wang, X.; Wang, B.; Feng, P. *Angew. Chem. Int. Ed.* **2004**,*43*, 1502-1505.

(102) Wang, C.; Li, Y.; Bu, X.; Zheng, N.; Feng, P. *J. Am. Chem. Soc.* **2002**, *124*, 12944-12945.

(103) Bu; X.; Zheng, N.; Feng, P. *J. Am. Chem. Soc.* **2002**, *124*, 12646-12647.

(104) Zheng, N.; Bu, X.; Feng, P. *Nature,* **2003**, *426*, 428-432.

(105) Zimmermann, C. ; Anson, C. E. ; Weigend, F.; Clérac, R; Dehnen, S. *Inorg. Chem.* **2005**, *44*, 5686-5695.

(106) Vaqueiro, P.; Romero,M. L. *J. Phy. Chem. Sol.* **2007**, *68*, 1239-1243.

(107) Vaqueiro, P.; Romero, M. L. *J. Am. Chem. Soc.* **2008**, *130*, 9630-9631.

(108) Vaqueiro, P.; Romero, M. L. *Inorg. Chem.* **2009**, *48*, 810-812.

(109) Vaqueiro, P.; Romero, M. L.; Rowan, B. C.; Richards, B. S. *Chem. Eur. J.* **2010**, *16*, 4462-4465.

(110) Manos, M. J.; Chrissafis, K.; Kanatzidis, M. G. *J. Am. Chem. Soc.*, 2006, **128**, 8875-8883.

(111) Zheng, N.; Bu, X.; Vu, H.; Feng, P. *Angew. Chem. Int. Ed.*, **2005**, *44*, 5299-5303.

(112) Wu, T.; Bu, X.; Zhang, J.; Feng, P. *Chem. Mater.* **2008**, *20*, 7377-7382.

(113) Wu, T.; Bu, X.; Liu, R.; Lin, Z.; Zhang, J.; Feng, P. *Chem. Eur. J.* **2008**, *14*, 7771-7773.

(114) Wu, T.; Zhang, J.; Bu, X.*; Feng, P. *Chem. Mater.* **2009**, *21*, 3830-3837.

(115) Wu, T.; Zhang, J.; Zhou, C.; Wang, L.; Bu, X; Feng, P. *J. Am. Chem. Soc.* **2009**, *131*, 6111-6113.

(116) Zhang, J.; Wu, T.; Zhou, C.; Chen, S.; Feng, P.; Bu, X. *Angew. Chem. Int. Ed.* **2009**, *48*, 2542-2545.

(117) Wu, T.; Wang, X. Q.; Bu, X.; Zhao, X.; Wang, L.; Feng, P. *Angew. Chem. Int. Ed.* **2009**, *48*, 7204 -7207.

(118) Wu, T.; Bu, X.; Zhao, X.; Khazhakyan, R.; Feng, P. *J. Am. Chem. Soc.* **2011**, *133*, 9616-9625.

(119) Wu, T.; Wang, L.; Bu, X.; Chau, V., Feng, P.*J. Am. Chem. Soc.* **2010**, *132*, 10823-10831.

(120) Wu, T.; Khazhakyan, R.; Wang, L.; Bu, X.; Zheng, S.; Chau, V.; Feng, P. *Angew. Chem. Int. Ed.* **2011**, *50*, 2536-2539.

Chapter 2

Porous Zeolitic Metal Imidazolate Frameworks

2.1 Introduction

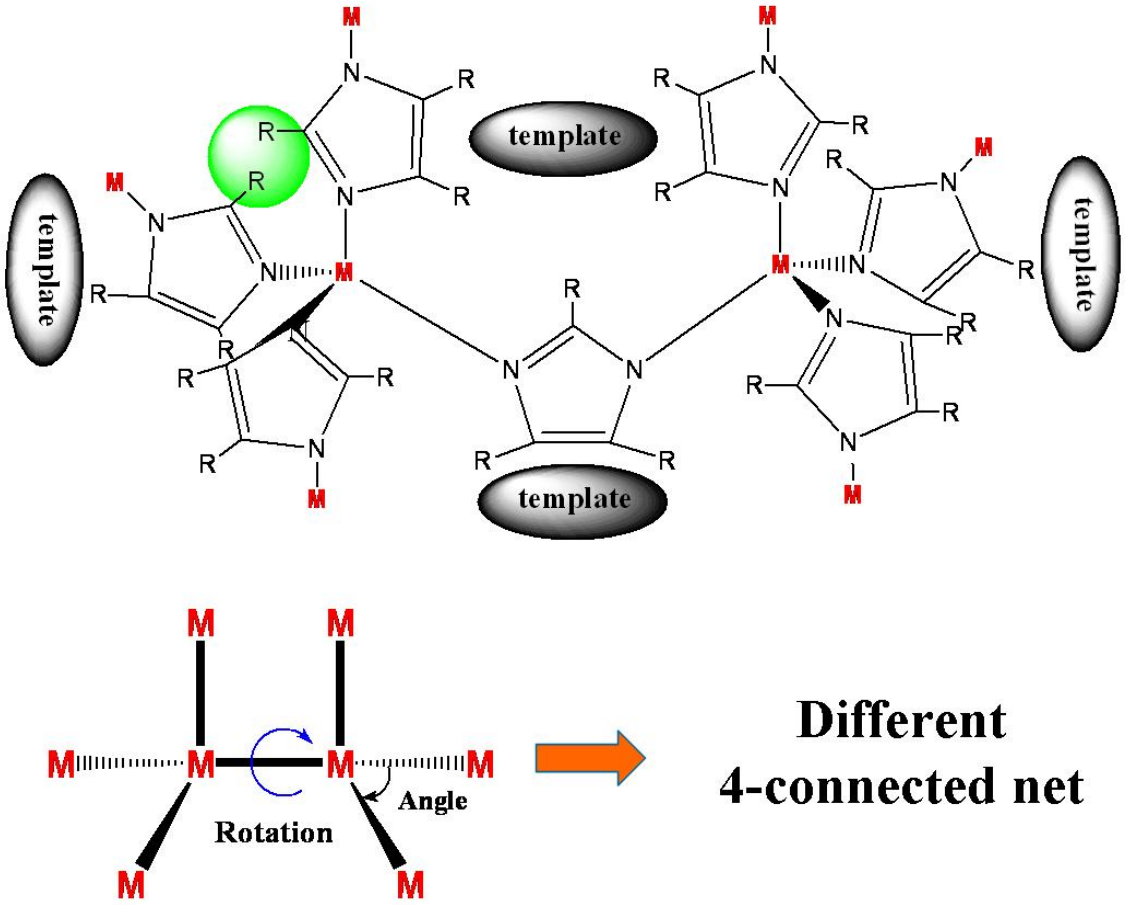
As two important families of crystalline microporous materials, porous inorganic framework materials (e.g., zeolites) and metal-organic frameworks (MOFs) have attracted much attention because of their applications in gas adsorption, separation, and catalysis etc.[1-9] In recent years, in order to combine their respective advantages, an increasing interest has been directed at synthetic development of metal-organic frameworks with topological features characteristic of those in 4-connected zeolites.[10-15] Among various efforts to extend zeolite framework types in MOFs and to tune their compositional and topological features, the exploration of tetrahedral imidazolate frameworks has been particularly successful.[11-15] In 4-connected imidazolate frameworks, divalent metal ions (such as Zn^{2+}, Co^{2+}) replace T atoms (tetrahedral atoms such as Si, Al, P) and imidazolates (Im^-) substitute for bridging O^{2-} in zeolites, resulting in a number of 4-connected frameworks with the general framework composition of $M(im)_2$ and topological types such as ANA(analcite), BCT, DFT, GIS(gismondine), GME(gmelinite), LTA, MER(merlinoite), RHO, and SOD(sodalite).

For zeolite scientists, one of the most desirable and intriguing topological features is the 3-ring (i.e., rings with three tetrahedral atoms or T-atoms, not counting bridging oxygen atoms), because it has been proposed that the 3-ring can lead to low-framework density and high pore volume.[16] Unfortunately, the 3-ring only occurs infrequently in 4-

connected structures because of the inherent strain associated with the small ring size.[17] Thus one synthetic strategy to create topologies with 3-rings is to lengthen the T-O distance. One specific example is the use of larger T-atoms such as Ge (compared with Al and Si).[18] Intuitively, the large T-L distance in the imidazolate framework should be conducive to the formation of 3-rings. However, despite some significant progresses, none of the known metal imidazolate frameworks is known to have 3-rings. Furthermore, these metal imidazolate frameworks contain only small and medium pore opening (i.e., eight or tem T-atoms in the ring). Another current limitation of known imidazolate structures is that they tend to adopt the same framework topology as those already found in aluminosilicate or phosphate structures.

In addition, in the synthesis of zeolites, extra-framework structure directing agents (e.g. tetraalkylammonium cations) play an important role in determining the framework topology. The structural diversity of zeolites is in a large part due to the effect of various structural directing agents. In metal imidazolates, while the structure directing effect of extra-framework species (usually solvents) may still be used to promote the crystallization and control the product topology, another important factor, the type of imidazolate ligand, has become a focus in the research into creating novel zeolitic topologies. In addition to the ligand-solvent interaction, the ligand-ligand interaction in metal imidazolates has been recognized as a variable that can be utilized to control the framework topology.[14b] Such ligand-ligand interactions can be tuned by the type, number, and position of substituents on the imidazolate ring. They can also be tuned by using two or more complementary imidazolate ligands in the same assembly process. So an in-

depth understanding of ligands' orientation and ligand-ligand interactions is vital for rational construction of novel zeolitic imidazolate frameworks (Scheme 2.1). One obstacle to the understanding of the role of ligand is the possible orientational disorder of the imidazolate ligand in a porous framework. Such a tendency to be disordered should be stronger when two different ligands are co-assembled into the same framework, particularly if the two ligands used do not differ significantly.



Scheme 2.1. Schematic display of the relative orientation of imidazolate rings which is strongly affected by the steric hindrance of substituted groups, size of template molecules, and the interactions between the substituted groups and template molecules (top); Schematic display of the relative position of adjacent 8 nodes, such as M-M-M angle and M-M-M-M torsion angle tuned by different orientation of imidaozlate, which induce the different zeolitic topology and porosity (bottom).

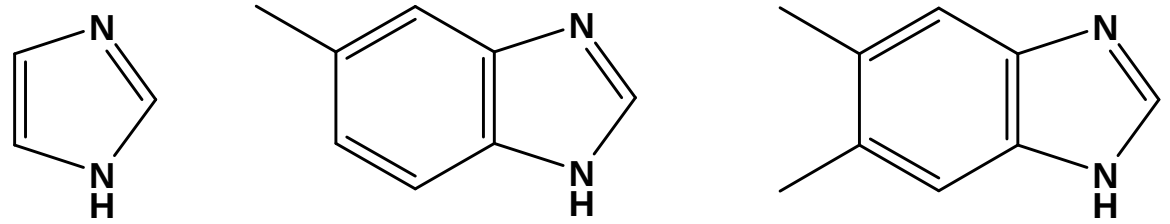
It is worth noting that prior to this work the 16-ring is not known in any 4-connected zeolite-type structures.

Here, we report five zeolitic structures (denoted as **TIF-n**, TIF = tetrahedral imidazolate framework, *n* = 1-5, Table 2.1) prepared by using the single-ligand or mixed-ligand synthetic strategy. These five structures exhibit five types of 4-connected topology. **TIF-1** possesses a previously unknown topology and highly open microporous framework. This new framework features both 3- and 16-rings (in addition to 4-, 10- and 12-rings), two new types of loop configurations, and multi-dimensional intersecting large pore channels. Other four **TIFs** are synthesized through the selection of two complementary ligands: one small-sized imidazole ligand with no substituent groups and one large-sized ligand with a relatively large substituent group (5-methylbenzimidazole, or 5, 6-dimethylbenzimidazole). An attractive feature of **TIF-2** and **TIF-3** is its cubic structural building unit (also called double four-ring units, d4R) which is well-known because of its presence in the industrially important zeolite A. However, the organization of d4R units in **TIF-2** and **TIF-3** is totally different from that in zeolite A. **TIF-2** has an unprecedented 4-conected topology and features one-dimensional large pore channels (i.e., the pore window with 12 tetrahedral vertices). **TIF-3** possesses the distorted body-centered cubic (bcc) arrangement of d4R units and its topological type (ACO) has not been previously found in metal imidazolates. **TIF-4** and **TIF-5** also have 4-connected tetrahedral frameworks and they are of particular interest because the strict ordering of two complementary ligands in their frameworks provides a unique opportunity for probing their synergistic effect in the self-assembly process.

Table 2.1. A Summary of Crystal Data and Refinement Results. [a]

Name	Framework Compostion	S. G.	*a* (Å)	*b* (Å)	*c* (Å)	*β* (°)	*R* (F)%	Net
TIF-1	$Zn(DMBim)_2$	$P4_2/mnm$	30.8800(8)	30.8800(8)	33.781(2)	90	11.79	*zea*
TIF-2	$Zn(Im)_{1.10}(MBim)_{0.90}$	*Pnma*	17.6356(5)	48.0644(13)	24.5539(7)	90	9.55	*zeb*
TIF-3	$Zn(Im)_x(MBim)_y$	*C2/c*	25.9164(10)	24.8826(10)	17.9542(6)	93.206(3)	12.70	*ACO*
TIF-4	$Zn(Im)_{1.5}(MBim)_{0.5}$	*Pbca*	15.6251(9)	16.3217(9)	18.1244(10)	90	7.09	*cag*
TIF-5-Zn	Zn(Im)(DMBim)	$I4_1/a$	16.7862(2)	16.7862(2)	21.3384(5)	90	9.38	*GIS*
TIF-5-Co	Co(Im)(DMBim)	$I4_1/a$	16.6286(2)	16.6286(2)	21.4148(4)	90	6.52	*GIS*

[a] Structures were solved from single-crystal data collected at 150K on a SMART CCD diffractometer with Mo Kα. $R(F) = \Sigma||F_o|-|F_c||/\Sigma|F_o|$ with $F_o > 4.0\sigma(F)$.



Imidazole (Im) | 5-Methyl-benzimidazole (5-MBim) | 5,6-Dimethyl-benzimidazole (5,6-DMBim)

Scheme 2.2 Imidazole and it derivatives.

2.2 Experimental Section

2.2.1 Materials and General Methods

All reagents and solvents employed in these synthetic studies were commercially available and used as supplied without further purification. Powder X-ray diffraction data were collected using a Bruker D8-Advance powder diffractometer operating at 40kV, 40mA with Cu Kα(λ =1.5406 Å) radiation (2θ range, 2-40°; step, 0.03°; scan speed, 60 s/step). Fourier-transform infrared spectra of sample prepared as KBr pellets were measured using a Nicolet FT-IR Impact 400 system.

2.2.2 Solvothermal Syntheses

Synthesis of TIF-1: $Zn(Ac)_2 \cdot 2H_2O$ (118.8mg), 5,6-dimethylbenzimidazole (157.6mg), (±)-2-amino-1- butanol (4.0mL) and benzene(3.2mL) are mixed in a Teflon-lined autoclave and stirred for half an hour. The autoclave was then sealed and heated at 150ºC for 5 days, followed by cooling to room temperature. A large amount of colorless crystals were obtained with a yield of 43.2% (based on zinc salt). The crystals were washed using ethanol three times and dried in air for other measurements. IR data for as-synthesized **TIF-1** (KBr, cm^{-1}): 1475s, 1337m, 1203m, 1167w,1093w, 1021w, 848m, 813w, 648w.

Synthesis of TIF-2: $Zn(Ac)_2 \cdot 2H_2O$ (117.8mg, 0.5367mmol), 5-methylbenzimidazole (70.3mg, 0.5320mmol), imidazole (44.2mg, 0.6492mmol), (±)-2-amino-1-butanol (4.0mL) and benzene (3.6mL) are mixed in a Teflon-lined autoclave and stirred for half an hour. The autoclave was then sealed and heated up at 150ºC for 5 days, followed by cooling down to room temperature. A large amount of small colorless

crystalline materials were obtained with a yield of 35.4 % (based on zinc salt). The crystals were washed using ethanol three times and dried in air for other measurements. Elemental analysis of as-synthesized sample: C 49.22; H 4.02; N 20.98. Elemental analysis of sample dried at 300^{o}C: C 47.93; H 3.78; N 20.78.

Synthesis of TIF-3: $Zn(Ac)_2 \cdot 2H_2O$ (116.2mg, 0.5294mmol), 5-methylbenzimidazole (71.2mg, 0.5387mmol), imidazole (41.7mg, 0.6125mmol), (±)-2-amino-1- butanol (4.0mL) and benzene(0.4mL) are mixed in a Teflon-lined autoclave and stirred for half an hour. The autoclave was then sealed and heated up at 150ºC for 6 days, followed by cooling to room temperature. Small colorless crystals were obtained as a minor phase, accompanied with a large amount of unidentified polycrystalline powder.

Synthesis of TIF-4: $Zn(Ac)_2 \cdot 2H_2O$ (114.5mg, 0.5216mmol), 5-methylbenzimidazole (26.9mg, 0.2035mmol), imidazole (57.6mg, 0.8461mmol), 3-amino-1-propanol (4.0mL) and benzene(2.0mL) are mixed in a Teflon-lined autoclave and stirred for half an hour. The autoclave was then sealed and heated up at 150ºC for 5 days, followed by cooling to room temperature. A large amount of colorless octahedral crystalline materials were obtained with a yield of 42.3 % (based on zinc salt). The crystals were washed using ethanol three times and dried in air for other measurements.

Synthesis of TIF-5-Zn: $Zn(Ac)_2 \cdot 2H_2O$ (122.7mg, 0.5590mmol), 5, 6-dimethylbenzimidazole (77.2mg, 0.5281mmol), imidazole (60.7mg, 0.8916), (±)-2-amino-1- butanol (3.0mL) and *p*-xylene (1.0mL) are mixed in Teflon-lined autoclave and stirred for half an hour. The autoclave was then sealed and heated up at 150ºC for 5 days, followed by cooling to room temperature. A large amount of colorless crystalline

materials were obtained with a yield of 35.5 % (based on zinc salt). The crystals were washed using ethanol three times and dried in air for other measurements.

Synthesis of TIF-5-Co: $Co(Ac)_2 \cdot 4H_2O$ (128.2mg, 0.5147mmol), 5, 6-dimethylbenzimidazole (80.2mg, 0.5486mmol), imidazole (50.9mg, 0.7476mmol), 3-amino-1-propanol (6.0mL) are mixed in a Teflon-lined autoclave and stirred for half an hour. The autoclave was then sealed and heated up at 150ºC for 5 days, followed by cooling to room temperature. A large amount of violet crystalline materials were obtained with a yield of 44.3% (based on cobalt salt). The crystals were washed using ethanol three times and dried in air for other measurements.

2.2.3. Single-crystal X-ray Structure Determination

Single-crystal X-ray analysis was performed on a Bruker Smart APEX II CCD area diffractometer with nitrogen-flow temperature controller using graphite-monochromated $Mo_{K\alpha}$ radiation (λ = 0.71073 Å), operating in the ω and φ scan mode. The SADABS program was used for absorption correction. The structure was solved by direct methods and the structure refinements were based on $|F^2|$. Most of non-hydrogen atoms were refined with anisotropic displacement parameters, except the atoms of disordered fragments, which were refined isotropically. Hydrogen atoms were placed in calculated positions. All crystallographic calculations were conducted with the SHELXTL software suites. Solvent in the large pores could not be resolved into definite chemical structures due to the high degree of statistical and positional disorder. So, the high *R(F)* value is mainly caused by the disorder of partial ligands and solvent molecules. It is note that the single crystal structure of **TIF-1** quickly shrinks by losing part of guest

molecules, which is identified by single-crystal data collection and powder X-ray diffraction (PXRD). As a result of structural shrinking, the as-made **TIF-1** washed by ethanol shows a right-shifted diffraction pattern relative to simulated pattern. Although the peaks in the range of 2θ=13-25º are obviously broadened, the 2-10º sharp peaks still remain, which answers for partial loss of crystalline integrity. CCDC-682400 for TIF-1. These data can be obtained free of charge at www.ccdc.cam.ac.uk/conts/retrieving.html [or from the Cambridge Crystallographic Data Centre, 12, Union Road, Cambridge CB2 1EZ, UK; fax: (internet.) +44-1223/336-033; E-mail: deposit@ccdc.cam.ac.uk].

2.2.4 Gas Adsorption Measurement

N_2 gas sorption experiments were carried out on a Micromeritics ASAP 2010 surface area and pore size analyzer. Prior to the measurement, the sample was treated using the following procedure. The as-synthesized samples of **TIF-1 and TIF-2** were soaked with anhydrous methanol for 10 hours, and the extract was discarded. The sample was then allowed to immerse in fresh methanol for about 15 hours to remove benzene and water solvates. The similar immersion was utilized to treat the sample with dichloromethane to remove methanol solvates. After the removal of dichloromethane by centrifuging, the wet sample was dried under vacuum at ambient temperature for 20 hours to yield an activated sample for gas adsorption measurements. Before the measurement, the sample was dried again by using the “degas” function of the surface area analyzer for 20 hours at 250ºC. The N_2 adsorption measurement was performed at 77K with liquid nitrogen.

2.3 Results and Discussion

2.3.1 A New Zeolitic Topology with Sixteen-membered Ring and Multidimensional Large Pore Channels in TIF-1

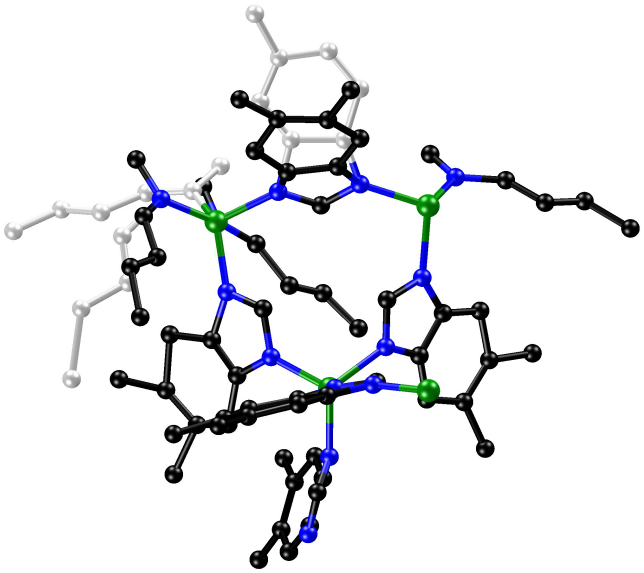


Figure 2.1. The asymmetric unit of **TIF-1Zn** (green balls for Zn atoms, blue balls for N atoms and black balls for C atoms; the disordered part of ligands are represented by pale grey sticks).

TIF-1 crystallizes in a highly symmetrical tetragonal space group $P4_2/mnm$. The asymmetric unit includes four zinc sites, of which only Zn4 is situated on a symmetry site with a 1/4 occupancy. This gives the ratio of 4:4:4:1 for these zinc sites (T_1, T_2, T_3 and T_4). Each unit cell contains 52 T atoms, leading to a large unit cell volume of 32212Å^3, which to our knowledge, is the largest primitive cell among 4-connected zeolitic frameworks. As in zeolites, each T atom is coordinated with four N atoms from four different ligands and each ligand links two T atoms. This unique framework contains three types of loop configurations (Figure 2.2a-c). The loop configuration of a T-atom is defined by the local coordination geometry of this T-atom to its adjacent T-atoms and

shows the distribution of 3- or 4-rings around this T-atom. It is worth noting that the loop configurations for T_1 and $T_{2,3}$ atoms are reported here for the first time.

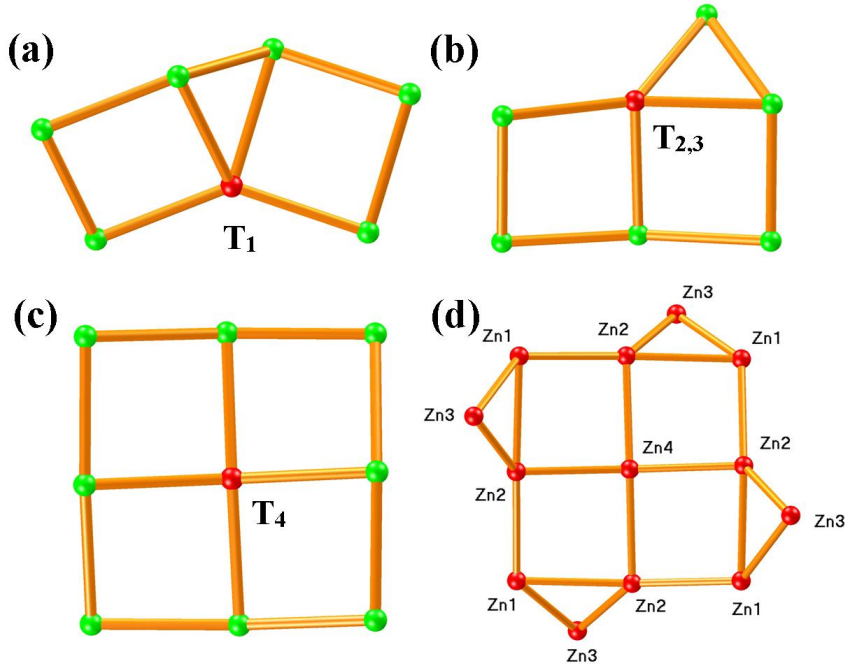


Figure 2.2. The loop configurations of four kinds of T-atoms (a, b, and c) in secondary building unit (d) in **TIF-1**.

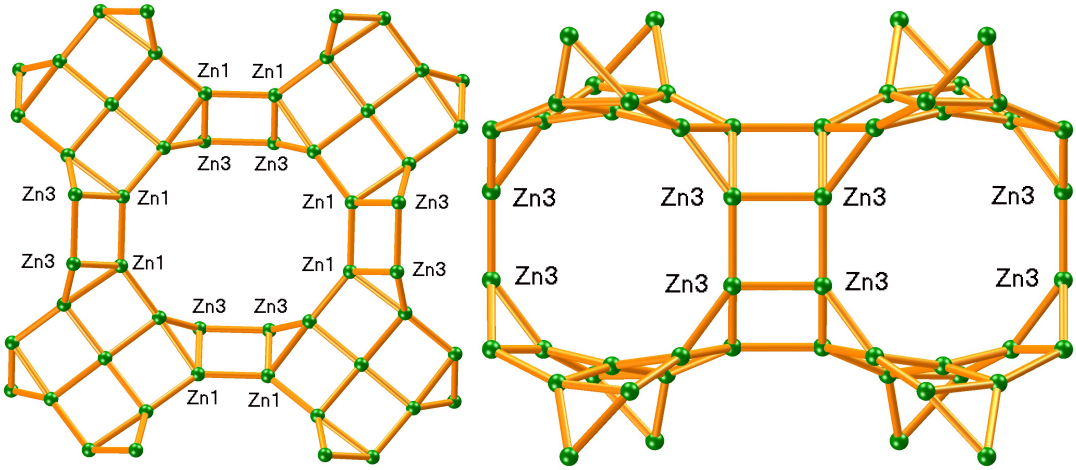


Figure 2.3. Connectivity of adjacent SBUs at the same layer (a) and neighboring layers (b).

Also unprecedented is the occurrence of a unique type of secondary building unit (SBU) composed of 13 T atoms (Figure 2.2d). Each SBU is bonded to four adjacent SBUs by $T_1T_1T_3T_3$ 4-rings to form a 2-D layer (Figure 2.3a). Two adjacent layers, related by 4_2 symmetry operation, are joined together in the ABAB sequence by $T_3T_3T_3T_3$ 4-rings (Figure 2.3b) to generate a 3-D framework (Figure 2.4). This network also represents new type of zeolitic topology with natural tilings $[3^8.4^{22}.10^4.12^4]+2[3^4.4^2.12^2]+[4^2.12^4]$ (Figure 2.5) [19].

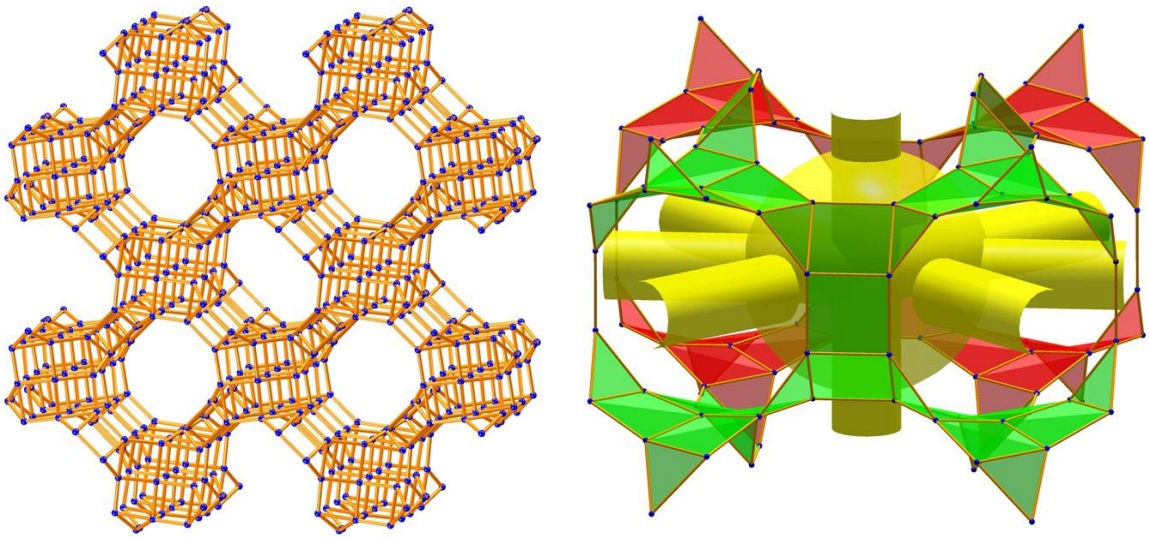


Figure 2.4. Left: the topological network of **TIF-1** viewed along [001]. Right: cross-sectional view of multi-dimensional channels.

One of the most striking features here is the co-existence of 3- and 16-membered rings that help to produce a framework with very low framework density and multidimensional channels. The presence of 16-rings is confirmed by vertex symbols of T-atoms ($3.12_5.4.4.12_2.16$ for T_1; $3.4.4.12_3.10.12_2$ for T_2; $3.4.4.10.12_2.16$ for T_3; and 4.4.4.4.10.10 for T_4) (Figure S4, Table S3). It is of interest to note that rings of five difference sizes co-exist here. Two of these ring sizes (i.e., 3- and 16-rings) are first

observed here for metal imidazolate frameworks (Table 2.2). The largest 16-ring has a window size of 28.5Å X 22.6 Å as measured using the interatomic distances.

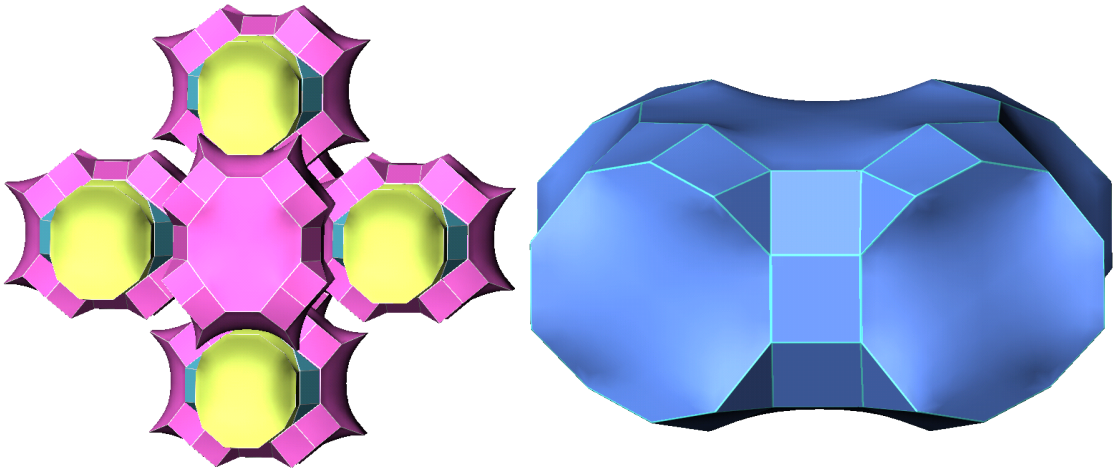


Figure 2.5. The frameworks of TIF-1 shown as natural tilings. The large cage is shown in purple (right) or blue (left).

Table 2.2. Coordination sequences and vertex symbols of TIF-1.

Nodes	1	2	5	3	4	6	7	8	9	10	Vertex Symbol [a]
T_1 (16, 1)	4	8	14	23	39	56	73	100	125	154	$3.12_5.4.4.12_2.16$
T_2 (16, 1)	4	8	13	22	37	53	77	98	123	151	$3.4.4.12_3.10.12_2$
T_3 (16, 1)	4	8	14	24	38	56	75	97	125	157	$3.4.4.10.12_2.16$
T_4 (4, $\bar{4}$)	4	8	12	20	34	48	76	96	118	144	4.4.4.4.10.10

[a] Size and number of the shortest ring on each angle of the T-atom [20].

As expected from the presence of both small (3-rings) and extra-large rings (16-rings), **TIF-1** has the lowest framework density among the tetrahedral imidazolate frameworks. The framework density (FD) is defined as the number of T-atoms per 1000Å^3, which is traditionally used to characterize the openness of zeolite frameworks.

Because of the large size of imidazolate ligand, the framework density of this topology is much lower than that of aluminosilicate zeolites or phosphates. Even compared to other metal imidazolate frameworks (SOD 2.50; RHO 2.01; LTA 2.04; GME 2.09), this framework density of TIF-1Zn (1.61) is the lowest.

Also of interest is the multidimensional large pore channel system with the ring size of 12, 12, 12, 10, and 10, respectively, for channels along various crystallographic directions. The channels along the [110] and [0-10] directions are very unusual because they are defined by alternating 16- and 12-rings. Figure 2.4 shows the cross-sectional view of multi-directional channels. Such multidimensional large pore channel system is truly exceptional, considering that known imidazolate frameworks do not have any pore opening larger than 10-rings.

2.3.2 Unprecedented Organization of d4R Units in TIF-2

TIF-2 crystallizes in an orthorhombic structure with space group *Pnma* and exhibits an unprecedented 4-connected zeolitic network. The asymmetric unit (Figure 2.6a) includes six zinc sites exhibiting three different secondary coordination environments in the ratio of 1:1:1 (T_1, T_2 and T_3). All of these T atoms possess the same loop configuration. As in zeolites, each T atom is coordinated with four N atoms from four different ligands and each ligand links two T atoms. Unfortunately, due to the disorder of some atoms on the ligands, the ratio between two ligands can not been determined by single-crystal X-ray diffraction. Elemental analysis gives a ratio of 0.9:1.1 between MBim and Im.

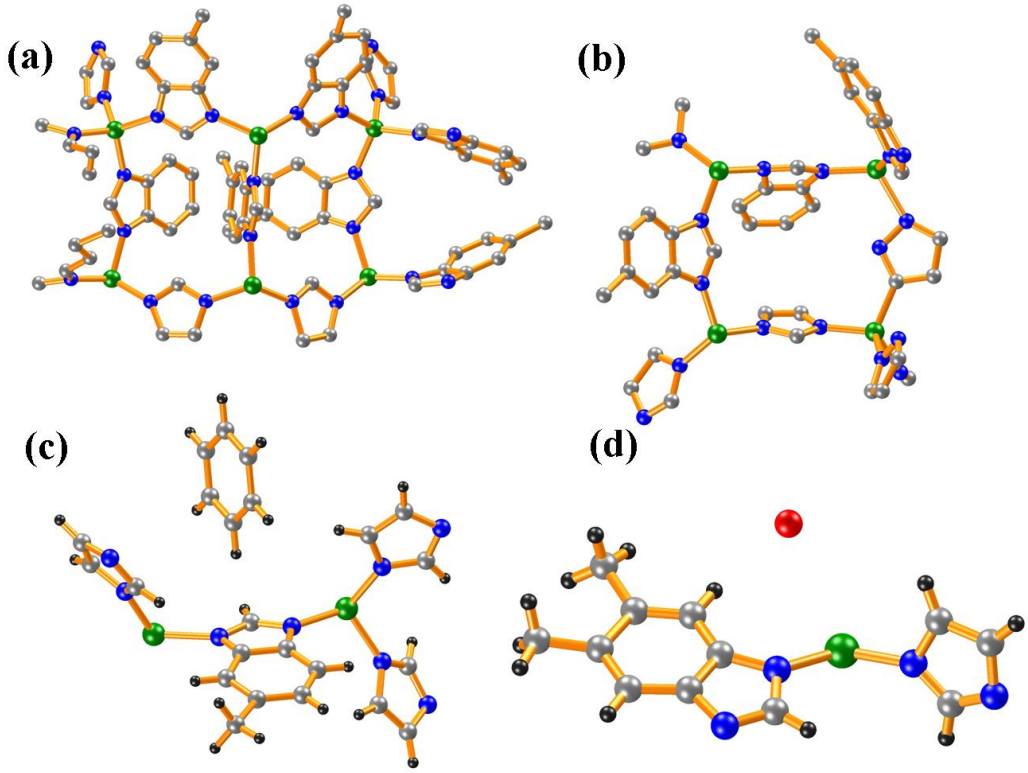


Figure 2.6. The asymmetric unit of **TIF-2** (a), **TIF-3** (b), **TIF-4** (c)**, TIF-5** (d) (green balls for Zn atoms, blue balls for N atoms, grey balls for C atoms, black balls for H atoms and red ball for O atoms).

Of particular interest is the existence of double 4-rings in **TIF-2**. Being a basic secondary building unit (SBU), 4-rings lead to two basic composite building units: double 4-ring (*d4R*) and double crankshaft chain (*dcc*), as shown in Figure 2.7b and 2.7c, respectively. Each *dcc* consists of only T_1 atoms while each *d4R* is composed of four T_2 atoms and four T_3 atoms (Figure 2.8). Figure 2.7b shows that each *d4R* is bonded to adjacent four *d4R* by T_3T_3 to form a 2-D layer parallel to (010) plane. Adjacent two 2-D layers are joined together by a set of *dcc* through T_1T_2 along the [001] direction to generate a 3-D framework (Figure 2.7a). Although *d4R* is an important composite building unit for the construction of some inorganic zeolite framework (such as ACO, -

CLO, LTA, UFI, UTL),[21, 22] it rarely occurs in metal-organic frameworks and prior to this work, only two examples of metal imidazolates containing *d4R* were reported. [14b, 15b]

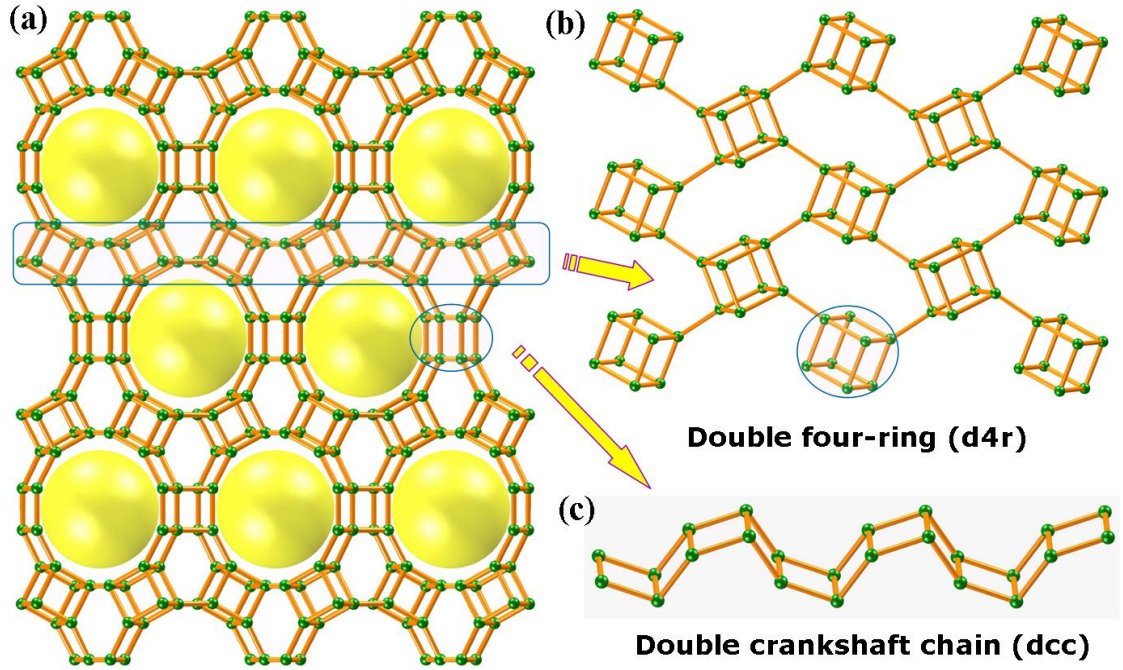


Figure 2.7. (a) The novel topology of **TIF-2** viewed along [001] direction; (b) 2-D layer viewed along [100], containing special double four-rings (*d4R*); (c) double crankshaft chain (*dcc*).

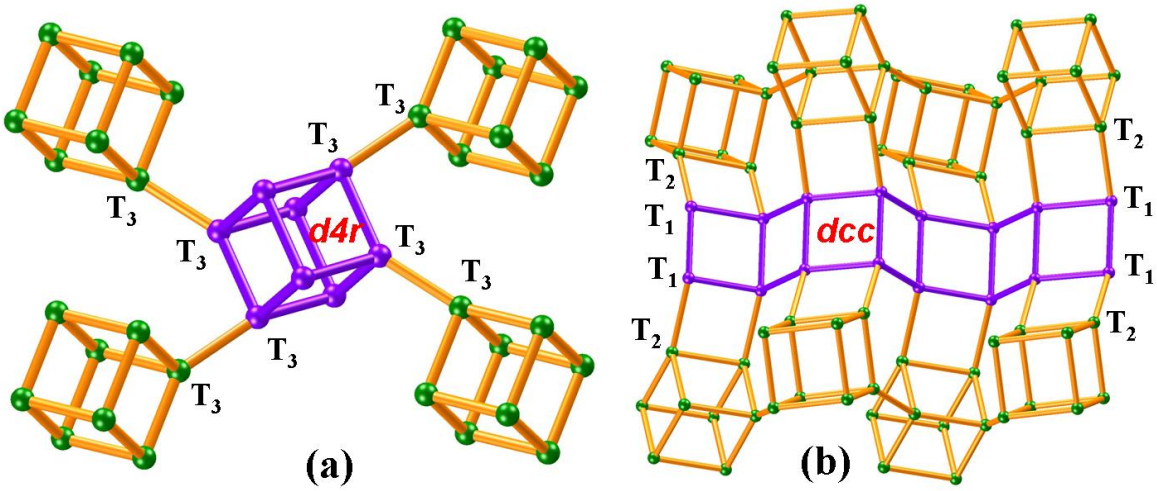


Figure 2.8. **TIF-2**: (a) Connectivity of adjacent *d4r* at the same layer; (b) connectivity of adjacent *d4r* and *dcc*.

Table 2.3. Coordination sequences and vertex symbols of TIF-2.

Nodes	1	2	3	4	5	6	7	8	9	10	Vertex Symbol [a]
T_1 (16, 1)	4	9	16	27	42	58	78	103	130	159	$4.6.4.10_3.4.10_5$
T_2 (16, 1)	4	9	16	26	41	60	80	102	128	157	4.4.4.6.4.10
T_3 (16, 1)	4	8	15	27	41	57	79	106	129	152	4.4.4.6.10.12

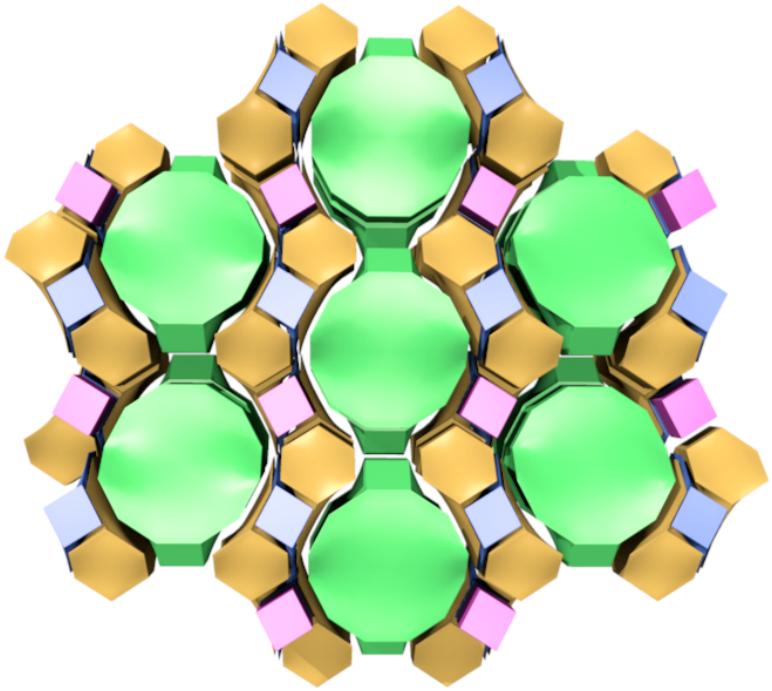


Figure 2.9. The frameworks of TIF-2 shown as natural tilings.

A striking feature of **TIF-2** is the presence of large 12-rings, which is confirmed by vertex symbols of T-atoms ($4.6.4.10_3.4.10_5$ for T_1; 4.4.4.6.4.10 for T_2; and 4.4.4.6.10.12 for T_3). (Table 2.3) The large 12-ring has a window size of 22.4Å × 20.8 Å as measured using the zinc interatomic distances. So far, only four types of 4-connected metal imidazolate topologies contain large 12-rings, ZIFs with the GME[15a], poz[15b] and moz[15b] topologies and **TIF-1**.[23] **TIF-2** possesses a 3-D channel system with 1-D large

pore 12-ring channel along the [001] direction, inter-connected by 10-ring channels along the [100] direction (Figure 2.7a). The calculation using PLATON indicates that **TIF-2** has 41.5% of the total volume occupied by solvent molecules.[24]

TIF-2 has an unprecedented 4-connected zeolitic topology with natural tilings $[4^6]+4^8.10^2.12^2]+2[4^2.6^2.10^2]+[4^2.10^2]$ (Figure 2.9).The topology of **TIF-2** is totally different from another 1-D large-pore metal imidazolate with the GME topology because the composite building units in the 4-connected and mono-nodal GME topology is double 6-rings (*d6r*) and double crankshaft chains (*dcc*) (Figure 2.10).

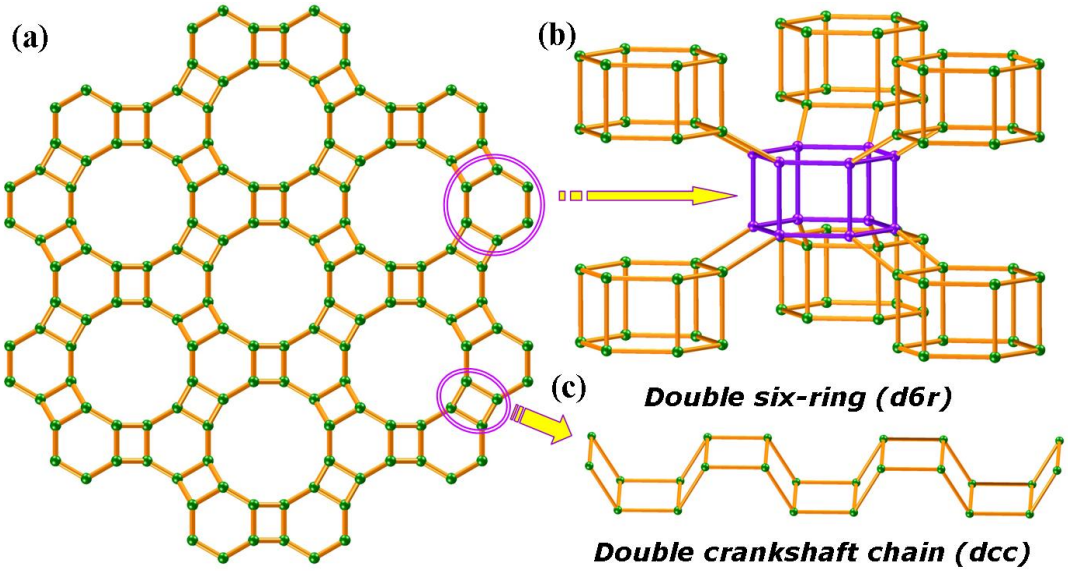


Figure 2.10. (a) GME topology viewed along [001] direction; (b) each double 6-rings (*d6r*) is joined to adjacent six *d6r*; (c) a basic double crankshaft chain (*dcc*) contained in GME framework.

2.3.3 Organization of Cubic Double 4-Ring Units into 3-D Distorted Body-Centered Cubic Framework

By reducing the amount of co-solvent benzene and tuning the solvent ratio from 4: 3.6 to 4: 0.4 between (±)-2-amino-1- butanol and benzene, the organization of d4R

units is dramatically altered, resulting in the formation of **TIF-3**. Similar to **TIF-2**, some atoms in bridging imidazolate ligands are disordered. However, the topology of **TIF-3** can be reliably determined from the location of tetrahedral Zn^{2+} sites with the Zn···Zn distances ranging from 5.90 to 5.93Å, which are typical in 4-connected zinc imidazolates. **TIF-3** possesses the uninodal ACO zeolite topology, which has only been found in a aluminum cobalt phosphate denoted as **ACP-1.**[25] Like **TIF-2**, *d4R* also exists in **TIF-3** as composite building unit, and each *d4R* is joined to adjacent four *d4R* to form a 2-D layer parallel to the (100) plane. However, unlike **TIF-2,** in which neighboring two 2-D layers are joined by a set of *dcc*, all 2-D layers in **TIF-3** are directly joined with adjacent ones to give a 3-D framework (containing 1-D channels with an elliptical 8-rings opening) (Figure 2.11a). In general, each *d4R* can connect eight adjacent *d4R* to form an ideal ACO topology with space group *Im*-3*m*, however, the presence of organic ligands contributes to the observed lower symmetry (i.e., monoclinic) in **TIF-3** (Figure 2.11b).

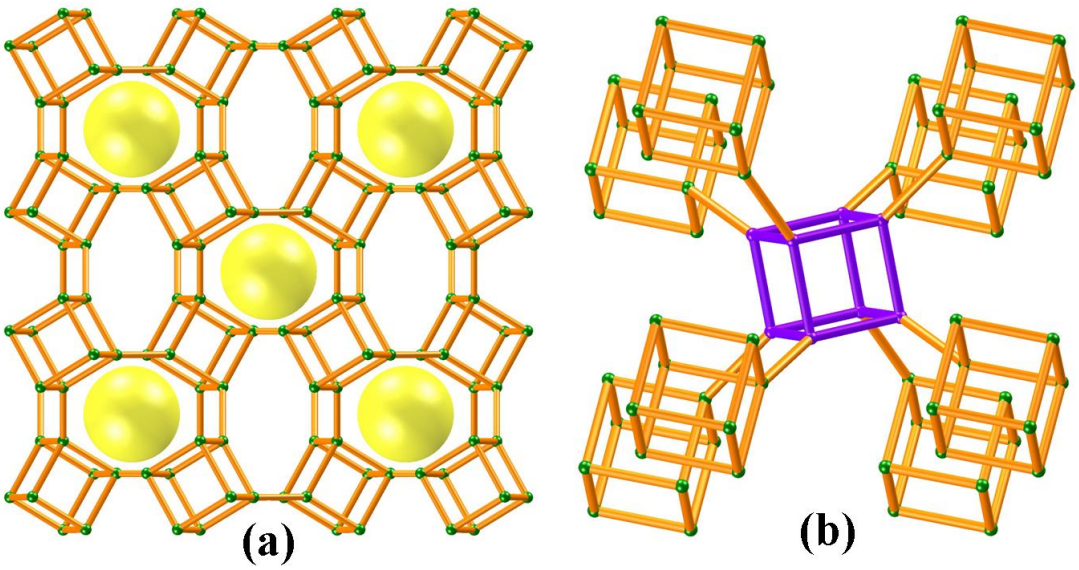


Figure 2.11. (a) ACO zeolite framework in **TIF-3** viewed along [001] direction; (b) each *d4R* is connected to 8 adjacent *d4R*.

2.3.4 Ordered Cooperative Assembly of Two Different Pairs of Complementary Ligands

By significantly increasing the ratio between imidazole and 5-methylbenzimidazole (from 1.2 to 4.2) and using a different solvent combination (3-amino-1-propanol and benzene, instead of (±)-2-amino-1-butanol and benzene for **TIF-2** and **TIF-3**), **TIF-4** with a topology totally different from **TIF-2** and **TIF-3** has been made. It crystallizes in orthorhombic space group *Pbca*, and each Zn ion is tetrahedrally coordinated to four nitrogen atoms from bridging imidazolates to furnish an infinite 3D framework. Structural analysis reveals the exact positions and compositions of both types of ligands. The ratio of Im and MBim is 3:1, which reflects the high Im to MBim ratio in the starting synthetic mixture. **TIF-4** possesses a cag (46^5) topological net which can be regarded as adjacent $Zn_2(Im)_3$ layer with 4.8.8 sheet connected by 5-methylbenzimidazolate (MBim) ligands. A view along the [010] direction shows 1-D channel with distorted hexagonal apertures, which are occupied by solvent benzene molecules. (Figure 2.12a) The solvent-accessible volume of **TIF-4** is about 28.5%. An analysis of the structure shows that all four-rings are composed of the small-sized imidazolate ligands while six- and eight-rings contain both small-sized imidazolate ligands and the large-sized 5-methylbenzimidazolate ligands, as shown in Figure 3b-3d. Such a distribution of different-sized ligands illustrates the cooperative effects of these ligands in forming rings of various sizes, which ultimately controls the topological features of the resulting 3-D framework.

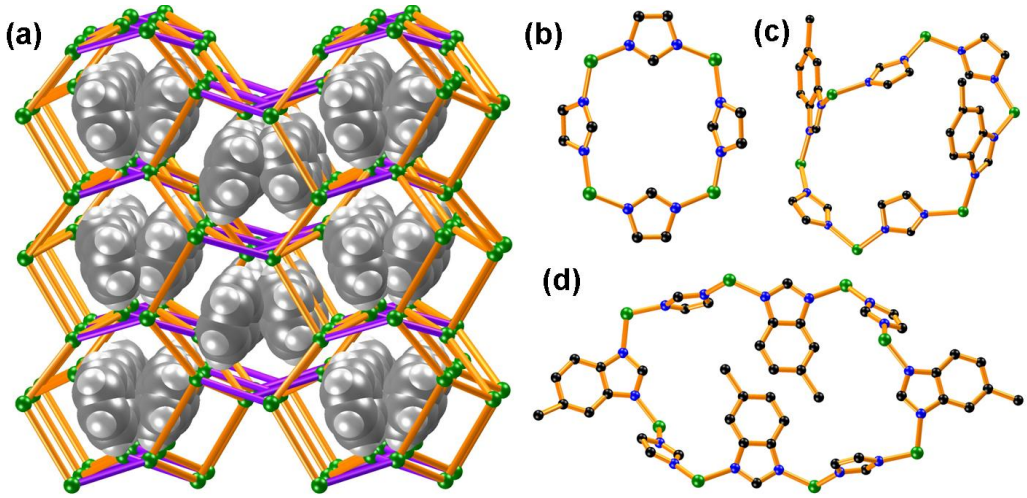


Figure 2.12. (a) Cag topology of **TIF-4** viewed along [001] direction (the space filling is C_6H_6, green atom for Zn atom, orange bar for imidazolate, purple bar for 5-methylbenzimidazolate), containing $Zn_4(Im)_4$ four-ring (b), $Zn_6(Im)_4(5\text{-MBim})_2$ six-ring (c), and $Zn_8(Im)_4(5\text{-MBim})_4$ eight-ring (d).

While **TIF-2**, **-3**, and **-4** were made with 5-methylbenzimidazole as one of the framework building units, **TIF-5Zn and TIF-5Co** contain 5, 6-dimethylbenzimidazole. **TIF-5Zn** crystallizes in a tetragonal space group $I4_1/a$. Structural analysis also reveals exact positions and compositions of two different ligands. The ratio of Im and DMBim is 1:1, as compared with the 3:1 ratio in **TIF-4**. **TIF-5Zn** possesses a GIS (gismondine) topological net constructed from basic composite building unit *dcc*. As shown in Figure S6, each *dcc* is formed by connecting $Zn_4(Im)_4$ rings with 5, 6-dimethylbezimidazolate, and neighboring *dcc* chains are further joined together by 5, 6-dimethylbenzimidazolate to give a 3-D framework. A view along the [100] direction reveals 1-D channels with distorted octagonal apertures, which are perpendicularly intersected by identical channels of 8-ring openings in the [010] direction (Figure 2.13a). In **TIF-5Zn**, half of four-rings are composed of $Zn_4(Im)_4$, and the second half of four-rings are made up of

$Zn_4(Im)_2(DMBim)_2$. All 8-rings consist of two small-sized imidazolate ligands and six large-sized $DMBim^-$ ligands, two of which point inward to the center of eight-rings (Figure 4b-4d). It is clear that the large-sized imidazolate ligands prefer large-sized rings. To prevent all the channel volume from being occupied by the substituents of these ligands, small-sized imidazolate ligands can be introduced into the large ring to tune the channel size. **TIF-5Co** is isostructural to **TIF-5Zn** except that Zn^{2+} is replaced by Co^{2+} in **TIF-5Co**. The solvent-accessible volume is approximately about 26.1%.

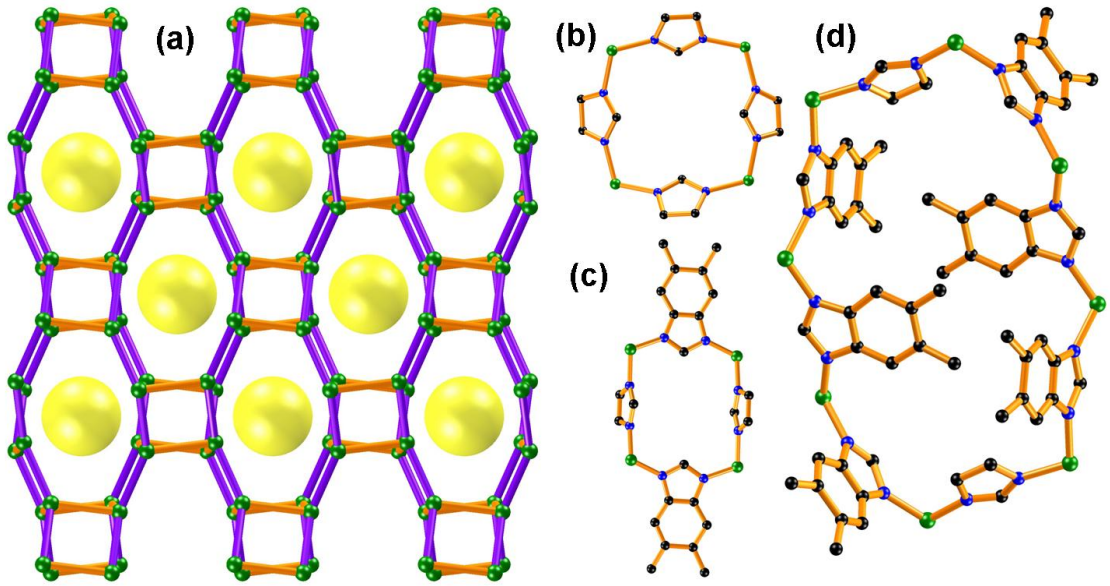


Figure 2.13. (a) GIS Topology of **TIF-5** viewed along [100] (green atom for Zn^{2+} or Co^{2+}, orange bar for imidazolate, purple bar for 5, 6-dimethylbenzimidazolate), containing $Zn_4(Im)_4$ four-ring (b), $Zn_4(Im)_2(5,6\text{-}DMBim)_2$ four-ring (c), and $Zn_8(Im)_2(5\text{-}MBim)_6$ eight-ring (d).

2.3.5 Thermal Stability

Despite the highly open framework topology and multidimensional large pore system, **TIF-1** exhibits very high thermal stability. Thermal gravimetric analysis (TGA) under the N_2 atmosphere performed on **TIF-1** (washed with ethanol and dried in air)

shows a gradual weight loss of 0.93% between 30-140ºC, likely due to the loss of residue solvent molecules. A long plateau in the temperature range between 150 and 440ºC was observed. Such thermal stability up to about 440 ºC is rather high for a framework structure containing organic building blocks.

TIF-2 also exhibits very high thermal stability. Thermal gravimetric analysis (TGA) under the N_2 atmosphere performed on **TIF-2** (washed with ethanol and dried in air) shows a gradual weight loss of 4.3% between 30-200ºC, due to the loss of benzene solvent molecules. A long plateau in the temperature range between 200 and 480ºC was observed. TGA of **TIF-4** shows loss of extra-framework benzene molecules below 284^{o}C (10.5%). There is no further weight lose in the temperature range of 284 – 478°C. **TIF-5Zn** exhibits a gradual weight loss of 9.3% below 386 ºC, indicating the removal of water molecules. The TG curve of **TIF-5Co** also gives a 9.7% of weight loss below 322 ºC.

2.3.6 Gas Sorption

The permanent porosity of **TIF-1 and TIF-2** were confirmed by gas adsorption measurements performed on Micromeritics ASAP 2010 surface area and pore size analyzer.

The sample for surface area analysis was activated by immersing as-synthesized **TIF-1** with methanol, and then dichloromethane, followed by evacuation at room temperature. The activated sample was characterized by XRD to confirm that it has the same structure with as-synthesized sample. The sample was degassed at 150ºC prior to the measurement. A Type I isotherm was observed, indicating that **TIF-1** is microporous (Figure 2.14). The Langmuir surface area of 667.5m^2/g and the pore size of 11.7Å were

calculated using the data in the range of P/P_0= 0.059-0.205. A single data point at relative pressure 0.250 gives a micropore volume of 0.231cm^3/g by Horvath-Kawazoe equation.

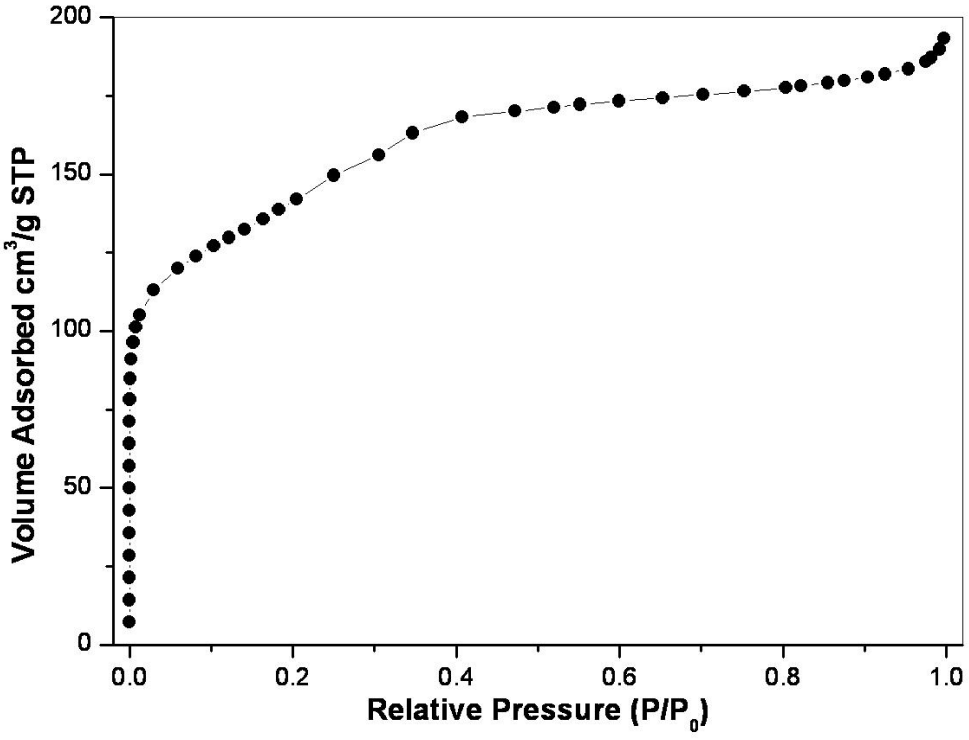


Figure 2.14. Nitrogen gas adsorption isotherm at 77K for **TIF-1**. P/P_0 is the ratio of gas pressure (P) to saturation pressure (P_0), with P_0=740 torr.

The sample for surface area analysis was activated by immersing as-synthesized **TIF-2** with methanol, and then dichloromethane, followed by evacuation at room temperature. The activated sample was characterized by XRD to confirm that it has the same structure with as-synthesized sample. The sample was degassed at 250ºC prior to the measurement. A Type I isotherm was observed, indicating that **TIF-2** is microporous (Figure 2.15). The Langmuir surface area is 618.2 m^2/g using the data in the range of P/P_0= 0.065-0.208. A single data point at relative pressure 0.208 gives a micropore

volume of 0.206cm^3/g by Horvath-Kawazoe equation. The median pore size of 14.1Å was also calculated.

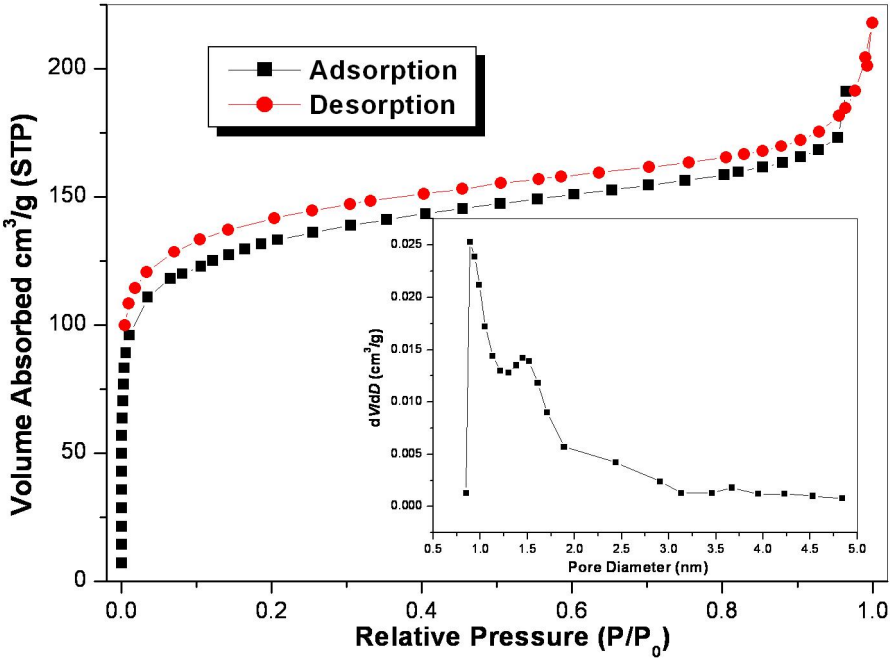


Figure 2.15. Nitrogen gas adsorption isotherm at 77K for **TIF-2**. P/P_0 is the ratio of gas pressure (P) to saturation pressure (P_0), with P_0=740 torr. Inset is the corresponding pore size distribution curves.

2.4 Conclusion

In conclusion, five 4-connected zeolitic metal imidazolate frameworks have been synthesized and structurally characterized. These materials exhibit five different 4-connected topologies. **TIF-1** exhibits permanent microporosity and has high thermal stability. It possesses unprecedented 4-connected topology that is neither found in known 4-connected structures nor theoretically predicted. This new framework features unusual topological features including 3-, and 16-rings, previously unknown structural building units, multidimensional large pore channels and underlines the rich synthetic and structural chemistry of imidazolate based porous frameworks that are yet to be explored. **TIF-2** possesses one-dimensional 12-ring channels and its topology is also not found in other 4-connected structures. It also exhibits permanent microporosity and has high thermal stability. **TIF-3** is the first known example of metal imidazolates with the zeolitic ACO topology. In **TIF-4**, **TIF-5Zn**, and **TIF-5Co**, two complementary ligands control the framework topology in a cooperative manner, which highlights the significance of framework building units (i.e., crosslinking ligands) in the control of the framework topology. This work also illustrates how a subtle change in the experimental conditions such as solvent ratio or ligand ratio can dramatically alter the framework structure. All these observations underline the rich synthetic and structural chemistry of metal-imidazolate-based porous frameworks.

2.5 References

(1) (a) Breck, D.W. *Zeolite Molecular Sieves*, Wiley, New York, **1974**. (b) Maesen, T. L. M.; Marcus, B. *Introduction to Zeolite Science and Practice*, **2001**, 1-9. (c) Van Bekkum, H.; Flanigen, E. M.; Jacobs, P. A.; Jansen, J. C. *Introduction to Zeolite Science and Practice*, Elsevier, Amsterdam**, 2001**. (d) Bu, X., Feng, P.; Stucky, G. D. *Science* **1997**, *278*, 2080-2085. (e) M. E. Davis, *Nature* **2002**, *417*, 813-821.

(2) (a) Xing, H. Z.; Li, J. Y.; Yan, W. F.; Chen, P.; Jin, Z.; Yu, J. H.; Dai, S.; Xu, R. R. *Chem. Mater.* **2008**, *20*, 4179-4181. (b) Li, Y.; Yu, J. H.; Xu, R. R.; Baerlocher, C.; McCusker, L. B. *Angew. Chem. Int. Ed.* **2008**, *47*, 4401-4405. (c) Zhao, L.; Li, J. Y.; Chen, P.; Li, G. H.; Yu, J. H.; Xu, R. R. *Chem. Mater.* **2008**, **20**, 17-19.

(3) (a) de Lill, D. T.; Cahill, C. L. *Crystal Growth & Design* **2007**, *7*, 2390-2393. (b) Knope, K. E.; Cahill, C. L. *Inorg. Chem.* **2007**, *46*, 6607-6612. (c) de Lill, D. T.; Cahill, C. L. *Chem. Commun.* **2006**, 4946-4948.

(4) (a) Oliver, S.; Kuperman, A.; Ozin, G. A. *Angew. Chem. Int. Ed.* **1998**, *37*, 46-62. (b) Oliver, S. ; Kuperman, A.; Lough, A.; Ozin, G. A. *Chem. Mater.* **1996**, *8*, 2391-2398.

(5) (a) Christensen, K. E.; Bonneau, C.; Gustafsson, M.; Shi, L.; Sun, J. L.; Grins, J.; Jansson, K.; Sbille, I.; Su, B. L.; Zou, X. D. *J. Am. Chem. Soc.* **2008**, *130*, 3758-3759. (b) Christensen, K. E.; Shi, L.; Conradsson, T.; Ren, T. Z.; Dadachov, M. S.; Zou, X. D. *J. Am. Chem. Soc.* **2006**, *128*, 14238-14239. (c) Zou, X. D.; Conradsson, T.; Klingstedt, M.; Dadachov, M. S.; O'Keeffe, M. *Nature*, **2005**, *437*, 716-719.

(6) (a) Pan, C. Y.; Liu, G. Z.; Zheng, S. T.; Yang, G. Y. *Chem. Eur. J.* **2008**, *14*, 5057-5063. (b) Zheng, S. T.; Zhang, J.; Yang, G. Y. *Angew. Chem. Int. Ed.* **2008**, *47*, 3909-3913. (c) Liu, G. Z.; Zheng, S. T.; Yang, G. Y. *Angew. Chem. Int. Ed.* **2007**, *46*, 2827-2830.

(7) (a) Chen, B. L.; Wang, L. B.; Zapata, F.; Qian, G. D.; Lobkovsky, E. B. *J. Am. Chem. Soc.* **2008**, *130*, 6718-6719. (b) Chen, B. L; Yang, Y.; Zapata, F.; Lin, G. N.; Qian, G. D. ; Lobkovsky, E. B. *Adv. Mater.* **2007**, *19*, 1693-1696.

(8) (a) Férey, G.; Mellot-Draznieks, C.; Serre, C.; Millange, F. *Acc. Chem. Res.* **2005**, *38*, 217-225. (b) Yaghi, O. M.; O'Keeffe, M.; Ockwig, N. W.; Chae, H.; Eddaoudi, M.; Kim, J. *Nature* **2003**, *423*, 705-714. (c) Liu, Y.; Eubank, J. F.; Cairns, A. J.; Eckert, J.; Kravtsov, V. C.; Luebke, R.; Eddaoudi, M. *Angew. Chem. Int. Ed.* **2007**, *46*, 3278-3283. (d) Mulfort, K. L.; Hupp, J. T.

J. Am. Chem. Soc. **2007**, *129*, 9604-9605. (e) Dinca, M.; Yu, A. F.; Long, J. R. *J. Am. Chem. Soc.* **2006**, *128*, 8904-8913. (f) Evans, O. R.; Lin, W. *Acc. Chem. Res.* **2002**, *35*, 511-512. (g) Lin, X.; Blake, A. J.; Wilson, C.; Sun, X. Z.; Champness, N. R.; George, M. W.; Hubberstey, P.; Mokaya, R.; Schröder, M. *J. Am. Chem. Soc.* **2006**, *128*, 10745-10753. (h) Lee, E. Y.; Suh, M. P. *Angew. Chem. Int. Ed.* **2004**, *43*, 2798-2801. (i) Kitagawa, S.; Kitaura, R.; Noro, I. S. *Angew. Chem. Int. Ed.* **2004**, *43*, 2334-2375.

(9) (a) Férey, G. *Chem. Soc. Rev.* **2008**, *37*, 191-214. (b) Kitagawa, S.; Matsuda, R. *Coord. Chem. Rev.* **2007**, *251*, 2490-2509. (b) Matsuda, R.; Kitaura, R.; Kitagawa, S.; Kubota, Y.; Belosludov, R. V.; Kobayashi, T. C.; Sakamoto, H.; Chiba, T.; Takata, M.; Kawazoe, Y.; Mita, Y. *Nature* **2005**, *436*, 238-241. (c) Kepert, C. J. *Chem. Commun.* **2006**, 696-700. (d) Fletcher, A. J.; Thomas, K. M.; Rosseinsky, M. J. *J. Solid State Chem.* **2005**, *178*, 2491-2510. (e) Kitagawa, S.; Uemura, K. *Chem. Soc. Rev.* **2005**, *34*, 109-119. (f) Bradshaw, D.; Claridhe, J. B.; Cussen, E. J.; Prior, T. J.; Rosseinsky, M. J. *Acc. Chem. Res.* **2005**, *38*, 273-282. (g) Ghosh, S. K.; Zhang, J. P.; Kitagawa, S. *Angew. Chem. Int. Ed.* **2007**, *46*, 7965-7968. (h) Serre, C.; Mellot-Draznieks, C.; Surble, S.; Audebrand, N.; Filinchuk, Y.; Férey, G. *Science* **2007**, *315*, 1828-1831. (i) Papaefstathiou, G. S.; MacGillivary, L. R. *Coord. Chem. Rev.* **2003**, *246*, 169-184. (j) Lee, Y. E.; Jang, S. Y.; Suh, M. P. *J. Am. Chem. Soc.* **2005**, *127*, 6374-6381. (k) Matsuda, R.; Kitaura, R.; Kitagawa, S.; Kubota, Y.; Kobayashi, T. C.; Horike, S.; Takata, M. *J. Am. Chem. Soc.* **2004**, *126*, 14063-14070.

(10) (a) Férey, G. ; Serre, C. ; Millange, F. ; Surble, S. ; Dutour, J.; Margiolaki, I. *Angew. Chem. Int. Ed.* **2004**, *43*, 6296-6301. (b) Fang, Q.; Zhu, G.; Xue, M.; Sun, J.; Wei, Y.; Qiu, S. L.; Xu, R. R. *Angew. Chem. Int. Ed.* **2005**, *44*, 3845-3848. (c) Navarro, J. A. R.; Barea, E.; Salas, J. M.; Masciocchi, N.; Galli, S.; Sironi, A.; Ania, C. O.; Parra, J. B. *Inorg. Chem.* **2006**, *45*, 2397-2399. (d) Guo, X. D.; Zhu, G. S.; Li, Z. Y.; Chen, Y.; Li, X. T.; Qiu, S. L. *Inorg. Chem.* **2006**, *45*, 4065-4070. (e) Liu, Y.; Kravtsov, V. C.; Larsen, R.; Eddaoudi, M. *Chem. Commun.* **2006**, 1488-1490. (f) Sava, D. F.; Kravtsov, V. C.; Nouar, F.; Wojtas, L.; Eubank, J. F.; Eddaoudi, M. *J. Am. Chem. Soc.* **2008**, *130*, 3768-3770.

(11) (a) Tian, Y. Q.; Cai, C. X.; Ji, Y.; You, X. Z.; Peng, S. M.; Lee, G. S. *Angew. Chem. Int. Ed.* **2002**, *41*, 1384-1386. (b) Tian, Y. Q.; Cai, C. X.; Ren, X. M.; Duan, C. Y.; Xu, Y.; Gao, S.; You, X. Z. *Chem. Eur. J.* **2003**, *9*, 5673-5685. (c) Tian, Y.-Q.; Chen, Z. X.; Weng, L.-H.; Guo, H. B.; Gao, S.; Zhao, D. Y. *Inorg. Chem.* **2004**, *43*, 4631-4635. (d) Tian, Y.-Q.; Xu, L.; Cai, C.-X.; Wei, J.-C.; Li, Y.-Z.; You, X. Z. *Eur. J. Inorg. Chem.* **2004**, 1039-1044.

(12) Tian, Y.-Q.; Zhao, Y.-M.; Chen, Z.-X.; Zhang, G.-N.; Weng, L.-H.; Zhao, D.-Y. *Chem. Eur. J.* **2007**, *13*, 4146-4154.

(13) (a) Huang, X.-C.; Lin, Y.-Y.; Zhang, J. P.; Chen, X.-M. *Angew. Chem. Int. Ed.* **2006**, *45*, 1557-1559. (b) Huang, X.-C.; Zhang, J.-P.; Chen, X.-M. *Chin. Sci. Bull.* **2003**, *48*, 1531-1534.

(14) (a) Park, K. S.; Ni, Z.; Côté, A. P.; Choi, J. Y.; Huang, R.; Uribe-Romo, F. J.; Chae, H. K.; O'Keeffe, M.; Yaghi, O. M. *Proc. Natl Acad. Sci. USA* **2006**, *103*, 10186-10191. (b) Hayashi, H.; Côté, A. P.; Furukawa, H.; O'Keeffe, M.; Yaghi, O. M. *Nature Materials* **2007**, *6*, 501-506.

(15) (a) Banerjee, R.; Phan, A.; Wang, B.; Knobler, C.; Furukawa, H.; O'keeffe, M.; Yaghi, O. M. *Science* **2008**, *319*, 939-943. (b) Wang, B.; Côté, A. P.; Furukawa, H.; O'Keeffe, M.; Yaghi, O. M. *Nature*, **2008**, *453*, 207-211.

(16) (a) Brunner, G. O.; Meier, W. M. *Nature* **1989**, *337*, 146-147. (b) Davis, M. E. *Nature* **2002**, *417*, 813-821.

(17) Baerlocher,C.; McCusker, L. B.; Olson, D. H. *Atlas of Zeolite Framework Types*, 6th Ed., Elsevier, Amsterdam, **2007**.

(18) Bu, X.; Feng, P.; Stucky, G. D. *J. Am. Chem. Soc.* **1998**, *120*, 11204-11205.

(19) Blatov, V. A., Delgado-Friedrichs, O., O'Keeffe, M.; Proserpio, D. M. *Acta Crystallogr. A* **2007**, *63*, 418-423.

(20) O'Keeffe, M.; Hyde, S. T. *Zeolites* **1997**, *19*, 370-374.

(21) Baerlocher, C.; McCusker, L. B.; Olson, D. H. *Atlas of Zeolite Framework Types*, 6th Ed., Elsevier, Amsterdam, **2007.**

(22) See database of Reticular Chemistry Structure Resource on the website: http://rcsr.anu.edu.au/.

(23) Wu, T.; Bu, X.; Liu, R.; Lin, Z. E.; Zhang, J.; Feng, P. *Chem. Eur. J.* **2008**, *14*, 7771-7773.

(24) Spek, A. L. *Acta Crystallogr. Sect. A* **1990**, *46*, C34.

(25) Feng, P.; Bu, X.; Stucky, G. D. *Nature* **1997**, *388*, 735-741.

Chapter 3

Zeolitic Boron Imidazolate Frameworks

3.1 Introduction

Crystalline porous materials lie at the center of many industrial applications such as petrochemical refining and air separation.[1-2] The current need for renewable energy and clean environment further fuels intensive efforts in search of functional porous materials. The early synthetic efforts focused on the replacement of cationic tetrahedral species such as Si^{4+} and Al^{3+} in zeolites with other cations such as P^{5+}, Ge^{4+}, Ga^{3+}, and Co^{2+}.[3-6] The interest in crystalline porous semiconductors has lead to the development of porous metal chalcogenides in which chemistry of anionic species becomes central.[7]

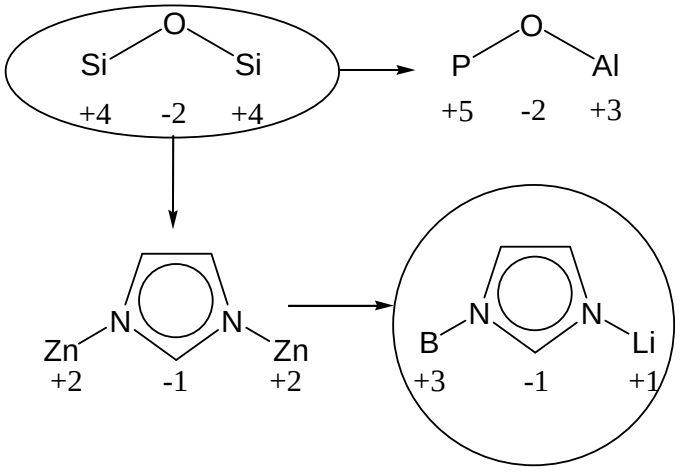
In addition, development of crystal engineering has inspired intense research interests in the synthesis of crystalline solid state materials with diverse compositions, structures, and properties. Among these materials, metal-organic frameworks (MOFs), which are formed through coordinate bonds between metal cations (or clusters) and organic ligands such as di- or tricarboxlates and diimines, are particularly intriguing and have undergone an explosive growth because of their potential applications in areas such as gas storage,[8-11] separation,[12-14] and catalysis.[15-16] A survey of the literature shows that the vast majority of reported porous MOFs are based on the elements beyond the third period of the periodic table including 3d metal cations (Zn, Cu, Cr, Mn) [17-19] and rather heavy lanthanide elements (such as Nd, Gd, Eu).[20-22] Recently, there has been a surge of interest in using *s*- and *p*-block elements such as Mg, Al, and In as framework polyhedral

nodes. [23-26] In particular, lightweight elements such as Mg and Al are considered highly desirable for constructing low-density MOFs as on-board hydrogen storage materials, in part because their low atomic weights can contribute to an increased gravimetric energy storage density.[23, 24] Being the lightest element capable of serving as polyhedral nodes in MOFs, lithium is of outstanding interest for developing lightweight MOFs. Furthermore, its high polarization ability may enhance the binding affinity for gas molecules. On the other hand, the high solvation energy of the lithium ion makes the crystallization of new lithium open-frameworks highly challenging. So far, few MOFs containing lithium are known in the literature.[27]

A more recent development is the synthesis of covalent organic frameworks (COFs) based on lightweight non-metallic elements (such as B, C, N, O).[28, 29] An area that remains largely unexplored is MOCOFs, materials that integrate bonding features (i.e., coordinate and covalent) of both MOFs and COFs. We envisage that the integration between MOFs and COFs should offer a unique opportunity for the development of porous materials that can combine unique advantages of MOFs (e.g., compositional and topological diversity, highly reversible bond formation leading to high crystallinity) and COFs (e.g., lightweight and possibly stronger bond).

We are particularly interested in zeolite-type tetrahedral frameworks, because they offer a wide range of highly porous topological possibilities that can be targeted for the synthetic design. For MOCOFs, we need to consider the selection of non-metallic as well as metallic elements as the tetrahedral nodes. In this aspect, boron imidazolate anions $(B(im)_4^-$ where *im* is imidazolyl or substituted imidazolyl at 2, 4, and/or 5

positions) represent an ideal tetrahedral building block. When crosslinked with tetrahedral metal cations (e.g., Li^+ and Cu^+), neutral zeolite-type frameworks can be expected as illustrated in Scheme 3.1, in a way analogous to recently reported zinc imidazolates (e.g., ZIFs), a family of MOFs with zeolite-type frameworks [30-36] and high capacity for CO_2 storage.[35]



Scheme 3.1. The charge distribution of all components in several neutral zeolitic frameworks.

Herein, we demonstrate such interesting and promising synthetic method that is capable of generating a large family of four-connected open boron imidazolate frameworks (BIFs) (Table 3.1). The method is based on the crosslinking of various pre-synthesized boron imidazolate complexes by monovalent cations (e.g., Li^+ and Cu^+) into extended frameworks. One advantage of this method is that it allows the use of ultra-light chemical elements (e.g., Li and B) as framework vertices, which has a great potential for the creation of high porosity zeolite-like adsorbents. Some of these materials also show good capability for capturing small molecule gas.

Table 3.1. A Summary of Crystal Data and Refinement Results. [a]

Name	Formula [b]	S. G.	*a* (Å)	*b* (Å)	*c* (Å)	*β* (°)	*R* (F)%	Net[c]
BIF-1-Li	$LiB(Im)_4$	$I4_1cd$	22.5041(3)	22.5041(3)	22.5041(3)	90	3.44	*zni*
BIF-1-Cu	$CuB(Im)_4$	$I4_1cd$	22.3798(2)	22.3798(2)	22.3798(2)	90	2.59	*zni*
BIF-2-Li	$LiB(2\text{-}Mim)_4$	*I*-4	7.5817(2)	7.5817(2)	7.5817(2)	90	4.61	*dia*
BIF-2-Cu	$CuB(2\text{-}Mim)_4$	*I*-4	7.6593(2)	7.6593(2)	7.6593(2)	90	2.20	*dia*
BIF-3-Li	$LiB(2\text{-}Mim)_4$	*P*-43*n*	16.0311(1)	16.0311(1)	16.0311(1)	90	3.38	*SOD*
BIF-3-Cu	$CuB(2\text{-}Mim)_4$	*P*-43*n*	16.0184(2)	16.0184(2)	16.0184(2)	90	6.05	*SOD*
BIF-9-Li	$LiB(4\text{-}Mim)_4$	*P*432	26.2923(3)	26.2923(3)	26.2923(3)	90	11.61	*RHO*
BIF-9-Cu	$CuB(4\text{-}Mim)_4$	*P*432	26.8152(1)	26.8152(1)	26.8152(1)	90	5.38	*RHO*
BIF-11-Li	$LiB(2,4\text{-}Dmim)_4$	*P*-43*n*	16.3139(1)	16.3139(1)	16.3139(1)	90	6.91	*SOD*
BIF-12-Li	$LiB(Bim)_4 \cdot$[(±)-2-AB]	$P2_1/c$	12.4369(3)	13.4869(3)	17.8943(3)	90.709(1)	5.48	*fes*
BIF-13-Li	$LiB(Bim)_4$	*P*-1	10.5980(4)	10.6009(5)	21.6596(9)	100.360(3)	17.06	*sql*
BIF-13-Cu	$CuB(Bim)_4$	*P*-1	10.6599(2)	10.6608(2)	21.2449(5)	79.483(1)	13.08	*sql*

[a] Structures were solved from single-crystal data collected at 150K on a SMART CCD diffractometer with Mo Kα. $R(F) = \Sigma||F_o|-|F_c||/\Sigma|F_o|$ with $F_o > 4.0\sigma(F)$. [b] Im = imidazolate, 2-Mim = 2-methyl-imidazolate, 4-Mim = 4-methyl-imidazolate, 2,4-Dmim = 2,4-Dimethyl-imidazolate, Bim = benzimidazolate. [c] For definitions of three-letter abbreviations, see Reticular Chemistry Structure Resource (http://rcsr.anu.edu.au/). For BIF-13-Li: α = 93.650(3)°, γ = 90.017(3)°; BIF-13-Cu: α = 86.2990(10)°, γ = 89.9890(10)°.

3.2 Experimental Section

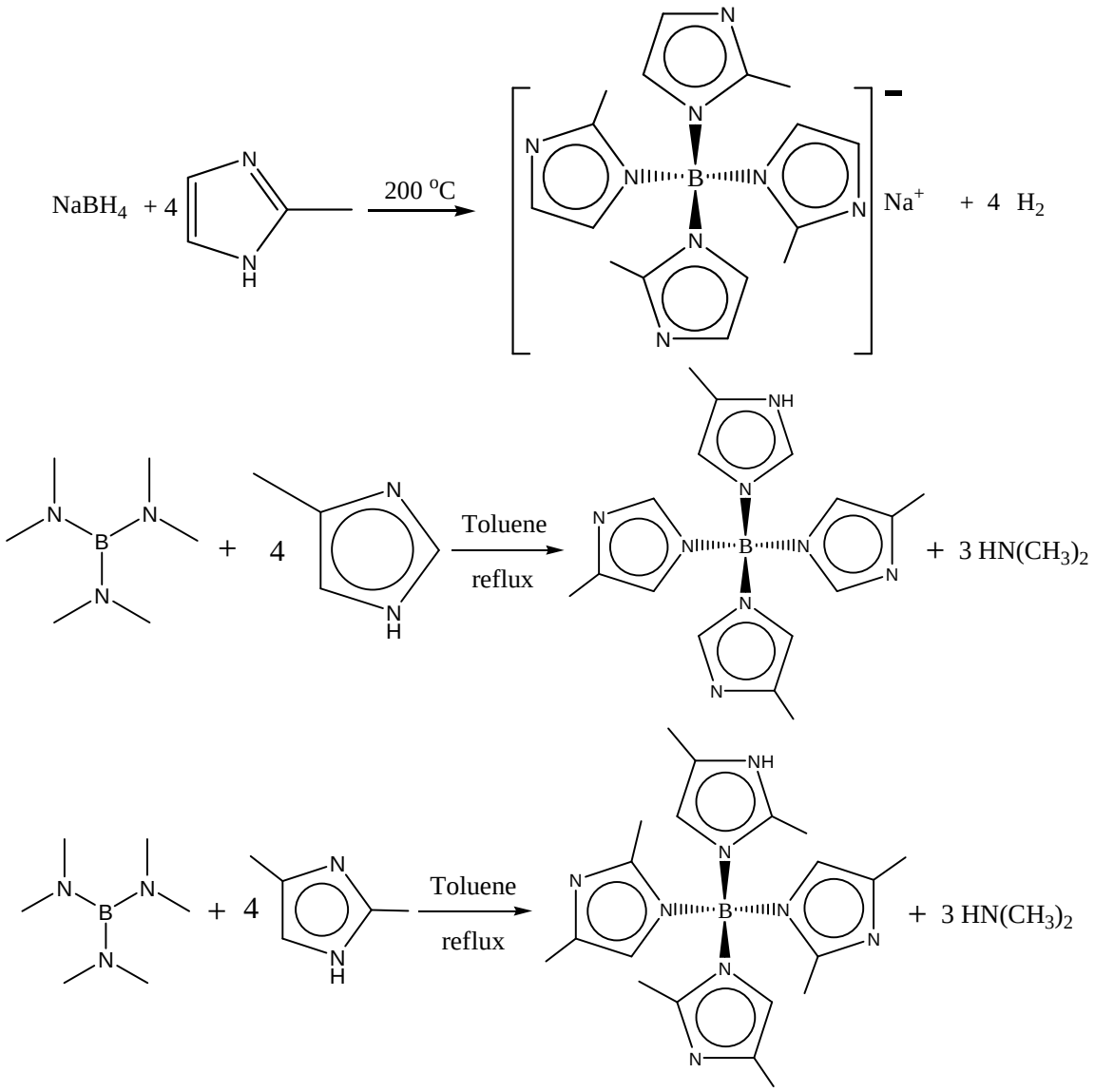
3.2.1 Materials and General Methods

Most of reagents and solvents employed in these synthetic studies were commercially available and used as supplied without further purification. Powder X-ray diffraction data were collected using a Bruker D8-Advance powder diffractometer operating at 40kV, 40mA with Cu Kα(λ =1.5406 Å) radiation (2θ range, 2-40°; step, 0.03°; scan speed, 60 s/step). The simultaneous DSC-TGA thermal analysis was performed on TA instruments SDT Q600. All samples was prepared by grinding single crystals into fine powder and heated between room temperature and 1200 ^{o}C at a heating rate of 5 ^{o}C/min under N_2 gas or air flow (100 ml/min).

3.2.2 Syntheses

Synthesis of Ligand NaB(2-Mim)$_4$: The synthesis of this material was similar to the literature procedure.[37] In a 300 mL nitrogen-flushed flask attached to an oil bubbler, 0.532g (14.1mmol) of sodium borohydride was mixed with 2-methylimidazole (4.641g, 56.4mol). The mixture was heated and stirred at 200^{o}C for 24 hours, then cooled to room temperature. The resulting off-white solid was washed with dry acetone (3×20 mL) and dry toluene (3×20 mL), respectively, and dried under reduced pressure at room temperature. The crude products (3.562g) were directly used for the following synthesis without further purification. The reaction equation is shown in Scheme 3.2.

Synthesis of Ligand HB(2-Mim)$_4$: The ligand was prepared according to the procedure in the reported literature. [38]



Scheme 3.2. The syntheses of B-Im system ligands.

Synthesis of Ligand HB(4-Mim)$_4$: The synthesis of this organic ligand was based on the procedure in the reported literature [38]. The reaction was carried out under dry nitrogen by using standard Schlenk techniques. 6.533g (0.0456mmol) of $B(NMe_2)_3$ was added to a solution of 4-methylimidazole (15.000g, 0.1827mol) in anhydrous toluene (80mL), and the resulting mixture was heated to reflux for 20 hours. The solvent was

then removed under vacuum, and the product was washed with dry hexane (3×20mL) and dried under reduced pressure at room temperature to give raw product (10.534g, yield 68.71%). A sample of the raw product was recrystallized by slow diffusion of anhydrous ethyl ether into a methanol solution to produce some colorless rhombic crystal suitable for X-ray crystallography. The solvated co-crystal of HB(4-methylimidazolate)$_4$ with (±)-2-amino-1-butanol and H_2O is also obtained. MS (ESI): *m*/*z*: 337.2069 $[M\text{-}H]^+$.

Synthesis of Ligand HB(2, 4-Dmim)$_4$: The synthesis was based on the procedure in the reported literature.[38] 3.720g (0.0260mmol) of $B(NMe_2)_3$ was added to a solution of 2, 4-dimethylimidazole (10.000g, 0.1040mol) in anhydrous toluene (50mL), and the resulting mixture was heated to flux for 24 hours. The solvent was then removed under vacuum, and the product was washed with dry hexane (4×20mL) and dried under reduced pressure at room temperature to give the raw product (7.253g, yield 68.71%). The raw sample was directly used for the following synthesis without further purification. The reaction equation is shown in Scheme 3.2.

Synthesis of Ligand HB(Bim)$_4$: The ligand was prepared according to the procedure in the reported literature.[38]

Synthesis of LiB(Im)$_4$ (BIF-1-Li): Sodium tetrakis(imidazoly)borate (0.0521 g, 0.13 mmol) and $LiNO_3$ (0.0342 g, 0.5 mmol) in a mixed 2-amino-1-butanol (1.533 g)/CH_3CN (1.023 g) solution were placed in a 20 ml vial. The sample was heated at 85 ^oC for 48 h, and then cooled to room-temperature. After washed by ethanol and distilled water, the colorless crystals were obtained (Yield: 85 %).

Synthesis of $CuB(Im)_4$ (BIF-1-Cu): Sodium tetrakis(imidazoly)borate (0.0543 g) and CuI (0.0552 g) in a DMF (2 mL) solution were placed in a 20 ml vial. The sample was heated at 85 ^oC for 48 h, and then cooled to room-temperature. After washed by ethanol and distilled water, the colorless crystals were obtained (Yield: 88 %).

Synthesis of $LiB(2\text{-}Mim)_4$ (BIF-2-Li): $HB(2\text{-methylimidazolate})_4$ (157.1 mg), Lithium butyl (0.5ml, 2.5M in hexane), (±)-2-amino-1- butanol (2.650g) and acetonitrile (1.059g) are mixed in a Teflon-lined autoclave and stirred for half an hour. The autoclave was then sealed and heated at 150ºC for 3 days, followed by cooling to room temperature. A large amount of colorless crystals (25.1mg) were obtained. The crystals were washed using acetonitrile three times and dried in air for other measurements. Note: Butyllithium solution is very reactive and sensitive to moisture. The great care should be exercised in handling it.

Synthesis of $CuB(2\text{-}Mim)_4$ (BIF-2-Cu): Tetrakis(2-methylane-imidazoly)boric acid (0.059 g) and $Cu(NO_3)_2{\cdot}3H_2O$ (0.143 g) in a mixed 2-amino-1-butanol (2.687 g)/CH_3CN (0.677 g) solution were placed in a 20 ml vial. The sample was heated at 100 ^oC for 7 days, and then cooled to room-temperature. After washed by ethanol and distilled water, the colorless crystals were obtained.

Synthesis of $LiB(2\text{-}Mim)_4$ (BIF-3-Li): $HB(2\text{-methylimidazolate})_4$ (72.1mg), Lithium butyl (0.5ml, 2.5M in hexane), (±)-2-amino-1- butanol (2.406g) and acetonitrile (2.706g) are mixed in a Teflon-lined autoclave and stirred for half an hour. The autoclave was then sealed and heated at 85ºC for 5 days, followed by cooling to room temperature.

A large amount of colorless crystals (30.5mg) were obtained. The crystals were washed using acetonitrile five times and dried at 85^{o}C in air for other measurements.

Synthesis of CuB(2-Mim)$_4$ (BIF-3-Cu): Sodium tetrakis(2-methylane-imidazoly)borate (0.0981 g) and CuI (0.0779 g) in a mixed 2-amino-1-butanol (1.1660 g)/CH_3CN (1.5 mL) solution were placed in a 20 ml vial. The sample was heated at 120 ^{o}C for 5 days, and then cooled to room-temperature. After washed by ethanol and distilled water, the colorless crystals were obtained (Yield: 80 %).

Synthesis of LiB(4-Mim)$_4$ (BIF-9-Li): HB(4-methylimidazolate)$_4$ (155.0mg, 0.461mmol), Lithium dicyclohexylamide (471.8.mg, 2.520mmol), (±)-2-amino-1-butanol (2.590g) and benzene (3.576g) are mixed in a Teflon-lined autoclave and stirred for one hour. The autoclave was then sealed and heated at 120ºC for 4 days, followed by cooling to room temperature. A large amount of colorless polyhedron crystals (30.5mg, yield 16.6%) were obtained. The crystals were washed using acetonitrile two times and dried at 85^{o}C in air for other measurements. Note: Although lithium dicyclohexylamind [$LiN(C_6H_{11})_2$] is very sensitive to moisture, it is not necessary to add these chemicals in dry box.

Synthesis of CuB(4-Mim)$_4$ (BIF-9-Cu): HB(4-methylimidazolate)$_4$ (72.1mg, 0.214mmol), CuI(74.5mg, 0.391mmol), (±)-2-amino-1-butanol (3.619g), benzene (6.501g), and acetonitrile (1.523g) are mixed in a Teflon-lined autoclave and stirred for half an hour. The autoclave was then sealed and heated at 85ºC for 8 days, followed by cooling to room temperature. A large amount of colorless crystals (35.5mg, yield 36.35%)

were obtained. The crystals were washed using acetonitrile five times and dried at 85^{o}C in air for other measurements.

Synthesis of Li[B(2, 4-Dmim)$_4$] (BIF-11): HB(2, 4-dimethylimidazolate)$_4$ (202.0mg), Li_2S (74.2mg), (±)-2-amino-1-butanol (1.315g), benzene (8.358g), and acetonitrile (2.199g) are mixed in a 20 mL vial and stirred for half an hour. The vial was then sealed and heated at 85ºC for 2 days, followed by cooling to room temperature. A large amount of colorless crystals (122.1mg, 60.91% based on (2, 4-dimethylimidazolate)$_4$) were obtained. The crystals were washed using acetonitrile five times and ethanol twice and dried at 85^{o}C in air for other measurements.

Synthesis of Li[B(Bim)$_4$][(±)-2-AB] (BIF-12): HB(benzimidazolate)$_4$ (198mg), butyllithium solution (0.5mL, 2.5M in hexanes), (±)-2-amino-1-butanol (2.602g) and benzene (1.590g) are mixed in a Teflon-lined autoclave and stirred for one hour. The autoclave was then sealed and heated at 120ºC for 5 days, followed by cooling to room temperature. A large amount of colorless rhombus crystals (145.3mg, 61.3% based on HB(benzimidazolate)$_4$) were obtained. The crystals were washed by using acetonitrile (2×5.0mL) and dried at room temperature in air for other measurements.

Synthesis of LiB(Bim)$_4$ (BIF-13): HB(benzimidazolate)$_4$ (178.1mg, 0.335mmol), Li_2S(92.4mg, 2.153mmol), (±)-2-amino-1-butanol (2.587g) and acetonitrile (1.761g) are mixed in a Teflon-lined autoclave and stirred for two hours. The autoclave was then sealed and heated at 150ºC for 5 days, followed by cooling to room temperature. A large amount of colorless plate crystals (50.3mg, 9.34%) were obtained.

Synthesis of $CuB(Bim)_4$ (BIF-13-Cu): $HB(benzimidazolate)_4$ (71.1mg, 0.134mmol), CuI (76.2mg, 0.4001mmol), (±)-2-amino-1-butanol (3.246g), acetone (2.480g) and benzene (6.649g) are mixed in a Teflon-lined autoclave and stirred for half an hour. The autoclave was then sealed and heated at 85ºC for 6 days, followed by cooling to room temperature. A large amount of colorless plate crystals (10.3mg, 14.16%) were obtained.

3.2.3 Gas Adsorption Measurement

Gas sorption experiments were carried out on a Micromeritics ASAP 2010 surface area and pore size analyzer. Prior to the measurement, the sample was treated using the following typical procedure. The as-made sample of BIF-n-Li was soaked with anhydrous acetonitrile for 24 hours, and the extract was discarded. The sample was then allowed to immerse in fresh acetonitrile for about 24 hours to remove benzene solvates. The wet sample was dried under vacuum at ambient temperature for two days to yield an activated sample for gas adsorption measurements. Before the measurement, the sample was dried again by using the "degas" function of the surface area analyzer for 48 hours at 200ºC. The as-synthesized sample of BIF-n-Cu was soaked with anhydrous acetonitrile for 20 hours, and the extract was discarded. The sample was then allowed to immerse in fresh acetonitrile for about 20 hours to remove benzene solvates. The similar immersion was utilized to treat the sample with anhydrous methanol to remove acetonitrile solvates. After the removal of methanol by centrifuging, the wet sample was dried under vacuum at ambient temperature for two days to yield an activated sample for gas adsorption measurements. Before the measurement, the sample was dried again by using the "degas"

function of the surface area analyzer for 36 hours at 200ºC. The N_2, H_2 and CO_2 adsorption measurement were performed at 77K, 77K, and 273K, respectively.

3.2.4. Single-crystal X-ray Structure Determination

Single-crystal X-ray analysis was performed on a Bruker Smart APEX II CCD area diffractometer with nitrogen-flow temperature controller using graphite-monochromated $Mo_{K\alpha}$ radiation (λ = 0.71073 Å), operating in the ω and φ scan mode. The SADABS program was used for absorption correction. The structure was solved by direct methods and the structure refinements were based on $|F^2|$. All atoms except those in disordered template molecules were refined with anisotropic displacement parameters. The hydrogen atoms were generated geometrically. All crystallographic calculations were conducted with the SHELXTL software suites. CCDC-693499 (BIF-1-Li), 693500 (BIF-1-Cu), 699084 (BIF-2-Li), 703703 (BIF-2-Cu), 703704 (BIF-3-Li), 697959 (BIF-3-Cu), 734221 (BIF-11-Li), 734222 (BIF-12-Li) contain the supplementary crystallographic data. These data can be obtained free of charge at www.ccdc.cam.ac.uk/conts/retrieving.html [or from the Cambridge Crystallographic Data Centre, 12, Union Road, Cambridge CB2 1EZ, UK; fax: (internet.) +44-1223/336-033; E-mail: deposit@ccdc.cam.ac.uk].

3.3 Results and Discussion

3.3.1 Two-Step Synthesis Strategy and Importance of Lithium Precursors

For the creation of 4-connected topologies, our strategy is reminiscent of the strategy that led to the discovery of microporous $AlPO_4$ by analogy with porous silica. Just as Al^{3+} and P^{5+} can replace two Si^{4+} sites in a porous silicalite, Li^{+} and B^{3+} can replace two Zn^{2+} sites in a $Zn(Im)_2$ type framework, as shown in Scheme 3.1. It has been demonstrated earlier that in the zinc imidazolate system, the type, number, and position of substituents on the imidazolate ring can dramatically alter framework topologies through the ligand-ligand steric interactions. However, unlike the zinc-imidazolate system in which zinc-imidazolate bonds are formed in situ from a zinc salt such as zinc nitrate and a neutral imidazole base during solvothermal synthesis, boron-imidazolate complexes have not been found to form *in situ* in the solvothermal synthesis and therefore need to be prepared by chemical synthesis prior to solvothermal crystal growth. As illustrated in Scheme 3.2, two different methods were employed to synthesize boron imidazolate complexes.

Prior to this work, some polymeric materials based on $[B(im)_4]^-$ and divalent metals (e.g., Pb, Mg, Ca, Sr) are known.[38] However, it was observed that such combinations between $[B(Im)_4]^-$ and M^{2+} have a tendency to produce layered materials. There is one known Li-B-im structure, however, half of the lithium sites in this phase contain terminal H_2O and CH_3OH ligands.[40]

By using above synthetic strategy, a total of decade of boron imidazolate framework materials have been made (Table 3.1). The use of lithium as the framework

building block is of outstanding interest because it is the lightest possible tetrahedral building block. The use of boron as the tetrahedral node has the potential to enhance the stability of the framework because of the shorter B-ligand bond (B-N bond in this work, which is isoelectronic with C-C bond), in addition to the advantage of having the low atomic mass.

The most unusual aspect of the solvothermal synthesis and crystallization is the critical effect of lithium precursors, or more sepcifically, the nature of counter anions in the lithium salt. A number of common lithium salts, such as $LiNO_3$, LiCl, LiOH and $LiPF_6$, have been studied as lithium sources without any success, demonstrating the great resistance to crystallization by these extended lithium-boron-imidazolate frameworks. The usage of these lithium salts with high solubility usually causes clear solution or transparent gel without any crystalline solid. On the other hand, we found that lithium salts that contain soft Lewis bases such as S^{2-} or R^- (alkyl groups such butyl) help to promote the crystallization of Li-B imidazolate frameworks. The possible reason is that the stable byproducts (HS^- and HR) lower the reversible transformation between HBL_4 and BL_4^-, which facilitates the crystallization of anions and cations. It is worth noting that the importance of sulfides or organometallic precursors in the synthesis of metal-organic framework materials has been very little appreciated until this work on Li-B imidazolates. It is conceivable that the use of such uncommon salts in other compositions may allow us to access a range of novel metal-organic framework materials, too.

3.3.2 Structure

BIF-1-Li exhibits a 3D tetrahedral framework in which each Li or B center is connected to four imidazoly (denoted as im) ligands to create a SiO_4-like tetrahedron (i.e., $Li(Im)_4$ and $B(im)_4$) (Figure 3.1a). Each im linker bridges one Li center and one B center with the Li···B distance ranging from 5.585 to 5.683 Å. The Li and B tetrahedra alternate through corner-sharing into a 4-connected 3-D *zni*-type framework containing 4-, 6-, and 12-membered rings (Figures 3.1b-f)).

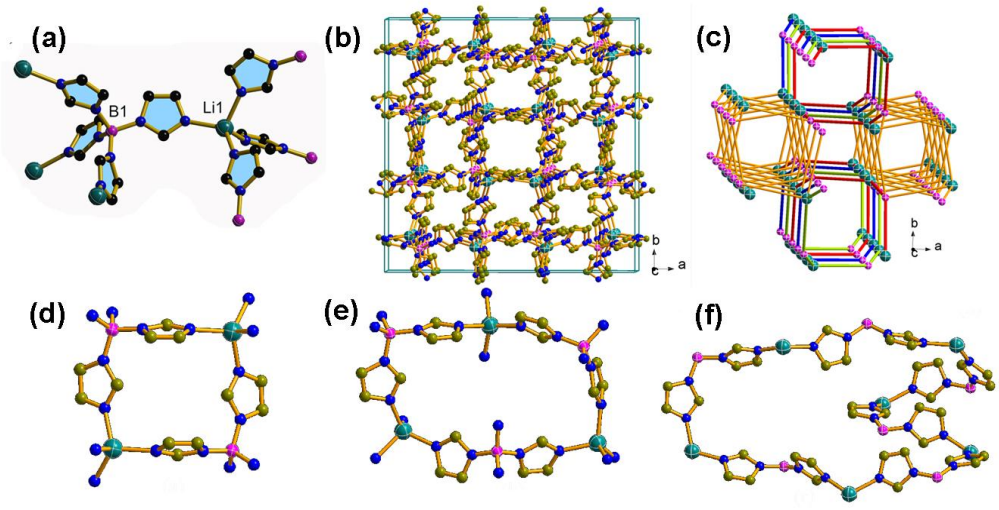


Figure 3.1. View of the coordination environment in BIF-1-Li showing the connectivity between the Li and B tetrahedral (a) and its 3-D framework structure (b) with zni net (c) and three different ring sizes (d-f).

BIF-2-Li, the second 3-D 4-connected Li-B imidazolate framework, was synthesized by using 2-methyl-imidazolate (2-Mim) as the crosslinking ligand and it possesses the non-interpenetrating diamond (*dia*) topology (Figure 3.2).

To demonstrate the general applicability of our synthetic strategy, we have also explored other M^+/M^{3+} combinations. We have found that the same framework topology found in BIF-1-Li and BIF-2-Li can also be synthesized by using Cu^+ in place of Li^+.

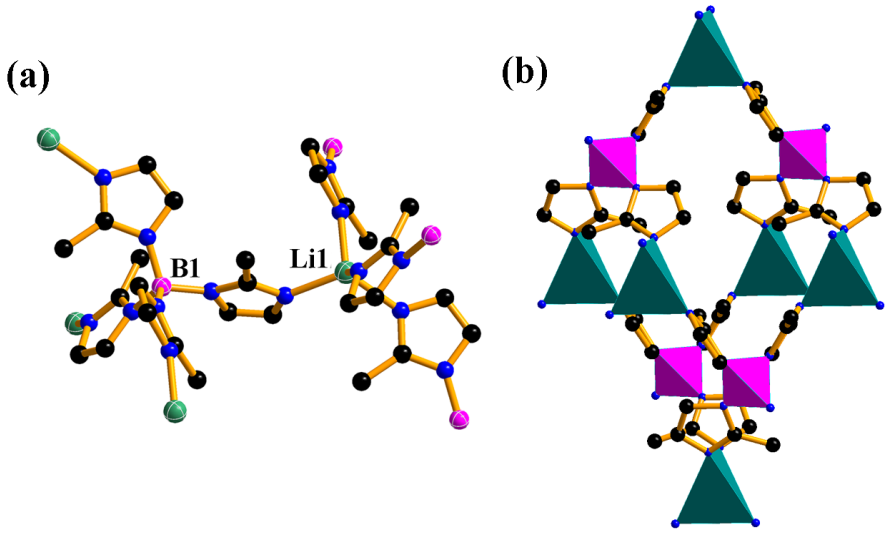


Figure 3.2. (a) View of the coordination environment and (b) the diamondoid unit in BIF-2-Li.

BLF-3-Li consists of one lithium ion and one-fourth of a tetrakis(2-methylane-imidazolyl)borate ligand in the asymmetric unit of a highly symmetrical cubic space group *P*-43*n*. It exhibits a neutral 3-D tetrahedral framework in which each Li or B is tetrahedrally linked to four 2-Mim ligands (B-N bond length 1.551Å; Li-N bond length 2.177Å) and each 2-Mim linker bridges one Li and one B with the Li···B distance of 5.768 Å. This four-connected net with alternating Li and B tetrahedral nodes has an uninodal zeolite sodalite (SOD) topology. (Figure 3.3) Salient features of the SOD topology include β cages with 24 vertices and 4- and 6-ring (i.e., 4 or 6 tetrahedral sites) windows. Each β cage is connected to other fourteen β cages by sharing 4-ring and 6-ring to form a 3-D framework. According O'Keeffe and coworkers, its natural tilling symbol is $[4^6.6^8]$ (…*mn*…means *m* kind of *n* face in each separate tilling, Figure 3.3). BIF-3-Cu is isostructural to BIF-3-Li.

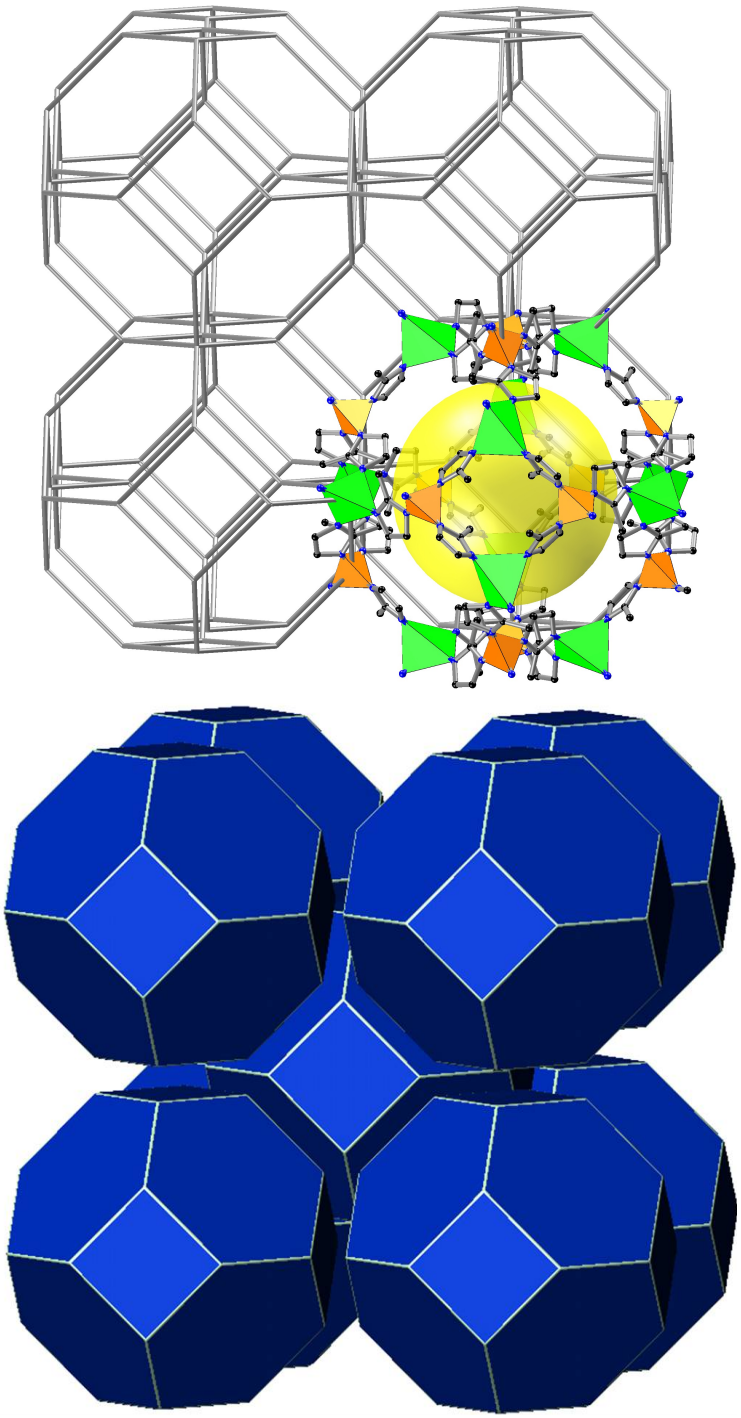


Figure 3.3. Top: diagram of SOD topology in $MB(Mim)_4$ ($M=Li^+$ or Cu^+); BN_4 tetrahedra are shown in orange, MN_4 tetrahedra in green, N in blue, and C in black; the big yellow sphere represents the void space in β cage. Bottom: SOD topology with natural tiling $[4^6.6^8]$.

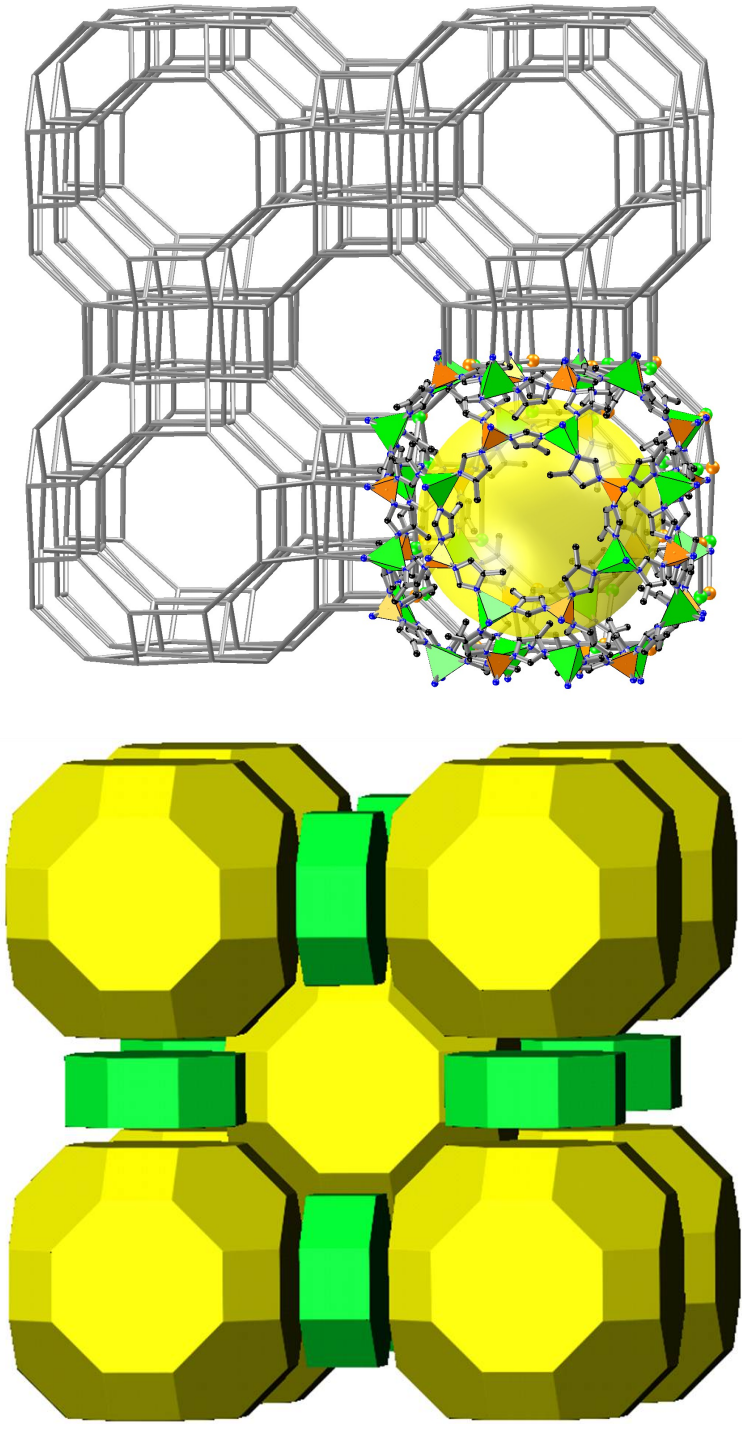


Figure 3.4. Top: diagram of RHO topology in $MB(Mim)_4$ ($M=Li^+$ or Cu^+); BN_4 tetrahedra are shown in orange, MN_4 tetrahedra in green, N in blue, and C in black; the big yellow sphere represents the void space in α cage. Bottom: RHO topology with natural tiling $[4^{12}.6^8.8^6]+3[4^8.8^2]$.

BIF-9-Li crystallizes in a highly symmetrical cubic space group *P*432. The asymmetric unit includes one lithium atom, one boron atom, four 4-methylimidazolate linkers (denoted as 4-Mim), and half of disordered solvent benzene molecule. It exhibits a neutral 3-D tetrahedral framework in which each Li or B is tetrahedrally linked to four 4-Mim (B-N bond length 1.486-1.561Å; Li-N bond length 1.961-2.078Å) and each 4-Mim linker bridges one Li and one B with the Li···B distance ranging from 5.263~~5~~.554Å. This distance is much shorter than the Zn···Zn distance (~5.9Å) in ZIFs[30-35] This 4-connected net with Li and B as tetrahedral nodes has an uninodal zeolite RHO topology. (Figure 3.3) Salient features of the RHO topology include a large α cage with 48 vertices and 4-, 6-, and 8-ring windows. Each α cage is connected to six other α cages by sharing *double 8-ring units* to form a 3-D framework. (Figure 3.4)

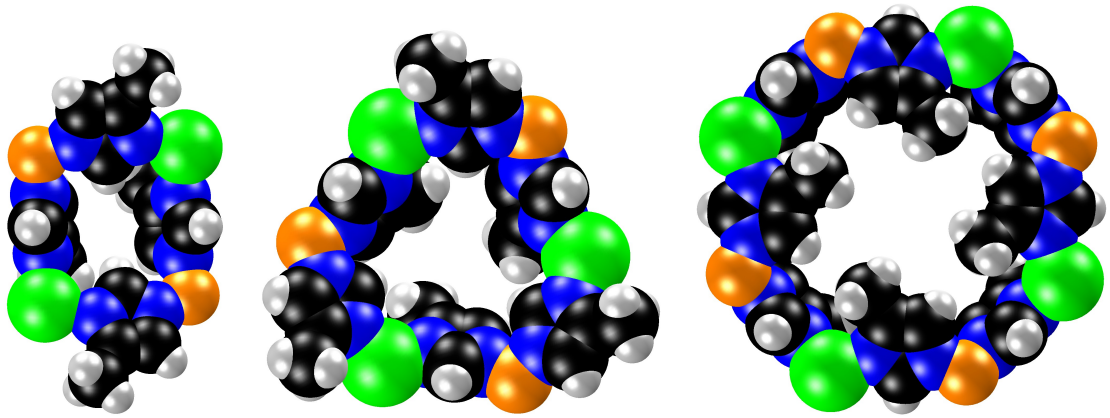


Figure 3.5. Space filling diagrams of 4-ring $M_2B_2(4\text{-Mim})_4$ (left), 6-ring $M_3B_3(4\text{-Mim})_6$ (middle) and 8-ring $M_4B_4(4\text{-Mim})_8$ (right) in RHO (M=Li or Cu, B in orange, N in blue, M in green, C in black, and H in grey). Obviously, the pore aperture size of 8-ring is larger than that of 6-ring and 4-ring.

As the atom nearest to the center of the cage is hydrogen, the cage diameter (14.4Å×15.3Å) and pore aperture diameter (4.2Å) are calculated by subtracting distances

between two diagonal H atoms by twice of *van der Waals* radius of 1.2 Å for H atom. The cage diameter and the aperture size of 8-ring is larger than kinetic diameters of most small-molecule gases, which allows BIF-9-Li to adsorb various gas molecules that can easily diffuse through the 8-ring aperture (but not through 4- and 6-rings due to their small aperture sizes) (Figure 3.5). The 8-ring aperture size is also much bigger than that in the corresponding ZIFs with the RHO topology (3.0Å). The total potential solvent-accessible volume is 8327.8Å^3 per unit cell volume and the pore volume ratio is 45.82% as calculated with the PLATON program [41].

BIF-9-Cu is isostructural to BIF-9-Li. However, the longer bond lengths (B-N bond 1.531-1.551Å; Cu-N bond 2.006-2.091Å) in BIF-9-Cu leads to a slightly larger cell parameter (26.8152Å) than that in BIF-9-Li (26.2923Å). Even though BIF-9-Cu has a larger solvent-accessible volume (9301.9Å^3, 48.24%) and unit cell volume (19281.60Å^3), it has a higher framework density (0.809g/cm^3) than that of BIF-9-Li (0.750g/cm^3), which results from the large difference in the formular weight.

BLF-11-Li also consists of one lithium ion and one-fourth of a tetrakis(2, 4-dimethylane-imidazolyl)borate ligand in the asymmetric unit of a highly symmetrical cubic space group *P*-43*n*, which exhibits 3-D SOD topological framework, similar to that in BIF-3-Li.

BIF-12-Li consists of one lithium ions, one tetrakis(benzimidazolyl)borate ligand, and one (±)-2-amino-1-butanol solvent molecule in its asymmetric unit. Unlike tetrahedral [B(2, 4-Dmim)$_4$]$^-$ ligand in BIF-11, each tetrahedral [B(Bim)$_4^-$] ligand only bridges to three Li sites through the nitrogen atom of three benzimidazoly groups, and the

fourth benzimidazoly is a terminating ligand. Li adopts LiN_3O tetrahedral coordination geometry with a terminal solvent molecule (±)-2-AB (Figure 3.6). BIF-12 possesses a 2-D wavy (4.8.8) layer (also called *fes* net) (Figure 3.6), in which the racemic solvent molecules (±)-2-AB are spontaneously separated into adjacent lithium ions (Figure 3.6).

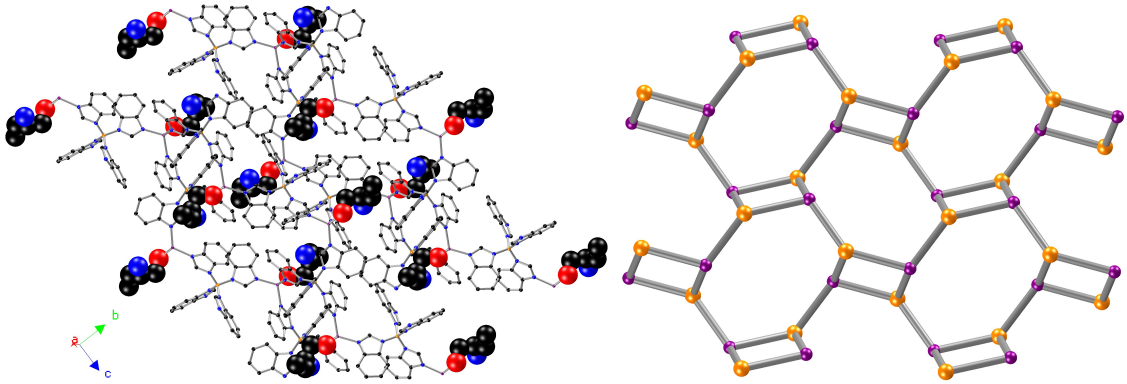


Figure 3.6. Left: The view of 2-D layer in BIF-12 viewed along *a* axis, the big spheres represent (±)-2-amino-1-butanol molecules. Right: 2-D (4.8^2) *fes* topology of BIF-12 (orange ball stands for boron, purple for lithium).

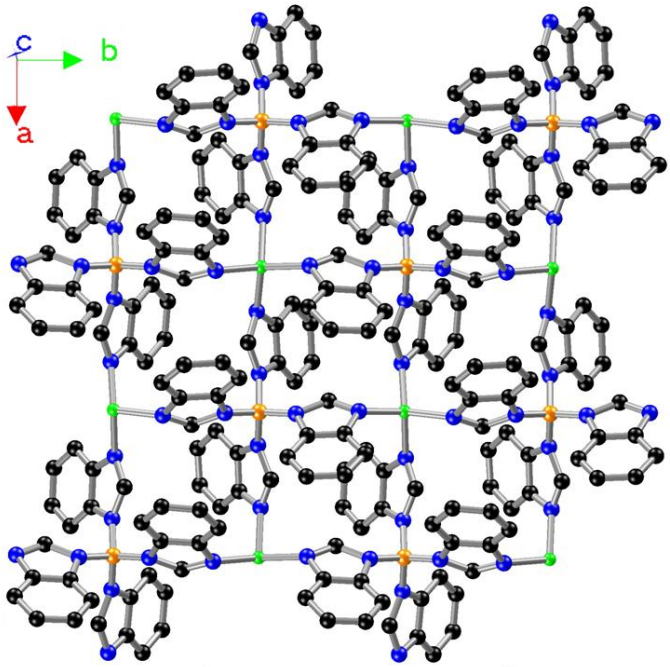


Figure 3.7. 2-D structure of [MB(benzimidazolate)$_4$] (M = Li or Cu) in BIF-13 viewed from *c* axis.

BIF-13 with $B(Bim)_4$ as ligand have layered structures with (4^4) net, with all benzene rings pointed outward away the 2-D plane. (Figure 3.7)

3.3.3 Gas Sorption

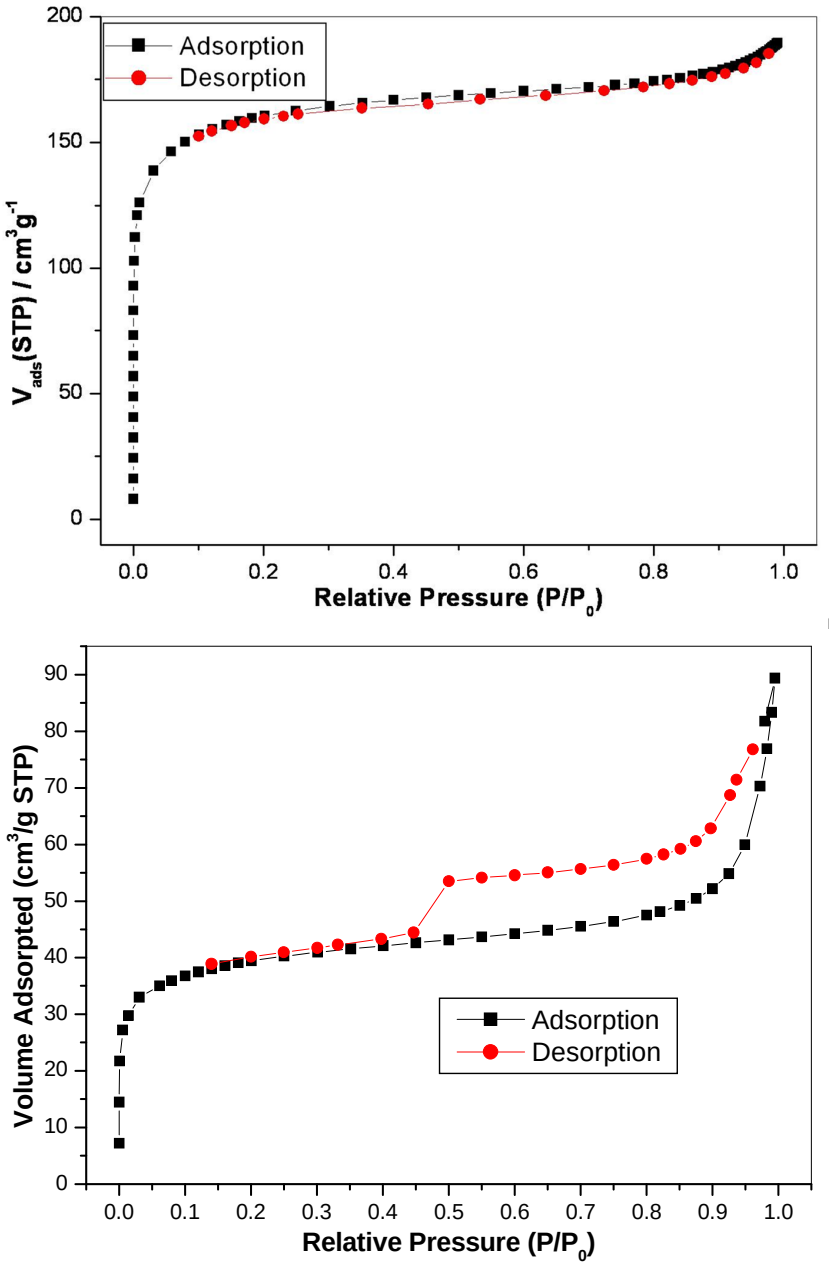


Figure 3.8. N_2 gas sorption isotherm of BIF-3-Li (top) and BIF-3-Cu (bottom) at 77K. P/P_0 is the ratio of gas pressure (P) to saturation pressure (P_0), with P_0=769 torr.

To determine zeolitic properties of such materials, BIF-3-Cu and BIF-3-Li with the sodalite topology were studied by gas adsorption measurements performed on Micromeritics ASAP 2010 surface area and pore size analyzer. The permanent porosity of these BIFs was demonstrated by N_2 adsorption measurements. The samples were degassed at 200ºC prior to the measurement, respectively. They exhibit type I isotherm, indicating the microporous nature. The Langmuir surface areas are 182.3 and 726.5 m^2/g for BIF-3-Cu and BIF-3-Li, respectively (Figure 3.8). The relatively lower surface area compared to the Zn analog may be due to the framework contract resulting from the shorter B-N bond. The CO_2 adsorption isotherms of BIF-3-Cu and BIF-3-Li at 273 K were also evaluated. As shown in Figure 3.9, the maximum adsorptions at ~1 atm are 21.9 and 34.5 $cm^3 \cdot g^{-1}$ for BIF-3-Cu and BIF-3-Li, respectively. These results show that BIF-3-Li outperforms BIF-3-Cu in the CO_2 adsorption capacity. The lighter density of BIF-3-Li may be one contributing factor.

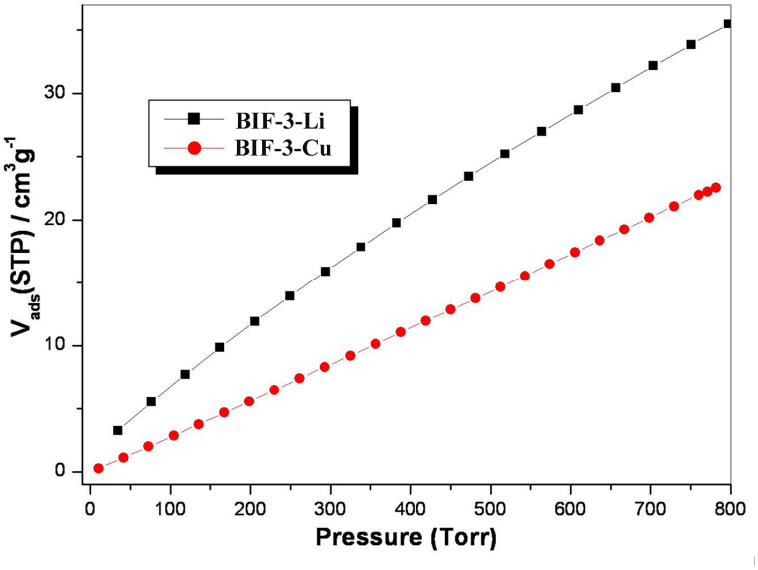


Figure 3.9. CO_2 adsorption isotherms of BIF-3-Li and BIF-3-Cu at 273 K.

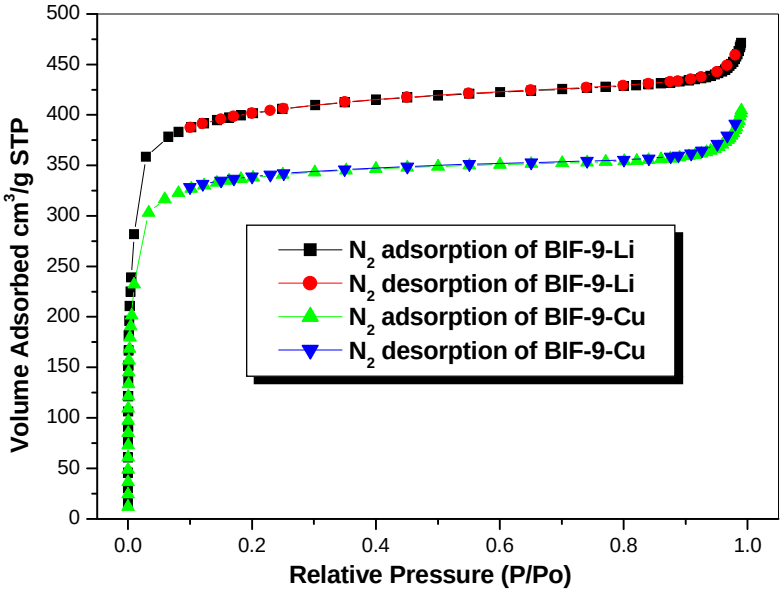


Figure 3.10. Nitrogen gas sorption isotherm at 77K for BIF-9-Li and BIF-9-Cu. P/P_0 is the ratio of gas pressure (P) to saturation pressure (P_0), with P_0=770 torr.

Thermal gravimetric analysis (TGA) shows both BIF-9-Li and BIF-9-Cu can be stable up to approximately 300^{o}C under the N_2 atmosphere. The permanent porosity of BIF-9 was also demonstrated by N_2 gas adsorption measurements. The samples for surface area analysis were activated by immersing as-synthesized BIF-9 with suitable solvents, followed by evacuation at room temperature. The activated samples were characterized by XRD to confirm the structural integrity. BIF-9 exhibit type I adsorption isotherm behavior typical of materials of permanent microporosity (Figure 3.10). The Langmuir surface areas were 1818 m^2/g and 1524 m^2/g for BIF-9-Li and BIF-9-Cu, respectively, demonstrating the effect of molecular weight. The BET method yields surface areas of 1523m^2/g, 1287m^2/g, respectively. A single data point at relative pressure 0.500 gives maximum micropore volume of 0.648cm^3/g and 0.540cm^3/g, respectively, by Horvath-Kawazoe equation.

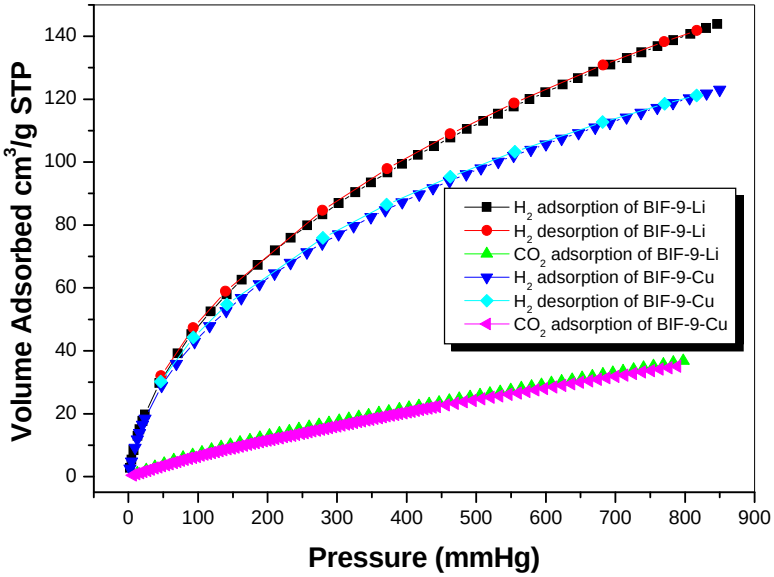


Figure 3.11. Gas sorption isotherm of BIF-9-Li and BIF-9-Cu for H_2 at 77K, and for CO_2 at 273K.

Hydrogen adsorption studies revealed that BIF-9-Li can adsorb 1.23 wt% (volumetric uptake of 9.23kg/m^3, calculated density: 0.750 g/cm^3) hydrogen at 760 Torr and 77K, significantly higher than that of BIF-9-Cu (1.06wt %; volumetric uptake of 8.58 kg/m^3, calculated density: 0.809g/cm^3) (Figure 3.11). CO_2 adsorption isotherms of BIF-9 were also investigated. The maximum adsorption amount at 760Torr and 273K are 35.6 cm^3/g (1.60 mmol/g) and 34.1 cm^3/g (1.53 mmol/g) for BIF-9-Li and BIF-9-Cu, respectively. The lighter framework density of BIF-9-Li may be an important contributing factor for better gas uptake behavior of BIF-9-Li than BIF-9-Cu.

3.3.4 Effect of Substituted Group on Framework Topology and Pore Size

In the previously reported Zn-imidazolate system, the ligand-ligand interaction is known to play a key role in the resultant framework topology. The shorter B-N distance (≈1.5Å) between boron and imidazolyl group (as compared to significantly larger metal-

ligand distances in MOFs, usually 2.0 Å or larger) in the B-im system leads to a significantly closer distance between the adjacent ligand groups, which further enhance the steric repulsion between substituent groups on imidazolyl rings. Initial work with boron imidazolate frameworks only led to quite dense network topologies such as zni (BIF-1), diamond (BIF-2). The much shorter B-N distance tends to narrow the pore aperture and places a serious limitation to the accessibility of internal pore surfaces. Even for porous material BIF-3-Li with the sodalite topology, the surface area is only 726m2/g, which is only 40% of the surface area for the corresponding zinc 2-methylimidazolate (ZIF-8) with the same topology, negating any potential advantages that the use of such lightest elements could bring.

We reason here that if a more open framework topology could be made, the large window size will more than compensate for the shorter B-N distance and the internal pore volume would then be more accessible. However, while benzimidazole (denoted Bim here) is well-known to form zeolite RHO type topology (ZIF-11 and ZIF-12), the reaction of HB(Bim)4 with lithium salts or copper salts only gave layered structures with (44) net, with all benzene rings pointed outward away the 2-D plane. The short B-N distance, coupled with the large benzo group, makes it sterically impossible to form the RHO topology in the boron system when Bim is used as the building block. Clearly, the creation of new zeolite-like boron imidazolates requires strategies that take into consideration of both synthetic and structural factors unique to boron imidazolates.

In fact, the need for topological control has to be balanced with the need to create the maximum porosity. While the size, number, and position of substituent groups on

imidazolyl rings do help to generate more open topology, they can block the pore access. That is why zinc 2-methylimidazolate (ZIF-8) having the relatively dense sodalite net with only 6- and 4-ring windows has a large Langmuir surface area based on N2 adsorption whereas zinc benzimidazolate (ZIF-11) having more open RHO topology with larger 8-, 6-, and 4-rings are actually nonporous towards N2. As shown in this work, this anomaly can be prevented by the selection of a suitably substituted imidazolyl ligand that strikes an ideal balance between structure directing effect and pore window blockage.

To achieve our goal of creating more open zeolitic topology with high surface areas (despite the short B-N distance), we choose 4-methyl imidazolate as the linker to create the zeolite RHO topology based on the following considerations: 1) 4-position mono-substituted methyl group is smaller than the benzo group in benzimidazole and therefore could better accommodate the shortened B-N distance; and 2) 4- and 5-position *di*-substituted groups are prone to lessen the pore volume of the resulting zeolitic frameworks.

It is shown here that the boron imidazolate zeolite RHO materials can be created that have a much greater surface area than the boron imidazolate materials with the sodalite net, in distinct contrast with the Zn-*im* system. Both BIF-9-Li and BIF-9-Cu are porous to N_2 gas while the Zn-Bim RHO (ZIF-11) is not, because the effect of the small subtituent in B-Mim RHO outweights the short B-N distance.

When two or more substituents are present, an intriguing question arises. Do these multiple substituents exhibit a synergistic and cooperative effect in controlling the final framework topology or each individual substituent can exhibit the structural directing

effect on the basis of its own preference? In the latter case where each individual substituent strives to exert its own topological control and thereby competing against each other, the determination of the dominating substituent becomes an issue. In this work, the use of 2, 4-dimethylimidazolate provides a unique opportunity to study such competitive structure-directing effects when more than one substituent are present.

It suggests that each individual substituent can exhibit its own topological control during the solvothermal assembly. This can be seen by a comparison of BIF-11 with BIF-3 and BIF-9. Mono-substitution by a methyl group in 2-position leads to the formation of lithium boron imidazolate frameworks with the SOD topology while mono-substitution by a methyl group in 4-position leads to the formation of lithium boron imidazolate frameworks with the RHO topology. Naturally, 2, 4-dimethylimidazolate becomes especially interesting because it provides an opportunity for us to examine how these two methyl groups control the crystallization when they co-exist in the same imidazolate. A large number of trials have been performed under various reaction conditions, invariably, BIF-11 with the SOD topology is obtained, suggesting that the methyl group at the 2-position dictates the crystallization process.

3.4 Conclusion

In conclusion, we have synthesized a family of boron imidazolate open-framework materials by crosslinking 4-connected boron imidazolate complexes with 4-connected Li^+ or Cu^+ centers. The compositions of these materials are very unique compared to either inorganic zeolites or metal-organic framework materials. As demonstrated here, this chemical system possesses a rich compositional and topological diversity. The materials reported here possess various 4-connected, 3-D open frameworks with topologies ranging from zeolitic SOD type to RHO type. The permanent microporosity for BIF-3 and BIF-9 has also been demonstrated. These MOCOF materials represent a unique family of materials that border between MOFs and covalent frameworks because the tetrahedral vertices (B, Li, and Cu) are joined together by a combination of covalent (B-N) and coordination bonds (Li-N and Cu-N). The synthetic method reported here has a great potential for the creation of a large family of materials with tunable framework compositions and topologies, which could lead to new applications in gas sorption, separation, catalysis *etc*.

3.5 References

(1) Davis, M. E. *Nature* **2002**, *417*, 813-821.

(2) Van Bekkum, H.; Flanigen, E. M.; Jacobs, P. A; Jansen, J. C. *Introduction to Zeolite Science and Practice*, Elsevier, Amsterdam**, 2001**.

(3) Wilson, S. T.; Lok, B. M.; Messina, C. A.; Cannan,T. R.; Flanigen, E. M. *J. Am. Chem. Soc.* **1982**, *104*, 1146-1147.

(4) Cheetham, A. K.; Férey, G.; Loiseau, T. *Angew. Chem. Int. Ed.* **1999**, *38*, 3268-3292.

(5) (a) Cooper, E. R.; Andrews, C. D.; Wheatley, P. S.; Webb, P. B.; Wormald P.; Morris, R. E. *Nature*, **2004**, *430*, 1012-1016. (b) Parnham, E. R.; Morris, R. E. *J. Am. Chem. Soc.* **2006**, *128*, 2204-2205. (c) Parnham, E. R.; Morris, R. E. *Acc. Chem. Res.* **2007,** *40*, 1005-1013.

(6) (a) Bu, X.; Feng, P.; Stucky, G. D. *Science* **1997**, *278*, 2080-2085. (b) Feng, P..; Bu, X.; Stucky, G. D. *Nature* **1997**, *388*, 735-740.

(7) (a) Bedard, R. L.; Wilson, S. T.; Vail, L. D.; Bennett, J. M.; Flanigen, E. M. in Zeolites: Facts, Figures, Future. Proceedings of the 8th International Zeolite Conference; Jacobs, P. A., van Santen, R. A., Eds.; Elsevier, Amsterdam 1989; p. 375. (b) Zheng, N.; Bu, X.; Wang, B.; Feng, P. *Science* **2002**, *298*, 2366-2369. (c) Li, H. L.; Laine, A.; O'Keeffe, M.; Yaghi, O. M. *Science* **1999**, *283*, 1145-1147.

(8) (a) Murray, L. J.; Dincă, M.; Long, J. R. *Chem. Soc. Rev.* **2009**, *38*, 1294-1314. (b) Dincă, M.; Long, J. R. *Angew. Chem., Int. Ed.* **2008**, *47*, 6766. (c) Dinca, M.; Yu, A. F.; Long, J. R. *J. Am. Chem. Soc.* **2006**, *128*, 17153.

(9) (a) Rosi, N. L.; Eckert, J.; Eddaoudi, M.; Vodak, D. T.; Kim, J.; O'Keeffe, M.; Yaghi, O. M. *Science* **2003**, *300*, 1127. (b) Rowsell, J. L. C.; Millward, A. R.; Park, K. S.; Yaghi, O. M. *J. Am. Chem. Soc.* **2004**, *126*, 5666. (c) Millward, A. R.; Yaghi, O. M. *J. Am. Chem. Soc.* **2005**, *127*, 17998. (d) Han, S. S.; Furukawa, H.; Yaghi, O. M.; Goddard, W. A. *J. Am. Chem. Soc.* **2008**, *130*, 11580.

(10) (a) Zhao, D.; Yuan, D.; Zhou, H.-C. *Energy En*V*iron. Sci.* **2008**, *1*, 222-235. (b) Sun, D.; Ma, S.; Ke, Y.; Collins, D. J.; Zhou, H.-C. *J. Am. Chem. Soc.* **2006**, *128*, 3896-3897. (c) Wang, X.-S.; Ma, S.; Sun, D.; Parkin, S.; Zhou, H.-C. *J. Am. Chem. Soc.* **2006**, *128*, 16474-16475. (d) Ma, S.; Sun, D.; Simmons, J. M.; Collier, C. D.; Yuan, D.; Zhou, H.-C. *J. Am. Chem. Soc.* **2008**, *130*, 1012-1016.

(11) Pan, L.; Parker, B.; Huang, X. Y.; Olson, D. H.; Lee, J.; Li, J. *J. Am. Chem. Soc.* **2006**, *128*, 4180.

(12) (a) Li, J. R.; Kuppler, R. J.; Zhou, H.-C. *Chem. Soc. Rev.* **2009**, *38*, 1477-1504. (b)Ma, S.; Sun, D.; Wang, X.; Zhou, H.-C. *Angew. Chem. Int. Ed.* **2007**, *46*, 2458-2462.

(13) (a) Wang, B.; Cote, A. P.; Furukawa, H.; O'Keeffe, M.; Yaghi, O. M. *Nature* **2008**, *453*, 207. (b) Britt, D.; Tranchemontagne, D.; Yaghi, O. M. *Proc. Natl. Acad. Sci.* **2008**, *105*, 11623-11627.

(14) Mueller, U.; Schubert, M.; Teich, F.; Puetter, H.; Schierle-Arndt, K.; Pastré, J. *J. Mater. Chem.* **2006**, *16*, 626-636.

(15) (a) Ma, L. Q.; Abney, C.; Lin, W. B. *Chem. Soc. Rev.* **2009**, *38*, 1248-1256. (b) Wu, C.; Hu, A.; Zhang, L.; Lin, W. *J. Am. Chem. Soc.* **2005**, *127*, 8940. (c) Wu, C.; Lin, W., *Angew. Chem., Int. Ed.* **2007**, 46, 1075.

(16) (a) Seo, J. S.; Whang, D.; Lee, H.; Jun, S. I.; Oh, J.; Jeon, Y. J.; Kim, K. *Nature* **2000**, *404*, 982. (b) Dybtsev, D. N.; Nuzhdin, A. L.; Chun, H.; Bryliakov, K. P.; Talsi, E. P.; Fedin, V. P.; Kim, K. *Angew. Chem., Int. Ed.* **2006**, *45*, 916. (c) Cho, S. H.; Ma, B. Q.; Nguyen, S. T.; Hupp, J. T.; Albrecht-Schmitt, T. E. *Chem. Commun.* **2006**, 2563. (d) Tanaka, K.; Oda, S.; Shiro, M. *Chem. Commun.* **2008**, 820.

(17) (a) Ma, L. Q.; Mihalcik, D. J.; Lin, W. B. *J. Am. Chem. Soc.* **2009**, *131*, 4610-4612. (b) Wu, S. T.; Ma, L. Q.; Long, L. S.; Zheng, L. S.; Lin, W. B. *Inorg. Chem.* **2009**, *48*, 2436-2442. (c) Wu, C. D.; Ma L. Q.; Lin, W. B. *Inorg. Chem.* **2008**, *47*, 11446-11448. (d) Taylor, K. M. L.; Rieter, W. J.; Lin, W. B. *J. Am. Chem. Soc.* **2008**, *130*, 14358-14359. (e) Ma L. Q.; Lin, W. B. *J. Am. Chem. Soc.* **2008**, *130*, 13834-13835.

(18) (a) Férey, G.; Mellot-Draznieks, C.; Serre, C.; Millange, F.; Dutour, J.; Surblé, S.; Margiolaki, I. *Science* **2005**, 309, 2040-2042. (b) Férey, G.; Millange, F.; Morcrette, M.; Serre, C.; Doublet, M. L; Grenèche, J. M.; Tarascon, J. M. *Angew. Chem. Int. Ed.* **2007**, *46*, 3259-3263.Hwang, Y. K.; Hong, D. Y.; Chang, J. S.; Jhung, S. H.; Seo, Y. K.; Kim, J. H.; Vimont, A.; Daturi, M.; Serre, C.; Férey, G. *Angew. Chem. Int. Ed.* **2008**, *47*, 4144-4148.

(19) (a) Rosi, N. L.; Kim, J.; Eddaoudi, M.; Chen, B. L.; O'Keeffe, M.; Yaghi, O. M. *J. Am. Chem. Soc.* **2005**, *127*, 1504. (b) Zhang, M. B.; Chen, Y. M.; Zheng, S. T.; Yang, G. Y. *Eur. J. Inorg. Chem.* **2006**, 1423. (c) Ma, C. B.; Chen, C. N.; Liu, Q. T.; Liao, D. Z.; Li, L. C.; Sun, L. C. *New J. Chem.* **2003**, *27*, 890. (d) Zhao, B.; Cheng, P.; Chen, X. Y.; Cheng, C.; Shi, W.; Liao, D. Z.; Yan, S. P.; Jiang, Z. H. *J. Am. Chem. Soc.* **2004**, *126*, 3012.

(20) (a) Taylor, K. M. L.; Jin, A.; Lin, W. B. *Angew. Chem. Int. Ed.* **2008**, *47*, 7722-7725. (b) Rieter, W. J.; Taylor, K. M. L.; An, H. Y.; Lin, W. L.; Lin, W. B. *J. Am. Chem. Soc.* **2006**, *128*, 9024-9025.

(21) Zhang, J.; Wu, T.; Chen, S. M.; Feng, P.; Bu, X. *Angew. Chem. Int. Ed.* **2009**, *48*, 3486-3490.

(22) (a) Chen, B.; Wang, L. B.; Xiao, Y. Q.; Fronczek, F. R.; Xue, M.; Cui. Y. J.; Qian, G. D. *Angew. Chem. Int. Ed.* **2009**, *48*, 500-503. (b) Chen, B.; Wang, L. B.; Zapata, F.; Qian, G. D.; Lobkovsky, E. B. *J. Am. Chem. Soc.* **2008**, *130*, 6718-6719.

(23) (a) Zhang, J.; Chen, S. M.; Zingiryan, A.; Bu, X. *J. Am. Chem. Soc.* **2008**, *130*, 17246-17247. (b) Zhang, J.; Chen, S. M.; Valle, H.; Wong, M.; Austria, C.; Cruz, M.; Bu, X. *J. Am. Chem. Soc.* **2007**, *129*, 14168-14169.

(24) (a) Dincă, M.; Long, J. R. *J. Am. Chem. Soc.* **2005**, *127*, 9376. (b) Rood, J. A.; Noll, B. C.; Henderson, K. W. *Inorg. Chem.* **2006**, *45*, 5521. (c) Loiseau, T.; Lecroq, L.; Volkringer, C.; Marrot, J.; Férey, G.; Haouas, M.; Taulelle, F.; Bourrelly, S.; Llewellyn, P. L.; Latroche, M. *J. Am. Chem. Soc.* **2006**, *128*, 10223. (c) Abrahams, B. F.; Hawley, A.; Haywood, M. G.; Hudson, T. A.; Robson, R.; Slizys, D. A. *J. Am. Chem. Soc.* **2004**, *126*, 2894. (d) Rood, J. A.; Boggess, W. C.; Noll, B. C.; Henderson, K. W. *J. Am. Chem. Soc.* **2007**, *129*, 13675.

(25) (a) Zhang, J.; Chen, S. M.; Wu, T.; Feng, P.; Bu, X. *J. Am. Chem. Soc.* **2008**, *130*, 12882-12883. (b) Zhang, J.; Chen, S. M.; Bu, X. *Angew. Chem. Int. Ed.* **2008**, *47*, 5434-5437.

(26) (a) Liu, Y. L; Kravtsov, V. Ch.; Beauchamp, D. A.; Eubank, J. F.; Eddaoudi, M. *J. Am. Chem. Soc.* **2005**, *127*, 7266. (b) Sun, J. Y.; Weng, L. H.; Zhou, Y. M.; Chen, J. X.; Chen, Z. X.; Liu, Z. C.; Zhao, D. Y. *Angew. Chem., Int. Ed.* **2002**, *41*, 4471. (c) Lin, Z. Z.; Jiang, F. L.; Yuan, D. Q.; Chen, L.; Zhou, Y. F.; Hong, M. C. *Eur. J. Inorg. Chem.* **2005**, 1927. (d) Lin, Z. Z.; Jiang, F. L.; Chen, L.; Yuan, D. Q.; Zhou, Y. F.; Hong, M. C. *Eur. J. Inorg. Chem.* **2005**, 77. (e) Gomez-Lor, B.; Gutierrez-Puebla, E.; Iglesias, M.; Monge, M. A.; Ruiz-Valero, C.; Snejko, N. *Chem. Mater.* **2005**, *17*, 2568.

(27) (a) Banerjee, D.; Kim, S. J.; Parise, J. B. *Cryst. Growth Des.* **2009**, *9*, 2500-2503. (b) Knop, O.; Bakshi, P. K. *Can. J. Chem.* **1995**, *73*, 151.

(28) (a) Côté, A. P.; Benin, A. I.; Ockwig, N .W.; O'Keeffe, M.; Matzger, A. J.; Yaghi, O. M. *Science* **2005**, *310*,1166-1170. (b) El-Kaderi, H. M.; Hunt, J. R.; Mendoza-Cortés, J. L.; Côté, A. P.; Taylor, R. E.; O'Keeffe, M.; Yaghi,

O. M. *Science* **2007**, *16*, 268-272. (c) Côté, A. P.; El-Kaderi, H. M.; Furukawa, H.; Hunt, J. R.; Yaghi, O. M. *J. Am. Chem. Soc*. **2007**, *129*, 12914-12915.

(29) (a) Wan, S.; Guo, J.; Kim, J.; Ihee, H.; Jiang, D. *Angew. Chem. Int. Ed.* **2008**, *47*, 8826-8830. (b) Kuhn, P.; Antonietti, M.; Thomas, A. *Angew. Chem. Int. Ed.* **2008**, *47*, 3450-3453. (c) Tilford, R.W.; Mugavero III, S. J.; Pellechia P. J.; Lavigne, J. J. *Adv. Mater.* **2008**, *2*0, 2741- 2746.

(30) (a) Tian, Y. Q.; Cai, C. X.; Ji, Y.; You, X. Z.; Peng, S. M.; Lee, G. S. *Angew. Chem. Int. Ed.* **2002**, *41*, 1384-1386. (b) Tian, Y. Q.; Cai, C. X.; Ren, X. M.; Duan, C. Y.; Xu, Y.; Gao, S.; You, X. Z. *Chem. Eur. J.* **2003**, *9*, 5673-5685. (c) Tian, Y.-Q.; Chen, Z. X.; Weng, L.-H.; Guo, H. B.; Gao, S.; Zhao, D. Y. *Inorg. Chem.* **2004**, *43*, 4631-4635. (d) Tian, Y.-Q.; Zhao, Y.-M.; Chen, Z.-X.; Zhang, G.-N.; Weng, L.-H.; Zhao, D.-Y. *Chem. Eur. J.* **2007**, *13*, 4146-4154.

(31) Huang, X.-C.; Lin, Y.-Y.; Zhang, J. P.; Chen, X.-M. *Angew. Chem. Int. Ed.* **2006**, *45*, 1557-1559.

(32) (a) Park, K. S.; Ni, Z.; Côté, A. P.; Choi, J. Y.; Huang, R.; Uribe-Romo, F. J.; Chae, H. K.; O'Keeffe, M.; Yaghi, O. M. *Proc. Natl Acad. Sci. USA* **2006**, *103*, 10186-10191. (b) Hayashi, H.; Côté, A. P.; Furukawa, H.; O'Keeffe, M.; Yaghi, O. M. *Nature Materials* **2007**, *6*, 501-506.

(33) (a) Morris, W. ; Doonan, C. J. ; Furukawa, H. ; Banerjee, R.; Yaghi, O. M. *J. Am. Chem. Soc.* **2008**, *130*, 12626-12627. (b) Banerjee, R.; Furukawa, H.; Britt, D.; Knobler, C.; O'Keeffe, M.; Yaghi, O. M. *J. Am. Chem. Soc.* **2009**, *131*, 3875-3877.

(34) (a) Wu, T.; Bu, X.; Zhang, J.; Feng, P. *Chem. Mater.* **2008**, *20*, 7377-7382. (b) Wu, T.; Bu, X.; Liu, R.; Lin, Z.; Zhang, J.; Feng, P. *Chem. Eur. J.* **2008**, *14*, 7771-7773.

(35) (a) Banerjee, R.; Phan, A.; Wang, B.; Knobler, C.; Furukawa, H.; O'keeffe, M.; Yaghi, O. M. *Science* **2008**, *319*, 939-943. (b) Wang, B.; Côté, A. P.; Furukawa, H.; O'Keeffe, M.; Yaghi, O. M. *Nature*, **2008**, *453*, 207-211.

(36) (a) Liu, Y. L.; Kravtsov, V.; Larsen, R.; Eddaoudi, M. *Chem. Commun.* **2006**, 1488-1490. (b) Sava, D. F.; Kravtsov, V.; Nouar, F.; Wojtas, L.; Eubank, J. F.; Eddaoudi, M. *J. Am. Chem. Soc.* **2008**, *130*, 3768–3770. (c) Nouar, F.; Eckert, J.; Eubank, J. F.; Forster, P.; Eddaoudi, M. *J. Am. Chem. Soc.* **2009**, *131*, 2864–2870.

(37) Trofimenko, S. *J. Am. Chem. Soc.* **1967**, *89*, 3170-3177.

(38) Bailey, P. J.; Lorono-Gonzales, D.; McCormack, C.; Millican, F.; Parsons, S.; Pfeifer, R.; Pinho, P. P.; Rudolphi, F.; Perucha, A. S. *Chem. Eur. J.* **2006**, *12*, 5293-5300.

(39) (a) Hamilton, B. H.; Ziegler, C. J. *Inorg. Chem.* **2004**, *43*, 4272-4277. (b) Hamilton, B. H.; Kelly, K. A.; Wagler, T. A.; Espe, M. P.; Ziegler, C. J. *Inorg. Chem.* **2004**, *43*, 50-56.

(40) Knop,O.; Bakshi, P. K. *Can. J. Chem.* **1995**, *73*, 151-160.

(41) Spek, A. L. J. *Appl. Crystallogr.* **2003**, *36*, 7-13.

Chapter 4

Synthetic Control of Selenide Supertetrahedral Clusters and Three-Dimensional Co-Assembly by Charge-Complementary Metal Cations

4.1 Introduction

Crystalline metal chalcogenides are an important family of semiconductors that have practical or potential applications in multiple areas such as photocatalysis[1] and thermoelectrics.[2] In recent years, research on crystalline porous chalcogenides has received increasing attention because the integration of open-framework architecture and semiconducting properties could lead to multi-functional materials such as high-surface-area photocatalysts and photoelectrodes.[3, 4] Furthermore, the basic structural building blocks of open-framework chalcogenides are often nano-sized tetrahedral clusters that can be considered as the smallest possible semiconductor quantum dots.[5-10] Indeed quantum confinement effects have been found in such clusters.[11]

In the synthetic design of supertetrahedral clusters and their porous covalent superlattices, it has been recognized that the charge of tetrahedral metallic cations plays a key role in the determination of the cluster size.[10a, 12] This is primarily because there are specific requirements for the local charge balance surrounding chalcogenide anions (X^{2-}, such as S^{2-} or Se^{2-}). To form the core of large supertetrahedral clusters such as T4 and T5 clusters (e.g., T4-$[Zn_4In_{16}S_{33}]^{10-}$ and T5-$[Cu_5In_{30}S_{54}]^{13-}$), tetrahedrally coordinated X^{2-}

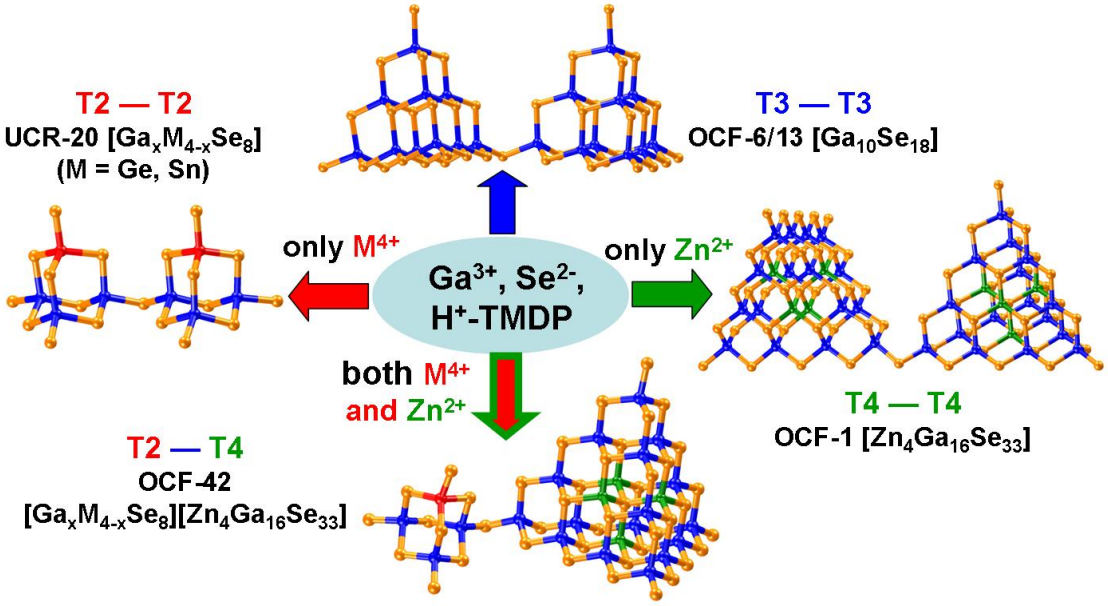
sites (in the form of M_4X, called anti-T1 supertetrahedral cluster) are essential. High-charged metal cations such as Ge^{4+} and Sn^{4+} are known to suppress the growth of the large clusters because of their inability to form Sn_4S^{14+} or Ge_4S^{14+} units. In comparison, low-charged metal cations such as Zn^{2+} and Cu^{+} promote the formation of core tetrahedral X^{2-} sites (e.g., Zn_4S^{6+}), leading to large supertetrahedral clusters (T4 or bigger).

By utilizing the above local-charge-balance principle, two distinct synthetic strategies have been developed to create open-framework chalcogenides with clusters of different sizes. The first one is based on the combination of tri- and divalent metal cations (such as In^{3+}/Zn^{2+}, or alternatively tri- and monovalent cations such as In^{3+}/Cu^{+}).[8d, 12] This strategy has allowed the synthesis of a series of open-framework chalcogenides containing large supertetrahedral clusters such as T4 and T5 clusters.

The second strategy is to mimic Al-Si-O zeolite compositions. By combining tetra- and trivalent cations ($M^{4+}/M^{3+}/X^{2-}$, M^{4+} = Ge^{4+} or Sn^{4+}, M^{3+} = Ga^{3+} or In^{3+}; X^{2-} = S^{2-} or Se^{2-}), a family of crystalline porous semiconducting chalcogenide zeolite analogs have been made.[13] These porous chalcogenides contain only T2 clusters. The T2 cluster (M_4X_8) is different from larger clusters (e.g., T3, T4...) because all anionic sites in T2 are bi-coordinated between two tetrahedral metal sites, an essential feature of MX_2 zeolite topologies. In comparison, T3 clusters contain tri-coordinated X^{2-} sites and T4 or larger clusters contain both tri- and tetra-coordinated X^{2-} sites.

The above synthetic strategies can be unified by using trivalent chalcogenide compositions (e.g., Ga-Se, Scheme 4.1) as a starting point. The M^{3+}/X^{2-} system normally

allows the synthesis of binary T3 clusters such as $[In_{10}S_{20}]^{10-}$. The incorporation of lower-valent M^{2+} or Cu^{+} cations leads to the growth of the M_4S core and larger ternary $M^{3+}/M^{2+}/X^{2-}$ (or $M^{3+}/M^{+}/X^{2-}$) clusters, whereas the addition of M^{4+} cations suppresses the formation of both tri- and tetra-coordinated X^{2-} sites, leading to the formation of ternary $M^{4+}/M^{3+}/X^{2-}$ T2 clusters with bi-coordinated X^{2-} sites only.



Scheme 4.1. Four different strategies to create supertetrahedral clusters and their co-assemblies through charge-complementary metal cations with different oxidization states. H^{+}-TMDP is protonated 4, 4'-trimethylenedipiperidine.

In seeking to develop new synthetic strategies to create new chalcogenide open-framework materials, we hypothesized that if we combine all three charge-complementary metal cations ($M^{4+}/M^{3+}/M^{2+}$ or $M^{4+}/M^{3+}/M^{+}$), we might be able to create a new synthetic system in which both zeolite AX_2-type building units (e.g., T2 clusters with ternary $M^{4+}/M^{3+}/X^{2-}$ compositions) and large supertetrahedral clusters (T4, T5 or

larger clusters with ternary $M^{3+}/M^{2+}/X^{2-}$ or $M^{3+}/M^{+}/X^{2-}$ compositions) can co-exist. By using amine-templated co-assembly of such two types of clusters, it should be possible to create a new family of open-framework chalcogenides with unprecedented quaternary compositions and unusual topological features (Scheme 4.1). Such materials will lie between 4-connected zeolite-type MX_2 frameworks and 3-D superlattices of nano-clusters, which would also provide a new path towards the control of electronic, optical, and electro-optic properties of the resulting materials because of the increased diversity and complexity in chemical compositions, cluster sizes, and their patterns of organization.

Here we report two new isostructural 3-D open-framework selenides (denoted as OCF-42-ZnGaGeSe-TMDP and OCF-42-ZnGaSnSe-TMDP) that illustrate the feasibility of this synthetic strategy. It is worth noting that even though a significant progress has been made in sulfides, very few three-dimensional open-framework selenides are known.[14] In fact, to our knowledge, no 3-D quaternary open-framework chalcogenides based on supertetrahedral clusters were known prior to this work, although an example of an isolated quaternary T3 cluster was reported recently.[15] Considering extended structures built from ternary (e.g., $M^{4+}/M^{3+}/X^{2-}$, $M^{3+}/M^{2+}/X^{2-}$) or binary (e.g., In-Se, Ga-Se) selenide clusters are well known, it is extraordinary that quaternary phases are formed in our system, instead of macroscopic phase separation into compositionally simpler selenides. Impressively, the phase separation did occur in the materials reported, albeit at the cluster-scale level, as reflected by the formation of three-dimensional frameworks containing both M^{4+}/M^{3+} T2 and M^{3+}/M^{2+} T4 clusters.

4.2 Experimental Section

4.2.1 Solvothermal Syntheses

OCF-42-ZnGaGeSe-TMDP: GeO_2 (12.1mg, 0.116mmol), Ga_2O_3 (113.2mg, 0.604mmol), Se (187.2mg, 2.371mmol), $Zn(NO_3)_2 \cdot 6H_2O$ (82.5mg, 0.277mmol), and TMDP (4, 4'-trimethylenedi-piperidine; 1.996g, 9.673mmol) were mixed with H_2O (3.028g, 168mmol) in 23-mL Teflon-lined stainless steel autoclave and stirred for one hour. The vessel was then sealed and heated to 200^oC for 6 days. After cooling to the room temperature, pale-yellow column crystals were obtained in a yield of 123.3mg.

OCF-42-ZnGaSnSe-TMDP: $SnCl_4 \cdot 5H_2O$ (36.3mg, 0.104mmol), Ga_2O_3 (106.9mg, 0.570mmol)), Se (161.6mg, 2.047mmol), $Zn(NO_3)_2 \cdot 6H_2O$ (73.0mg, 0.247mmol) and TMDP (4, 4'-trimethylene-dipiperidine; 2.011g, 9.746mmol) were mixed with H_2O (3.122g, 173mmol) in 23-mL Teflon-lined stainless steel autoclave and stirred for two hours. The vessel was then sealed and heated to 200^oC for 6 days. After cooling to the room temperature, yellow block crystals were obtained in a yield of about 145.2mg.

4.2.2 Structure Determination

Single-crystal X-ray analysis was performed on a Bruker Smart APEX II CCD area diffractometer with nitrogen-flow temperature controller using graphite-monochromated $Mo_{K\alpha}$ radiation (λ = 0.71073 Å), operating in the ω and φ scan mode. The SADABS program was used for absorption correction. The structure was solved by direct methods and the structure refinements were based on $|F^2|$. All non-hydrogen atoms were refined with anisotropic displacement parameters. All crystallographic calculations

were conducted with the SHELXTL software suites.[16] Crystallographic data of OCF-42-ZnGaGeSe-TMDP (CSD Number 420826): $[(Ga_{2.4}Ge_{1.6}Se_8)(Zn_4Ga_{16}Se_{33})_4]\cdot(template)_x$, tetragonal, *I*-4*c*2, $a = b = 36.5659(3)$ Å, $c = 46.6103(8)$ Å, $V = 62321.0(13)$Å^3, $Z = 16$, $2\theta_{max} = 35$ ($-30 \leq h \leq 30$, $-30 \leq k \leq 30$, $-39 \leq l \leq 39$), $T = 150$K, 105460 measured reflections, $R_1 = 0.0932$ for 9901 reflections ($I > 2\sigma(I)$), GOF = 1.097; $[(Ga_{2.4}Sn_{1.6}Se_8)(Zn_4Ga_{16}Se_{33})_4]\cdot(template)_x$ (CSD Number 420827), tetragonal, *I*-4*c*2, $a = b = 36.0137(5)$ Å, $c = 46.7190(16)$ Å, $V = 60594(2)$Å^3, $Z = 16$, $2\theta_{max} = 35$ ($-30 \leq h \leq 30$, $-30 \leq k \leq 30$, $-39 \leq l \leq 39$), $T = 150$ K, 147639 measured reflections, $R_1 = 0.1048$ for 9618 reflections ($I > 2\sigma(I)$), GOF = 1.150. Further details of the crystal structure investigations may be obtained from Fachinformationszentrum Karlsruhe, 76344 Eggenstein-Leopoldshafen, Germany (fax: (+49)7247-808-666; e-mail: crysdata@fiz-karlsruhe.de, http://www.fiz-karlsruhe.de/request_for_deposited_data.html) on quoting the appropriate CSD number.

4.2.3 Powder X-ray Diffraction

Room temperature X-ray powder diffraction experiments were performed on a Bruker D8 Advance powder diffractometer, equipped with a Sol-X detector using Cu $K\alpha_1$ radiation ($\lambda = 1.5406$ Å). The simulated XRD pattern was calculated from the structure data using the Mercury 2.4 software.

4.2.4 Optical Properties

Fluorescent spectra were measured on a SPEX Fluorolog-3 Tau3 system equipped with a 450W xenon lamp and double monochromators on both excitation and emission sides. The band gaps were determined through the UV/vis/near-IR diffuse reflectance spectra measured on a Shimadzu UV-3101PC double-beam, double-monochromator

spectrophotometer. $BaSO_4$ powder was used as both reference (100% reflectance) and sometimes base material for the coating of samples. Absorption (α/S) data were calculated from the reflectance data by using the Kubelka-Munk function: $\alpha/S = (1-R)^2/R$, where R is the reflectance at a given wavelength, α is the absorption coefficient, and S is the scattering coefficient.

4.2.5 Thermal Analysis

The simultaneous DSC-TGA thermal analysis was performed on TA instruments SDT Q600. All samples was prepared by grinding single crystals into fine powder and heated between room temperature and 1200 ^oC at a heating rate of 5 ^oC/min under N_2 gas or air flow (100 ml/min).

4.3 Results and Discussion

4.3.1 Synthesis

Both $M^{4+}/M^{3+}/Se^{2-}$ T2 clusters and $M^{3+}/M^{2+}/Se^{2-}$ T4 clusters have been reported before, what is unprecedented in OCF-42s is their uniform and nanoscale integration. One of the greatest challenges in developing multinary compositions is the likely phase separation into simpler compositions such as ternary (e.g., $M^{3+}/M^{2+}/Se^{2-}$, $M^{4+}/M^{3+}/Se^{2-}$) and binary compositions (e.g., Ga^{3+}/Se^{2-}). Indeed, these simpler compositions are well known. For examples, the T2 cluster is known in zeolite-type UCR-20, -21, and -22,[13] and T4 supertetrahedral cluster ($Zn_4Ga_{16}Se_{33}$) reported here is also found in OCF-1-ZnGaSe-TMDP.[14] In the work reported here, instead of macroscopic phase separation into simpler ternary phases such as OCF-1 and UCR-20, quaternary OCF-42s are formed by integrating both T2 and T4 clusters in the same crystalline material.

In order to avid formation of large amount of impurities or phase separation, the key point on synthetic control is to adjust the amount of tetravalent M^{4+} metal ions. Too small amount of M^{4+} added into reaction system will result in forming large amount of OCF-5-ZnGaSe-TMDP, however, adding large amount of M^{4+} cations will easily cause the formation of UCR-20-MGaSe-TMDP. Systematic change in the amount of tetravalent metal ions has been carried out for controlling purity of products. The final phase purity was supported by PXRD (Figure 4.1). The presence of *di*-, *tri*- and tetravalent elements was confirmed by the energy dispersive X-ray (EDAX) spectroscopy performed on a scanning electron microscope (SEM) (Figure 4.2). The determination of the Sn^{4+}/Ga^{3+} ratios was performed by single crystal analysis based on the large difference in the scattering power between Sn^{4+} and Ga^{3+} cations.[16] The Ge/Ga ratio could not be refined reliably and the value given was estimated by comparison with OCF-42-ZnGaSnSe-TMDP.

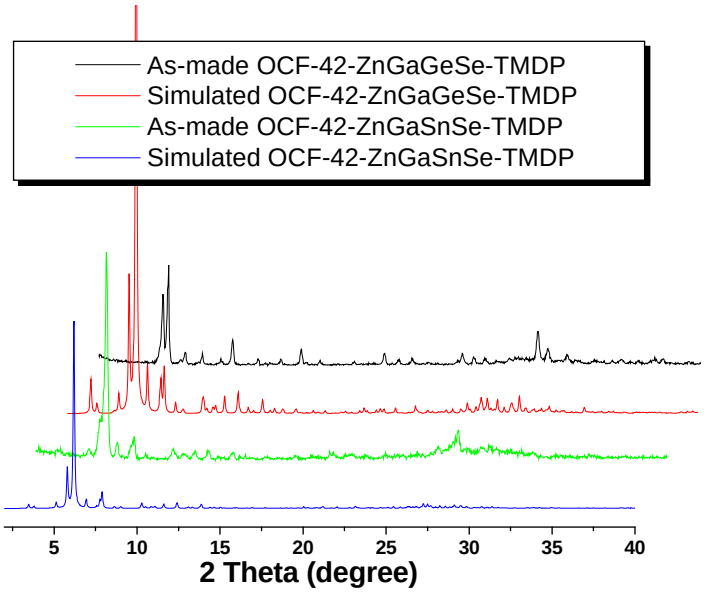


Figure 4.1. The powder X-ray diffraction (PXRD) pattern of OCF-42.

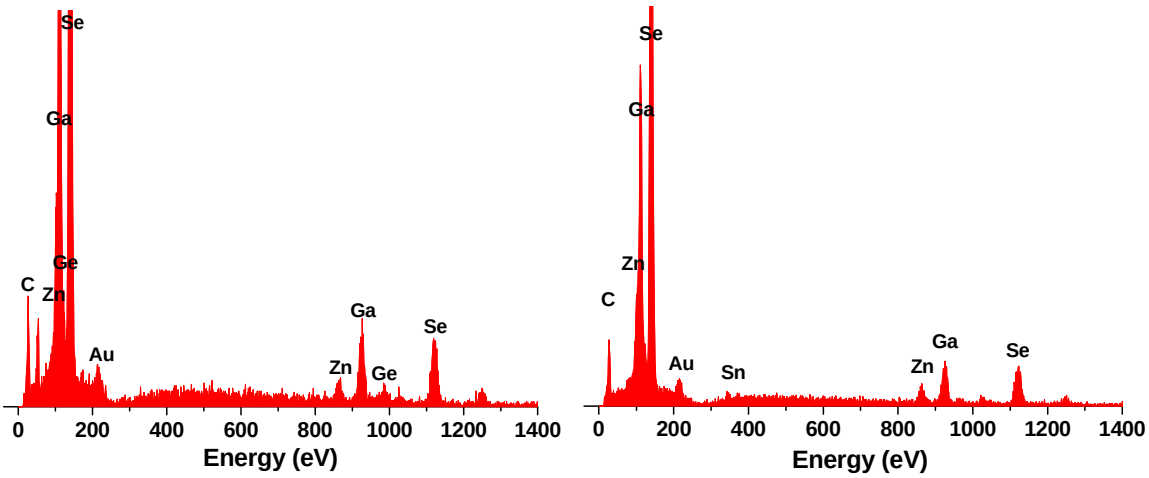


Figure 4.2. The energy dispersive X-ray (EDAX) spectroscopy of OCF-42-ZnGaGeSe-TMDP (left) and OCF-42-ZnGaSnSe-TMDP (right).

4.3.2 Structure

One of the most unusual features of OCF-42s is their extraordinary quaternary composition integrating three charge-complementary metal cations. Note that the charge complementarity is an essential feature of this synthetic strategy. The 3-D open-framework of OCF-42s is composed of $M^{4+}/Ga^{3+}/Se^{2-}$ T2 and $Ga^{3+}/Zn^{2+}/Se^{2-}$ T4 supertetrahedral clusters. In both clusters, all metal sites are four-coordinated. For $M^{4+}/M^{3+}/Se^{2-}$ T2 clusters, all Se^{2-} sites are bi-coordinated, similar to O^{2-} in zeolites.[17] In comparison, in $M^{3+}/M^{2+}/Se^{2-}$ T4 clusters, in addition to 18 bi-coordinated Se^{2-} sites on six edges, there are also 12 tri-coordinated Se^{2-} ions on each face, and one tetrahedral Se^{2-} at the core of T4 supertetrahedron. To satisfy Pauling's electrostatic valence rule, the central tetrahedral Se^{2-} site is surrounded by four zinc ions to give a bond valence sum of +2, which is consistent with the valence of Se^{2-}.

Three-dimensional covalent open-frameworks of OCF-42s are formed from corner-sharing T2 and T4 supertetrahedral clusters. (Figure 4.3) The M-Se-M bond

angles at corner sites range from 104.5 to 109.9°. Few examples of open-framework chalcogenides containing two types of supertetrahedral clusters are known.[18] Those few known examples also have simpler binary (e.g. In-S) or ternary compositions (e.g., Zn-In-S), which make them fundamentally different from the quaternary materials reported here.

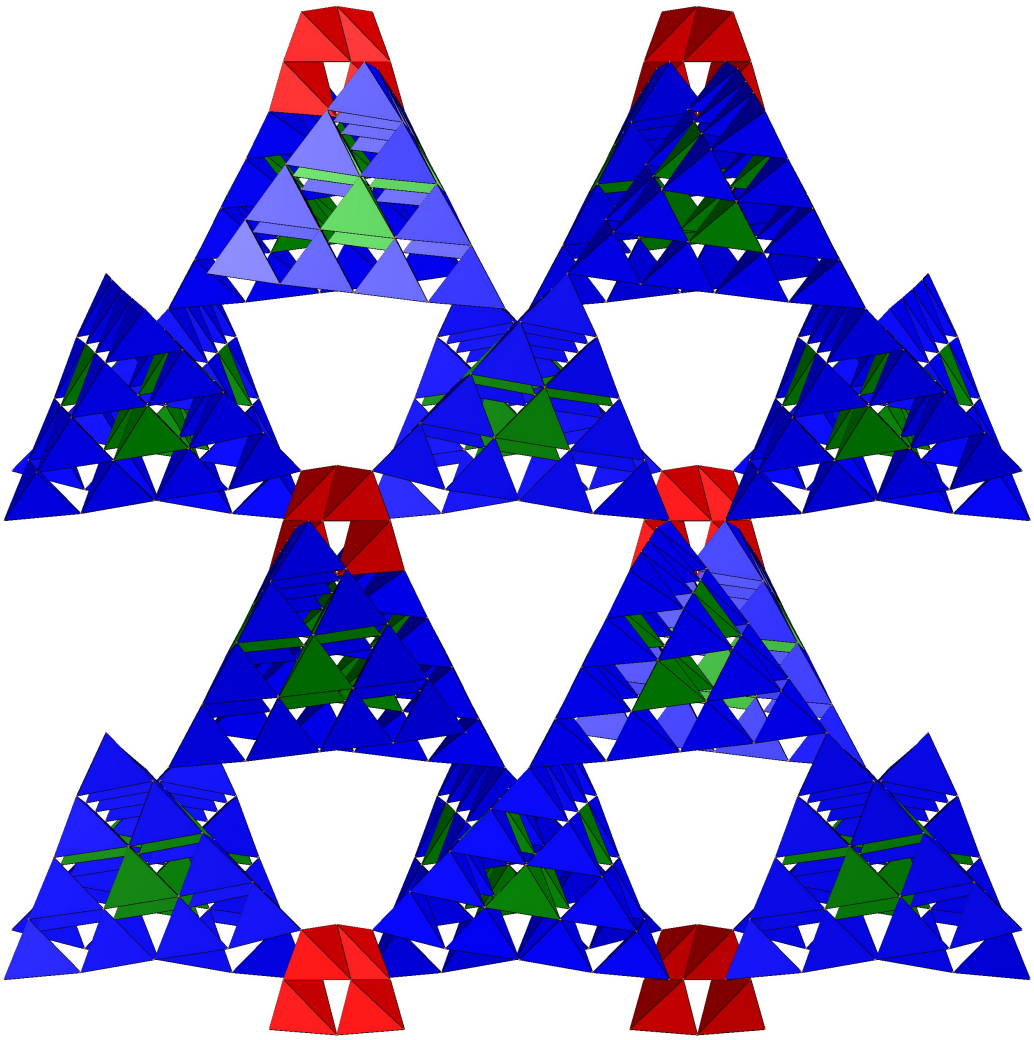


Figure 4.3. The 3-D open frameworks of OCF-42 viewed along *b* axis. The red sites highlight the location of T2 clusters and blue sites highlight the location of T4 clusters, and green sites highlight the location of Zn in T4 clusters. Note that the ratio between T4 and T2 clusters is 4, which is unprecedented for this type of materials.

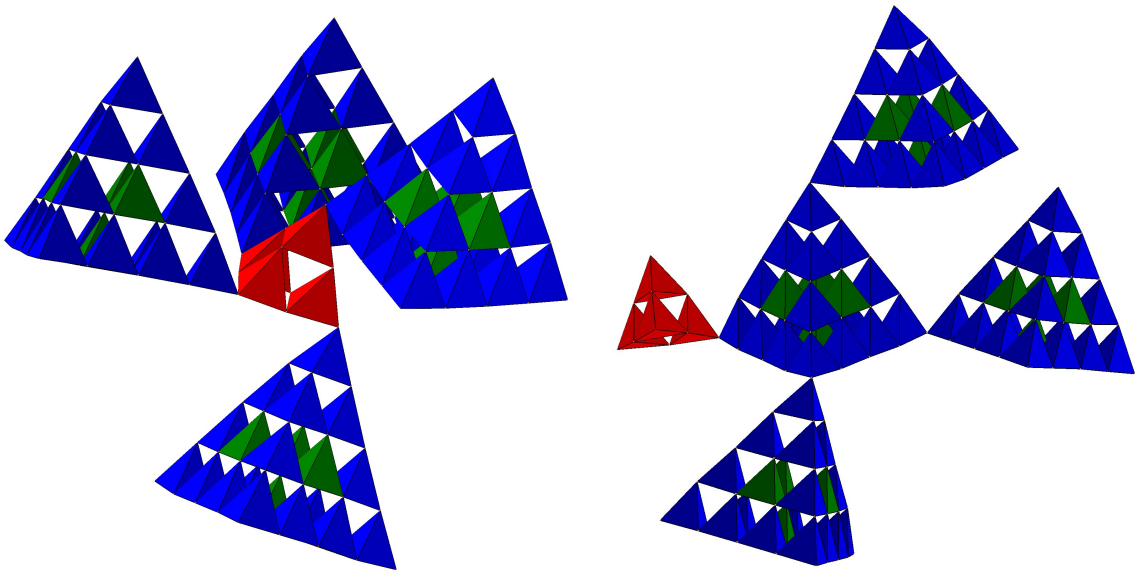


Figure 4.4. The connectivity of T2 and T4 clusters in OCF-42. Each T2 cluster is connected to four T4 clusters (left), and each T4 cluster is corner-shared to one T2 and three T4 clusters (right).

Another uncommon feature in OCF-42 is the unequal ratio between T2 and T4 clusters. Such an ability to have unequal ratios can greatly increase the diversity of such materials. In OCF-42, instead of alternating T2 and T4 clusters, each T2 cluster is connected to four T4 clusters with a center-to-center distance of 12.03Å, and each T4 cluster is corner-shared to one T2 and three T4 clusters. (Figure 4.4) So the ratio between T2 and T4 clusters is 1:4.

Two distinct tetrahedral nets can be derived from OCF-42s and both nets are previously unknown. For the topological analysis of the zeolite-type net, the T2 cluster is unique, because its four tetrahedral metal sites can be treated as four individual tetrahedral nodes, or alternatively the whole T2 cluster can be treated as a single

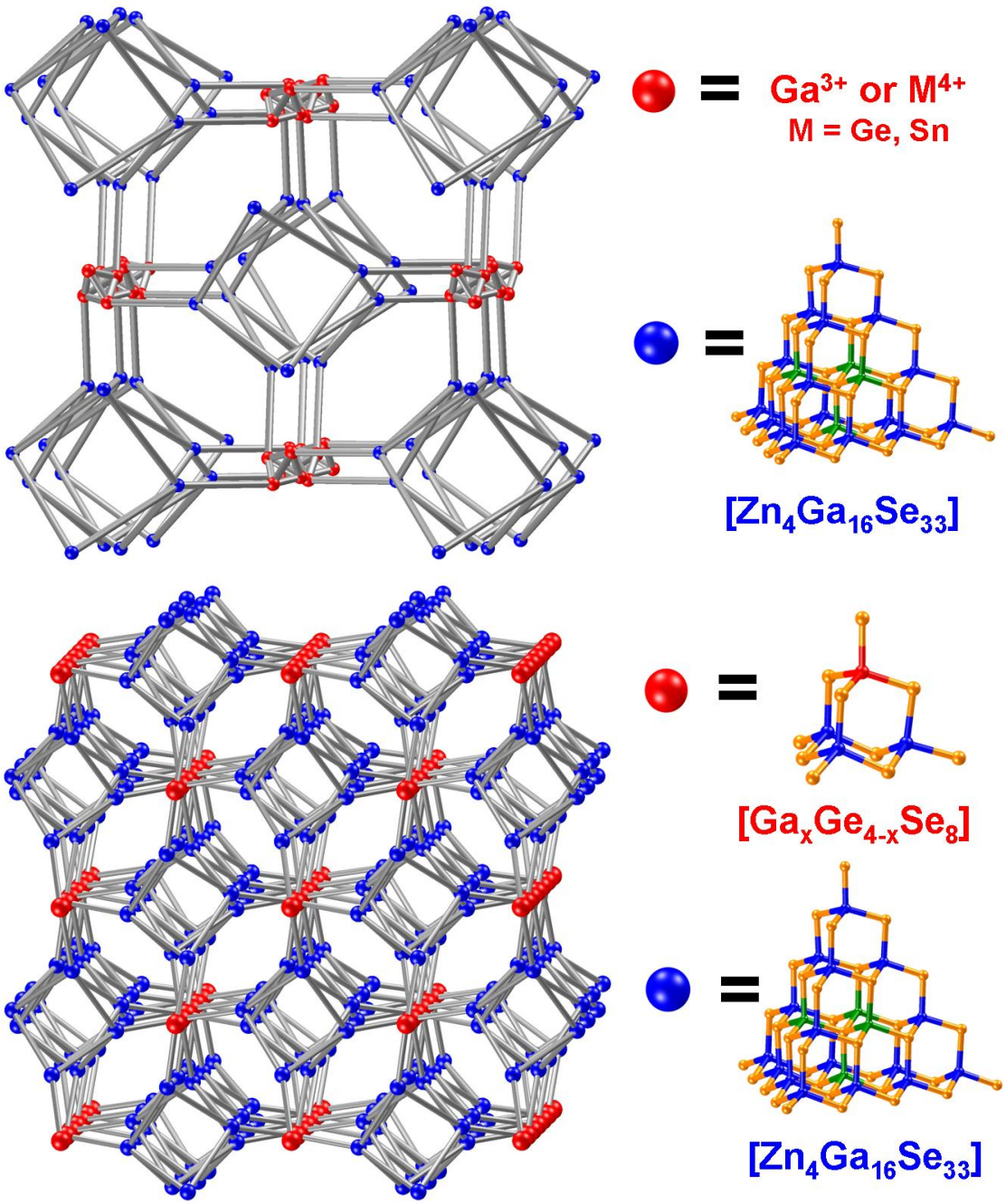


Figure 4.5. Because T2 clusters can be treated as a single pseudo-tetrahedral site or a zeolite-type secondary building unit with four tetrahedral sites, two different topological nets can be derived depending on the treatment of T2 clusters. Top: a new non-interpenetrated zeolitic topology in OCF-42 when only the T4 clusters are considered as the artificial 4-connected atom; Bottom: a new topological framework when both supertetrahedral T2 and T4 clusters are treated as 4-connected nodes.

tetrahedral node. In contrast, the T4 cluster can only be treated as a pseudo-tetrahedral atom, because of the presence of 3- and 4-coordinated Se^{2-} sites. When the T2 clusters are treated as four individual nodes, the framework can be simplified into a new zeolite-type topology with vertex symbol of $[3.10_2.3.10_8.3.10_8][4.10_{11}.6_2.10_2.6_2.10_5]$. (Figure 4.5) When the T2 clusters are treated as a single tetrahedral node, the framework can also be simplified into a new zeolite-like topological framework with vertex symbol of $[8_8.8_8.8_8.8_8.8_2.8_2]$ $[4.8_{11}.6_2.8_2.6_2.8_5]$. (Figure 4.5 and Figure 4.6) It is clear that our synthetic strategy, which aims to integrate zeolite-type structural features with supertetrahedral clusters, has the potential for generating both multinary compositions and new framework topologies.

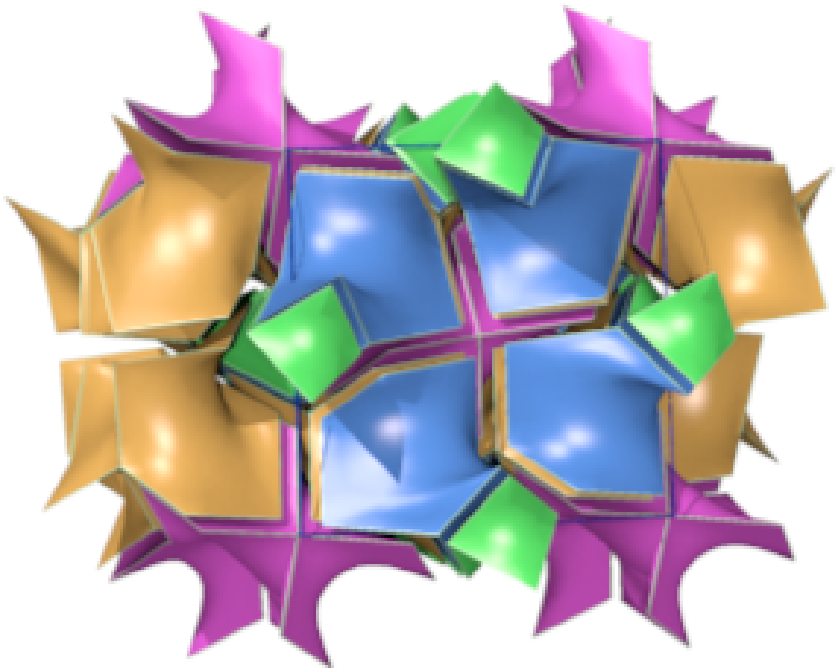


Figure 4.6. Natural tilling framework with the symbol $[4^2.6^2]+2[6.8^2]+3[8^4]$ (…*mn*…means *n* kind of *m* face in each separate tilling) in OCF-42 when T2 and T4 supertetrahedral clusters were treated as artifical tetrahedral atoms. The net is in the RCSR database (http://rcsr.anu.edu.au) as “wut”.

Although all framework atoms are unambiguously determined, extra-framework species (protonated amine molecules) are disordered within the large cavities, and their atomic positions could not be determined. These disordered extra-framework species occupy approximately 64.51% of the crystal volume as calculated using the PLATON software.[19]

4.3.3 Thermal Analysis

Thermogravimetric analysis (Figure 4.7 and Figure 4.8), studied on TA instruments SDT Q600 under flowing N_2 atmosphere or static air, followed by X-ray powder diffraction (Figure 4.9), showed that OCF-42 were stable up to 300^{o}C when solvent molecules trapped in the pore or adsorbed on the surface were lost (lost weight 1.6%). An abrupt weight loss between 300-500^{o}C is attributed to the decomposition of the charge-balancing ammonium cations. The black residue obtained after heating the sample at 600^{o}C in N_2 shows the loss of crystallinity. The combustion of OCF-42 in the static air leads to co-existence of several metal oxide phases, as shown in Figure 4.9 and Figure 4.10.

4.3.4 Optical Properties

The quaternary open-framework compositions achieved with our synthetic strategy add an extra freedom in the control of electronic or optical properties such as electronic band gap. The solid-state diffuse reflectance spectra of OCF-42s were performed on a Shimadzu UV-3101PC double-beam double monochromator spectrophotometer by using $BaSO_4$ powder as 100% reflectance reference. The optical absorption data calculated from reflectance data by using the Kubelka-Munk function [20]

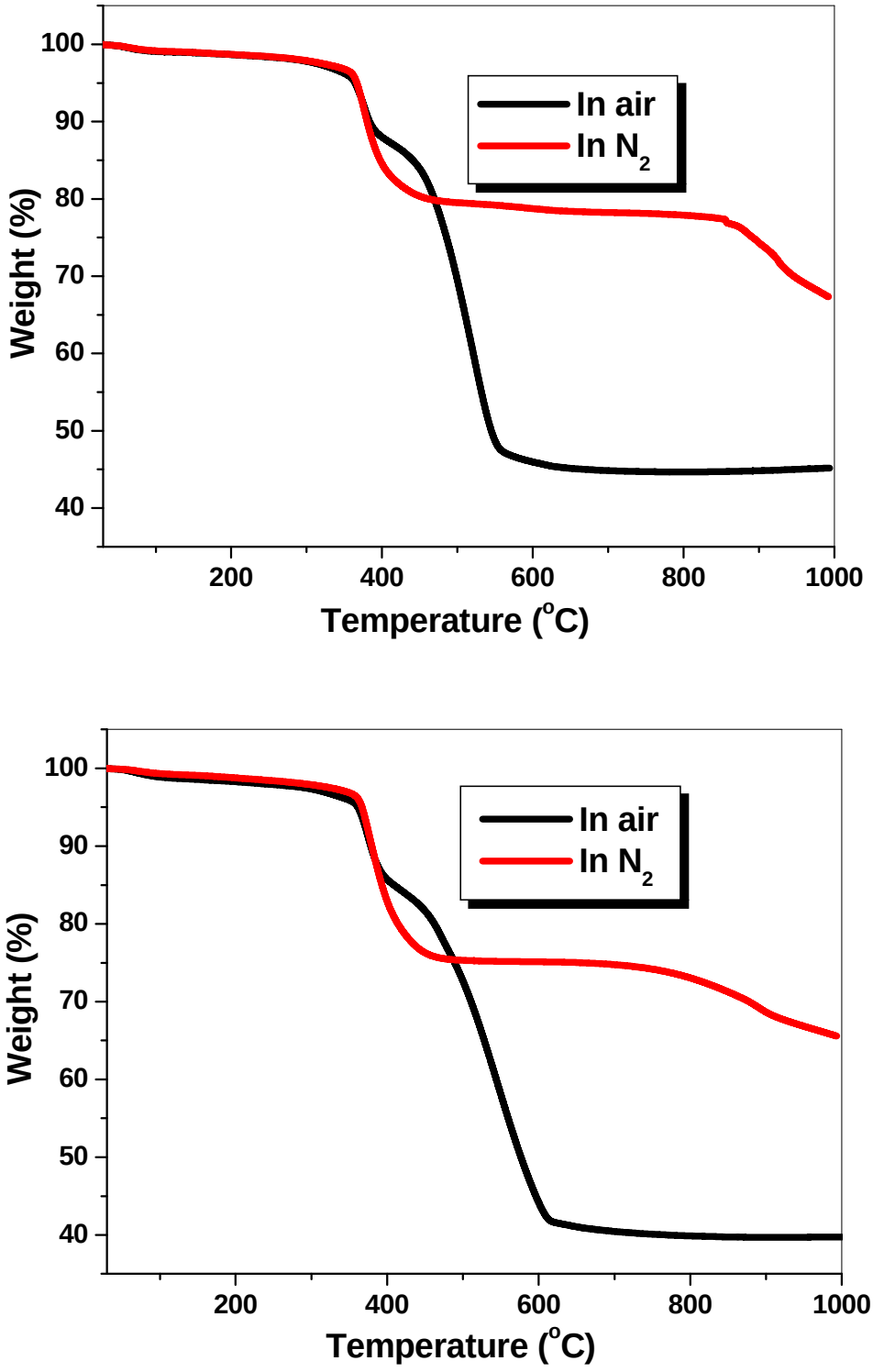


Figure 4.7. Thermogravimetric analysis of OCF-42-ZnGaGeSe-TMDP (top) and OCF-42-ZnGaSnSe-TMDP (bottom) in static air and flowing N_2 atmosphere.

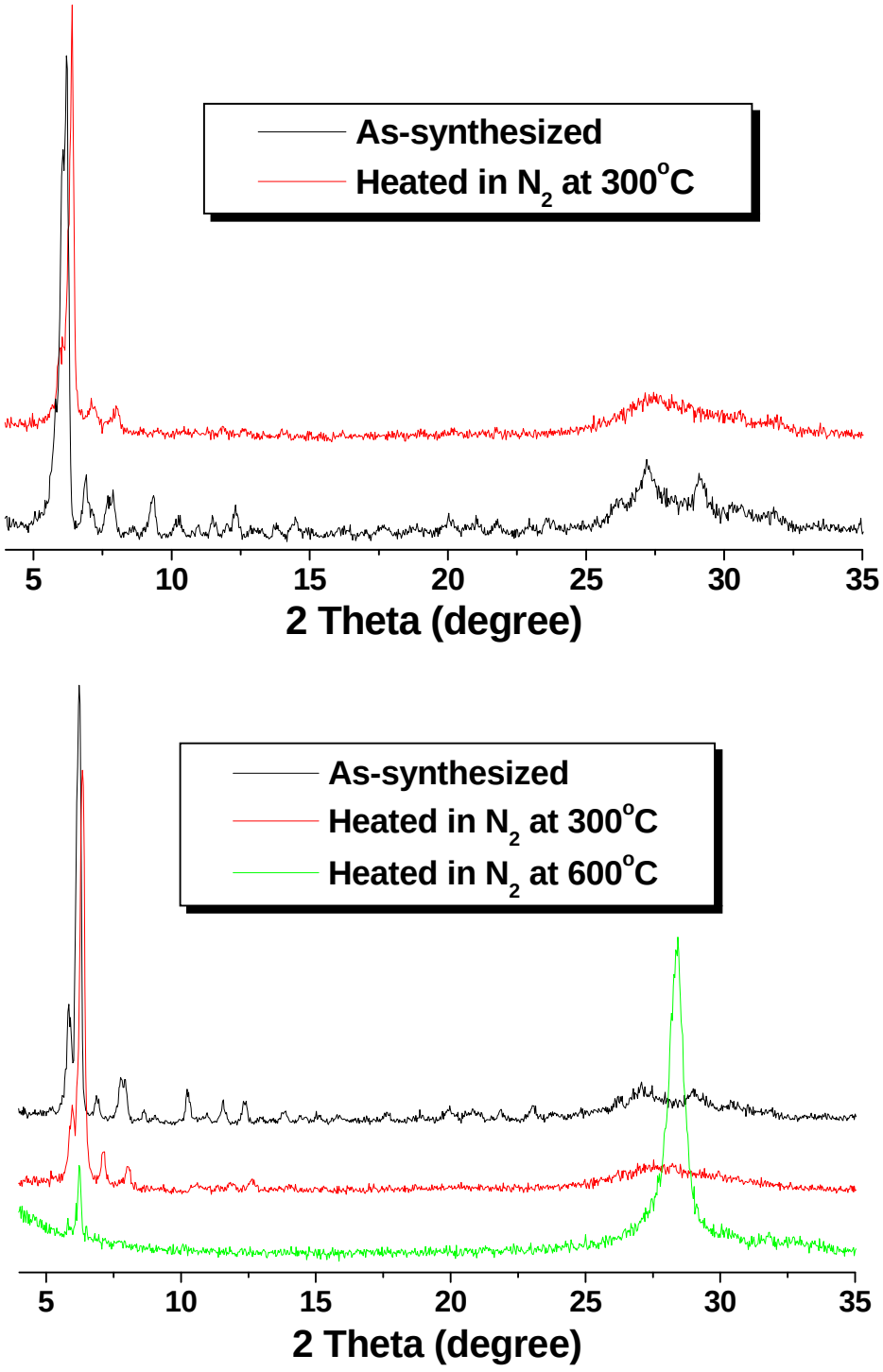


Figure 4.8. PXRD of OCF-42-ZnGaGeSe-TMDP (left) and OCF-42-ZnGaSnSe-TMDP (bottom).

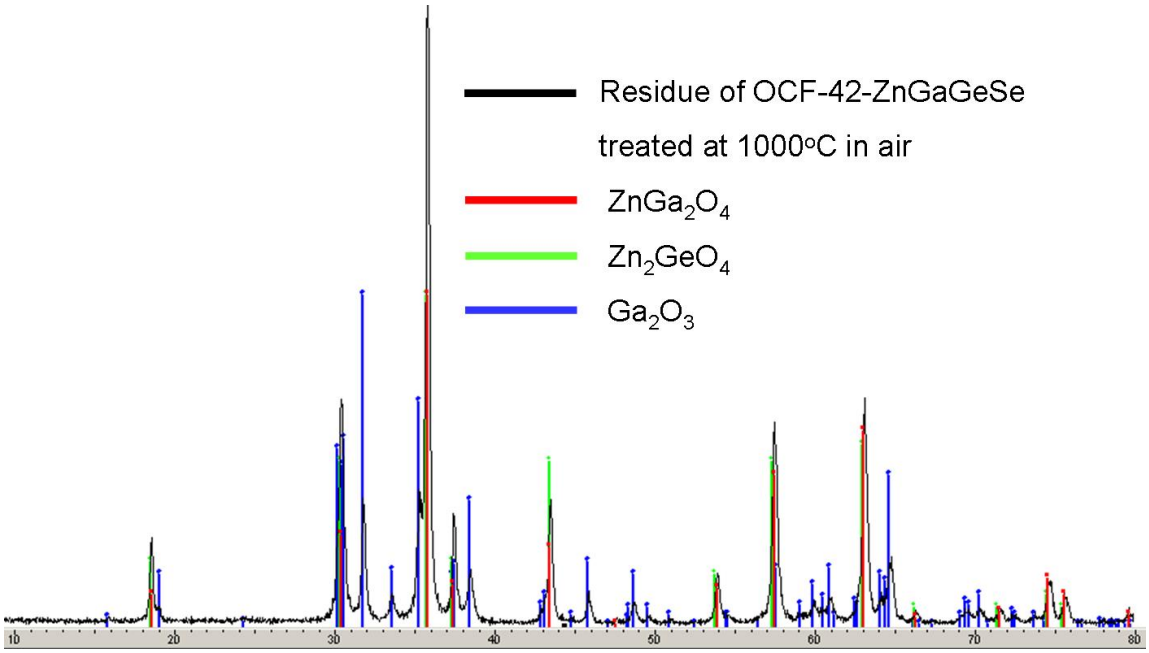


Figure 4.9. PXRD of the residue of OCF-42-ZnGaGeSe-TMDP heated at 1000°C in air. The residue of OCF-42-ZnGaGeSe is identified as the mixture of cubic $ZnGa_2O_4$, monoclinic Ga_2O_3, and cubic Zn_2GeO_4 phase.

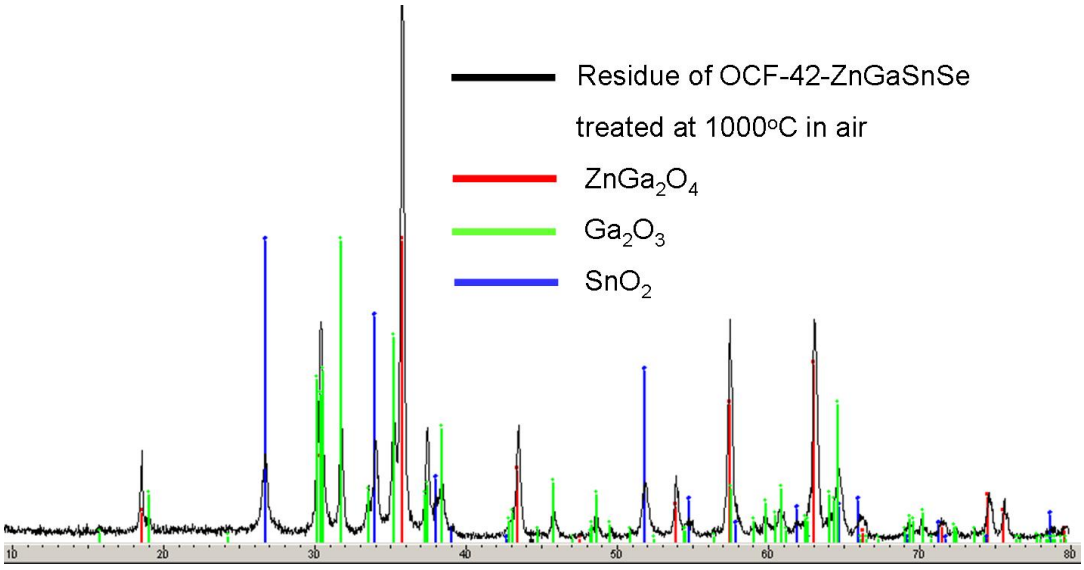


Figure 4.10. PXRD of residue of OCF-42-ZnGaSnSe-TMDP heated at 1000°C in air. The residue of OCF-42-ZnGaSnSe treated in air at 1000°C is composed of the mixture of cubic $ZnGa_2O_4$, monoclinic Ga_2O_3, and tetragonal SnO_2 phase.

show that OCF-42-ZnGaGeSe has the absorption onset at about 855 nm, corresponding to a band gap of 1.45 eV (Figure 4.11). The replacement of Ge^{4+} with Sn^{4+} gives a comparable band gap of 1.54eV in OCF-42-ZnGaSnSe. The band gaps of such quaternary selenides lie between the band gaps of binary gallium selenides (OCF-6-GaSe-TMDP, 1.43 eV) [14] and some ternary selenides (such as OCF-1-ZnGaSe-TMDP, 1.76 eV;[14] $[Cd_{15}Sn_{12}Se_{46}]^{14-}$, 2.00 eV;[21] $[Cd_4Sn_3Se_{13}]^{6-}$, 2.33 ev;[21] and $[M_4(\mu_4\text{-}Se)(SnSe_4)_4]^{10-}$ (M = Zn, Mn, Cd, Hg), 2.2-2.6 eV [22]), which demonstrates the possibility to tune the band gap of chalcogenides by combining different metal cations into superlattices.

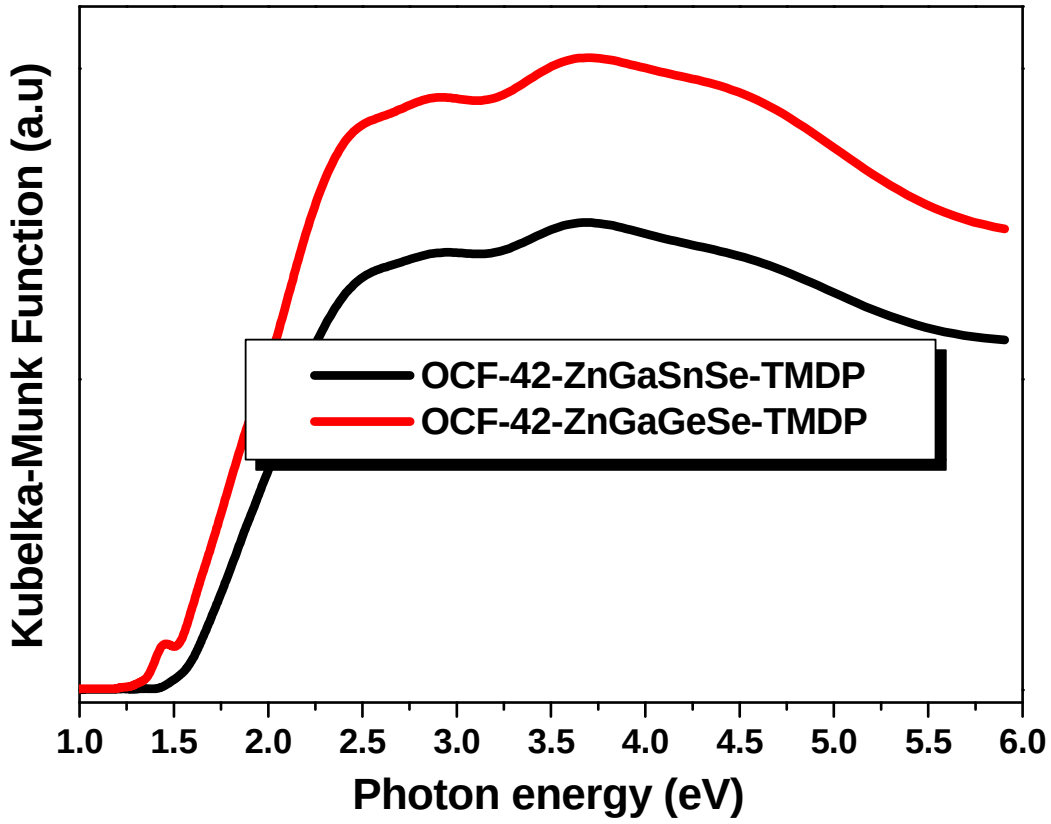


Figure 4.11. Solid-state UV/Vis absorption spectra of OCF-42s.

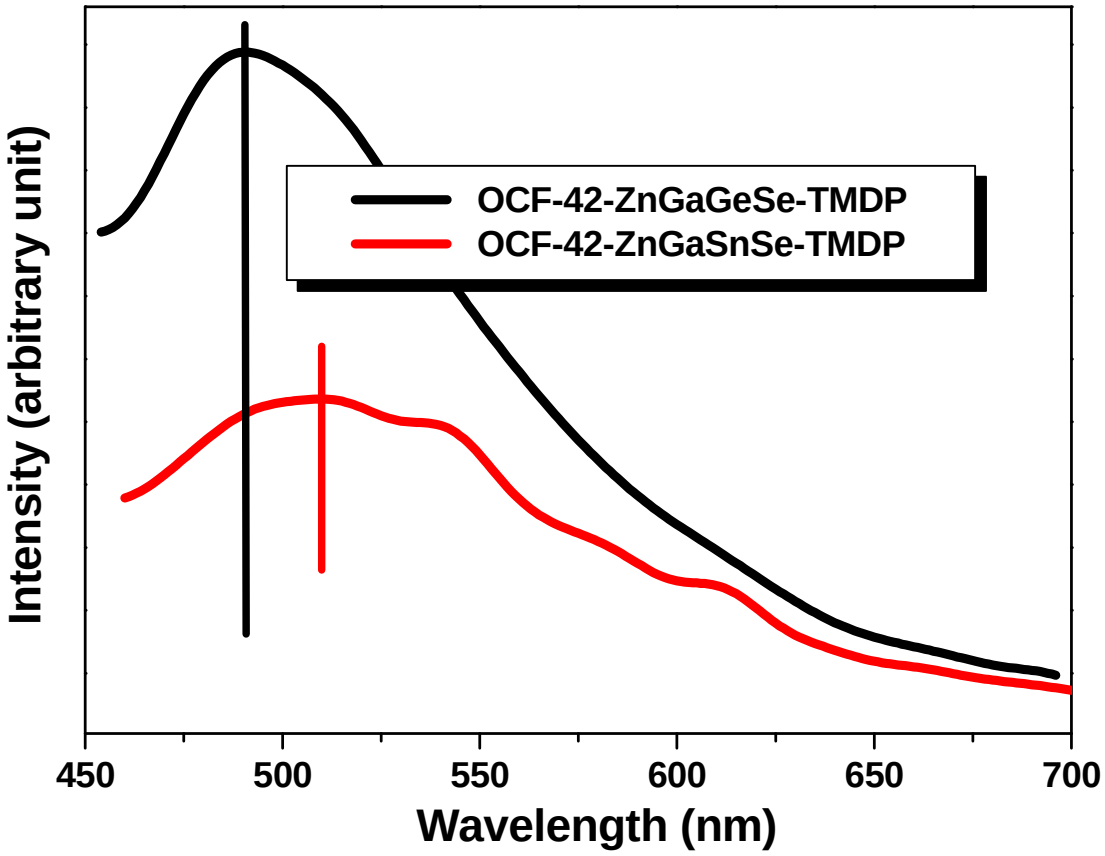


Figure 4.12. Photoluminescent emission spectra of OCF-42 excited at wavelength 420nm.

OCF-42s are photoluminescent and can be excited with wavelength from 380nm to 450nm. When excited at 420nm at room temperature, OCF-42-ZnGaGeSe and OCF-42-ZnGaSnSe exhibit strong photoluminescence with maximum wavelength centered at 490nm, 510nm, respectively. (Figure 4.12) These transitions are attributed to the charge transfer from Se^{2-}-dominated valence band to $M^{4+}/Ga^{3+}/Zn^{2+}$-dominated conduction band.

4.4 Conclusion

In conclusion, the first quaternary 3-D open-framework selenide superlattices based on T2 and T4 supertetrahedral clusters have been synthesized using three types of charge-complementary (+2/+3/+4) and yet geometry-matching metal cations such as $Zn^{2+}/Ga^{3+}/Ge^{4+}$. Such charge-complementary metal cations control the cluster size and co-assembly through differing bond valence requirements of *di*-, *tri*-, and *tetra*-coordinated Se^{2-} sites. The M^{4+}/M^{3+} combination assists the formation of small T2 cluster, while the M^{3+}/M^{2+} combination helps the formation of large T4 clusters. The T2 and T4 clusters are further joined into 3-D covalent superlattices with an extraordinary unequal 1:4 ratio, leading to a framework topology that can be simplified into two previously unknown tetrahedral nets. The formation of the quaternary $M^{4+}/M^{3+}/M^{2+}/Se^{2-}$ composition with the cluster-scale phase separation is extraordinary, considering that multiple competing crystallization processes for the formation of structures with simpler ternary and binary compositions are possible. The cluster-scale phase separation controlled by charge-complementary metal cations illustrates that a high degree of control is possible even in the complicated quaternary compositions.

4.5 References

(1) a) Z. Lei, W. You, M. Liu, G. Zhou, T. Takata, M. Hara, K. Domen, C. Li, *Chem. Commun.* **2003**, *17*, 2142-2143; b) D. Chen, J. H. Ye, *J. Phys. Chem. Solids* **2007**, *68*, 2317-2320; c) K. Kobayakawa, A. Teranishi, T. Tsurumaki, Y. Sato, A. Fujishima, *Electrochim. Acta* **1992**, *37*, 465-467.

(2) a) K. F. Hsu, S. Loo, F. Guo, W. Chen, J. S. Dyck, C. Uher, T. Hogan, E. K. Polychroniadis, M. G. Kanatzidis, *Science* **2004**, *303*, 818-821; b) B. A. Cook, M. J. Kramer, J. L. Harringa, M. K. Han, D. Y. Chung, M. G. Kanatzidis, *Adv. Funct. Mater.* **2009**, *19*, 1254-1259; c) I. U. Arachchige, J. Wu, V. P. Dravid, M. G. Kanatzidis, *Adv. Mater.* **2008**, *20*, 3638-3642. d) M. G. Kanatzidis, S. P. Huang, *Inorg. Chem.* **1989**, *28*, 4667-4669.

(3) a) C. Zimmerman, M. Melullis, S. Dehnen, *Angew. Chem. Int. Ed.* **2002**, *41*, 4269-4272; b) S. Dehnen, M. K. Brandmayer, *J. Am. Chem. Soc.* **2003**, *125*, 6618-6619; c) S. Dehnen, M. Melullis, *Coord. Chem. Rev.* **2007**, *251*, 1259-1280.

(4) N. Zheng, X. Bu, H. Vu, P. Feng, *Angew. Chem., Int. Ed.* **2005**, *44*, 5299-5303.

(5) a) Vaqueiro, P. *Inorg. Chem.* **2008**, *47*, 20-22; b) Vaqueiro, P.; Romero, M. L. *Chem. Commun*. **2007**, 3282-3284.

(6) a) C. L. Cahill, J. B. Parise, *Chem. Mater.* **1997**, *9*, 807-811; b) C. L. Cahill, Y. Ko, J. B. Parise, *Chem. Mater*. **1998**, *10*, 19-21; c) C. L. Cahill, Y. Ko, J. C. Hanson, K. Tan, J. B. Parise, *Chem. Mater.* **1998**, *10*, 1453-1458; d) C. L. Cahill, J. B. Parise, *J. Chem. Soc., Dalton Trans.* **2000**, 1475-1482.

(7) a) R. L. Bedard, S. T. Wilson, L. D. Vail, J. M. Bennett, E. M. Flanigen, in *Zeolites: Facts, Figures, Future. Proceedings of the 8th International Zeolite Conference* (eds.: P. A. Jacobs, R. A. van Santen) Elsevier, Amsterdam, **1989,** p.375-387. b) C. L. Bowes, A. J. Lough, A. Malek, G. A. Ozin, S. Petrov, D. Young, *Chem. Ber.* **1996**, *129*, 283-287; c) C. L. Bowes, W. U. Huynh, S. J. Kirkby, A. Malek, G. A. Ozin, S. Petrov, M. Twardowski, D. Young, R. L. Bedard, R. Broach, *Chem. Mater.* **1996**, *8*, 2147; d) H. Ahari, A. Garcia, S. Kirkby, G. A. Ozin, D. Young, A. J. Lough, *J. Chem. Soc., Dalton Trans.* **1998**, 2023-2028.

(8) a) H. Li, A. Laine, M. O'Keeffe, O. M. Yaghi, *Science* **1999**, *283*, 1145-1147; b) H. Li, M. Eddaoudi, A. Laine, M. O'Keeffe, O. M. Yaghi, *J. Am. Chem. Soc.* **1999**, *121*, 6096-6097; c) O. M. Yaghi; Z. Sun, D. A. Richardson, T. L. Groy, *J. Am. Chem. Soc.* **1994**, *116*, 807-808; d) H. Li, J.

Kim, T. L. Groy, M. O'Keeffe, O. M. Yaghi, *J. Am. Chem. Soc.* **2001**, *123*, 4867-4868.

(9) a) G. S. H. Lee, D. C. Craig, I. Ma, M. L. Scudder, T. D. Bailey, I. G. Dance, *J. Am. Chem. Soc.* **1988**, *110*, 4863-4864; b) I. G. Dance, K. G. Fisher, *Prog. Inorg. Chem.* **1994**, *41*, 637-803; c) D. Fenske, N. Zhu, T. Langetepe, *Angew. Chem. Int. Ed.* **1998**, *37*, 2640-2644; d) S. Dehnen, A. EichhOfer, D. Fenske, *Eur. J. Inorg. Chem.* **2002**, *2*, 279-317; e) W. Su, X. Huang, J. Li, H. Fu, *J. Am. Chem. Soc.* **2002**, *124*, 12944-12 945.

(10) a) P. Feng, X. Bu, N. Zheng, *Acc. Chem. Res.* **2005**, *38*, 293-303; b) N. Zheng, X. Bu, P. Feng, *Nature* **2003**, *426*, 428-432.

(11) N. Zheng, X. Bu, H. Lu, Q. Zhang, P. Feng, *J. Am. Chem. Soc.* **2005** *127*, 11963-11965.

(12) a) X. Bu, N. Zheng, P. Feng, *Chem. Eur. J.* **2004**, *10*, 3356-3362; b) C. Wang, Y. Li, X. Bu, N. Zheng, O. Zivkovic, C. S. Yang, P. Feng, *J. Am. Chem. Soc.* **2001**, *123*, 11506-11507; c) X. Bu, N. Zheng, Y. Li, P. Feng, *J. Am. Chem. Soc.* **2002**, *124*, 12646-12647.

(13) N. Zheng, X. Bu, B. Wang, P. Feng, *Science* **2002**, *298*, 2366-2369.

(14) X. Bu, N. Zhen, X. Wang, B. Wang, P. Feng, *Angew. Chem. Int. Ed.* **2004**, *43*, 1502-1505.

(15) G. H. Xu, P. Guo, S. Y. Song, H. J. Zhang, C. Wang, *Inorg. Chem.* **2009**, *48*, 4628-4630.

(16) Shelxtl 6.10, Bruker Analytical Instrumentation, Madison, Wisconsin, USA, **2000**.

(17) M. E. Davis, *Nature* **2002**, *417*, 813-821.

(18) a) P. Vaqueiro, M. L. Romero, *J. Phys. Chem. Solids.* **2007**, *68*, 1239-1243. b) C. Wang, X. Bu, N. Zheng, P. Feng, *J. Am. Chem. Soc.* **2002**, *124*, 10268-10269; c) N. Zheng, X. Bu, P. Feng, *J. Am. Chem. Soc.* **2003**, *125*, 1138-1139.

(19) Spek, A. L. *Acta Crystallogr. Sect. A* **1990**, *46*, C34.

(20) W. W. Wedlandt, W. H. Hecht, *Reflectance Spectroscopy*, Interscience Publishers, New York, **1966**.

(21) N. Ding, M. G. Kanatzidis, *Angew. Chem., Int. Ed. Engl.* **2006**, *45*, 1397-1401.

(22) M. K. Brandmayer, R. Clérac, F. Weigend, S. Dehnen, *Chem.Eur. J.* **2004**, *10*, 5147-5157.

Chapter 5

Isolated Inorganic Supertetrahedral T4 Clusters

5.1 Introduction

Since the first synthesis of chalcogenide open framework materials in 1989[1], research on crystalline porous chalcogenide frameworks has attracted great attention [2-4] because such materials are capable of integrating porosity with semiconductivity and have many potential applications. Unlike crystalline porous materials based on inorganic oxide frameworks[5] (e.g., zeolites) or more recently developed porous coordination polymers (also called metal-organic frameworks, MOFs)[6-8], chalcogenide open frameworks have distinct structural features and many of them are composed of nano-sized tetrahedral clusters[3]. Such clusters can behave as artificial tetrahedral atoms to allow the creation of semiconducting zeolite-like 4-connected porous frameworks[9]. On the other hand, these clusters can also be considered as the smallest possible semiconductor quantum dots, and because of their precisely defined composition and structure, they may exhibit unique properties, in addition to serve as model systems for less-well-defined colloidal nanoparticles[10-11]. Such a close relevance of chalcogenide clusters to crystalline porous semiconductors and semiconductor quantum dots places them in a unique family of materials whose study will have significant multidisciplinary impacts.

There are now four well-known series of tetrahedral chalcogenide nanoclusters: supertetrahedral cluster (T*n*), pentasupertetrahedral cluster (P*n*), capped supertetrahedral

(C*n*) cluster, and super-supertetrahedral cluster (T*p*, *q*) (*n*, *p*, and *q* are related to the size of the cluster and in known clusters range from 1 to 5 for T*n*, 1-2 for P*n*, and 1-3 for C*n* clusters)[3, 12]. Examples of T2, P1, C1, and C2 clusters are $[Cd_4(SPh)_{10}]^{2-}$ (or $[M_4Q_{10}]^{4-}$, M = Ge, Sn, Q = Se, S), $[Cd_8S(SPh)_{16}]^{2-}$ (or $[M_4Sn_4Q_{17})]^{10-}$ (M = Zn, Mn, Co, Fe; Q = Se, S)[4d-4f], $[Cd_{17}S_4(SPh)_{28}]^{2-}$, and $[Cd_{32}S_{14}(SPh)_{36}(DMF)_4]$, respectively. Among these clusters, supertetrahedral T*n* clusters are the most fundamental series and other series of clusters can be geometrically derived from T*n* clusters.

For many years, the synthesis of large crystallographically defined chalcogenide clusters (i.e., to increase *n*) has remained a formidable challenge. For supertetrahedral T*n* clusters, it has been actually more difficult to create discrete molecular clusters than to synthesize covalently linked clusters. For example, T3 clusters (e.g., $[Cd_{10}S_4(SPh)_{16}]^{4-}$)[13] have remained as the largest discrete supertetrahedral T*n* clusters for many years, even though some new compositions have recently been made (e.g., $[M_5Sn_5S_{20}]^{10-}$, M = Zn, Co)[4g] and both T4 and T5 clusters are known in extended frameworks[2e].

There has always been a strong interest in discrete molecular clusters that can serve as precursors to allow the more rational construction of porous frameworks through modular assembly processes, in a way similar to the construction of coordination polymers[14-17]. Discrete clusters are also more directly comparable to semiconductor nanoparticles in terms of properties such as quantum confinement effects. Furthermore, discrete soluble clusters are amenable for solution processing into various forms such as thin films, functionalized semiconducting mesoporous structure[18] or porous gels and aerogels[19-20].

One of the key structural features of tetrahedral chalcogenide clusters, which is also related to the difficulty in synthesizing them, is their usually negative charge that increases dramatically as the size of the cluster gets bigger. The reason for the negative charge is that while the coordination sphere of tetrahedral metal sites is saturated with four S^{2-}/Se^{2-} sites, surface S^{2-}/Se^{2-} sites are bonded to fewer-than-four metal sites, leading to excess anionic sites (i.e., anion/metal>1). As the cluster gets larger, the increase in the surface area of the cluster leads to a large number of such underbonded S^{2-}/Se^{2-} sites, which contribute to a dramatic increase in the magnitude of the negative charge per cluster. Thus, a key strategy in synthesizing large clusters is to find methods to stabilize or lower the large negative charge.

There are two common ways to reduce the negative charge: incorporating surface organic ligands or introducing surface high-valent (3+ or 4+) metal cations. For chalcogenide clusters made of entirely divalent metal ions such as Cd^{2+}, the charge reduction is achieved through covalently attached surface organic ligands (in the form of thiolates or selenolates). For example, the T3 $[Cd_{10}S_{20}]^{20-}$ cluster only exists with its edge and corner S^{2-} sites bonded to organic groups (e.g., T3 $[Cd_{10}S_4(SPh)_{16}]^{4-}$)[13]. The T4 cluster in this series is not known yet, even though larger T4 and T5 clusters have been found as nodes in two- or three-dimensional covalent frameworks [21-24].

When high-valent metal ions (e.g., Ga^{3+} or In^{3+}) are present on the surface of clusters, the valence requirements of surface S^{2-}/Se^{2-} can be satisfied even if the S^{2-}/Se^{2-} site is bonded to fewer-than-four metal sites. This eliminates or reduces the need for organic ligands, which helps to form inorganic supertetrahedral chalcogenide clusters

such as $In_{10}S_{18}^{6-}$. Furthermore, there have been reports of some very interesting clusters that contain both trivalent cations and organic ligands (generally at the corners of the cluster, e.g., T3 cluster $[Ga_{10}S_{16}(C_7H_9N)_4]^{2-}$, C_7H_9N= 3,5-Lutidine)[4h-4i]. Such clusters make use of both types of charge reduction mechanisms.

Tetravalent metals such as Sn^{4+} have had an interesting history in their roles for the cluster and framework formation. In the early years of open framework chalcogenides, such tetravalent metal ions were selected as the primary framework metal species in efforts to emulate silica-like structures[1]. Low-valent metal ions (e.g., Mn^{2+}) were initially used to play the secondary role such as crosslinking small clusters (e.g., Ge_4S_8) into extended frameworks, instead of forming heterometallic clusters with Ge-S[14]. Later, it was found that Sn^{4+} could participate in the formation of inorganic clusters such as P1 and T3, in combination with divalent metal ions, as demonstrated by groups of Dehnen and Kanatzidis[4d-4g]. These clusters that usually have the molar ratio of 1 between Sn^{4+} and M^{2+} (e.g., Zn) are some early examples that demonstrate the charge reduction role of tetravalent metal ions in the formation of tetrahedral clusters[4d-4g]. Our own work in $M^{4+}/M^{3+}/X^{2-}$ system (M^{4+} =Ge^{4+}, Sn^{4+}, M^{3+}=Ga^{3+}, In^{3+}, X^{2-}= S^{2-}, Se^{2-}) highlighted the charge reduction role of M^{4+} in the formation of T2 clusters. Furthermore, a recent example ($[Sn_4Ga_4Zn_2Se_{20}]^{8-}$) also contains Sn^{4+} at the corner of discrete T3 cluster, even though it needs to be stabilized by covalently attached metal complex ($[(TEPA)Mn]^{2+}$, TEPA= tetraethylenepentamine)[25].

The aforementioned examples demonstrate the feasibility to synthesize large supertetrahedral clusters through the incorporation of high-valent metal ions such as In^{3+}

and Sn^{4+}. However, the relative concentrations of M^{4+}, M^{3+}, and M^{2+} (or M^{+}) need to be carefully controlled, because M^{4+} and M^{3+} could suppress the formation of tetrahedrally coordinated S^{2-} (or Se^{2-}) sites (e. g., M_4S) that are essential for the formation of large clusters. On the other hand, the control of the cluster charge is only one aspect in the cluster synthesis. Even more difficult is the crystallization of clusters, because it requires proper charge balancing species that also needs to posses suitable geometry to fill the intercluster cavities. Given the great difficulty in finding such charge balancing species from a large library of organic molecules, one of the best ways to induce the crystallization of large clusters is to use a complex chemical system that contains multiple charge-complementary metal ions in different oxidation states (e.g., $M^{+}/M^{3+}/M^{4+}$ or $M^{2+}/M^{3+}/M^{4+}$, M^{+} or M^{2+} is essential for the formation of the core of the cluster while M^{3+}/M^{4+} serves to meet the valence requirement of underbonded surface anions). By allowing the possibility to adjust the ratio of these different metal ions within the cluster, it would create a degree of freedom for the cluster to self-adjust its charge density to match that of the organic cationic species during crystallization. This strategy, which further extends the earlier methods in M^{4+}/M^{2+},[4d-4g] M^{4+}/M^{3+},[9] $M^{4+}/M^{3+}/M^{2+}$,[25] and related systems, is similar to that used for the synthesis of zeolite-like cobalt aluminophosphates in which the ratio between Co^{2+} and Al^{3+} within the phosphate framework can be adjusted to tune the framework negative charge so that the inorganic framework has a better chance of matching the charge density of organic structure-directing agents for crystallization[26]. The synthesis of $[Sn_4Ga_4Zn_2Se_{20}]^{8-}$) by Wang et al. represents one successful example.[25] It is worth noting that the use of such tri-metal systems can also

lead to other possibilities as shown by the synthesis of OCF-42 in which the framework was constructed by connecting T2 ($Ga^{3+}/Sn^{4+}/Se^{2-}$) clusters with T4 ($Zn^{2+}/Ga^{3+}/Se^{2-}$) [27].

Here we report the application of the above synthetic strategy in synthesizing a family of discrete supertetrahedral T4 clusters. A total of eight distinct crystalline phases containing discrete T4 clusters, but differing in chemical compositions, have been synthesized, all of which are denoted as OCF-40s (OCF stands for organically directed chalcogenide frameworks). These clusters can be made as both sulfides and selenides (Table 5.1). Different combinations of metal cations have also been achieved (Table 5.1), further increasing the level of control over their electronic band structures. OCF-40s represent the largest isolated supertetrahedral (T*n* series) chalcogenide nanoclusters known to date. To better appreciate the extraordinary synthetic conditions under which these record-breaking clusters are synthesized, we also report here three related framework structures (collectively denoted as OCF-5s here) in which T4 clusters (with previously unknown chemical compositions) are joined into 3D covalent structures.

Table 5.1. A Summary of Crystal Data and Refinement Parameters for OCF-5s and OCF-40s.[a]

Name	Formula	S. G.	*a* (Å)	*c* (Å)	*R* (F)%
OCF-5-CuGaSnSe-DPM	$[Cu_2Ga_{16}Sn_2Se_{33}]\cdot$(template)	$I4_1/acd$	23.9286(2)	42.0821(5)	5.85
OCF-5-ZnGaSnSe-2-MPR	$[Zn_4Ga_{14}Sn_2Se_{33}]\cdot$(template)	$I4_1/acd$	24.1584(12)	41.931(4)	4.88
OCF-5-ZnGaSnSe-3-MPR	$[Zn_4Ga_{14}Sn_2Se_{33}]\cdot$(template)	$I4_1/acd$	24.0693(3)	42.2601(10)	7.33
OCF-40-CuGaSnSe-PR	$[Cu_2Ga_{16}Sn_2Se_{35}]\cdot 12(C_5NH_{12})$	*I*-43*m*	18.8019(1)	18.8019(1)	3.28
OCF-40-ZnGaSnSe-PR	$[Zn_4Ga_{14}Sn_2Se_{35}]\cdot 12(C_5NH_{12})$	*I*-43*m*	18.8951(1)	18.8951(1)	4.08
OCF-40-MnGaSnSe-PR	$[Mn_4Ga_{14}Sn_2Se_{35}]\cdot 12(C_5NH_{12})$	*I*-43*m*	18.8626(2)	18.8626(2)	4.17
OCF-40-CuGaSnSe-4-MPR	$[Cu_2Ga_{16}Sn_2Se_{35}]\cdot 12(C_6NH_{14})^e$	*I*-43*m*	19.387(2)	19.387(2)	/
OCF-40-ZnGaSnSe-4-MPR	$[Zn_4Ga_{14}Sn_2Se_{35}]\cdot 12(C_6NH_{14})$	*I*-43*m*	19.2020(3)	19.2020(3)	/
OCF-40-CuGaSnS-PR	$[Cu_2Ga_{16}Sn_2S_{35}]\cdot 12(C_5NH_{12})$	*I*-43*m*	18.4280(3)	18.4280(3)	5.38
OCF-40-ZnGaSnS-PR	$[Zn_4Ga_{14}Sn_2S_{35}]\cdot 12(C_5NH_{12})$	*I*-43*m*	18.2580(15)	18.2580(15)	5.84
OCF-40-MnGaSnS-PR	$[Mn_4Ga_{14}Sn_2S_{35}]\cdot 12(C_5NH_{12})$	*I*-43*m*	18.3783(11)	18.3783(11)	4.26

[a] Structures were solved from single-crystal data collected at 150K on a SMART CCD diffractometer with Mo Kα. $R(F) = \Sigma||F_o|-|F_c||/\Sigma|F_o|$ with $F_o > 4.0\sigma(F)$.

5.2 Experimental Section

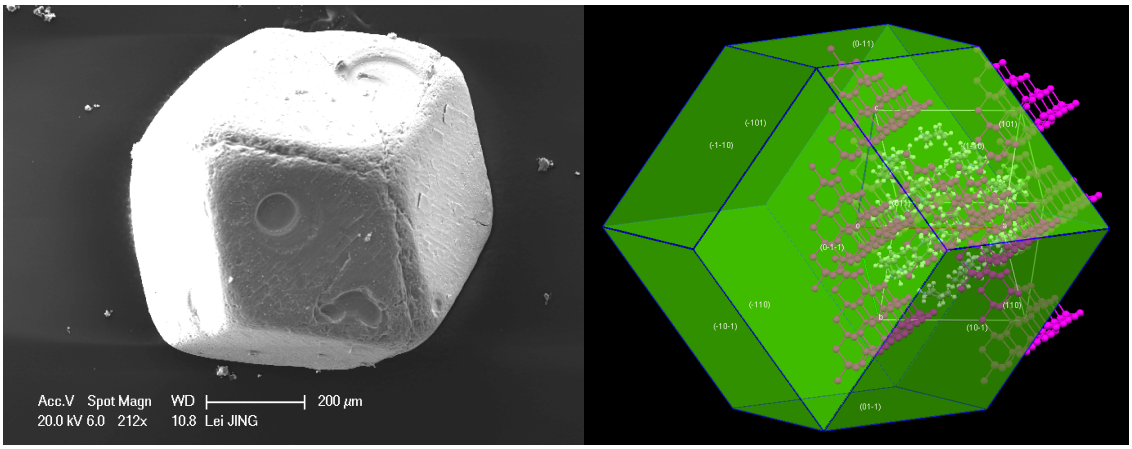
5.2.1 Materials and General Methods

All reagents and solvents employed in these synthetic studies were commercially available and used as supplied without further purification. Solid-state reflectance spectra were recorded on a SHIMADZU UV-3101PC UV-VIS-NIR Scanning Spectrophotometer by using $BaSO_4$ powder as 100% reflectance reference. Powder X-ray diffraction data were collected using a Bruker D8-Advance powder diffractometer operating at 40kV, 40mA with Cu Kα(λ =1.5406 Å) radiation (2θ range, 2-40°; step, 0.03°; scan speed, 60 s/step). Semi-quantitative elemental analyses of the compounds were performed with a Philips FEI XL30 scanning electron microscope (SEM) equipped with energy dispersive spectroscopy (EDS) detector.

5.2.2 Solvothermal Syntheses

OCF-5-CuGaSnSe-DPM and OCF-40-CuGaSnSe-PR: $SnCl_2$ (30.4mg, 0.160mmol), $Ga(NO_3)_3$ (255.2mg, 0.997mmol), Se (177.7mg, 2.251mmol), $Cu(NO_3)_2 \cdot 3H_2O$ (31.9mg, 0.132mmol), and DPM (dipiperidinomethane; 2.061g, 11.305mmol) were mixed with H_2O (2.977g, 165.39mmol) in 23-mL Teflon-lined stainless steel autoclave and stirred for half an hour. The vessel was then sealed and heated to 200^oC for 9 days. After cooling to the room temperature, pale-yellow octahedral crystals and red block crystals were simultaneously observed in the approximate 1:1 ratio estimated using an optical microscope. The mixture was ultrasonically treated and washed with ethanol to remove some amorphous solid, then

dried in air for other measurements. Crystals of OCF-40-CuGaSnSe-PR were in the form of rhombic dodecahedral shape (Figure 5.1).



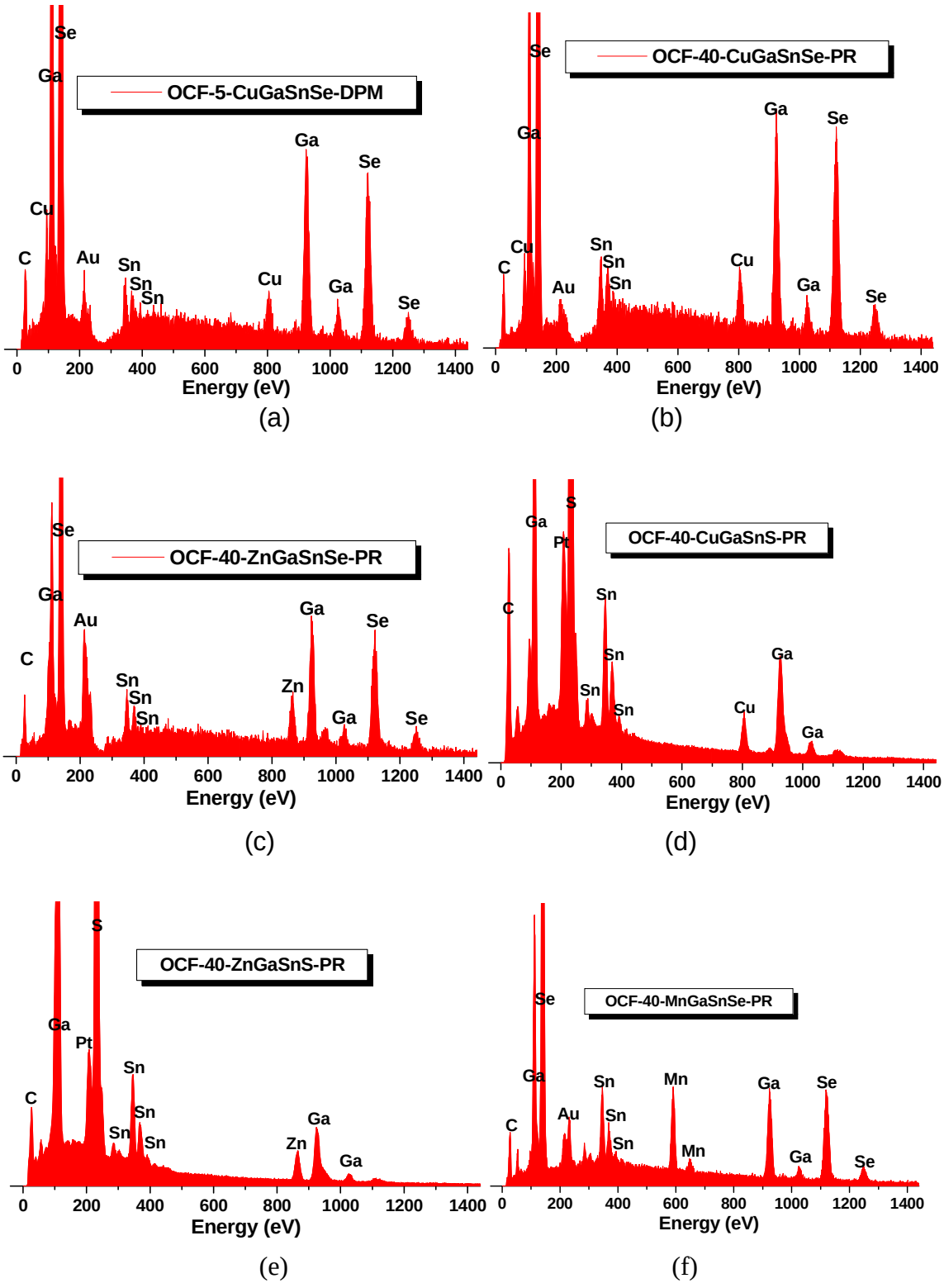
(a) (b)

Figure 5.1. The SEM picture of OCF-40-CuGaSnSe-PR: (a) rhombic dodecahedron shape. The rhombic dodecahedron shape is in agreement with the predicated crystal morphology (b) from the internal crystal structure according to Bravais Friedel Donnay Harker (BFDH) method.

OCF-40-ZnGaSnSe-PR: $SnCl_2$ (34.9mg, 0.184mmol), $Ga(NO_3)_3$ (252.7mg, 0.988mmol), Se (176.3mg, 2.233mmol), $Zn(NO_3)_2 \cdot 6H_2O$ (76.9mg, 0.259mmol) and DPM (dipiperidinomethane; 2.074g, 11.376mmol) were mixed with H_2O (2.481g, 137.8mmol) in 23-mL Teflon-lined stainless steel autoclave and stirred for two hours. The vessel was then sealed and heated to 200^{o}C for 10 days. After cooling to the room temperature, only yellow block crystals were obtained in a yield of about 115.3 mg. Elemental analysis (%): Calcd. For $[(Zn_4Ga_{14}Sn_2Se_{35}) \cdot 12(C_5NH_{12})]$: C, 13.66; H, 2.76; N, 3.19; Found: C, 13.61; H, 2.57; N, 3.15.

The method to enhance the yield and purity of OCF-40-CuGaSnSe-PR and OCF-40-ZnGaSnSe-PR: Method I (increasing reaction time): $SnCl_2$ (32.0mg, 0.169mmol), $Ga(NO_3)_3$ (258.6mg, 1.011mmol), Se (172.3mg, 2.182mmol), $Cu(NO_3)_2 \cdot 3H_2O$ (33.4mg, 0.138mmol), and DPM (dipiperidinomethane; 2.051g, 11.25mmol) were mixed with H_2O (3.225g, 179.16mol) in 23-mL Teflon-lined stainless steel autoclave and stirred for one hour. The vessel was then sealed and heated to 200^oC for 15 days. After cooling to the room temperature, only dark red block crystals were obtained in a yield of 221.2mg. OCF-5-CuGaSnSe-DPM, which was observed with shorter reaction time, was completed converted into OCF-40-CuGaSnSe-PR. Method II: The synthesis procedure is similar to the above, except that dipiperidinomethane was replaced with piperidine. Elemental analysis (%): Calcd. for $[(Cu_2Ga_{16}Sn_2Se_{35}) \cdot 12(C_5NH_{12})]$: C, 13.65; H, 2.76; N, 3.19; Found: C, 13.58; H, 2.52; N, 3.11. Unless noted, Method II was used for the preparation of OCF-40s in all different compositions.

The presence of multiple elements in OCF-5-CuGaSnSe-DPM and all variations of OCF-40s was confirmed by the energy dispersive X-ray (EDAX) spectroscopy performed on a scanning electron microscope (SEM) (Figure 5.2). The molar ratio of Cu : Ga : Sn in OCF-40-CuGaSnSe-PR determined by AAS analysis is 1 : 8.263 : 1.124, and the molar ratio of Zn : Ga : Sn in OCF-40-ZnGaSnSe-PR is 1: 3.593 : 0.525, in good agreement with results from single-crystal structure refinement based on significantly different atomic scattering power between Ga and Sn.


OCF-5-CuGaSnSe-DPM
OCF-40-CuGaSnSe-PR
OCF-40-ZnGaSnSe-PR
OCF-40-CuGaSnS-PR
OCF-40-ZnGaSnS-PR
OCF-40-MnGaSnSe-PR
Energy (eV)
(a)
(b)
(c)
(d)
(e)
(f)

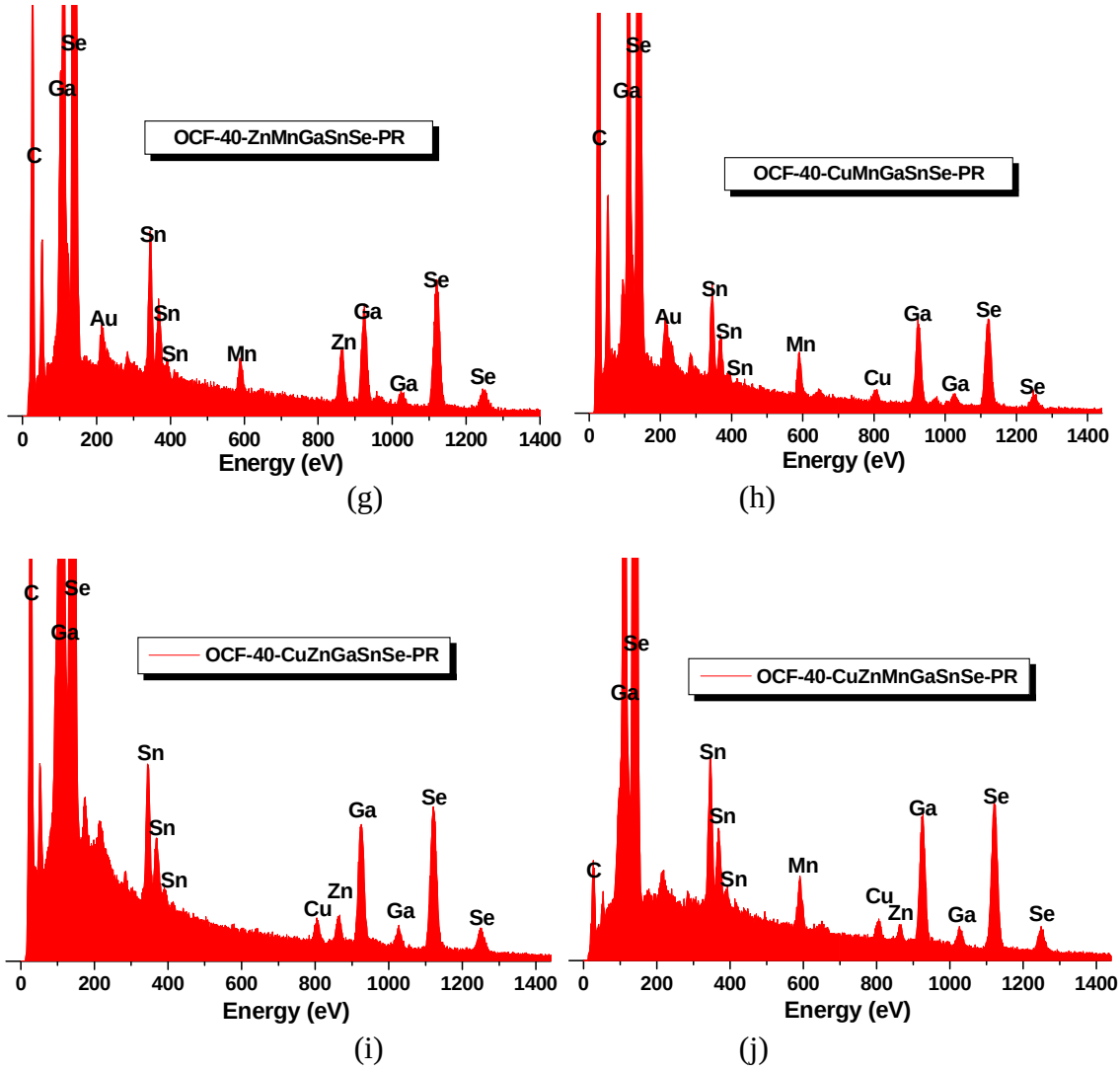


Figure 5.2. The energy dispersive X-ray (EDAX) spectroscopy of OCF-5-CuGaSnSe-DPM (a), OCF-40-CuGaSnSe-PR (b), OCF-40-ZnGaSnSe-PR (c), OCF-40-CuGaSnS-PR d), OCF-40-ZnGaSnS-PR (e), OCF-40-MnGaSnSe-PR (f), OCF-40-ZnMnGaSnSe-PR (g), OCF-40-CuMnGaSnSe-PR (h), OCF-40-CuZnGaSnSe-PR (i) and OCF-40-CuZnMnGaSnSe-PR (j).

Table 5.2 Syntheses of OCF-5s and OCF-40s [a].

Compound Code of Products	Reactants						Yield
	Metal A/B/C	Metal D	Metal E	Se/S	Amine	H_2O	
OCF-5-CuGaSnSe-DPM	A 31.9mg	255.2mg	30.4mg	177.7mg	2.061g	2.977g	/
OCF-5-ZnGaSnSe-2-MPR	B 75.8mg	257.6mg	32.2mg	175.9mg	2.512g	2.978g	/
OCF-5-ZnGaSnSe-3-MPR	B 77.1mg	256.5mg	32.9mg	176.8mg	2.533g	3.102g	120.5mg
OCF-40-CuGaSnSe-PR	A 33.4mg	258.6mg	32.0mg	172.3mg	2.051g	3.225g	221.2mg
	A 32.2mg	256.3mg	32.4mg	175.5mg	2.125g	3.156g	235.3mg
OCF-40-ZnGaSnSe-PR	A 76.9mg	252.7mg	34.9mg	176.3mg	2.074g	2.481g	115.3mg
	A 77.2mg	255.6mg	35.6mg	178.2mg	2.189g	2.247g	160.3mg
OCF-40-MnGaSnSe-PR	C 66.8mg	257.9mg	35.5mg	176.8mg	2.221g	2.245g	40.2mg
OCF-40-CuGaSnSe-4-MPR	A 33.6mg	255.5mg	34.5mg	177.3mg	2.579g	2.533g	102.6mg
OCF-40-ZnGaSnSe-4-MPR	B 77.4mg	258.9mg	33.5mg	176.4mg	2.496g	2.475g	123.5mg
OCF-40-CuGaSnS-PR	A 33.7mg	254.6mg	35.5mg	75.3mg	2.085mg	2.514g	75.3mg
OCF-40-ZnGaSnS-PR	B 75.9mg	258.4mg	36.5mg	74.6mg	2.138g	2.291g	68.7mg
OCF-40-MnGaSnS-PR	C 68.7mg	255.5mg	38.5mg	73.9mg	2.041g	2.538g	/

Notes: [a] PR = piperidine, $C_5H_{11}N$; 2-MPR= 2-methylpiperidine, $C_6H_{13}N$; 3-MPR= 3-methylpiperidine, $C_6H_{13}N$; 4-MPR= 4-methylpiperidine, $C_6H_{13}N$; DPM = dipiperidinomethane, $C_{11}H_{22}N_2$; A = $Cu(NO_3)_2 \cdot 3H_2O$; B = $Zn(NO_3)_2 \cdot 6H_2O$; C = $Mn(AC)_2 \cdot 4H_2O$; D = $Ga(NO_3)_3$; E = $SnCl_2$

OCF-5-ZnGaSnSe-2-MPR and OCF-40-ZnGaSnSe-2-MPR: The procedure is similar to that for OCF-40-ZnGaSnSe-PR, except that piperidine was replaced with 2-methylpiperidine (Table 5.2). The resulting products contain very a very small amount of OCF-5-ZnGaSnSe-2-MPR and a large amount of OCF-40-ZnGaSnSe-2-MPR.

OCF-5-ZnGaSnSe-3-MPR: The synthesis procedure is similar to that for OCF-40-ZnGaSnSe-PR, except that piperidine was replaced with 3-methylpiperidine. The resulting product is pure.

OCF-40-CuGaSnSe-4-MPR: The synthesis procedure is similar to that for OCF-40-CuGaSnSe-PR, except that piperidine was replaced with 4-methylpiperidine.

OCF-40-ZnGaSnSe-4-MPR. The synthesis procedure is similar to that for OCF-40-ZnGaSnSe-PR, except that piperidine was replaced with 4-methylpiperidine.

OCF-40-MnGaSnSe-PR: The synthesis procedure is similar to that for OCF-40-CuGaSnSe-PR, except that $Cu(NO_3)_2 \cdot 3H_2O$ was replaced with $Mn(Ac)_2 \cdot 4H_2O$. Small amount of red crystals (OCF-40-MnGaSnSe-PR) were obtained.

OCF-40-CuGaSnS-PR: The synthesis procedure is similar to that for OCF-40-CuGaSnSe-PR, except that Se was replaced with S. Large amount of red crystals were obtained.

OCF-40-ZnGaSnS-PR: The synthesis procedure is similar to that for OCF-40-ZnGaSnSe-PR, except that Se was replaced with S. Large amount of pale-yellow crystals were obtained.

OCF-40-MnGaSnS-PR: The synthesis procedure is similar to that for OCF-40-MnGaSnSe-PR, except that except that Se was replaced with S. Small amount of red

crystals (OCF-40-MnGaSnS-PR) and large amount of yellowish unidentified amorphous solids were obtained.

5.2.3. Single-crystal X-ray Structure Determination

Crystallographic data of OCF-5-CuGaSnSe-DPM: tetragonal, $I4_1/acd$, $a = b =$ 23.9286(2) Å, c = 42.0821(5) Å, V= 24095.3(4)Å^3, Z = 8, $2\theta_{max}$= 48 ($-27 \leq h \leq 27$, $-24 \leq k \leq 27$, $-48 \leq l \leq 48$), T = 150K, 131661 measured reflections, R_1 = 0.0585 for 4741 reflections ($I > 2\sigma(I)$), GOF = 1.060; OCF-5-ZnGaSnSe-2-MPR: tetragonal, $I4_1/acd$, $a = b$ = 24.1584(12) Å, c = 41.931(4) Å, V= 24472(3)Å^3, Z = 8, $2\theta_{max}$= 40 ($-23 \leq h \leq 23$, $-23 \leq k \leq 23$, $-38 \leq l \leq 40$), T = 150K, 46728 measured reflections, R_1 = 0.0484 for 2855 reflections ($I > 2\sigma(I)$), GOF = 1.069; OCF-5-ZnGaSnSe-3-MPR: tetragonal, $I4_1/acd$, $a = b$ = 24.0693(3) Å, c = 42.2601(10) Å, V= 24482.6(7)Å^3, Z = 8, $2\theta_{max}$= 42 ($-24 \leq h \leq 24$, $-24 \leq k \leq 24$, $-42 \leq l \leq 42$), T = 150K, 52078 measured reflections, R_1 = 0.0684 for 3287 reflections ($I > 2\sigma(I)$), GOF = 1.190; OCF-40-CuGaSnSe-PR: cubic, I-43m, $a = b = c =$ 18.80190(10) Å, V= 6646.69(6)Å^3, Z =2, $2\theta_{max}$= 55 ($-18 \leq h \leq 24$, $-24 \leq k \leq 24$, $-22 \leq l \leq 24$), T = 150 K, 26479 measured reflections, R_1 = 0.0328 for 1151 reflections ($I > 2\sigma(I)$), GOF = 1.087; OCF-40-ZnGaSnSe-PR: cubic, I-43m, $a = b = c$ = 18.89510(10) Å, V= 6746.02(6)Å^3, Z =2, $2\theta_{max}$=60 ($-17 \leq h \leq 25$, $-26 \leq k \leq 24$, $-26 \leq l \leq 26$), T = 150 K, 27073 measured reflections, R_1 = 0.0408 for 1842 reflections ($I > 2\sigma(I)$), GOF = 1.115; OCF-40-MnGaSnSe-PR: cubic, I-43m, $a = b = c$ = 18.8626(2) Å, V= 18.8626(2)Å^3, Z =2, $2\theta_{max}$=50 ($-22 \leq h \leq 10$, $-20 \leq k \leq 19$, $-12 \leq l \leq 21$), T = 150 K, 8954 measured reflections, R_1 = 0.0417 for 1119 reflections ($I > 2\sigma(I)$), GOF = 1.074. OCF-40-CuGaSnS-PR: cubic, I-43m, $a = b = c$ = 18.4280(3) Å, V= 6257.99(18)Å^3, Z =2,

$2\theta_{max}$=50 (-10 ≤ h ≤ 21, -13 ≤ k ≤ 21, -17 ≤ l ≤ 19), T = 150 K, 4820 measured reflections, R_1 = 0.0538 for 1025 reflections ($I > 2\sigma(I)$), GOF = 1.045; OCF-40-ZnGaSnS-PR: cubic, I-43m, $a = b = c$ = 18.2580(15) Å, V= 6086.4(9)Å^3, Z =2, $2\theta_{max}$=56 (-4 ≤ h ≤ 23, -1 ≤ k ≤ 24, -11 ≤ l ≤ 16), T = 150 K, 4455 measured reflections, R_1 = 0.0584 for 1342 reflections ($I > 2\sigma(I)$), GOF = 1.061; OCF-40-MnGaSnS-PR: cubic, I-43m, $a = b = c$ = 18.2580(15) Å, V= 6086.4(9)Å^3, Z =2, $2\theta_{max}$=56 (-4 ≤ h ≤ 23, -1 ≤ k ≤ 24, -11 ≤ l ≤ 16), T = 150 K, 6203 measured reflections, R_1 = 0.0426 for 786 reflections ($I > 2\sigma(I)$), GOF = 1.146. Single-crystal X-ray analysis was performed on a Bruker Smart APEX II CCD area diffractometer with nitrogen-flow temperature controller using graphite-monochromated $Mo_{K\alpha}$ radiation (λ = 0.71073 Å), operating in the ω and φ scan mode. The SADABS program was used for absorption correction. The structure was solved by direct methods and the structure refinements were based on $|F^2|$. All atoms except those in disordered template molecules in OCF-5s were refined with anisotropic displacement parameters. The hydrogen atoms were generated geometrically. All crystallographic calculations were conducted with the SHELXTL software suites. CCDC reference numbers 753143-753148, 765560-765561 for OCF-5-CuGaSnSe-DPM, OCF-5-ZnGaSnSe-2-MPR, OCF-5-ZnGaSnSe-3-MPR, OCF-40-CuGaSnSe, OCF-40-ZnGaSnSe-PR, OCF-40-MnGaSnSe-PR, OCF-40-CuGaSnS-PR, and OCF-40-ZnGaSnS-PR, respectively. These data can be obtained free of charge at www.ccdc.cam.ac.uk/conts/retrieving.html [or from the Cambridge Crystallographic Data Centre, 12, Union Road, Cambridge CB2 1EZ, UK; fax: (internet.) +44-1223/336-033; E-mail: deposit@ccdc.cam.ac.uk].

5.3 Results and Discussion

5.3.1 Transformation from 3D Covalent Framework to Discrete T4 Clusters

As shown in Table 5.2, isolated T4 clusters have been synthesized in a variety of compositions. It is, however, interesting to note that our original discovery of isolated T4 clusters in the Cu-Ga-Sn-Se system resulted from an unusual and unprecedented phenomenon in the metal chalcogenide chemistry: the hydrothermal transformation from the 3D covalent T4 framework into isolated 0D T4 clusters. Upon reacting $SnCl_2$, $Ga(NO_3)_3$, Se, $Cu(NO_3)_2 \cdot 3H_2O$, dipiperidinomethane (DPM) and deionized water under hydrothermal conditions (200^oC for 9 days), the pale-yellow octahedral crystals (OCF-5-CuGaSnSe-DPM comprising covalently linked T4 clusters) and dark red block crystals (OCF-40-CuGaSnSe-PR containing discrete T4 clusters, PR = piperidine) were obtained in the approximate 1:1 ratio. Longer reaction time led to OCF-40-CuGaSnSe-PR as the only product, suggesting the transformation from 3D covalent OCF-5-CuGaSnSe-DPM into molecular OCF-40-CuGaSnSe-PR. This is a totally unexpected observation, because the previous research has repeatedly shown that the polymeric framework, which OCF-5-CuGaSnSe-DPM has, is a far more favorable product under such synthesis conditions. The fact that such isolated T4 clusters can not only be synthesized, but at the cost of a well-known stable 3D OCF-5 framework, is truly extraordinary.

The mechanism for the above unusual transformation was revealed by single crystal structure analysis, which shows completely disordered amine molecules in OCF-5-CuGaSnSe-DPM and highly ordered protonated piperidine ($[C_5H_{10}NH_2]^+$) in OCF-40-

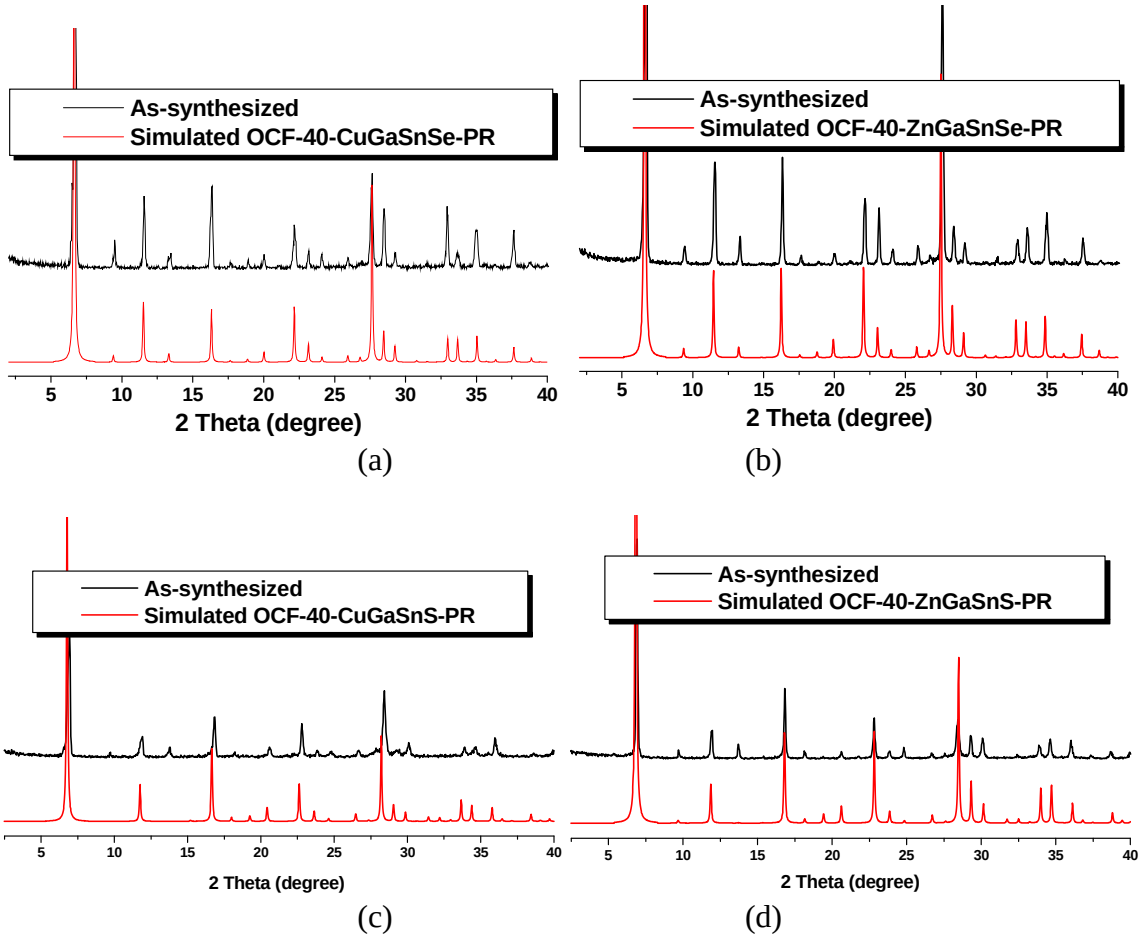


Figure 5.3. The powder X-ray diffraction (PXRD) patterns: (a) pure OCF-40-CuGaSnSe-PR; (b) pure OCF-40-ZnGaSnSe-PR; (c) pure OCF-40-CuGaSnS-PR; (d) pure OCF-40-ZnGaSnS-PR.

CuGaSnSe-PR. It is clear that the piperidinium cations came from the decomposition of DPM. With this knowledge, pure OCF-40-CuGaSnSe-PR can be synthesized directly by using piperidine as template with yield higher than that by using DPM, as evidenced by PXRD (Figure 5.3). Thus one driving force for the transformation from 3D OCF-5-CuGaSnSe-DPM to molecular OCF-40-CuGaSnSe-PR is the gradual decomposition of DPM into piperidine, which causes the dissolution of covalent OCF-5 and subsequent re-assembly into molecular OCF-40 (Figure 5.4). The kinetics of the DPM decomposition

and the associated 3D-to-0D conversion is dependent on the type of metal cations. For example, when replacing $Cu(NO_3)_2 \cdot 3H_2O$ with $Zn(NO_3)_2 \cdot 6H_2O$, the OCF-5 phase could not be detected and the pure OCF-40-ZnGaSnSe-PR is the only product, even when different reaction times are used. The subsequent synthesis of OCF-40s with other compositions is performed by using piperidine or substituted piperidine (Table 5.1).

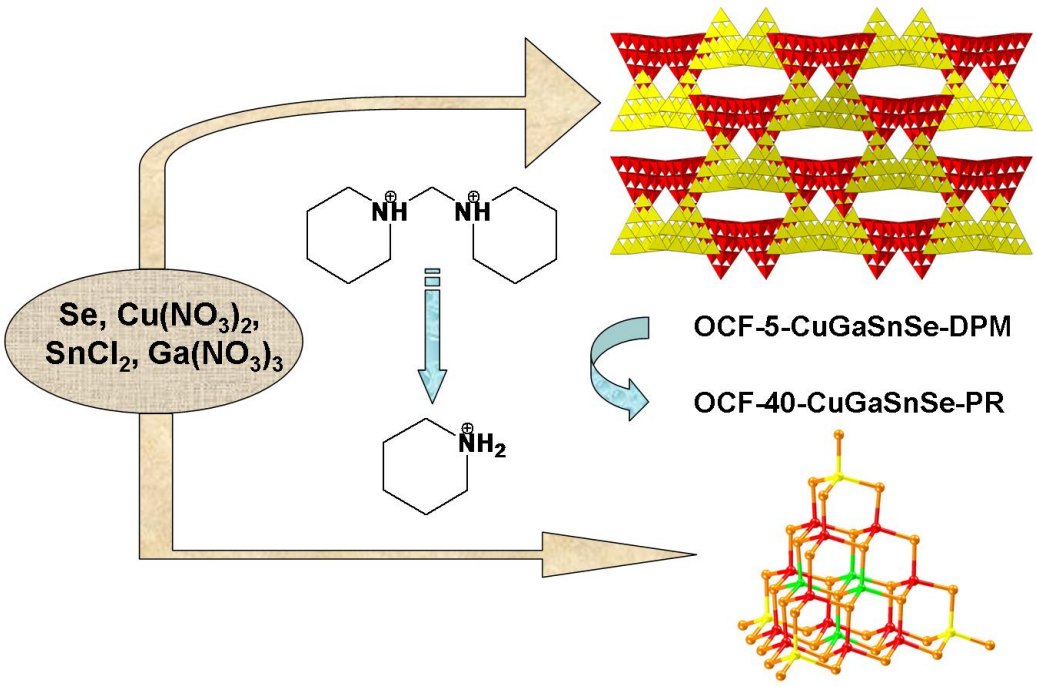
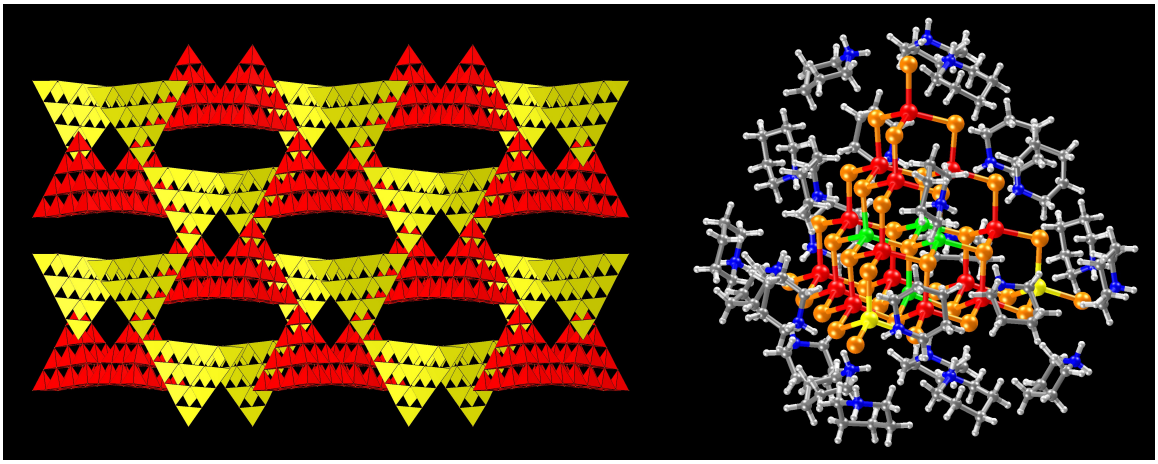


Figure 5.4. Possible transformation from OCF-5-CuGaSnSe-DPM to OCF-40-CuGaSnSe-PR triggered by gradual dissociation of DPM into piperidine.

5.3.2 Geometric and Charge-density Matching Between T4 Clusters and Organic Templates

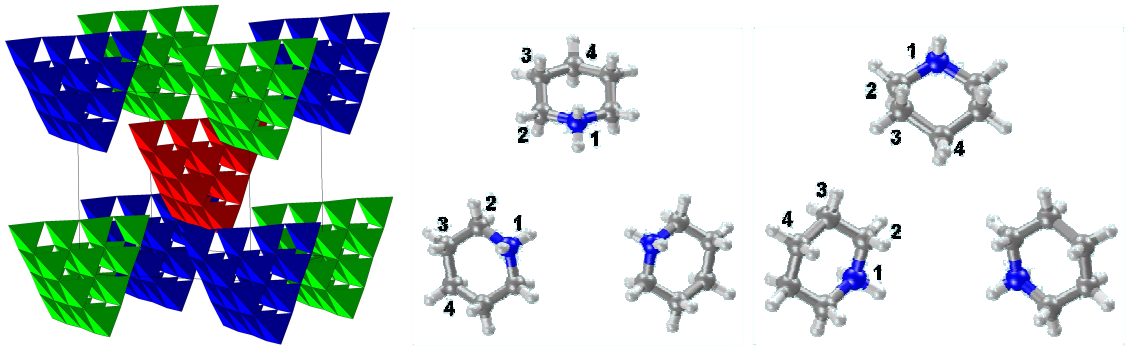
OCF-5-CuGaSnSe-DPM and OCF-40-CuGaSnSe-PR comprise the same supertetrahedral T4 nanocluster $[Cu_2Ga_{16}Sn_2Se_{35}]$ with 18 bicoordinate Se^{2-} sites on six edges, 12 tricoordinate Se^{2-} ions on four faces, and one tetrahedral Se^{2-} at the core of the T4 supertetrahedron. The difference is that there are four monocoordinate terminal Se^{2-}

ions at the four corners of the T4 supertetrahedron in OCF-40-CuGaSnSe-PR, whereas in OCF-5-CuGaSnSe-DPM, these corner Se sites are shared with other four adjacent clusters to form a 3-D extended open framework with 2-fold interpenetrated diamond topology, (Figure 5.5a) first found in the Cd-In-S system[22].



(a) (b)

Figure 5.5. (a) The two-fold interpenetrated (red and yellow) 3D framework constructed by corner-sharing supertetrahedral T4 clusters in OCF-5-MGaSnSe (M=Cu, Zn); (b) The isolated supertetrahedral T4 cluster surrounded by twenty-four protonated piperidine molecules in OCF-40s (red ball stands for Ga, orange for Se/S, yellow for Sn, green for Zn or Mn or mixed Cu/Ga, blue for N, grey for C, white for H).



(a) (b)

Figure 5.6. (a) The body-centered cubic (BCC) packing pattern in one unit cell; (b) the spatial orientation of three adjacent piperidinium cations.

The isolated clusters in OCF-40-CuGaSnSe-PR pack in body-centered cubic pattern (BCC) with piperidinium cations occupying the inter-cluster space. (Figure 5.6a) Single-crystal structure refinement based on the large difference in the scattering power between Sn^{4+} and Ga^{3+} shows that there are only two Sn^{4+} ions statistically distributed at two of four corner sites. To satisfy Pauling's electrostatic valence rule, the central tetrahedral Se^{2-} site is surrounded by two Cu^{+} ions and two Ga^{3+} ions to give a bond valence sum of +2, consistent with the valence of Se^{2-}. OCF-40-ZnGaSnSe-PR is isostructural to OCF-40-CuGaSnSe, but the central Se^{2-} site is tetrahedrally coordinated to four zinc ions to satisfy Pauling's electrostatic valence rule. The Sn/Ga-Se bond distances at four corners in three selenide phases, OCF-40-MGaSnSe-PR (M = Mn, Cu, Zn), range from 2.4583 to 2.5146 Å, which lies between previously reported Sn-Se (2.490-2.521Å)[9, 27] and the Ga-Se bond lengths (2.379-2.418Å)[28]. Three sulfide phases, OCF-40-MGaSnS-PR (M = Cu, Zn, Mn), are isostructural to OCF-40-MGaSnSe-PR, but the shorter M-S bond lengths give rise to the smaller T4 cluster and smaller unit cells (Table 5.1).

While the single crystal X-ray analysis of OCF-40-CuGaSnSe-PR only produces a statistically average structure with two Cu^{+} and two Sn^{4+} sites per cluster, the distribution of Cu^{+} and Sn^{4+} sites in each cluster is unlikely to be random from the chemical point of view. Ideally, two Cu^{+} sites bonded to the central Se^{2-} site should be located at positions closer to two corner Sn^{4+} sites so that the valence sum from cations to the anionic site is distributed as evenly as possible. The preliminary theoretical calculation on Mulliken

charge distribution reveals the presence of more negative charge centers at the corners of supertetrahedron and also at the center of each edge (Figure 5.7).

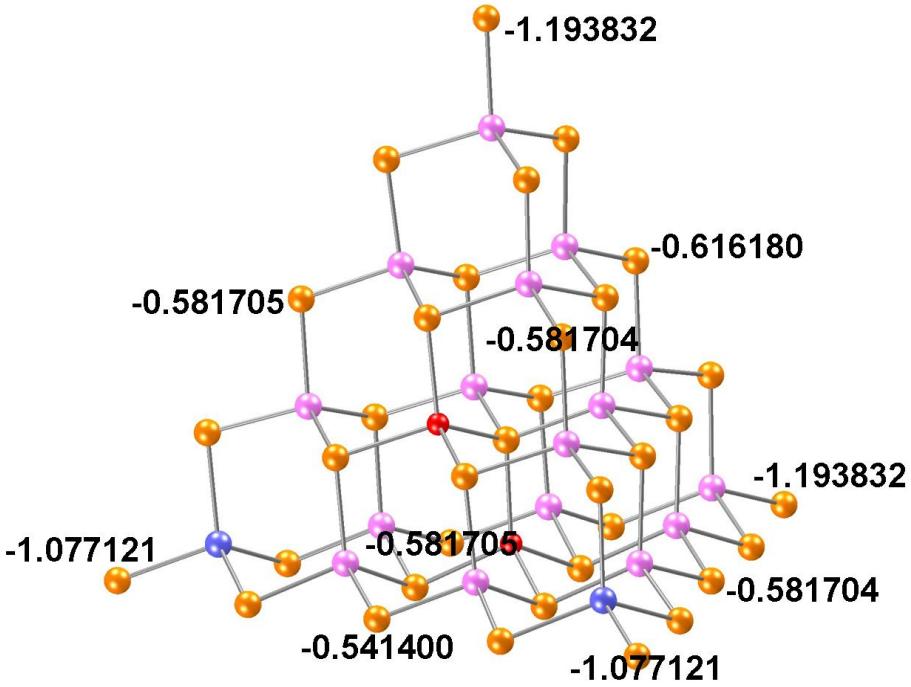
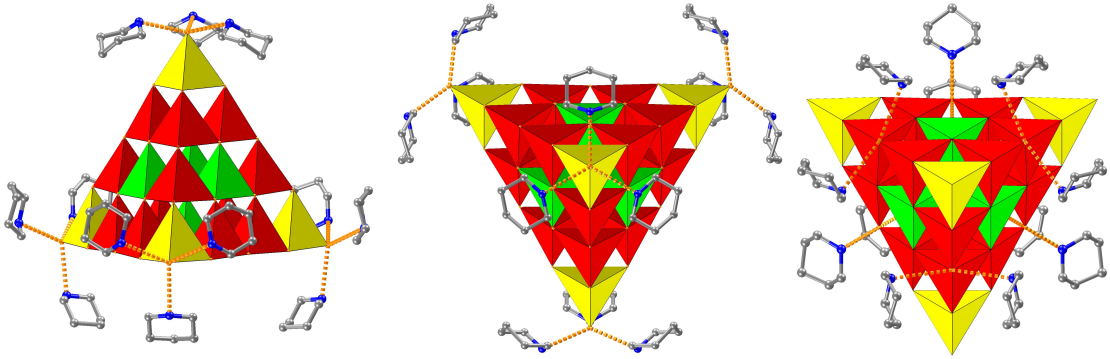


Figure 5.7. The Mulliken charge distribution of Se^{2-} at the four corners and six edge-centers by RB3LYP/LANL2DZ theoretical calculation on OCF-40-CuGaSnSe-PR (Pink ball stands for Ga, orange for Se, blue for Sn, red for Cu.)



(a) (b) (c)

Figure 5.8. The strong N-H···Se hydrogen bond formed between corner Se^{2-} and protonated piperidine viewed along one side of the cluster (a), down C_3 axis (b), edged Se^{2-} and protonated piperidine cations viewed down C_3 axis (c).

The fact that isolated T4 clusters can be obtained from the disintegration of covalently linked T4 clusters suggests the extraordinary stability of the isolated T4 clusters. Such a high stability comes from the perfect match between the piperidinium and the T4 clusters, in terms of charge density, geometry, and mutual interactions (electrostatic and hydrogen bonding). In OCF-40-CuGaSnSe-PR, each Se^{2-} at the edge center of supertetrahedron interacts with two piperidinium cations *via* weak N-H···Se hydrogen bond with the N···Se distance of 3.29Å, and each corner Se^{2-} is bonded to three piperidinium with the N···Se distance of 3.11Å, (Figure 5.8) much smaller than the sum of Se and N *van der Waals* radii (3.41Å). So each isolated T4 cluster is surrounded by a total of 24 piperidinium cations (4*3+6*2=24) (Figure 5.5b). Since each piperidinium has Y-shaped connection to one corner Se^{2-} from one cluster and one central Se^{2-} on the edge center from another cluster, the negative charge (-12) per cluster exactly matches the positive charge (+24/2=+12) of piperidinium cations.

The above discussion about the perfect match between piperidinium cations and T4 clusters highlights the great significance in the choice of amines and in using charge-complementary metal cations ($M^{+}/M^{3+}/M^{4+}$ or $M^{2+}/M^{3+}/M^{4+}$) to tune the charge of the clusters. The incorporation of two Sn^{4+} ions into two out of the twenty metal sites is critical for the crystallization of OCF-40 by reducing the charge of the T4 cluster from -14 in $[Cu_2Ga_{18}Se_{35}]^{14-}$ to -12 in $[Cu_2Ga_{16}Sn_2Se_{35}]^{12-}$. Indeed, in control experiments without any tin salt, OCF-40 could not be synthesized.

5.3.3 Solubility Behaviors and Stabilization of T4 Clusters with Surface Organic Cations

Because of their molecular nature, the solubility of OCF-40s is of particular interest. A large number of solvents have been examined in this work. It was found that OCF-40s have a rather peculiar solubility property. They are not soluble in many common aprotic polar or nonpolar organic solvents, such as chloroform, benzene, toluene, hexane, cyclohexane, petroleum ether, acetonitrile, and triethylamine. Neither are they soluble in common protic polar solvents, such as water, ethanol, methanol, and even aqueous CsCl (1M) with high ionic strength. However, OCF-40s exhibit appreciable solubility in aprotic weak base solvents, such as DMF, DMSO and piperidine. The resulting DMSO solutions were characterized by UV-Vis adsorption spectroscopy (Figure 5.9), which shows that solutions of metal selenides exhibit broader adsorption band than those of metal sulfides. One possible reason for the appreciable solubility in DMF and DMSO may be that they serve as hydrogen-bond acceptor for piperidinium to facilitate the dissolution of the solid samples, in addition to act as good solvents for piperidine. Crystalline samples of OCF-40s are stable in air and their solutions in DMF and DMSO are also stable when stored in the capped vials. However, upon exposure to air for several days, unidentified black powder is observed to precipitate from selenide solutions. OCF-40s can be also digested in strong base solutions such as KOH (0.1M), which is likely through the deprotonation of piperidinium cations.

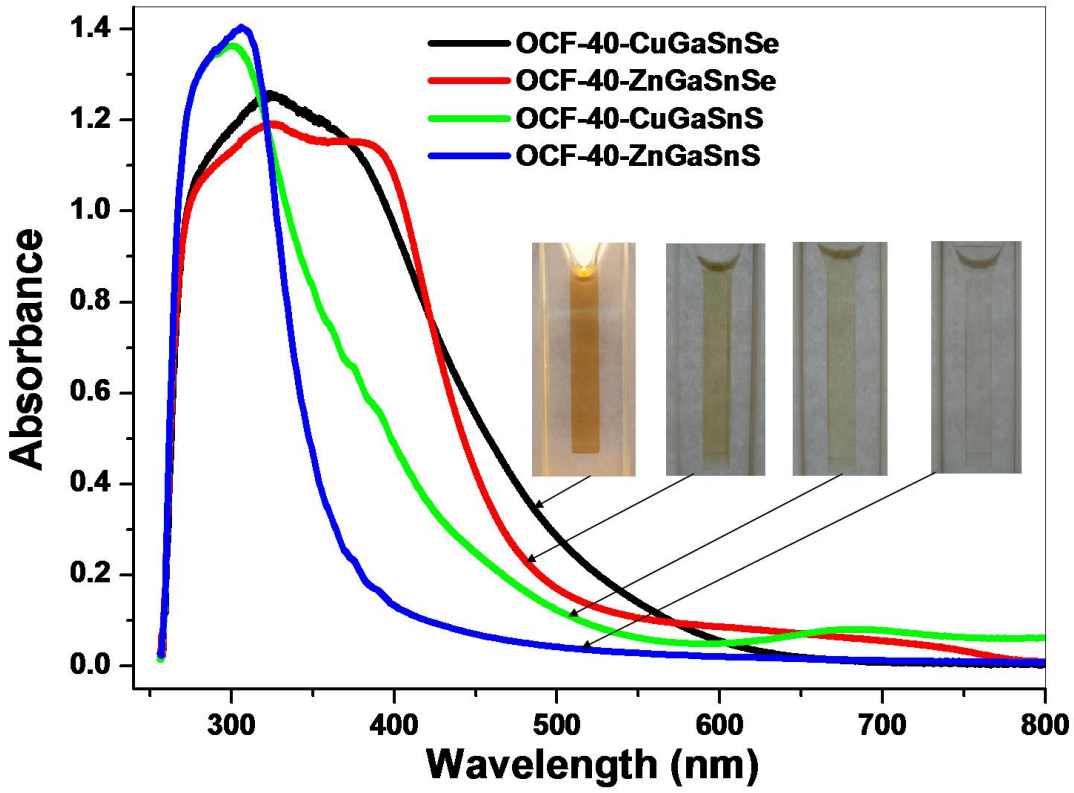


Figure 5.9. Effects of Cu^{+} vs. Zn^{2+} and Se^{2-} vs. S^{2-} on band structures in solution. The UV-Vis adsorption spectra of the filtrate of crystalline OCF-40s (15mg) immersed and stirred in 5ml DMSO, respectively, at room temperature.

Of particular interest is the apparent existence of stable "ion pair" composed of one isolated T4 anion cluster and 12 piperidinium cations. OCF-40s have significant solubility in piperidine itself. However, the dissolution or dissociation behavior of OCF-40s in piperidine is different from that in DMSO. The dissolution of OCF-40-MGaSnSe-PR (M=Cu, Zn) in DMSO results in a significant increase in the electrical conductivity whereas the dissolution of OCF-40-MGaSnSe-PR (M=Cu, Zn) in piperidine results in no change in the electrical conductivity. This suggests that in DMSO at least some of the dissolved species exist as negatively-charged T4 clusters and positively-charged piperidinium. On the other hand, in piperidine, the solid dissolves into neutral ion pairs,

$[(T4)^{12-}\cdot 12(C_5H_{12}N)^+]$, which is unusual in metal chalcogenide chemistry. It reveals a new way for the stabilization of chalcogenide clusters, because in general chalcogenide clusters are stabilized by covalently attached organic ligands, not organic cations bonded to the cluster surface through electrostatic force as reported here. It also further supports the strong interaction between piperidinium and T4 cluster. Such strong interaction greatly stabilizes the discrete T4 cluster and creates a thermodynamic driving force for the extraordinary transformation from 3D OCF-5-CuGaSnSe-DPM to molecular OCF-40-CuGaSnSe-PR.

5.3.4 Tunable Optical Properties in Solution and Solid State

These isostructural OCF-40s show a remarkable effect of different d^{10} metal ions (Cu^+ and Zn^{2+}) and chalcogen anions (Se^{2-} and S^{2-}) on the sample colors and band gap of semiconductor materials. The dark red selenide sample of OCF-40-CuGaSnSe-PR has a wider UV-Vis adsorption peak than the yellow sample of OCF-40-ZnGaSnSe-PR (Figure 5.10). The similar difference is also found in sulfides between OCF-40-CuGaSnS-PR and OCF-40-ZnGaSnS-PR. The solid-state diffuse reflectance spectra performed on a Shimadzu UV-3101PC double-beam double monochromator spectrophotometer by using $BaSO_4$ powder as 100% reflectance reference reveal that OCF-40s are semiconductors with a range of band gaps: OCF-40-CuGaSnSe-PR (1.91eV), OCF-40-ZnGaSnSe-PR (2.71eV), OCF-40-CuGaSnS-PR (2.11eV), and OCF-40-ZnGaSnS-PR (3.59eV), as calculated from reflectance data by using Kubelka-Munk function[29]. It is clear that with other factors being equal, Cu^+ or Se^{2-} gives materials with much lower band gaps.

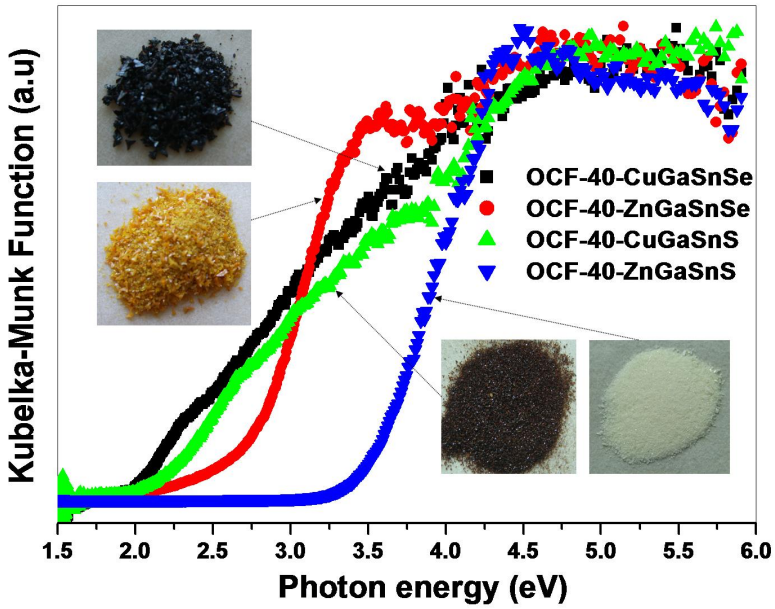


Figure 5.10. Effects of Cu^{+} vs. Zn^{2+} and Se^{2-} vs. S^{2-} on band structures in solid state. Normalized solid-state UV-Vis absorption spectra of OCF-40s. The inset gives the photos of the as-synthesized crystalline materials.

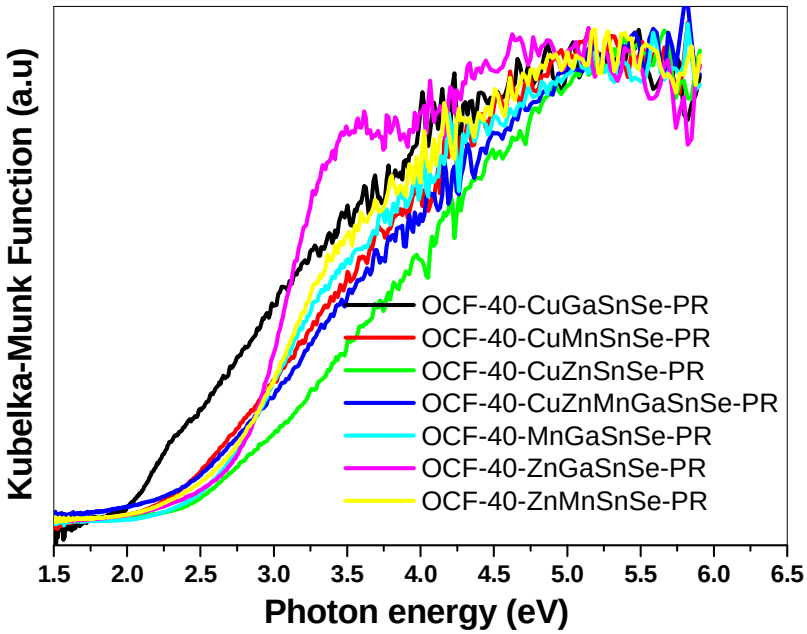


Figure 5.11. Effects of different metal ions (Mn^{2+}, Cu^{+}/Mn^{2+}, Zn^{2+}/Mn^{2+}, Cu^{+}/Zn^{2+}, and $Cu^{+}/Zn^{2+}/Mn^{2+}$) on band structures. Normalized solid-state UV-Vis absorption spectra of OCF-40-MnGaSnSe-PR, OCF-40-CuMnGaSnSe-PR, OCF-40-ZnMnGaSnSe-PR, OCF-CuZnGaSnSe-PR and OCF-40-CuZnMnGaSnSe-PR.

In the field of chalcogenide cluster chemistry, there are a rather limited number of examples in which clusters exist in both discrete and covalently-linked forms[30]. Thus OCF-5s and OCF-40s reported here present a unique opportunity to examine the effect of structures (0D vs. 3D) on the optical properties. The significant difference in band gap between molecular OCF-40-CuGaSnSe-PR (1.91eV) and 3D covalent OCF-5-CuGaSnSe-DPM (1.50eV) is likely caused by quantum confinement effect. The zero-dimensional nano-scale cluster is expected to exhibit a blue-shift in adsorption compared with covalent frameworks or condensed phases with comparable compositions.

In addition to offer the tunability in the charge of the cluster, which is essential for the successful crystallization, the quaternary cluster composition provides a convenient way to tune electronic properties of discrete T4 clusters by allowing the variation of the cluster compositions based on types of metal ions and chalcogenide anions (S^{2-} or Se^{2-}). In the above, we have already shown that the use of Cu^{+}, Zn^{2+}, S^{2-}, and Se^{2-} makes it possible to tune the electronic band gaps over a wide range. As shown in Table 5.1, other metal ions such as Mn^{2+} can also be employed to further tune the semiconducting properties of the T4 cluster compound as evidenced by the syntheses of the OCF-40-MnGaSnSe-PR and OCF-40-MnGaSnS-PR. In addition, it is possible to develop even more complex cluster compositions by combining two or more low-valent metal ions (Cu^{+}, Zn^{2+}, Mn^{2+}) in the reaction system. Various permutations of these metal ions have allowed the synthesis of OCF-40-CuZnGaSnSe-PR, OCF-40-ZnMnGaSnSe-PR, OCF-40-CuMnGaSnSe-PR, and OCF-40-CuZnMnGaSnSe. All of these compositions have

been verified by qualitative elemental analysis using EDAX (Figure 5.2). Solid-state UV-Vis adsorption measurement also shows the tunable band gap (Figure 5.11).

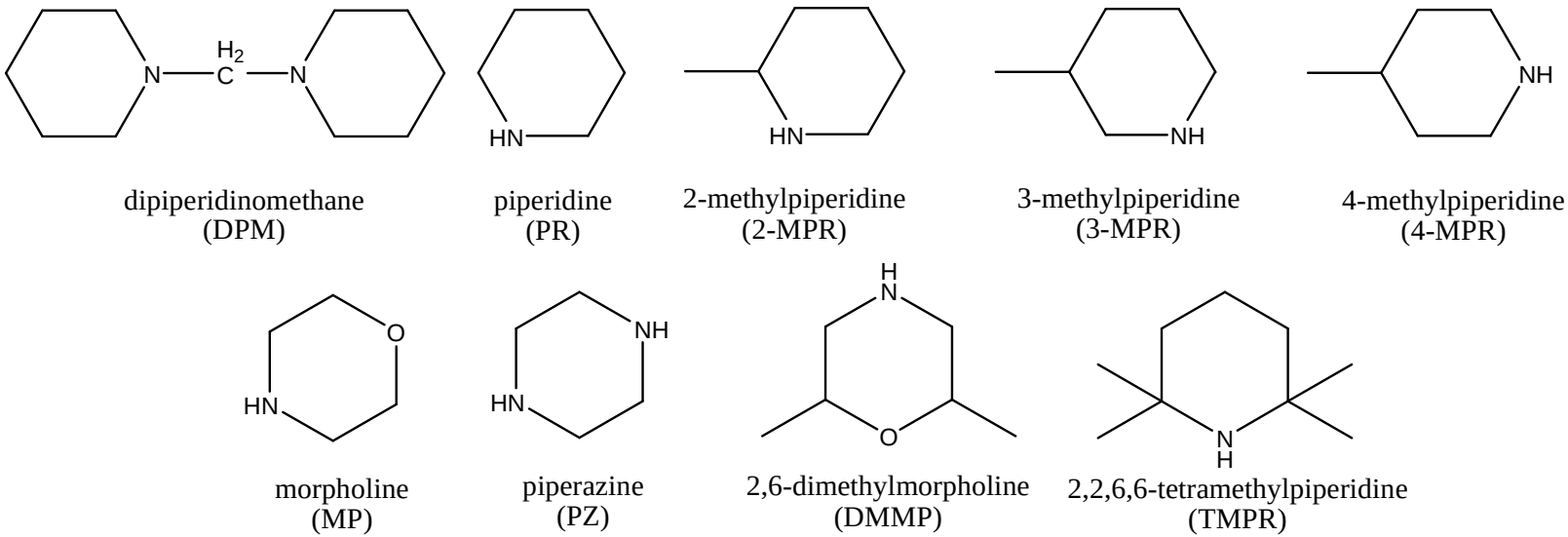
5.3.5. Effects of Organic Templates on the Competing Crystallization of OCF-5 vs. OCF-40 and on Properties of OCF-40

While much of this work centers on the control of semiconducting properties by varying the composition of T4 clusters, we are also interested in the role of organic component in the structural control and in modifying properties (e.g., solubility and stability) of the solids. To this end, we have further investigated the effect of various piperidine-like molecules on the final structures. Seven amines (Scheme 5.1) were chosen to replace piperidine in the hydrothermal synthesis. These amines possess different basicity and steric hindrance. It is observed that similar reaction processes, but with different amines lead to two types of frameworks, OCF-5s and OCF-40s (Table 5.3). Their phase purity and structure are verified by powder X-ray diffraction (Figure 5.12) and single-crystal X-ray diffraction.

As described above, the formation of discrete T4 clusters (OCF-40) faces the inherent competition for the crystallization of covalently-linked T4 clusters (OCF-5). We have already shown that the length of reaction time and the type of metal ions have an effect on whether OCF-5 or OCF-40 (or both) will be formed. Here, we have also found that the type of organic templates can dictate whether OCF-5 or OCF-40 will be formed. Before discussing the individual role of organic amines, it is necessary to have an overview of how amines behave in chalcogenides of various dimensionality. In 3-D chalcogenide frameworks, extra-framework protonated amines are almost always

Table 5.3. Effects of different amine templates on the competing crystallization of OCF-5s and OCF-40s.

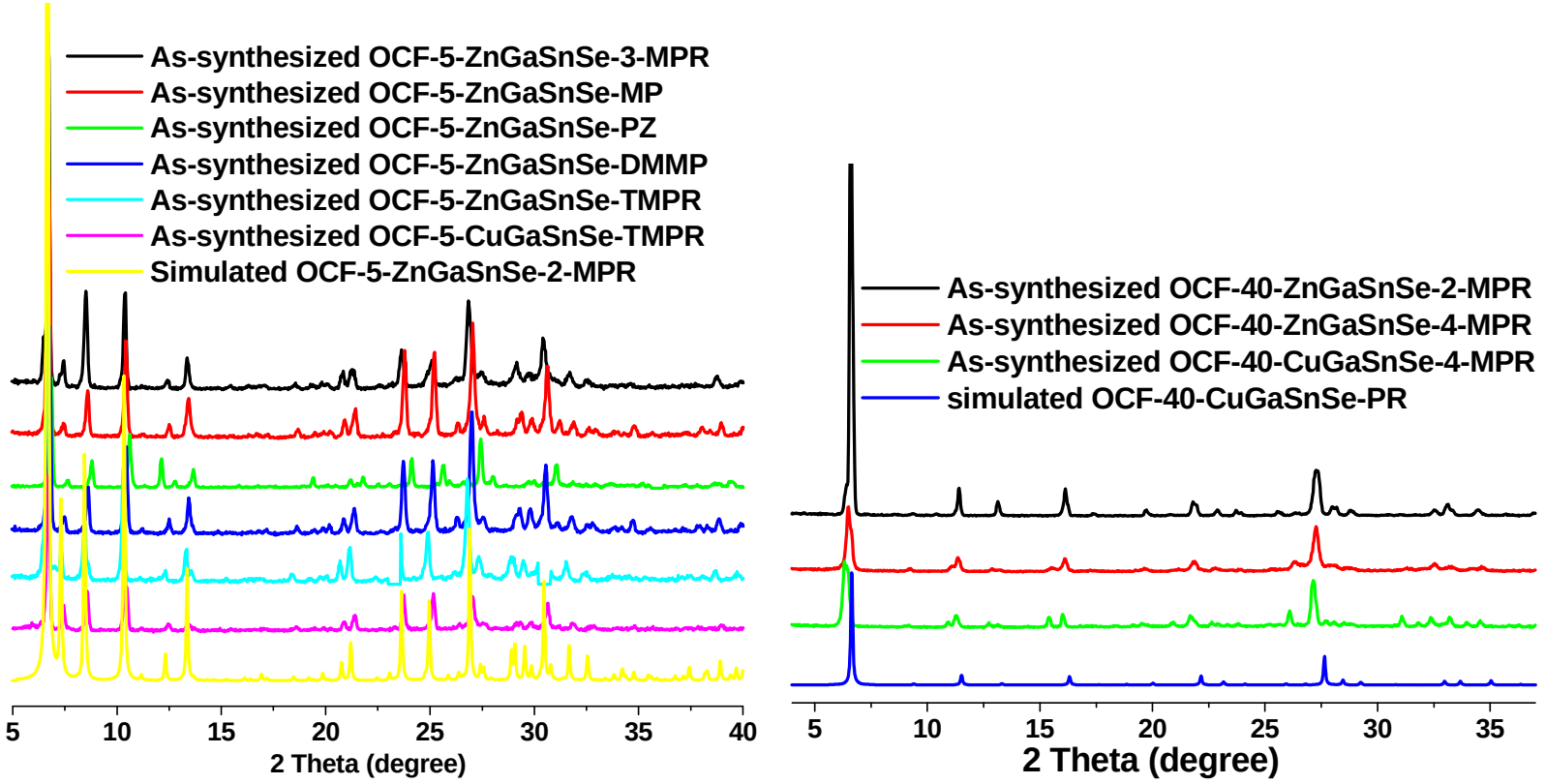
	PR	2-MPR	3-MPR	4-MPR	MP	PZ	DMMP	TMPR
$Zn(NO_3)_2$	OCF-40	OCF-5 (minor) & OCF-40 (major)	OCF-5	OCF-40	OCF-5	OCF-5	OCF-5	OCF-5
$Cu(NO_3)_2$	OCF-40	/	/	OCF-40	/	/	/	OCF-5



dipiperidinomethane (DPM) | piperidine (PR) | 2-methylpiperidine (2-MPR) | 3-methylpiperidine (3-MPR) | 4-methylpiperidine (4-MPR)

morpholine (MP) | piperazine (PZ) | 2,6-dimethylmorpholine (DMMP) | 2,2,6,6-tetramethylpiperidine (TMPR)

Scheme 5.1. Molecular structures and names of eight similar amine templates including their abbreviations.



(a) (b)

Figure 5.12. The XRPD patterns of as-synthesized samples containing several different amine templates with OCF-5s (a) and OCF-40s (b) structures.

disordered to the extent that it is impossible to locate them in the crystallographic analysis. This suggests that the role of amines is mainly for charge-balancing and pore-filling and that the formation of 3-D frameworks is more tolerant of small variations in the size and shape of amines. In comparison, amines in low-dimensional structures are generally ordered and there is a better match between structural features of amines and the chalcogenide units. Being zero-dimensional, OCF-40 represents an extreme case. Therefore, the formation of low-dimensional chalcogenide units, 0-D in particular, has a more stringent requirement for the organic amines, which explains why OCF-5 tends to occur more often than OCF-40 in this work.

The template amines with highly steric hindrance and strong protonation ability easily give OCF-5 with the 3D covalent framework, while 2-methylpiperidne and 4-methylpiperidine induce the formation of OCF-40 with discrete clusters. This is because it is easier to fit bulky amines within the cavities of 3D OCF-5 than to fit them orderly on the surface of OCF-40. This point is further highlighted by comparing 3-methylpiperidine with 2- or 4-methylpiperidine.

A detailed analysis of the tri-piperidinium aggregates near the corner of T4 cluster indicates that the 3-position in piperidine exhibits a much higher steric hindrance than 2- or 4-position. (Figure 3b), making it difficult to arrange multiple 3-methylpiperidinium around the cluster surface. It is worth noting that the 4-position methyl group gives a significantly larger unit cell, which is likely related to the two distinct orientations of methyl group in the chair configuration. Such orientational disorder of 4-methylpiperidine leads to a lower crystal quality and yet the weakening in the packing

force contributes to the faster dissolution rate and increased solubility of 4-methylpiperidine templated OCF-40 in piperidine, as compared to piperidine templated OCF-40. Also worth noting is that the substitution of piperidinium by 4-methylpiperdidinium in OCF-40s leads to a significant change in electronic properties (Figure 5.13).

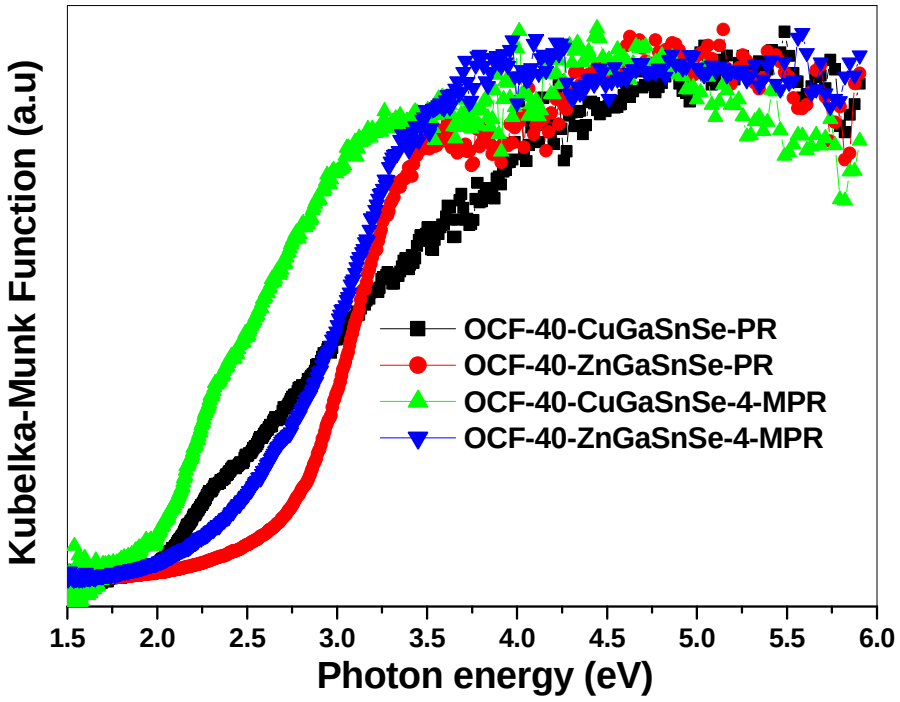


Figure 5.13. Effects of surface organic templates on band structures. Normalized solid-state UV-Vis absorption spectra of OCF-40-CuGaSnSe-4-MPR (band gap 1.80eV) and OCF-40-ZnGaSnSe-4-MPR (band gap 2.60eV), compared to OCF-40-CuGaSnSe-PR and OCF-40-ZnGaSnSe-PR.

5.4 Conclusion

In conclusion, we have synthesized and characterized a family of discrete chalcogenide supertetrahedral T4 clusters ($M_xGa_{18-x}Sn_2Q_{35}^{12-}$, x=2 or 4; M = Mn, Cu, Zn; Q=S, Se) with tunable electronic and optical properties. By doubling the size of the previous known T3 cluster (in terms of the number of metal sites), these molecular T4 clusters are currently the largest exact fragment of the cubic ZnS-type lattice. The synthetic success demonstrates the great potential of our synthetic strategy based on the charge-density tuning (by using multiple charge-complementary metal cations) in the generation of large chalcogenide clusters and in their subsequent crystallization. Specifically, the introduction of tetravalent metal ion Sn^{4+} into the corners of M-Ga-Q (M=Cu, Zn, Mn; Q=Se, S) based T4 chalcogenide clusters allows the lowering of charge density of the cluster to an optimum value that matches perfectly with the templating organic cations. Resulting soluble molecular clusters exhibit a wide range of electronic band properties. The synthesis of such clusters demonstrates the feasibility for the continued success in the quest for even larger tetrahedral chalcogenide clusters that will eventually seamlessly blend the size gap between chalcogenide clusters and colloidal semiconductor nanoparticles.

5.5 References

(1) Bedard, R. L.; Wilson, S. T.; Vail, L. D.; Bennett, J. M.; Flanigen, E. M. *Stud. Surf. Sci. Catal. A* **1989**, *49*, 375-387.

(2) (a) Ding, N.; Kanatzidis, M. G. *Nature Chemistry* **2010**, *2*, 187-191. (b) Mertz, J.; Ding, N.; Kanatzidis, M. G. *Inorg. Chem.* **2009**, *48*, 10898-10900. (c) Ding, N.; Kanatzidis, M. G. *Angew. Chem. Int. Ed.* **2006**, *45*, 1397-1401. (d) Ding, N.; Chung, D.-Y.; Kanatzidis, M. G. *Chem. Commun.* **2004**, 1170-1171. (e) Feng, P.; Bu, X.; Zheng, N. *Acc. Chem. Res.* **2005**, *38*, 293-303. (f) Bu, X.; Zheng, N.; Feng, P. *Chem. Eur. J.* **2004**, *10*, 3356-3362.

(3) Li, H.; Laine, A.; O'Keeffe, M.; Yaghi, O. M. *Science* **1999**, *283*, 1145-1147.

(4) (a) Dehnen, S.; Melullis, M. *Coord. Chem. Rev.* **2007**, *251*, 1259-1280. (b) Vaqueiro, P. *Inorg. Chem.* **2008**, *47*, 20-22. (c) Vaqueiro, P.; Romero, M. L. *J. Phys. Chem. Solids* **2006**, *68*, 1239-1243. (d) Dehnen, S.; Brandmayer, M. K. *J. Am. Chem. Soc.* **2003**, *125*, 6618-6619. (e) Palchik, O.; Lyer, R. G.; Liao, J. H.; Kanatzidis, M. G. *Inorg. Chem.* **2003**, *42*, 5052-5054. (f) Zimmermann, C.; Melullis, M.; Dehnen, S. *Angew. Chem. Int. Ed.* **2002**, *41*, 4269-4272. (g) Zimmermann, C. ; Anson, C. E. ; Weigend, F.; Clérac, R; Dehnen, S. *Inorg. Chem.* **2005**, *44*, 5686-5695. (h) Vaqueiro, P.; Romero, M. L. *Chem. Commun.* **2007**, 3282-3284. (i) Vaqueiro, P.; Romero, M. L. *Inorg. Chem.* **2009**, *48*, 810-812.

(5) (a) Cheetham, A. K.; Férey, G. ; Loiseau, T. *Angew. Chem. Int. Ed.* **1999**, *38*, 3268-3292. (b) Davis, M. E *Nature* **2002**, *417*, 813-821.

(6) (a) Ma, L.; Abney, C.; Lin, W. *Chem. Soc. Rev.* **2009**, *38*, 1248-1256. (b) Xie, Z.; Ma, L.; deKrafft, K. E.; Jin, A.; Lin, W. *J. Am. Chem. Soc.* **2010**, *132*, 922-923. (c) deKrafft, K. E.; Xie, Z.; Cao, G.; Tran, S.; Ma, L.; Zhou, O. Z.; Lin, W. *Angew. Chem. Int. Ed.* **2009**, *48*, 9901- 9904.

(7) (a) Férey, G. *Chem. Soc. Rev.* **2008**, *37*, 191-214. (b) Férey, G.; Serre, C. *Chem. Soc. Rev.* **2009**, *38*, 1380-1399. (c) Férey, G.; Draznieks, C. M.; Serre, C.; Millange, F. *Acc. Chem. Res.* **2005**, *38*, 217-225.

(8) (a) O'Keeffe, M. *Chem. Soc. Rev.* **2009**, *38*, 1215-1217. (b) Li, J.-R.; Kuppler, R. J.; Zhou, H.-C. *Chem. Soc. Rev.* **2009**, *38*, 1477-1504. (c) Farha, O. K.; Malliaks, C. D.; Kanatzidis, M. G.; Hupp, J. T. *J. Am. Chem. Soc.* **2010**, *132*, 950-952. (d) Kitagawa, S.; Kitaura, R.; Noro, S. *Angew. Chem. Int. Ed.* **2004**, *43*, 2334-2375. (e) Murray, L. J.; Dincă, M.; Long, J. R. *Chem. Soc. Rev.* **2009**, *38*, 1294-1314. (f) Uemura, T.; Yanai, N.; Kitagawa, S. *Chem. Soc. Rev.* **2009**, *38*, 1228-1236.

(9) Zheng, N.; Bu, X.; Wang, B.; Feng, P. *Science* **2002**, *298*, 2366-2369.

(10) (a) Herron, N.; Calabrese, J. C.; Farneth, W. E.; Wang, Y. *Science* **1993**, *259*, 1426-1428. (b) Zheng, N.; Bu, X.; Lu, H.; Zhang, Q.; Feng, P. *J. Am. Chem. Soc.* **2005**, *127*, 11963-11965.

(11) Corrigan, J. F.; Fuhr, O.; Fenske, D. *Adv. Mater.* **2009**, *21*, 1867-1871.

(12) Li, H.; Kim, J.; O'Keeffe, M.; Yaghi, O. M. *Angew. Chem. Int. Ed.* **2003**, *42*, 1819-1821.

(13) (a) Choy, A.; Craig, D.; Dance, I.; Scudder, M. L. *J. Chem. Soc., Chem. Commun.* **1982**, 1246-1247. (b) Dance, I. G.; Chony, A.; Scudder, M. L. *J. Am. Chem. Soc.* **1984**, *106*, 6285-6295.

(14) Yaghi, O. M.; Sun, Z.; Richardson, D. A.; Groy, T. L. *J. Am. Chem. Soc.* **1994**, *116*, 807-808.

(15) (a) Vaqueiro, P.; Romero, M. L. *J. Am. Chem. Soc.* **2008**, *130*, 9630-9631.

(16) (a) Tan, K.; Darovsky, A.; Parise, J. B. *J. Am. Chem. Soc.* **1995**, *117*, 7039-7040. (b) Cahill, C. L.; Parise, J. B. *Chem. Mater.* **1997**, *9*, 807-811.

(17) Ahari, H.; Garcia, A.; Kirkby, S.; Ozin, G. A.; Young, D.; Lough, A. J. *J. Chem. Soc., Dalton Trans.* **1998**, 2023-2027.

(18) (a) Wachhold, M.; Rangan, K. K.; Billinge, S. J. L.; Petkov, V.; Heising, J.; Kanatzidis, M. G. *Adv. Mater.* **2000**, *12*, 85-91. (b) Ding, N.; Takabayashi, Y.; Solari, P. L.; Prassides, K.; Pcionek, R. J.; Kanatzidis, M. G. *Chem. Mater.* **2006**, *18*, 4690-4699.

(19) Mohanan, J. L.; Arachchige, I. U.; Brock, S. L. *Science* **2005**, *307*, 397-400.

(20) (a) Bag, S.; Trikalitis, P. N.; Chupas, P. J.; Armatas, G. S.; Kanatzidis, M. G. *Science* **2007**, *317*, 490-493. (b) Bag, S.; Arachchige, I. U.; Kanatzidis, M. G. *J. Mater. Chem.* **2008**, *18*, 3628-3632.

(21) Li, H.; Kim, J.; Groy, T. L.; O'Keeffe, M.; Yaghi, O. M. *J. Am. Chem. Soc.* **2001**, *123*, 4867-4868.

(22) Wang, C.; Li, Y.; Bu, X.; Zheng, N.; Zivkovic, O.; Yang, C.-S.; Feng, P. *J. Am. Chem. Soc.* **2001**, *123*, 11506-11507.

(23) (a) Wang, C.; Li, Y.; Bu, X.; Zheng, N.; Zivkovic, O.; Yang, C.-S.; Feng, P. *J. Am. Chem. Soc.* **2001**, *123*, 11506-11507. (b) Bu, X.; Zheng, N.; Li, Y.;

Feng, P. *J. Am. Chem. Soc.* **2002**, *124*, 12646-12647. (c) Wang, L.; Wu, T.; Zuo, F.; Zhao, X.; Bu, X.; Wu, J.; Feng, P. *J. Am. Chem. Soc.* **2010**, *132*, 3283-3285.

(24) Su, W.; Huang, X.; Li, J.; Fu, H. *J. Am. Chem. Soc.* **2002**, *124*, 12944-12945.

(25) Xu, G.-H.; Guo, P.; Song, S.-Y.; Zhang, H.-J.; Wang, C. *Inorg. Chem.* **2009**, *48*, 4628-4630.

(26) Feng, P.; Bu, X.; Stucky, G. D. *Nature* **1997**, *388*, 735-741.

(27) Wu, T.; Wang, X.; Bu,X.; Zhao, X.; Wang, L.; Feng, P. *Angew. Chem. Int. Ed.* **2009**, *48*, 7204-7207.

(28) Bu, X.; Zheng, N.; Wang, X.; Wang, B.; Feng, P. *Angew. Chem. Int. Ed.* **2004**, *43*, 1502-1505.

(29) Wendlandt, W. W.; Hecht, H. G. *Reflectance Spectroscopy* **1966**, Interscience, New York.

(30) (a) Melullis, M.; Clérac, R.; Dehnen, S. *Chem. Commun.* **2005**, 6008-6010. (b) Manos, M. J.; Iyer, R. G.; Quarez, E.; Liao, J. H.; Kanatzidis, M. G. *Angew. Chem. Int. Ed.* **2005**, *44*, 3552-3555.

Chapter 6

Phase Selection and Site-Selective Distribution by Tin and Sulfur in Supertetrahedral Zinc Gallium Selenides

6.1 Introduction

For several decades, solid state chalcogenide semiconducting materials have been extensively studied owing to their wide applications in thermoelectrics, photoelectrics, and photocatalysis *etc.*.[1-3] Recently, research on crystalline porous chalcogenides with various structural topologies and compositions has attracted increasing attention because these materials integrate open-framework architecture with semiconducting properties, and their high surface area and size/shape selectivity could contribute to improved device efficiency and may also help to generate new applications.[4]

For both dense or porous semicondutors, great efforts have been made to tune their band structures. In this aspect, designing materials with new compositions/structures and tuning properties of known materials represent two potent ways to create materials with desirable electronic structures. Towards this goal, we and others have studied a variety of self-assembly processes involving mono- or di-valent transition metal ions (such as Cu^{+}, Zn^{2+}), high-valent main group metal ions (such as Ga^{3+}, In^{3+}, Ge^{4+}, Sn^{4+}) and chalcogenide anions (S^{2-}, Se^{2-}, Te^{2-}).[5-13] Many of the resulting open-framework covalent superlattices are built up from corner-shared supertetrahedral clusters (denoted as Tn clusters, where *n* is the number of metal sites on each edge of the cluster).[11h] These previous studies on supertetrahedral clusters were mostly focused on the metal sulfide

composition. In comparison with sulfides, the metal selenide Tn clusters have received less attention or their synthesis has been far less successful.[12]

The use of doping to tune electronic structures is a well-established method that has been successfully used for many years, usually for dense phase solid materials.[14-16] In general, the distribution of metal and non-metal dopants in the crystal lattice is random. As the trend towards the use of semiconductor nanoparticles accelerates and as the applications of porous materials becomes more widespread, chalcogenide clusters and open frameworks have become the focus of studies by many researchers.[8-13] In addition to chemical compositions, these cluster-based open framework materials provide an additional level of control over the electronic properties through their varying degree of porosity and patterns of spatial assemblies between clusters. To further control the electronic properties of these materials, it is useful to also study the doping chemistry in these cluster-based open framework materials.

In this work, we aim to study how the compositions, structures, and electronic properties can be controlled by the combined amine-templating, Sn- and S-doping in the Zn-Ga-Se system. The selection of Sn(IV) and S has distinct advantages in providing tunable framework charge density because Sn(IV) decreases the overall negative charge of the cluster and increase the cluster size, while S decreases the cluster size. Furthermore, because Sn-doping into Ga site generally causes a red shift while S-doping into Se sites causes a blue shift, this doping strategy allows a large range of band gaps to be achieved. By changing the amine type and doping strategy (no doping, Sn-doping only, S-doping only, and dual Sn- and S-doping), we have investigated a large number of synthetic

systems (for each amine type, there are four different doping permutations). Here we report a series of selenide compounds composed of T4 cluster and amine templates. These compounds are collectively named as OCF-*n*-composition-template (OCF = organically-directed-chalcogenide frameworks, and *n* designates a specific framework topology, Table 6.1). Multi-component supertetrahedral T4 clusters, such as ternary (T4-ZnGaSe), quaternary (T4-ZnGaSeS and T4-ZnGaSnSe) and pentanary (T4-ZnGaSnSeS), have been systematically synthesized and their optical properties investigated. Of particular interests are (1) the subtle control of different framework topologies via host-guest interactions tunable via Sn- and S-doping, (2) different Sn- and S-doping levels at different crystallographic sites and in materials with different topologies, (3) site selective distribution of metal ions and non-metal ions, and (4) effects of these tunable compositional and structural features on the electronic properties.

Table 6.1. Summary of crystal data and refinement results. [a]

Name	Framework Composition	S. G.	*a* (Å)	*c* (Å)	*R*(F)
OCF-1-ZnGaSeS-TMDP	$[Zn_4Ga_{16}Se_{33-x}S_x]$	*I*-42*d*	42.093(6)	16.690(3)	9.09
OCF-5-ZnGaSe-AEP	$[Zn_4Ga_{16}Se_{33}]$	*I*4$_1$/*acd*	23.5937(8)	42.620(3)	6.03
OCF-5-ZnGaSnSe-AEP	$[Zn_4Ga_{13.58}Sn_{2.42}Se_{33}]$	*I*4$_1$/*acd*	23.0701(4)	41.4975(13)	5.94
OCF-5-ZnGaSnSe-ECHA	$[Zn_4Ga_{16-x}Sn_xSe_{33}]$	*I*4$_1$/*acd*	24.0985(4)	42.1852(6)	/
OCF-5-ZnGaSnSe-PZ	$[Zn_4Ga_{16-x}Sn_xSe_{33}]$	*I*4$_1$/*acd*	24.1267(3)	42.2013(8)	/
OCF-5-ZnGaSnSe-MP	$[Zn_4Ga_{16-x}Sn_xSe_{33}]$	*I*4$_1$/*acd*	24.0745(2)	42.1653(5)	/
OCF-5-ZnGaSnSe-DMMP	$[Zn_4Ga_{16-x}Sn_xSe_{33}]$	*I*4$_1$/*acd*	24.1324(6)	42.1976(4)	/
OCF-5-ZnGaSnSe-TMPR	$[Zn_4Ga_{16-x}Sn_xSe_{33}]$	*I*4$_1$/*acd*	24.1687(3)	42.2724(3)	/
OCF-5-ZnGaSeS-AEP	$[Zn_4Ga_{16}Se_{16.89}S_{16.11}]$	*I*4$_1$/*acd*	22.8934(12)	41.516(4)	7.04
OCF-5-ZnGaSeS-DPM	$[Zn_4Ga_{16}Se_{20.67}S_{12.33}]$	*I*4$_1$/*acd*	23.5451(2)	41.2267(8)	5.92
OCF-5-ZnGaSnSeS-TMDP	$[Zn_4Ga_{12.93}Sn_{3.07}Se_{28.13}S_{5.01}]$	*I*4$_1$/*acd*	24.1157(2)	41.9575(6)	6.80
OCF-5-ZnGaSnSeS-DAMP	$[Zn_4Ga_{13.87}Sn_{2.13}Se_{27.67}S_{5.39}]$	*I*4$_1$/*acd*	23.7021(3)	42.1858(8)	7.44
OCF-5-ZnGaSnSeS-ECHA	$[Zn_4Ga_{13.06}Sn_{2.94}Se_{29.70}S_{3.30}]$	*I*4$_1$/*acd*	23.6724(2)	42.2660(8)	7.07
OCF-5-ZnGaSnSeS-PR	$[Zn_4Ga_{14.17}Sn_{1.83}Se_{27.57}S_{5.52}]$	*I*4$_1$/*acd*	23.5849(3)	41.8710(17)	6.39
OCF-40-ZnGaSnSeS-PR	$[Zn_4Ga_{14}Sn_2Se_{31.71}S_{3.29}]$	*I*-43*m*	18.7047(10)	18.7047(10)	3.45

[a] The elemental composition ratio in some selected good crystals is determined by structural refinement.

6.2 Experimental Section

6.2.1 Materials and General Methods

All chemicals and solvents were of reagent grade and were used as purchased without further purification. Solid-state diffuse reflectance spectra were recorded on a SHIMADZU UV-3101PC UV-VIS-NIR Scanning Spectrophotometer by using BaSO4 powder as 100% reflectance reference. Powder X-ray diffraction data were collected using a Bruker D8-Advance powder diffractometer operating at 40 kV, 40mA with Cu Kα(λ =1.5406 Å) radiation (2θ range, 2-40°; step, 0.03°; scan speed, 60 s/step). Semi-quantitative elemental analyses were performed with a Philips FEI XL30 scanning electron microscope (SEM) equipped with energy dispersive spectroscopy (EDS) detector.

6.2.2 Solvothermal Syntheses

The sulfur source and tin source used in this paper are dimethyl sulfoxide (DMSO) and anhydrous tin(II) chloride, respectively. All reactions were carried out at 200^{o}C.

Typical synthesis of quaternary sulfur-doped OCF-1-ZnGaSeS-TMDP: $Ga(NO_3)_3{\cdot}xH_2O$(255.7mg, ~1.0mmol), $Zn(NO_3)_3{\cdot}6H_2O$ (75.0mg, 0.25mmol), Se (177mg, 2.24mmol), and TMDP (4, 4'-trimethylenedipiperidine, 2.0g, 9.51mmol) were mixed with H_2O (3.0g, 166.7mmol) and dimethylsulfoxide (DMSO, 2.0g, 25.60mmol) in 23-mL Teflon-lined stainless steel autoclave and stirred for half an hour. The vessel was then sealed and heat up to 200^{o}C for 9 days. After cooling to the room temperature, a large amount of pale-yellow octahedral crystals were obtained. These raw products were then washed by water and ethanol, and dried in air for other measurement. Yield: 121.2mg.

Typical synthesis of tertiary un-doped OCF-5-ZnGaSe-AEP: $Ga(NO_3)_3{\cdot}xH_2O$(255.7mg, ~1.0mmol), $Zn(NO_3)_3{\cdot}6H_2O$ (75.0mg, 0.25mmol), Se (177mg, 2.24mmol), and AEP (N-(2-aminoethyl)piperazine, 2.5g, 19.35mmol) were mixed with H_2O (3.0g, 166.7mmol) in 23-mL Teflon-lined stainless steel autoclave and stirred for one hour. The vessel was then sealed and heat up to 200^{o}C for 9 days. After cooling to the room temperature, a large amount of pale-yellow octahedral crystals were obtained. These raw products were then washed by water and ethanol, and dried in air for other measurement. Yield: 165.3mg.

Typical synthesis of quaternary tin-doped OCF-5-ZnGaSnSe-ECHA: This compound was prepared in a synthetic procedure similar to that for OCF-5-ZnGaSe-AEP, only adding $SnCl_2$ (50.0mg, 0.264mmol) into the mixture and replacing AEP with ECHA (N-ethylcyclohexanamine, 2.5g, 19.64mmol). Yield: 119.6mg.

Typical synthesis of quaternary sulfur-doped OCF-5-ZnGaSeS-AEP: This compound was prepared in a synthetic procedure similar to that for OCF-5-ZnGaSe-AEP, only adding DMSO (2.0g, 25.60mmol) into the mixture. Yield: 135.6mg.

Typical synthesis of pentanary tin- and sulfur-doped OCF-5-ZnGaSnSeS-TMDP: This compound was prepared in a synthetic procedure similar to that for OCF-1-ZnGaSeS-TMDP, only adding $SnCl_2$ (50.0mg, 0.246mmol) into the mixture. Yield: 105.8mg.

Typical synthesis of pentanary tin- and sulfur-doped OCF-40-ZnGaSnSeS-PR: This compound was prepared in a synthetic procedure similar to that for OCF-5-

ZnGaSnSeS-TMDP, only replacing TMDP with piperidine (PR, 2.5g, 29.36mmol) and decreasing DMSO to 1.0g. Yield: 128.9mg.

6.2.3 Single-Crystal X-ray Crystallography Studies

Single-crystal X-ray analysis was performed on a Bruker Smart APEX II CCD area diffractometer with nitrogen-flow temperature controller using graphite-monochromated $Mo_{K\alpha}$ radiation (λ = 0.71073 Å), operating in the ω and φ scan mode with a scan width of 0.5°. Raw data collection was done at 150K. Data reduction was performed using SAINT^{+}. The SADABS program was used for absorption correction. The structure was solved by direct methods and the structure refinements were based on $|F^2|$. All non-hydrogen atoms were refined with anisotropic displacement parameters. Extra-framework organic amine molecules in OCF-1 and OCF-5 series of structures can not be located owing to their disorder, which is the case in nearly all 3-D structures constructed from chalcogenide clusters. For molecular OCF-40, amine molecules are ordered and hydrogen atoms were placed in calculated positions. All crystallographic calculations were conducted with the SHELXTL software suites. Three constraint instructions (EXYZ, EADP, and SUMP) were used to refine relative occupancy factors of the mixed Sn/Ga sites and mixed Se/S sites.

Chemical compositions are determined by crystallographic refinements and are further confirmed by EDAX. (Figure 6.1) and their phase purity is supported by power X-ray diffraction (PXRD) (Figure 6.2).

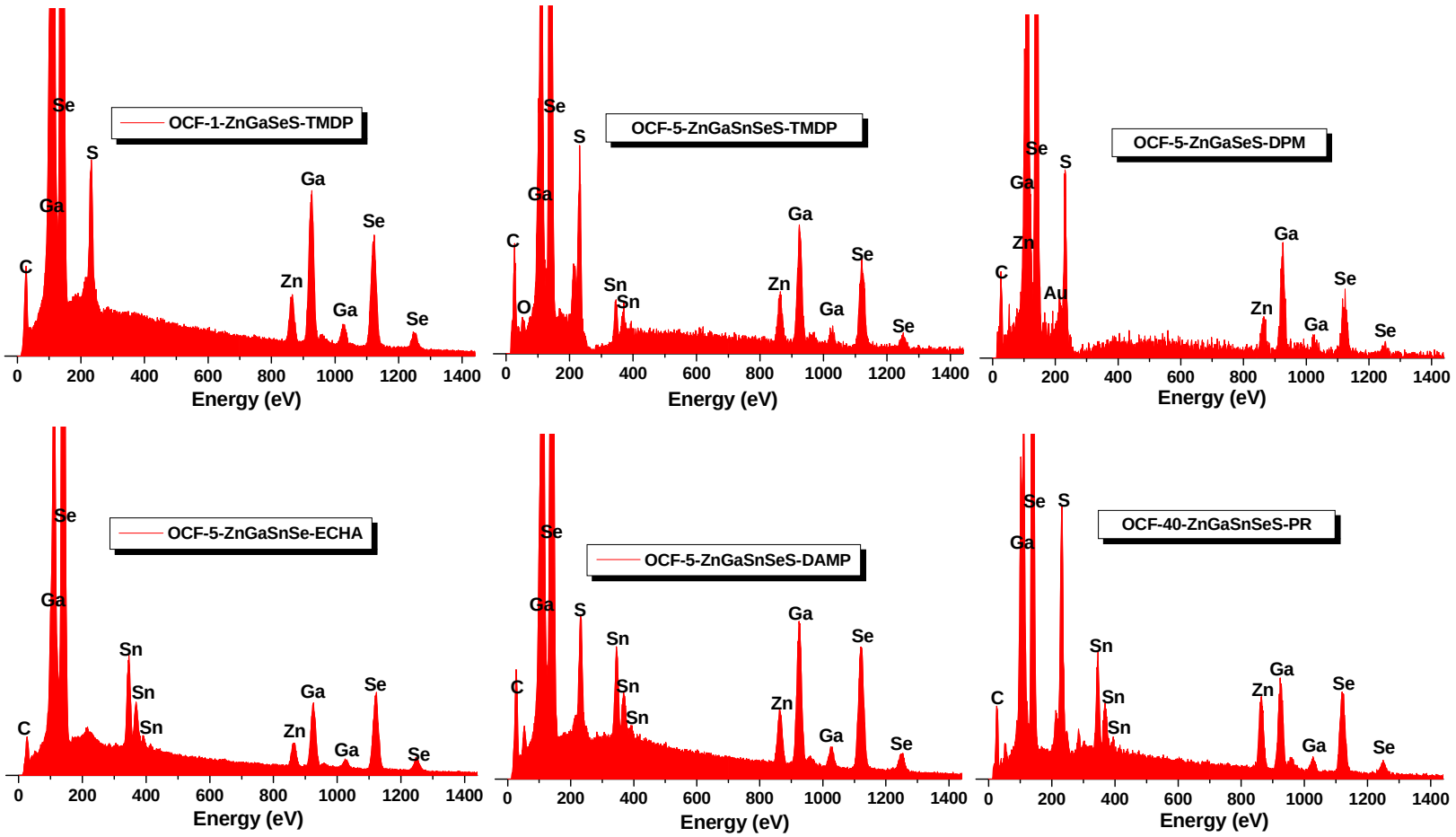


Figure 6.1. The energy dispersive X-ray (EDAX) spectroscopy of OCF-n.

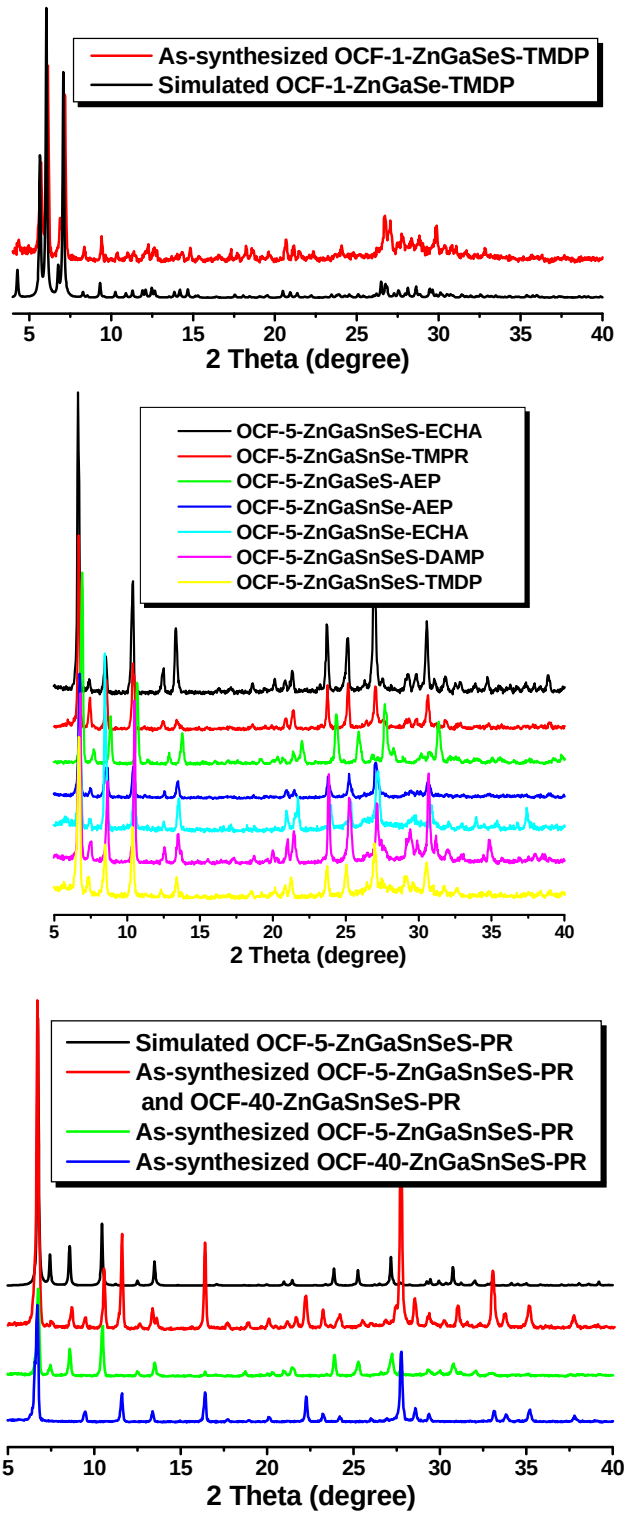


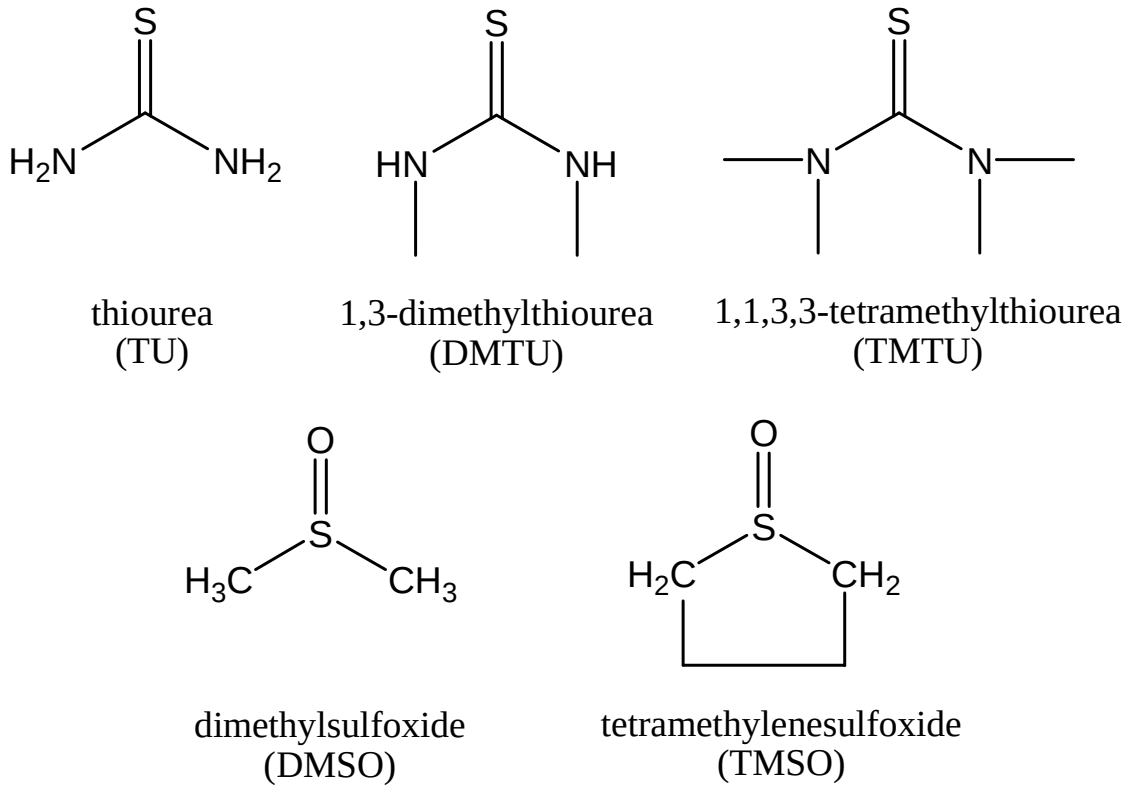
Figure 6.2. The powder X-ray diffraction patterns on OCF-1, OCF-5s and OCF-40.

6.3 Results and Discussion

6.3.1 Determination and Selection of Optimum Synthesis Parameters

The large difference in the scattering factors between Se and S (and between Ga and Sn) makes it possible to determine the site-selective distribution of Se/S and Ga/Sn among different sites in the T4 cluster. However, the low crystal quality often exhibited by crystals containing large clusters can compromise the accuracy of the crystallographic results. To ensure the reliability in the determination of occupancy factors of Se/S and Ga/Sn, the quality of crystal data is essential. For this reason, a large number of synthetic trials were performed to identify the synthetic conditions for growing high quality crystals. All the data used for occupancy refinement reported here are based on the high quality diffraction data.

Although both Sn element and anhydrous tin(II) chloride allow the introduction of tin(IV) (through oxidation by Se) into Zn-Ga-Se compounds, tin(II) chloride is the preferred tin source, because metal tin usually gives poor-quality crystals, contaminated with inseparable impurities. Sulfur element was initially used as the sulfur doping reagent. While the doping of sulfur in T4 cluster was confirmed by the energy dispersive X-ray (EDAX) spectroscopy, poor crystal quality prevents the precise determination of the site distribution within the crystal. Dimethyl sulfoxide (DMSO) was later proved to be a good sulfur doping source for preparing sulfur-doped metal selenides with good crystal quality. In addition to DMSO, a number of other sulfoxide and thiourea reagents (Scheme 6.1), were also investigated as the sulfur source, but none forms crystals of sufficient quality for occupancy refinements.



Scheme 6.1. The structure of thiourea and sulfone molecules with different substituent groups used as sulfur sources.

Obviously, the doping level of sulfur in metal selenides can be tuned by adjusting the amount of DMSO. A low amount of DMSO may cause the co-existence of undoped T4-ZnGaSe and slightly-doped T4-ZnGaSeS cluster in the same framework. The low doping level makes it difficult to determine the sulfur distribution in the T4 cluster through crystallographic refinement. Since we are interested in chemical and structural factors that control the maximum possible doping level, all reactions in this work use an excess amount of sulfur source (typically, the molar ratio of Se *vs* DMSO is 1:~10). In addition, the Sn/Zn molar ratio is limited to about 1 because experiments have shown that

higher ratios led to the formation of UCR-20-SnGaSeS[12a]. Because of the heterogeneous nature of the reactants, a high temperature of 200^{o}C is employed.

Finally, the type of organic amines plays a key role in the final composition and topology of the framework. To examine effects of the amine-type on T4 clusters with different framework compositions (such as undoped T4-ZnGaSe, sulfur-doped T4-ZnGaSeS, tin-doped T4-ZnGaSnSe, and sulfur- and tin-doped T4-ZnGaSnSeS), a systematic study has been performed by using different amines (Scheme 6.2) with and without the addition of the sulfur and tin sources.

6.3.2 Cluster and Crystal Structures

In a typical un-doped T4 [$Zn_4Ga_{16}Se_{35}$] cluster, there are 18 bi-coordinated Se^{2-} sites on six edges, 12 tri-coordinated Se^{2-} ions on four faces, and one tetrahedral Se^{2-} at the core of T4, and the four terminal Se^{2-} ions. To satisfy Pauling's electrostatic valence rule, the core Se^{2-} site is surrounded by four zinc ions to give a bond valence sum of +2. All the structures in this work (OCF-1, OCF-5, and OCF-40) are based on this type of T4 cluster [12c, 12e]. OCF-40 is a molecular crystal consisting of isolated T4 clusters surrounded by protonated amine templates. However, both OCF-1 and OCF-5 have 3-D framework structures formed though corner-sharing T4 clusters, and they have different framework topologies, as shown in Figure 6.3. By treating each T4 cluster as a pseudo-tetrahedral atom, OCF-1 has the non-interpenetrating 3-D four-connected network, while OCF-5 has two-fold interpenetrating diamond topology. Table 6.1 consists of a series of OCF-5 phases, each possessing some unique aspects, such as new amine type and cluster composition.

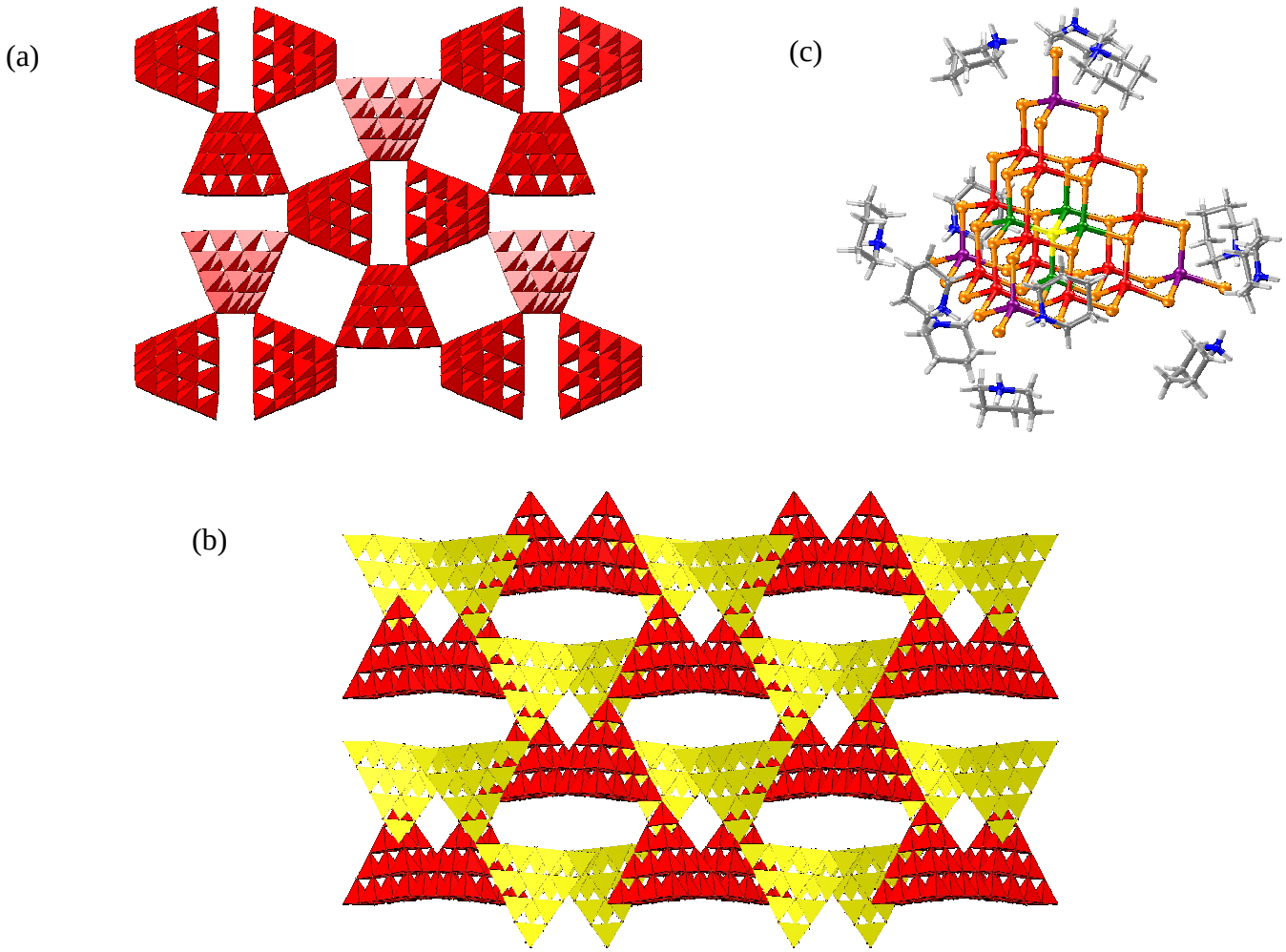
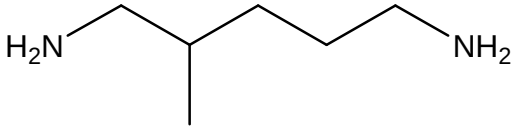
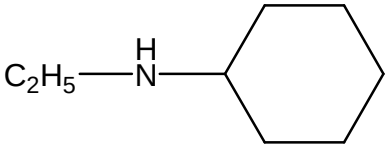


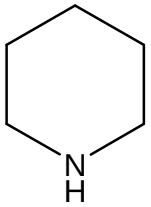
Figure 6.3. The structures of OCF-1 (a), OCF-5 (b) and OCF-40 (c). The disordered amine template molecules in OCF-1 and OCF-5 are omitted for clarity. Red spheres stand for Ga, yellow for S, green for Zn, purple for Sn/Ga, orange for Se/S.



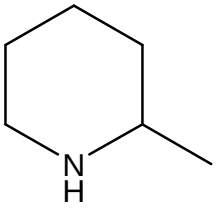
1, 5-diamino-2-methylpentane
(DAMP)



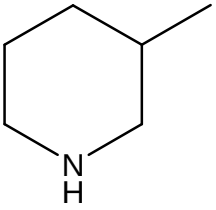
N-ethylcyclohexanamine
(ECHA)



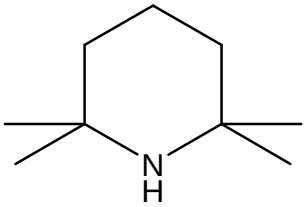
piperidine
(PR)



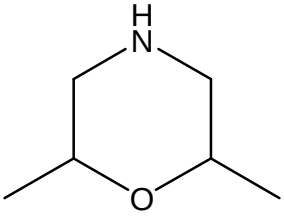
2-methylpiperidine
(2-MPR)



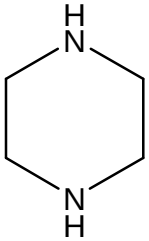
3-methylpiperidine
(3-MPR)



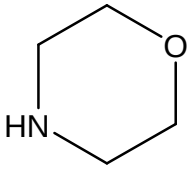
2,2,6,6-tetramethylpiperidine
(TMPR)



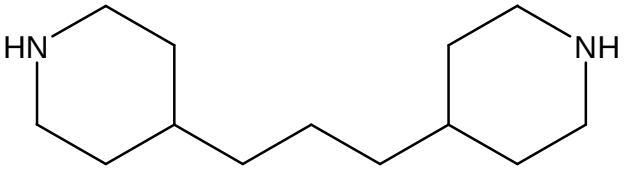
2,6-dimethylmorpholine
(DMMP)



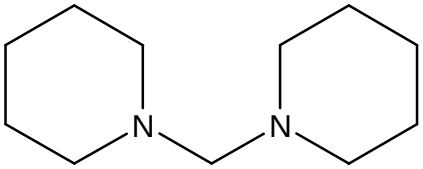
piperazine
(PZ)



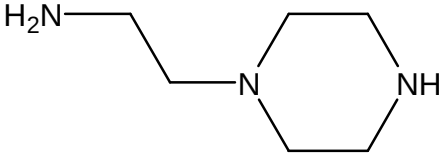
morpholine
(MP)



4, 4'-trimethylenedipiperdine
(TMDP)



dipiperidinomethane
(DPM)



N-(2-aminoethyl)piperazine
(AEP)

Scheme 6.2. The name (including abbreviation) and structure of amine templates.

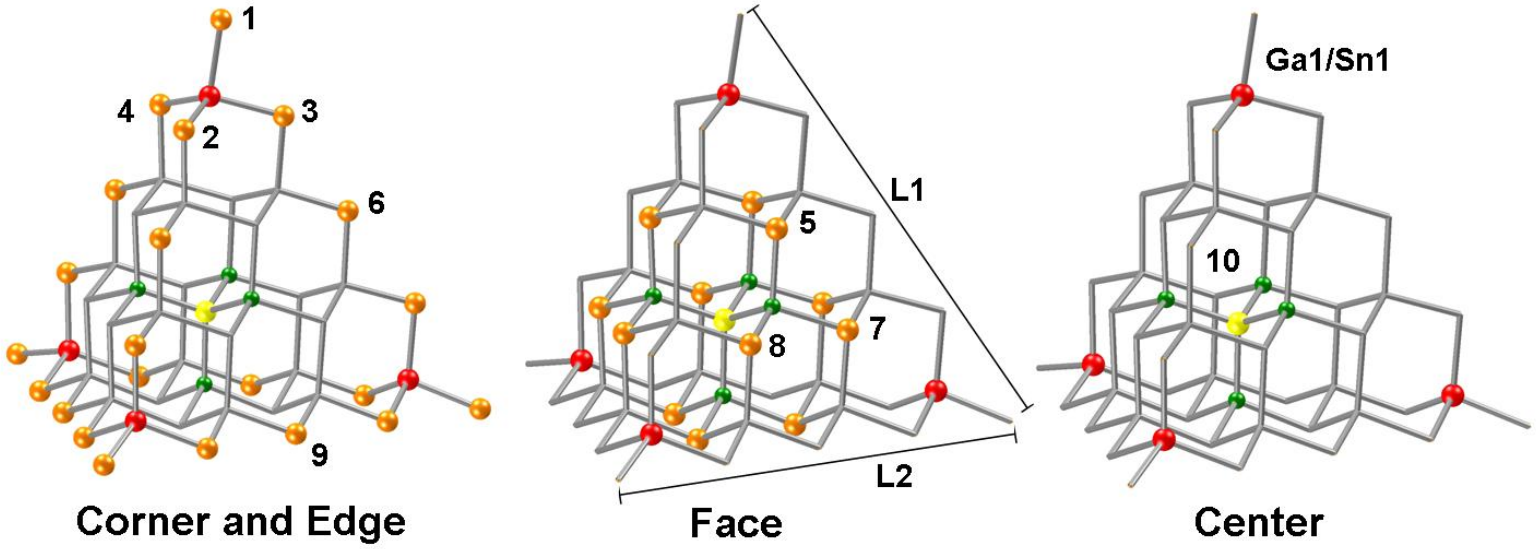


Figure 6.4. The labelling scheme for various Se^{2-} or S^{2-} sites in the T4 supertetrahedral cluster. The green spheres stand for Zn^{2+}, red for Ga^{3+}/Sn^{4+}, yellow for S^{2-}, orange for Se^{2-}/S^{2-}. L1 and L2 indicate the edge distance.

Table 6.2. The refined occupancy factors of Ga/Sn and Se/S in OCF-5-ZnGaSnSeS-TMDP and OCF-5-ZnGaSnSeS-DAMP at various crystallographic sites with T4 clusters.

Crystal		Position Occupancy Between Se and S										
		Ga1/Sn1	Se1/S1	Se2/S2	Se3/S3	Se4/S4	Se5/S5	Se6/S6	Se7/S7	Se8/S8	Se9/S9	Se10/S10
TMDP	Batch 1	0.27108/ 0.72892	1.00021/ -0.00013	0.93875/ 0.06124	0.90794/ 0.09205	0.96855/ 0.03144	0.80725/ 0.19276	0.95363/ 0.04636	0.73756/ 0.26244	0.70643/ 0.29358	0.97258/ 0.02743	0.00853 / 0.99144
	Batch 2	0.23172/ 0.76829	1.03378/- 0.03377	0.93606/ 0.06394	0.90514/ 0.09485	0.95784/ 0.04215	0.81735/ 0.18267	0.95674/ 0.04327	0.74483/ 0.25517	0.71896/ 0.28104	0.95390/ 0.04610	0.00390/ 0.99609
	Batch 3	0.22650/ 0.77353	1.00027/ -0.00017	0.94810/ 0.05188	0.90033/ 0.09963	0.94828/ 0.05176	0.80801/ 0.19200	0.96635/ 0.03368	0.74684/ 0.25313	0.72822/ 0.27176	0.96760/ 0.03242	0.00078/ 0.99920
DAMP	Batch 1	0.46808/ 0.53192	1.01501/ -0.01501	0.90722/ 0.09278	0.87416/ 0.12583	0.93302/ 0.06699	0.77301/ 0.22700	0.96795/ 0.03206	0.74809/ 0.25191	0.72047/ 0.27953	0.96889/ 0.03111	0.00511/ 0.99488
	Batch 2	0.49967/ 0.50033	0.98540/ 0.01461	0.90224/ 0.09775	0.82651/ 0.17348	0.86948/ 0.13051	0.78870/ 0.21131	0.96103/ 0.03897	0.78580/ 0.21420	0.74828/ 0.25172	0.98617/ 0.01383	0.00584/ 0.99414
	Batch 3	0.47656/ 0.52343	1.01320/ -0.01318	0.89566/ 0.10431	0.86174/ 0.13824	0.91584/ 0.08414	0.77558/ 0.22443	0.97172/ 0.02831	0.75356/ 0.24643	0.73777/ 0.26222	0.97244/ 0.02756	0.00424/ 0.99574

Table 6.3. The refined occupancy factors of Se/S and Ga/Sn in select OCF-n at various crystallographic sites with T4 clusters.

Compounds	Position Occupancy Between Se and S										
	Ga1/Sn1	Se1/S1	Se2/S2	Se3/S3	Se4/S4	Se5/S5	Se6/S6	Se7/S7	Se8/S8	Se9/S9	Se10/S10
OCF-5-ZnGaSe-AEP	0.97712/ 0.02279	1.00614/- 0.00572	0.99829/ 0.00160	1.00173/- 0.00159	0.97324/ 0.02659	0.96672/ 0.03341	1.00500/- 0.00433	1.00049/- 0.00061	1.00099/- 0.00110	1.00095/- 0.00095	0.96498/ 0.03502
OCF-5-ZnGaSnSe-2-MPR	0.53279/ 0.46701	1.00030/ -0.00018	0.93759/ 0.06247	0.92535/ 0.07436	0.95530/ 0.04464	0.94763/ 0.05247	0.99973/ 0.00042	0.95552/ 0.04430	0.94978/ 0.05034	0.97590/ 0.02403	0.96790/ 0.03212
OCF-5-ZnGaSnSe-3-MPR	0.52924/ 0.47128	1.00017/ -0.00010	0.93761/ 0.06237	0.92595/ 0.07407	0.95463/ 0.04530	0.94879/ 0.05132	0.99943/ 0.00053	0.95565/ 0.04436	0.94912/ 0.05082	0.97620/ 0.02382	0.96655/ 0.03335
OCF-5-ZnGaSeS-AEP	0.96331/ 0.03670	0.66814/ 0.33187	0.55827/ 0.44173	0.59762/ 0.40238	0.52932/ 0.47067	0.37655/ 0.62344	0.77252/ 0.22750	0.41888/ 0.58114	0.35519/ 0.64480	0.73872/ 0.26128	0.00484/ 0.99515
OCF-5-ZnGaSeS-DPM	0.99592/ 0.00415	0.81754/ 0.18249	0.69128/ 0.30865	0.67769/ 0.32226	0.72125/ 0.27869	0.46558/ 0.53454	0.85722/ 0.14272	0.48110/ 0.51889	0.43253/ 0.56743	0.86581/ 0.13420	0.00006/ 0.99985
OCF-5-ZnGaSnSeS-ECHA	0.26530/ 0.73467	0.99987/ 0.00014	0.91915/ 0.08080	0.89542/ 0.10457	0.93166/ 0.06824	0.81132/ 0.18871	0.98431/ 0.01578	0.76170/ 0.23807	0.74781/ 0.25189	1.00031/ -0.00020	0.01811/ 0.98278
OCF-5-ZnGaSnSeS-PR	0.54242/ 0.45824	1.00118/ -0.00093	0.89507/ 0.10475	0.88077/ 0.11895	0.91571/ 0.08423	0.73406/ 0.26554	0.99074/ 0.00926	0.75240/ 0.24707	0.71630/ 0.28333	0.96298/ 0.03717	0.03447/ 0.96554
OCF-40-ZnGaSnSeS-PR	0.50346/ 0.48654	0.91855/ 0.08146	0.97970/ 0.02027	0.97970/ 0.02027	0.97970/ 0.02027	0.89230/ 0.10777	0.88395/ 0.11605	0.89230/ 0.10777	0.89230/ 0.10777	0.88395/ 0.11605	0.26824/ 0.73178

6.3.3 Site Selective Distribution of S and Sn in Zn-Ga-Se-based T4 Cluster

To conveniently describe the site-selective distribution of Se/S in the T4 cluster, all the Se^{2-} sites are labeled as shown in Figure 6.4. For doping by Sn, the situation is simpler, because both crystallographic refinements and consideration of bond valence indicate that dopant Sn^{4+} ions will occupy the corner metal sites. The refined occupancy factors for corner metal Sn/Ga and anionic Se/S sites are listed in Tables 6.2 & 6.3. As discussed below, the site-selective distribution of Se/S and Ga/Sn is dictated by chemical and structural factors. Samples synthesized from different batches show the consistent pattern of distribution within the experimental errors, as demonstrated by the analysis of three randomly selected crystals for both dual-doped OCF-5-ZnGaSnSeS-TMDP and OCF-5-ZnGaSnSeS-DAMP (Table 6.2). The reliability of occupancy refinement was supported by "control experiments" in which Se/S and Ga/Sn ratios are refined for samples made without Sn and/or S-doping. For example, for OCF-5-ZnGaSe-AEP obtained with neither Sn nor DMSO, the occupancy refinement gives the ratio of Sn/Ga close to 0:1 and the ratio of Se/S near 1:0.

In OCF-5-ZnGaSnSeS-TMDP with dual Sn- and S-doping, nearly 75% of Ga at the corner site is replaced by tin(IV). For anionic sites, sulfur doping occurs primarily at the core site (position 10, nearly 100% replacement) and at twelve face sites (positions 5, 7, 8, about 25%), while other sites remain relatively free from sulfur-doping. OCF-5-ZnGaSnSeS-ECHA has a similar doping pattern.

The doping pattern in dual-doped OCF-5-ZnGaSnSeS-DAMP is somewhat similar to that in OCF-5-ZnGaSnSeS-TMDP with two main differences: (1) a smaller

degree of doping by Sn (about 50% of Ga) at the corner site is observed; and (2) a greater degree of doping by sulfur at near-corner edge sites (positions 2, 3, 4). OCF-5-ZnGaSnSeS-PR has a similar doping pattern as OCF-5-ZnGaSnSeS-DAMP.

For sulfur-only-doped OCF-5-ZnGaSeS-AEP and OCF-5-ZnGaSeS-DMP (no Sn at corner sites!), the core site (position 10) is also completely replaced by S^{2-}, as in Sn and S dual-doped samples. However, the sulfur-doping level at other positions is obviously different from that in dual-doped OCF-5-ZnGaSnSeS. The sulfur-doping level at facial sites (positions 5, 7, 8) is greater than that in dual-doped OCF-5-ZnGaSnSeS-TMDP. Furthermore, even the corner (position 1) and edge sites (position 2, 3, 4, 6, 9) are partially doped by S^{2-}.

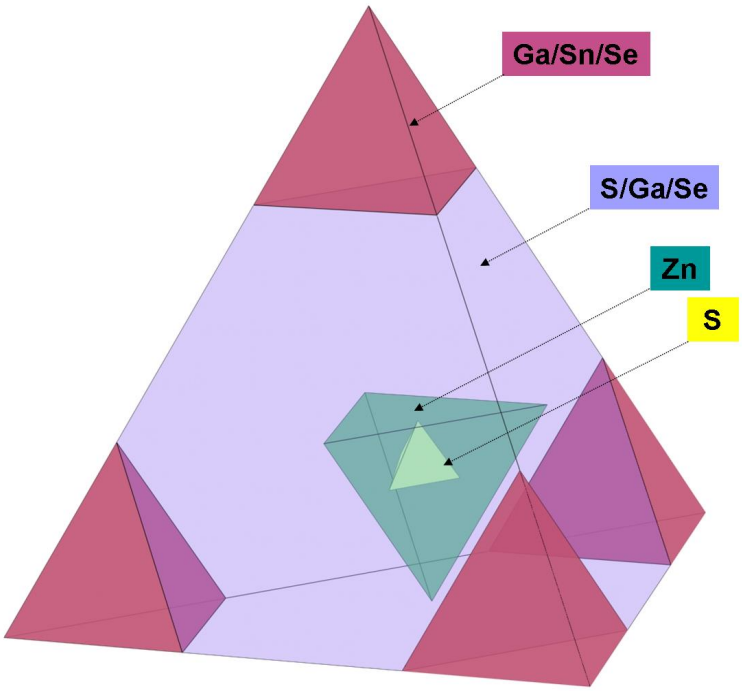


Figure 6.5. Illustration of selective elemental distribution in pentanary T4-ZnGaSnSeS cluster in OCF-5-ZnGaSnSeS-TMDP.

All the above observed doping behavior can be rationalized by a combination of Pauling's valence sum rule and Pearson's hard and soft acid base (HSAB) theory. First, the valence sum rule requires that four Zn^{2+} sites should surround the core Se^{2-} (or S^{2-} after doping) site in the middle of T4 cluster and that high-valent Sn^{4+} sites should occupy the corner sites. Such a distribution of Zn^{2+} and Sn^{4+} then dictate the distribution of Se and S on the basis of HSAB theory. Sulfur prefers to occupy sites adjacent to Zn^{2+}, while selenium favors the sites closer to Sn^{4+} (Figure 6.5). In the un-doped Zn-Ga-Se sample, the coordination environment of the core Se^{2-} site and twelve facial sites are Zn_4Se and $ZnGa_2Se$, respectively. As a result, the core site Se^{2-} is most easily replaced by S^{2-}, while partial Se^{2-} replacement by S^{2-} occurs at facial sites. It is particularly worth noting that the doping by Sn^{4+} suppresses the doping by sulfur. For example, in OCF-5-ZnGaSeS without Sn^{4+}, an average of approximately 50% of all Se sites is replaced by sulfur. In comparison, in Sn^{4+}-containing OCF-5-ZnGaSnSeS-TMDP, only an average of about 15% of Se sites are replaced by sulfur.

6.3.4 Effects of Amine-Type on Sn- and S-Doping and on Size and Charge of T4 cluster

From the above, it is clear that the level of Sn^{4+}-doping, to a large degree, determines the level of S-doping in the Zn-Ga-Se system, in the reverse relationship. How is the level of Sn^{4+} doping controlled? The answer lies in the fundamental difference between Sn-doping and S-doping: the Sn-doping reduced the negative charge of the cluster while the S-doping has no effect on the charge of the cluster. Because Sn-doped clusters have a lower charge, it is therefore favored by organic amines with a low charge

density based on the concept of the global (i.e., host-guest) charge-density matching. For this reason, protonated amine molecules such as TMDP (the C/N ratio 6.5) and ECHA (the C/N ratio 8) induce more tin doping at corner metal sites than DAMP (the C/N ratio 3) and PR (the C/N ratio 5) (The use of the C/N is only a rough estimate of the charge density of protonated amines; other factors such as molecular shape can also be relevant). In the present study, we have achieved two different ratios (i.e., 1:1 and 3:1) of Sn/Ga at corner sites are, corresponding to $[Zn_4Ga_{14}Sn_2Se_{33}]^{8-}$ and $[Zn_4Ga_{13}Sn_3Se_{33}]^{7-}$, respectively. Thus, organic amines control the level of Sn-doping through host-guest charge density matching, which in turn controls the S-doping through the HSAB principle.

Table 6.4. Summary of M-Q (M = Zn, Ga, Sn; Q = S, Se) bond lengths.

Bond length (Å)	Zn	Ga	Sn
S	2.306-2.315	2.225-2.324	2.390-2.449
Se	2.399-2.438	2.369-2.424	2.421-2.562

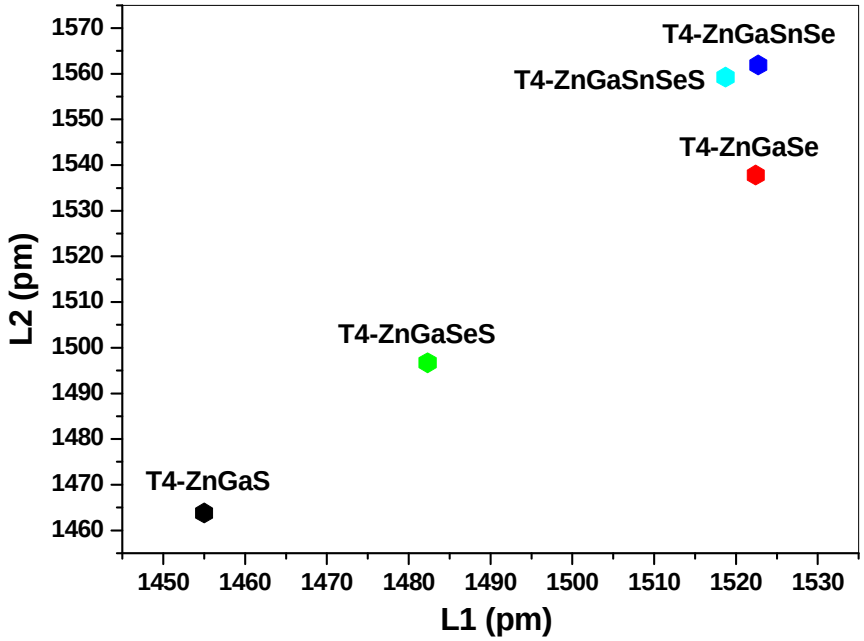
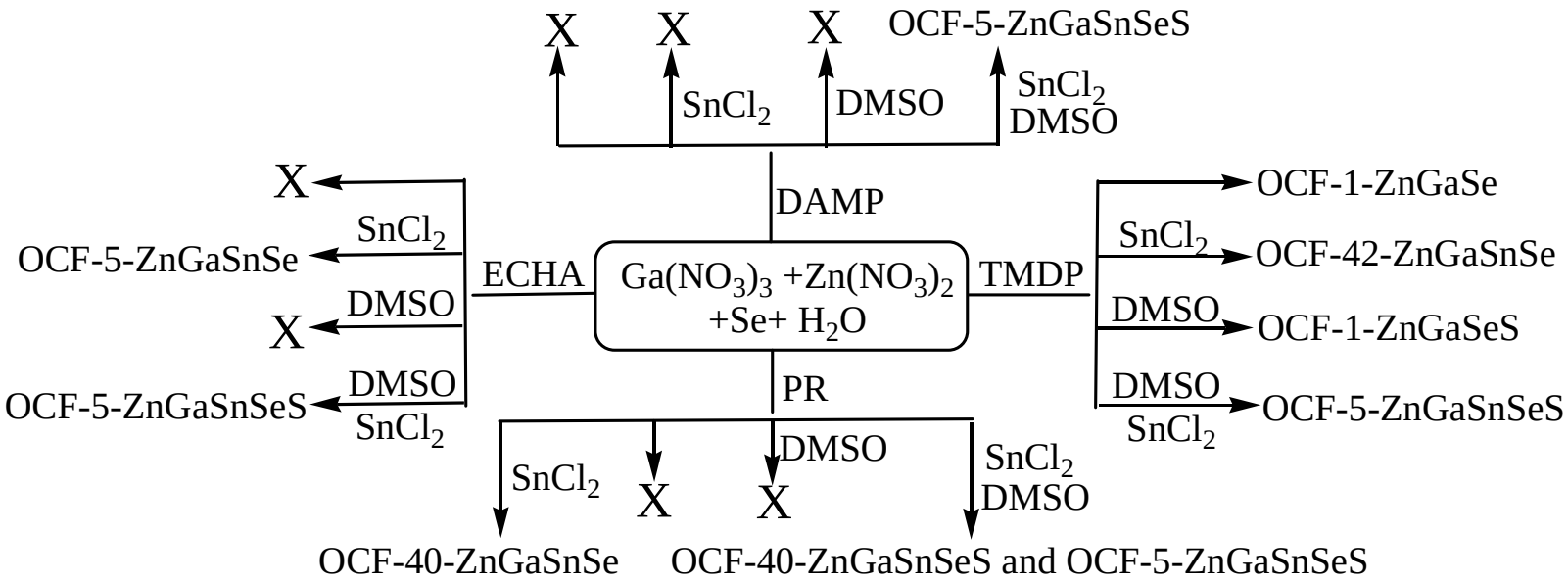


Figure 6.6. The size of five types of T4 clusters in OCF-5. The definition of L1 and L2 is shown in figure 6.4.

The Sn- and S-doping induce a systematic change in unit cell dimensions, as seen in OCF-5s (Table 6.1). In essence, it is the size of T4 clusters (and inter-cluster cavities) that is altered by doping (Figure 6.4). As expected from ionic radii (Se vs. S, and Ga vs. Sn) and related bond distances (Table 6.4), the size of the cluster increases with the doping level of Sn and decreases with the level of sulfur (Figure 6.6). Thus, T4-ZnGaSeS cluster is smaller than T4-ZnGaSe cluster, while T4-ZnGaSnSe cluster is larger than T4-ZnGaSe cluster. The dual-doping with Sn and S has two opposite effect on the cluster size. Thus the size of T4-ZnGaSnSeS cluster lies between those of T4-ZnGaSnSe and T4-ZnGaSeS clusters. It is worth emphasizing that a minor change in the dimension of clusters is sometimes essential for achieving host-guest charge-density matching needed for crystallization and can also lead to a different framework topology, as discussed below.

6.3.5 Phase Selectivity Controlled by Amine-Type, Sn- and S-Doping

Because amine-type, Sn- and S-doping can be individually changed when preparing reactant mixtures, it is possible to achieve synthetic controls using any of these three factors. Scheme 6.3 summarizes the effects of Sn- and S-doping when four different types of amines are used. ECHA and DAMP represent the simplest case, as both give OCF-5 only. The difference is that DAMP gives OCF-5-ZnGaSnSeS-DAMP only through dual Sn- and S-dopings where ECHA can form OCF-5 with either single Sn-doping or with dual doping. Other reaction conditions (e.g., no doping, or no Sn-doping) results in no crystallization. Thus for both ECHA and DAMP, the incorporation of Sn is essential for crystallization.



Scheme 6.3. Schematic of reactions in presence of different amine templates and auxiliary reactants. X means no crystalline products are obtained.

Piperidine (PR) is similar to DAMP and ECHA, in a sense that Sn is required for crystallization. However, the product is quite different and involves two different phases (OCF-40 and OCF-5). With no or small amount of DMSO, OCF-40-ZnGaSnSe is the only product. However, as more DMSO is added, a mixture of OCF-40-ZnGaSnSeS-PR (minor phase) and OCF-5-ZnGaSnSeS-PR (major phase) is obtained.

TMDP is more versatile and can generate three different phases (OCF-1, OCF-5, and OCF-42) (Scheme 3). As long as Sn is absent, the product is OCF-1-ZnGaSe-TMDP (without Sn, DMSO causes S-doping in OCF-1, but does not affect the framework topology). When only Sn (no DMSO) is added, a totally different structure containing both T2 and T4 clusters, OCF-42-ZnGaSnSe-TMDP, is formed. Finally, like other three amines, OCF-5-ZnGaSnSeS-TMDP is formed with dual-doping.

The correlation between the doping strategy and the structure type can be summarized as the following. In the absence of any doping or with only S-doping, OCF-1 is obtained with TMDP (no crystallization with other amines). With both Sn- and S-doping, OCF-5 is obtained (for all four amine types). The most sensitive phase selectivity by amines come when only Sn-doping is used, resulting in three different phases, OCF-5 (for ECHA), OCF-40 (for PR), and OCF-42 (for TMDP).

6.3.6 Effects of Cluster Size and Charge on the Phase Selectivity

The above observed phase selectivity reveals important factors that control the crystallization of chalcogenide clusters. For a particular phase to crystallize, organic amine molecules need to possess proper charge, size and shape for matching with the charge of the cluster and size of the inter-cluster cavity, the latter is dependent on the Sn-

and S-doping. This concept is denoted as the global charge density matching. Given a particular amine, the synthetic system endowed with more ways to tune its framework charge density is more likely to find a way to crystallize, which is easily proved by Scheme 6.3.

Scheme 6.3 shows a total of 16 synthetic paths. With no doping and minimum flexibility in charge density tuning, only 1 out 4 paths leads to crystallization. The S-doping only slightly reduces the cluster size, but does not alter the charge of the cluster. It is not surprising that only 1 out 4 paths leads to crystallization. The Sn-only doping provides the flexibility to alter both charge and size of the cluster, which provides a greater freedom in the charge density tuning. As a result, 3 out 4 paths lead to crystallization. The greatest flexibility comes from the combined S- and Sn-doping, which leads the crystallization in 4 out of 4 paths.

It is worth noting that while the size reduction caused by S-doping is in itself not adequate for the phase selectivity, it does exhibit a controlling effect when used in combination with Sn-doping. For example, Sn-only-doped OCF-5-ZnGaSnSe-TMDP can not be made, possibly because protonated TMDP does not match with $[Zn_4Ga_{13}Sn_3Se_{33}]^{7-}$ to generate OCF-5-ZnGaSnSe-TMDP. However, TMDP does match the S- and Sn-dual-doped size-shrunken $[Zn_4Ga_{13}Sn_3Se_{33-x}S_x]^{7-}$ T4 cluster to form OCF-5-ZnGaSnSeS-TMDP. The same is true for OCF-5-ZnGaSnSeS-DAMP and OCF-5-ZnFaSnSeS-PR, both of which require dual S- and Sn-doping.

OCF-42-ZnGaSnSe, made by TMDP and the only Sn-doping, reveals another way to realize the global charge density matching. It is composed of Sn-doped $[Sn_{1.6}Ga_{2.4}Se_8]$

T2 cluster and undoped $[Zn_4Ga_{16}Se_{33}]^{10-}$ T4 cluster, instead of Sn-doped T4 $[Zn_4Ga_{13}Sn_3Se_{33}]^{7-}$ cluster seen in OCF-5. Why isn't T4 cluster doped with Sn? Clearly, the charge of Sn-doped $[Zn_4Ga_{13}Sn_3Se_{33}]^{7-}$ T4 cluster in combination with T2 cluster does not match with protonated TMDP, which only matches the more negative $[Zn_4Ga_{16}Se_{33}]^{10-}$ T4 cluster and T2 clusters to form OCF-42-ZnGaSnSe-TMDP.

The synthesis of OCF-40 using piperidine has an unusual feature not found in other amine-templated systems. This feature is that OCF-40 can accept a very limited amount of the S-doping and an increased amount of DMSO shifts the phase selection from OCF-40 to OCF-5. OCF-40-ZnGaSnSe-PR is composed of isolated Sn-doped $[Zn_4Ga_{14}Sn_2Se_{35}]^{12-}$ cluster and piperidinium. Twenty four piperidinium ions compactly cover the surface the T4 cluster by Se…H-N hydrogen bonds. In this case, the charge balance and size match between the cluster and 24 amine cations are critical to the formation of OCF-40-ZnGaSnSe-PR. In fact, it has been found that the substituted piperidine (such as 2-MPR, 3-MPR, and 2,2,6,6-TMPR) tend to give OCF-5-ZnGaSnSe, which is because the Sn-doped $[Zn_4Ga_{14}Sn_2Se_{35}]^{12-}$ T4 cluster does not have enough surface area to accommodate these more bulky amines to form OCF-40-ZnGaSnSe.

While the Sn-doped T4 $[Zn_4Ga_{14}Sn_2Se_{35}]^{12-}$ cluster in OCF-40 can not generally accommodate amine molecules other than piperidine, it does allow a limited amount of S-doping to give somewhat smaller Sn- and S-dual doped $[Zn_4Ga_{14}Sn_2Se_{35-x}S_x]^{12-}$ T4 cluster. However, the level of S-doping in OCF-40-ZnGaSnSeS-PR, as evidenced by the sulfur occupancy factor at both core site and facial sites is much lower than that in OCF-5-ZnGaSnSeS-PR. This means that the core site in OCF-40 can not be completely

occupied by S^{2-}. As a matter of fact, OCF-40-ZnGaSnSeS-PR is the "co-crystal" of Sn-doped $[Zn_4Ga_{14}Sn_2Se_{35}]^{12-}$ T4 cluster and dual-doped $[Zn_4Ga_{14}Sn_2Se_{35-x}S_x]^{12-}$ T4 cluster. With an increased amount of $[Zn_4Ga_{14}Sn_2Se_{35-x}S_x]^{12-}$ clusters, OCF-5-ZnGaSnSeS-PR becomes the preferred framework for better matching with the protonated piperidine.

6.3.7 Optical Properties

Since optical properties (such as electronic band gaps) of solid-state semiconductors are strongly influenced by chemical compositions and crystal structures, the ability to create these multi-component chalcogenides with different structures makes it possible to achieve a wide range of band structures in these materials. In this work, the fact that Sn-doping causes a red shift while S-doping causes a blue shift (Figures 6.7-6.8) greatly boosts the range of band gaps that can be achieved (e.g., 1.54eV for Sn-doped OCF-42-ZnGaSnSe-TMDP and 3.37eV for S-doped OCF-1-ZnGaSeS-TMDP).

The synthesis of a series of framework materials (e.g., OCF-5 series) with the same framework topology, but different framework compositions provides an excellent opportunity for probing effects of chemical compositions on band structures, without the complications caused by the variation in framework topologies. As shown by Figure 6.7, the Sn-doping into the gallium leads to a red shift in the band gap, as demonstrated by undoped OCF-5-ZnGaSe-AEP (band gap, 3.23eV) and Sn-doped OCF-5-ZnGaSnSe-AEP (band gap, 2.49eV). On the other hand, S-doping causes a blue shift in the band gap, as evidenced by undoped OCF-1-ZnGaSe-TMDP (band gap, 1.71eV) and S-doped OCF-1-ZnGaSeS-TMDP (band gap, 3.37eV) (Figure 6.8). The similar S-doping effect is also

observed in Sn-doped OCF-5-ZnGaSnSe-ECHA (band gap, 2.24eV) and dual-doped OCF-5-ZnGaSnSeS-ECHA (band gap, 2.54eV) (Figure 6.9).

Because Sn-doping and S-doping have opposite effects on the band gaps, the dual-doped sample is expected to have a band gap between Sn-doped and S-doped phases. However, a complication occurs when comparing the undoped sample and the dual-doped sample, in which case the direction of the shift by the dual-doped sample would depend on which dopant (Sn or S) plays a dominant role. A comparison between undoped OCF-5-ZnGaSe-AEP (band gap, 3.23eV) and dual-doped OCF-5-ZnGaSnSeS-ECHA (band gap, 2.54eV) seems to suggest that Sn has a stronger effect than S (if the difference in the amine-type is not taken into consideration). Note that it is possible that the S-doping can cause a more dramatic shift than the Sn-doping, when each dopant is applied individually (i.e., when comparing S-doped sample with Sn-doped sample). However, in the case of dual doping by both Sn and S, the level of S-doping is suppressed (as discussed above based on the HSAB principle) by the Sn-doping, which may lead to the greater control of the band gap by Sn rather than S.

In addition to Sn- and S-doping, the nature of organic amines also affects the electronic properties. Organic amines can not only affect the topological types, but also the level of doping and distribution of dopant in different sites. Still, given the same framework structure, effects of organic amines on band structures appear to be smaller than Sn- and/or S-doping, as seen for OCF-5-ZnGaSnSeS-TMDP, OCF-5-ZnGaSnSeS-DAMP, and OCF-5-ZnGaSnSeS-ECHA (Figure 6.10).

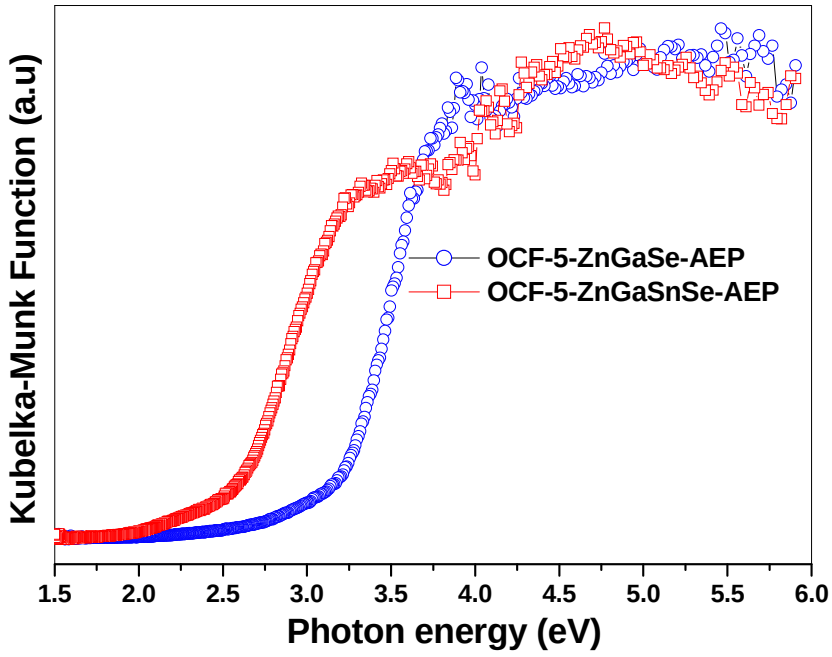


Figure 6.7. Normalized solid-state Uv-vis adsorption spectra of OCF-5-ZnGaSe-AEP and OCF-5-ZnGaSnSe-AEP, showing the red shift caused by Sn-doping.

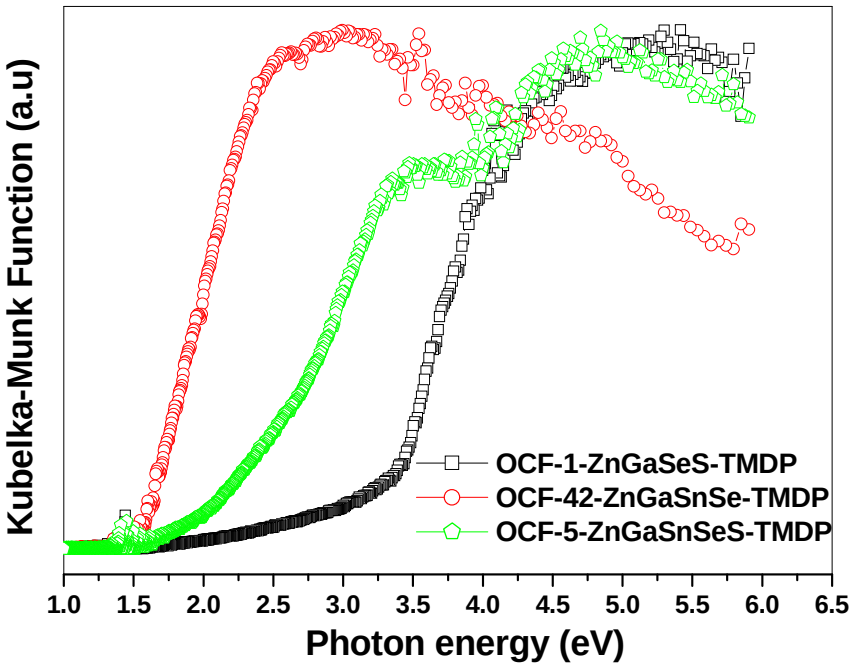


Figure 6.8. Normalized solid-state Uv-vis adsorption spectra of OCF-1-ZnGaSeS-TMDP, OCF-5-ZnGaSnSeS-TMDP and OCF-42-ZnGaSnSe-TMDP.

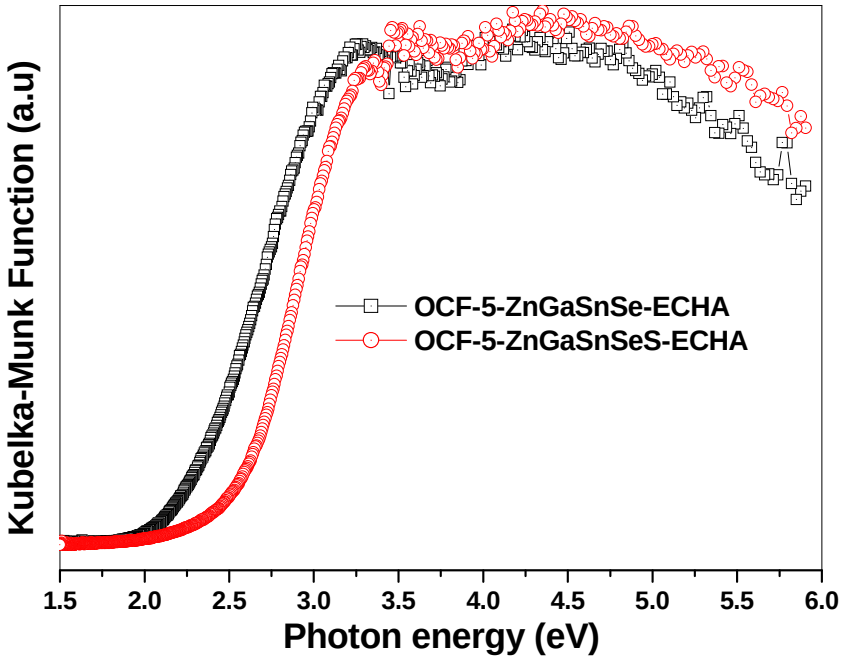


Figure 6.9. Normalized solid-state Uv-vis adsorption spectra of OCF-5-ZnGaSnSe-ECHA and OCF-5-ZnGaSnSeS-ECHA, showing the blue shift caused by S-doping.

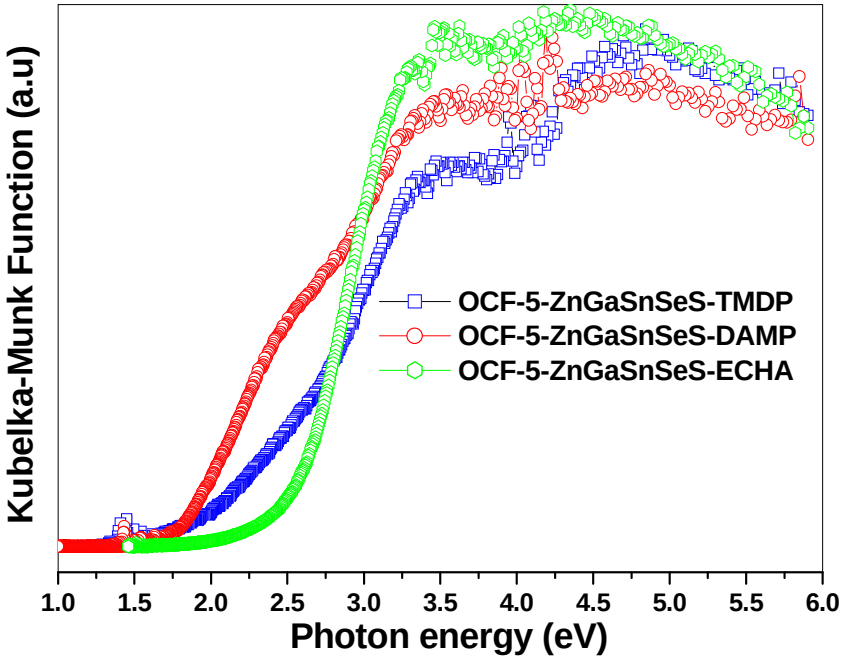


Figure 6.10. Normalized solid-state Uv-vis adsorption spectra of OCF-5-ZnGaSnSeS-TMDP, OCF-5-ZnGaSnSeS-DAMP and OCF-5-ZnGaSnSeS-ECHA.

6.4 Conclusion

We have synthesized a series of Sn- and/or S-doped open-framework covalent selenide superlattices and isolated nanoscale molecules, all of which are composed of multi-component supertetrahedral T4 cluster and protonated amine templates. It is discovered that Sn- and S-doping has a dramatic effect on the crystallization of Zn-Ga-Se clusters and frameworks, because of the extraordinarily high sensitivity of the framework formation process to the charge and size of both organic templates and the size and charge of the T4 clusters, the latter of which can be fine-tuned by Sn- and S-doping. It is demonstrated that a chemical system with the greatest flexibility in self-adjusting the cluster size and pore dimension (e.g., through the presence of metal ions such as $Sn^{4+}/Ga^{3+}/Zn^{2+}$ with comparable bonding geometry, but complementary oxidation states) is the easiest to form a crystalline framework capable of accommodating different types of template amine molecules being employed. Amines with low charge density encourage a higher level of Sn-doping because the replacement of Ga^{3+} by Sn^{4+} serves to reduce the negative charge of the cluster and framework. A high level of S-doping (up to 100% at certain sites) is possible. Yet, when co-doped with Sn^{4+}, the doping level of S can be suppressed by the Sn-doping because of the Sn's stronger affinity for Se. The highly site selective distribution of Sn within the T4 clusters is controlled by the valence sum rule while the site selective distribution of S within the T4 cluster is largely controlled by sulfur's affinity for Zn. The availability of a diversity of compositions and structures has made it possible to tune the electronic band gap over a large range from about 1.5 to 3.4eV.

6.5 References

(1) (a) Kobayakawa, K.; Teranishi, A.; Tsurumaki, T.; Sato, Y.; Fujishima, A. *Electrochim. Acta* **1992**, *37*, 465-467. (b) Lei, Z; You, W.; Liu, M.; Zhou, G.; Takata, T.; Hara, M.; Domen, K.; Li, C. *Chem. Commun.* **2003**, *17*, 2142-2143. (c) Chen, D.; Ye, J. H. *J. Phys. Chem. Solids* **2007**, *68*, 2317-2320.

(2) (a) Kanatzidis, M. G.; Huang, S. P. *Inorg. Chem.* **1989**, *28*, 4667-4669. (b) Mrotzek, A.; Kanatzidis, M. G. *Acc. Chem. Res.* **2003**, *36*, 111-119. (c) Hsu, K. F.; Loo, S.; Guo, F.; Chen, W.; Dyck, J. S.; Uher, C.; Hogan, T.; Polychroniadis, E. K.; Kanatzidis, M. G. *Science* **2004**, *303*, 818-821. (d) Arachchige, I. U.; Wu, J.; Dravid, V. P.; Kanatzidis, M. G. *Adv. Mater.* **2008**, *20*, 3638-3642. (e) Cook, B. A.; Kramer, M. J.; Harringa, J. L.; Han, M. K.; Chung, D. Y.; Kanatzidis, M. G. *Adv. Funct. Mater.* **2009**, *19*, 1254-1259.

(3) (a) Mohanan, J. L.; Brock, S. L. *J. Non-Cryst. Solids* **2004**, *350*, 1-8. (b) Mohanan, J. L.; Arachchige, I. U.; Brock, S. L. *Science,* **2005**, *307*, 397-401. (c) Mohanan, J. L.; Brock, S. L. *J. Sol-Gel. Sci. Techn.* **2006**, *40*, 341-350. (d) Brock, S. L.; Arachchige, I. U.; Kalebaila. K. K. *Comments on Inorganic Chemistry* **2006**, *27*, 103-126. (e) Yu, H.; Brock, S. L. *ACS Nano* **2008**, *2*, 1563-1570. (f) Yao, Q.; Arachchige, I. U.; Brock, S. L. *J. Am. Chem. Soc.* **2009**, *131*, 2800-2801. (g) Yao, Q.; Brock, S. L. *Nanotechnology* **2010**, *21*, 115502/1-115502/10. (h) Pawsey, S.; Kalebaila, K. K.; Moudrakovski, I.; Ripmeester, J. A.; Brock, S. L. *J. Phys. Chem. C* **2010**, *114*, 131871-3195.

(4) (a) Zheng, N.; Bu, X.; Feng, P. *Nature* **2003**, *426*, 428-432. (b) Zheng, N. ; Bu, X. ; Vu, H.; Feng, P. *Angew. Chem., Int. Ed.* **2005**, *44*, 5299-5303.

(5) (a) Zimmerman, C.; Melullis, M.; Dehnen, S. *Angew. Chem. Int. Ed.* **2002**, *41*, 4269-4271. (b) Dehnen, S.; Brandmayer, M. K. *J. Am. Chem. Soc.* **2003**, *125*, 6618-6619. (c) Zimmermann, C. ; Anson, C. E. ; Weigend, F.; Clérac, R; Dehnen, S. *Inorg. Chem.* **2005**, *44*, 5686-5695. (d) Dehnen, S.; Melullis, M. *Coord. Chem. Rev.* **2007**, *251*, 1259-1280.

(6) (a) Parise, J. B.; Tan, K. *Chem. Commun*. **1996**, 1687-1688. (b) Cahill, C. L.; Parise, J. B. *Chem. Mater*. **1997**, *9*, 807-811. (c) Cahill, C. L.; Ko, Y.; Parise, J. B. *Chem. Mater*. **1998**, *10*, 19-21. (d) Cahill, C. L.; Parise, J. B. *J. Chem. Soc., Dalton Trans.* **2000**, 1475-1482.

(7) (a) Lee, G. S. H.; Craig, D. C.; Ma, I.; Scudder, M. L.; Bailey, T. D.; Dance, I. G. *J. Am. Chem. Soc.* **1988**, *110*, 4863-4864. (b) Dance, I. G.; Fisher, K. G. *Prog. Inorg. Chem.* **1994**, *41*, 637-803. (c) Fenske, D.; Zhu, N.;

Langetepe, T. *Angew. Chem. Int. Ed.* **1998**, *37*, 2640-2644. (d) Soloviev, V. N.; Eichhofer, A.; Fenske, D.; Banin, U. *J. Am. Chem. Soc.* **2001**, *123*, 2354-2364. (e) Dehnen, S.; EichhOfer, A.; Fenske, D. *Eur. J. Inorg. Chem.* **2002**, *2*, 279-317. (f) Corrigan, J. F.; Fuhr, O.; Fenske, D. *Adv. Mater.* **2009**, *21*, 1867-1871.

(8) (a) Yaghi, O. M.; Sun, Z.; Richardson, D. A.; Groy, T. L. *J. Am. Chem. Soc.* **1994**, *116*, 807-808. (b) Li, H.; Laine, A.; O'Keeffe, M.; Yaghi, O. M. *Science* **1999**, *283*, 1145-1147. (c) Li, H.; Eddaoudi, M.; Laine, A.; O'Keeffe, M.; Yaghi, O. M. *J. Am. Chem. Soc.* **1999**, *121*, 6096-6097. (d) Li, H.; Kim, J.; Groy, T. L.; O'Keeffe, M.; Yaghi, O. M. *J. Am. Chem. Soc.* **2001**, *123*, 4867-4868. (e) Li, H.; Kim, J.; O'Keeffe, M.; Yaghi, O. M. *Angew. Chem. Int. Ed.* **2003**, *42*, 1819-1821.

(9) (a) Vaqueiro, P.; Romero, M. L. *J. Phys. Chem. Solids* **2007**, *68*, 1239-1243. (b) Vaqueiro, P.; Romero, M. L. *Chem. Commun.* **2007**, 3282-3284. (c) Vaqueiro, P.; Romero, M. L. *J. Am. Chem. Soc.* **2008**,*130,* 9630-9631. (d) Vaqueiro, P.; Romero, M. L.; Rowan, B. C.; Richards, B. S. *Chem. Eur. J.* **2010**, *16*, 4462-4465.

(10) Su, W.; Huang, X.; Li, J.; Fu, H. *J. Am. Chem. Soc.* **2002**, *124*, 12944-12945.

(11) (a) Wang, C.; Li, Y.; Bu, X.; Zheng, N.; Zivkovic, O.; Yang, C. S.; Feng, P. *J. Am. Chem. Soc.* **2001**, *123*, 11506-1507. (b) Bu, X.; Zheng, N.; Li, Y.; Feng, P. *J. Am. Chem. Soc.* **2002**, *124*, 12646-12647. (c) Wang, C.; Bu, X.; Zheng, N.; Feng, P. *Angew. Chem. Int. Ed.* **2002**, *41*, 1959-1961. (d) Zheng, N.; Bu, X.; Feng, P. *J. Am. Chem. Soc.* **2003**, *125*, 1138-1139. (e) Bu, X.; Zheng, N.; Li, Y.; Feng, P. *J. Am. Chem. Soc.* **2003**, *125*, 6024-6025. (f) Zheng, N.; Bu, X.; Feng, P. *Angew. Chem. Int. Ed.* **2004**, *43*, 4753-4755. (g) Bu, X.; Zheng, N.; Feng, P. *Chem. Eur. J.* **2004**, *10*, 3356-3362. (h) Feng, P.; Bu, X.; Zheng, N. *Acc. Chem. Res.* **2005**, *38*, 293-303. (i) Zhang, Q.; Bu, X.; Zhang, J.; Wu, T.; Feng, P. *J. Am. Chem. Soc.* **2007**, *129*, 8412-8413. (j) Zhang, Z.; Zhang, J.; Wu, T.; Bu, X.; Feng, P. *J. Am. Chem. Soc.* **2008**, *130*, 15238-15239. (k) Wang, L.; Wu, T.; Zuo, F.; Zhao, X.; Bu, X.; Wu, J.; Feng, P. *J. Am. Chem. Soc.* **2010**, *132*, 3283-3285.

(12) (a) Zheng, N.; Bu, X.; Wang, B.; Feng, P. *Science* **2002**, *298*, 2366-2369. (b) Wang, C.; Bu, X.; Zheng, N.; Feng, P. *Chem. Commun.* **2002**, 1344-1345. (c) Bu, X.; Zheng, N.; Wang, X.; Wang, B.; Feng, P. *Angew. Chem. Int. Ed.* **2004**, *43*, 1502-1505. (d) Wu, T.; Wang, X.; Bu, X.; Zhao, X.; Wang, L.; Feng, P. *Angew. Chem., Int. Ed.* **2009**, *44*, 7340-7343. (e) Wu, T.; Wang, L.; Bu, X.; Chau, V., Feng, P. *J. Am. Chem. Soc.* **2010**, *132*, 10823-10831.

(13) (a) Ding, N.; Chung, D. Y.; Kanatzidis, M. G. *Chem. Commun.* **2004**, 1170-1171. (b) Manos, M. J.; Iyer, R. G.; Quarez, E.; Liao, J. H.; Kanatzidis, M. G. *Angew. Chem. Int. Ed.* **2005**, *44*, 3552-3555. (c) Tsamourtzi, K.; Song, J. H.; Bakas, T.; Freeman, A. J.; Trikalitis, P. N.; Kanatzidis, M. G. *Inorg. Chem.* **2008**, *47*, 11920-11929. (d) Manos, M. J.; Chrissafis, K.; Kanatzidis, M. G. *J. Am. Chem. Soc.* **2006**, *128*, 8875-8883.

(14) (a) DeGroot, M. W.; Rösner, H.; Corrigan, J. F. *Chem. Eur. J.* **2006**, *12*, 1547-1554. (b) Pradhan, N.; Goorskey, D.; Thessing, J.; Peng, X. *J. Am. Chem. Soc.* **2005**, *127*, 17586-17587. (c) Pradhan, N.; Peng, X. *J. Am. Chem. Soc.* **2007**, *129*, 3339-3347. (d) Deng, Z. T.; Yan, H.; Liu, Y. *J. Am. Chem. Soc.* **2009**, *131*, 17744-17745. (e) Srivastava, B. B.; Jana, S.; Pradhan, N. *J. Am. Chem. Soc.* **2011**, *133*, 1007-1015.

(15) (a) Rothenberger, A.; Morris, C.; Wang, H. H.; Chung, D. Y.; Kanatzidis, M. G. *Inor. Chem.* **2009**, *48*, 9036-9040. (b) Manos, M. J.; Kanatzidis, M. G. *J. Am. Chem. Soc.* **2009**, *131*, 6599-6607.

(16) (a) Lips, F.; Dehnen, S. *Inorg. Chem.* **2008**, *47*, 5561-5563. (b) Ruzin, E.; Zent, E.; Matern, E.; Massa, W.; Dehnen, S. *Chem. Eur. J.* **2009**, *15*, 5230-5244.

Chapter 7

Three-Dimensional Covalent Co-Assembly between Inorganic Supertetrahedral Clusters and Imidazolates

7.1 Introduction

Supertetrahedral chalcogenide clusters are of high current interest because their unique compositions and structures allow them to border several research areas including semiconductor nanoparticles, crystalline porous materials, and inorganic-organic hybrid framework materials.[1-8] While each of these research areas has undergone dramatic growth in the recent decades, the integration of synthetic and structural concepts from these different areas into a coherent synthetic methodology to develop new families of materials that combine functionalities of these individual material types is still at a nascent stage.[4] Composite materials in which chalcogenide clusters and organic functional molecules are covalently assembled into ordered 3D arrays belong to such new families of materials.

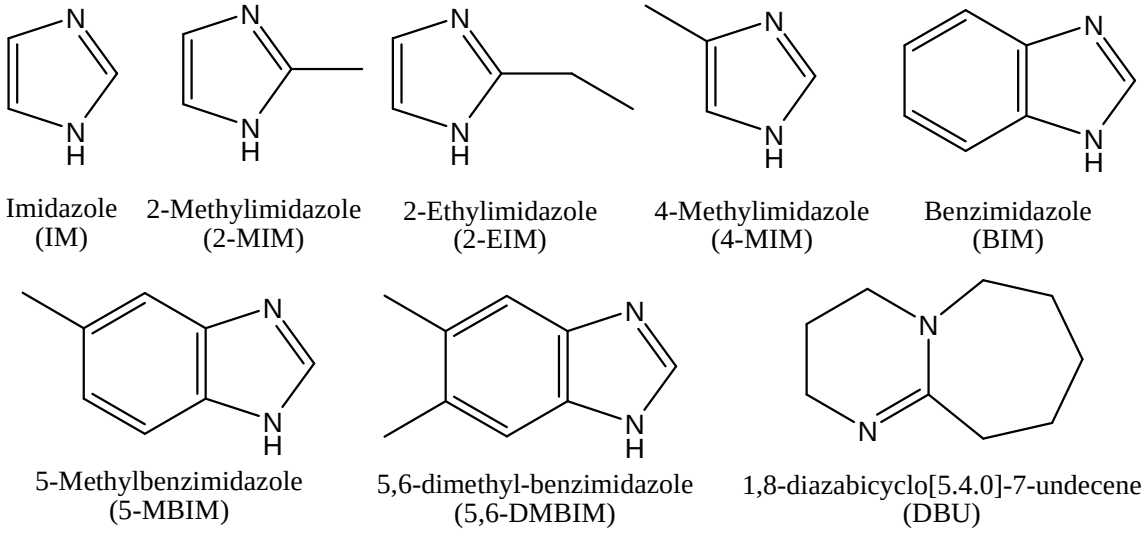
The assembly of chalcogenide clusters into extended frameworks generally occurs via sharing of anionic sulfur (or selenium) sites at four corners of each cluster, leading to extended frameworks with all linkages made through inorganic components.[9] For example, 3-D inorganic frameworks made from T3 (e. g., $[In_{10}S_{20}]^{10-}$), T4 (e. g., $[In_{16}Cd_4S_{35}]^{14-}$), and T5 (e. g., $[Cu_5In_{30}S_{56}]^{17-}$) clusters are all known.[10] This type of inter-cluster linkage mode (i. e., M-X-M, X=S, Se) is common, in part because of the compatibility between inter-cluster bonds (M-X) and intra-cluster bonds (M-X too). A

more complex situation occurs when attempts are made to use organic ligands to crosslink inorganic clusters, because of the need for matching the disparate intra-cluster (M-X bonds) with inter-cluster (M-L bonds, L=organic ligands) bond types. For example, the strong M-L interaction could lead to the extraction of metal ions from chalcogenide clusters to form coordination polymers with monomeric metal sites.[11]

The integration of organic components into the chalcogenide superlattices offers opportunities for not only new structures types, but also synergistic properties resulting from inorganic and organic components through their uniform integration at the molecular level. During the past decade, the covalent organization of Cd-S-SPh based tetrahedral clusters into 1-D chains and 2-D layers has been achieved.[12] Recently, additional progresses have been made, leading to the 1-D and 2-D assembly of inorganic Ga-S supertetrahedral clusters.[4, 13] Despite these promising progresses, a number of limitations still exist prior to this work including: (1) only neutral organic ligands (usually bipyridine types) have been shown to function as crosslinkers between tetrahedral clusters; (2) only low-dimensional 0-D, 1-D, and 2-D superlattices have been made; and (3) for supertetrahedral clusters, the size of the cluster is limited to T3 with 10 metal sites.[4]

In this work, we seek to explore a new type of chemistry at the interface of two seemingly unrelated types of materials: (1) inorganic chalcogenide clusters and frameworks (e.g., CdInS-44-$[Cd_4In_{16}S_{33}]^{10-}$, UCR-17-$[Cu_5In_{30}S_{54}]^{13-}$), and (2) zeolitic imidazolate frameworks, commonly called ZIFs (e.g., [Zn(2-methylimidazolate)$_2$])[14]. We report here a new family of 3-D four-connected superlattices (denoted as supertetrahedral

cluster imidazolate frameworks, **SCIFs**) comprising supertetrahedral chalcogenide T3 and T4 clusters linked by imidazolate ligands (Scheme 7.1 and Table 7.1). The size and geometry of their pore space can be influenced by the size of the cluster and the type of substituents on the imidazolate. Their semiconducting properties (e.g. electronic band gaps) can also vary. One member of this family also displays permanent porosity with the CO_2 uptake capacity comparable to some porous metal-organic framework materials. [15]



Scheme 7.1. Imidazole and its derivatives and template amine.

7.2 Experimental Section

7.2.1 Solvothermal Syntheses

SCIF-1: Li_2S (76.3mg, 1.66mmol), $In(NO_3)_3{\cdot}xH_2O$ (98.1mg, 0.326mmol based on anhydrous indium nitrate), imidazole (72.5mg, 1.07mmol) are mixed with 2-amino-1-butanol (1.647g, 18.5mmol), acetonitril (1.220g, 29.7mmol), 1,8-diazabicyclo[5.4.0]-7-undecene (DBU, 1.614g, 10.6mmol) in a 23-mL Teflon-lined stainless steel autoclave for

half an hour. This vessel is then sealed and heated at 150^{o}C for 12days. The autoclave is subsequently cooled to room temperature. Some semi-transparent octahedral crystals (7.9mg) are obtained after washed with ethanol and dried. Elemental analysis: C 21.6 H 3.18 N 7.04 Li 0.1.

SCIF-2: A mixture of Li_2S (58.5mg, 1.27mmol), $In(NO_3)_3{\cdot}xH_2O$ (96.3mg, 0.320mmol based on anhydrous indium nitrate), 2-methylimidazole (131.4mg, 1.60mmol), 2-amino-1-butanol (1.609g, 18.1mmol), acetonitril (1.114g, 27.1mmol), DBU (2.322g, 15.3mmol) is prepared and stirred in a 23-mL Teflon-lined stainless steel autoclave for half an hour. After the vessel is sealed and heated at 150^{o}C for 12 days, the autoclave is subsequently cooled to room temperature. Semi-transparant polyhedron crystals are obtained with a yield of 13.2mg after purification.

SCIF-3: Li_2S (62.3mg, 1.36mmol), $In(NO_3)_3{\cdot}xH_2O$ (96.3mg, 0.326mmol based on anhydrous indium nitrate), 2-ethylimidazole (142.4mg, 1.48mmol) are mixed with 2-amino-1-butanol (1.800g, 20.2mmol), acetonitril (1.776g, 43.3mmol), 1,8-diazabicyclo[5.4.0]-7-undecene (DBU, 1.681g, 11.0mmol) in a 23-mL Teflon-lined stainless steel autoclave for half an hour. This vessel is then sealed and heated at 150^{o}C for 12days. The autoclave is subsequently cooled to room temperature. Some semi-transparent octahedral crystals (6.9mg) are obtained after washed with ethanol and dried. Elemental analysis: C 21.85 H 3.34 N 6.295 Li 0.67.

SCIF-4: Li_2S (91.6mg, 1.99mmol), $In(NO_3)_3{\cdot}xH_2O$ (131.7mg, 0.438mmol based on anhydrous indium nitrate), 4-methylimidazole (120.2mg, 1.46mmol) are mixed with 2-amino-1-butanol (1.931g, 21.7mmol), acetonitril(2.075g, 50.5mmol), 1,8-

diazabicyclo[5.4.0]-7-undecene (DBU, 2.583g, 17.0mmol) in a 23-mL Teflon-lined stainless steel autoclave for half an hour. This vessel is then sealed and heated at 150^{o}C for 12days. The autoclave is subsequently cooled to room temperature. Some semi-transparent octahedral crystals (13.3mg) are obtained after washed with ethanol and dried. Elemental analysis: C 23.05 H 3.49 N 7.22 Li 0.035.

SCIF-5: A mixture of Li_2S (98.6mg, 2.15mmol), $In(NO_3)_3{\cdot}xH_2O$ (136.9mg, 0.455mmol based on anhydrous indium nitrate), benzimidazole (150.2mg, 1.27mmol), 2-amino-1-butanol (2.859g, 27.0mmol), acetonitril (1.637g, 39.9mmol), 1,8-diazabicyclo[5.4.0]-7-undecene (DBU, 2.322g, 18.8mmol) is prepared and stirred in a 23-mL Teflon-lined stainless steel autoclave for half an hour. After the vessel is sealed and heated at 150^{o}C for 12 days, the autoclave is subsequently cooled to room temperature. Semi-transparant polyhedron crystals are obtained with a yield of 18.2mg after purification. Elemental analysis: C 23.9 H 3.23 N 6.42 Li 0.066.

SCIF-6: Li_2S (62.3mg, 1.36mmol), $In(NO_3)_3{\cdot}xH_2O$ (97.6mg, 0.324mmol based on anhydrous indium nitrate), 5-methylbenzimidazole (149.8mg, 1.13mmol) are mixed with 2-amino-1-butanol (1.619g, 18.2mmol), acetonitril (1.218g, 29.7mmol), 1,8-diazabicyclo[5.4.0]-7-undecene (DBU, 1.947g, 12.8mmol) in a 23-mL Teflon-lined stainless steel autoclave for half an hour. This vessel is then sealed and heated at 150^{o}C for 12days. The autoclave is subsequently cooled to room temperature. 6.8mg of semi-transparent octahedral crystals are obtained after washed with ethanol and dried.

SCIF-7: A mixture containing Li_2S (62.1mg, 1.35mmol), $In(NO_3)_3{\cdot}xH_2O$ (97.7mg, 0.325mmol based on anhydrous indium nitrate), 5,6-dimethylbenzimidazole (136.5mg,

0.934mmol), 2-amino-1-butanol (1.676g, 18.8mmol), acetonitril (1.238g, 30.2mmol), 1,8-diazabicyclo[5.4.0]-7-undecene (DBU, 1.757g, 11.5mmol) is stirred in a 23-mL Teflon-lined stainless steel autoclave for half an hour. This vessel is then sealed and heated at 150^{o}C for 12 days. The autoclave is subsequently allowed to cool to room temperature. 10.5mg of semi-transparent octahedral crystals are obtained after purification. Elemental analysis: C 26.0 H 3.38 N 6.65 Li 0.11.

SCIF-8: A 23-mL Teflon-lined stainless steel autoclave containing Li_2S (63.1mg, 1.37mmol), $In(NO_3)_3{\cdot}xH_2O$ (96.3mg, 0.320mmol based on anhydrous indium nitrate), $Cd(NO_3)_2{\cdot}4H_2O$ (5.5mg, 0.018mmol), 2-ethylimidazole (182.5mg, 1.90mmol), 2-amino-1-butanol (1.615g, 18.1mmol), acetonitril (1.220g, 29.7mmol), 1,8-diazabicyclo[5.4.0]-7-undecene (DBU, 2.522g, 16.6mmol) is sealed and heated to 150^{o}C for 12 days, then allowed to cool to room temperature, 7.9mg of pale-yellow cuboid crystals are obtained after purification. Elemental analysis: C 19.2 H 3.01 N 5.255 Li 0.37.

SCIF-9: Li_2S (61.3mg, 1.33mmol), $In(NO_3)_3{\cdot}xH_2O$ (98.2mg, 0.326mmol based on anhydrous indium nitrate), $Cd(NO_3)_2{\cdot}4H_2O$ (16.4mg, 0.053mmol), 5, 6-dimethylbenzimidazole (207.8mg, 1.42mmol), 2-amino-1-butanol (1.609g, 18.1mmol), acetonitril (1.242g, 30.3mmol), 1,8-diazabicyclo[5.4.0]-7-undecene (DBU, 2.523g, 16.6mmol) are mixed in a 23-mL Teflon-lined stainless steel autoclave for half an hour. This vessel is then sealed and heated at 150^{o}C for 12days. The autoclave is subsequently cooled to room temperature. 6.6mg of pale-yellow octahedral crystals are obtained after washed with ethanol and dried. Elemental analysis: C 20.8 H 2.99 N 5.01 Li 0.34.

Table 7.1. Summary of crystal data and refinement results.[a]

Name	Framework Composition	S. G.	S. B. U.	*a* (Å)	*b* (Å)	*c* (Å)	*R*(F)	Net
SCIF-1	$[In_{10}S_{16}(IM)_2]^{4-}$	*Pbca*	T3 cluster ($In_{10}S_{16}$)	22.5121(6)	22.6610(6)	33.3409(10)	0.0521	D. D.
SCIF-2	$[In_{10}S_{16}(2\text{-}MIM)_2]^{4-}$	*C*2/*c*		49.9905(16)	68.2851(21)	25.5907(8)	0.0938	D. D.
SCIF-3	$[In_{10}S_{16}(2\text{-}EIM)_2]^{4-}$	*I*-42*d*		25.0958(2)	25.0958(2)	36.6912(5)	0.0785	D. D.
SCIF-4	$[In_{10}S_{16}(4\text{-}MIM)_2]^{4-}$	*Pbca*		22.6617(3)	22.5629(4)	33.7015(4)	0.0710	D. D.
SCIF-5	$[In_{10}S_{16}(BIM)_2]^{4-}$	$P2_12_12_1$		21.2772(10)	21.4180(10)	36.0100(17)	0.0724	D. D.
SCIF-6	$[In_{10}S_{16}(MBIM)_2]^{4-}$	*Pbca*		22.4388(11)	22.4165(10)	33.9940(16)	0.0547	D. D.
SCIF-7	$[In_{10}S_{16}(DMBIM)_2]^{4-}$	*Pbca*		22.5220(3)	22.4835(4)	34.4841(5)	0.0571	D. D.
SCIF-8	$[In_{16}Cd_4S_{31}(2\text{-}EIM)_2]^{8-}$	*I*-42*d*	T4 cluster ($In_{16}Cd_4S_{31}$)	30.8096(46)	30.8096(46)	16.6159(25)	0.0649	T. D.
SCIF-9	$[In_{16}Cd_4S_{31}(DMBIM)_2]^{8-}$	*Pbca*		25.7722(10)	25.6993(11)	48.340(2)	0.1459	D. D.
OCF-31	$[In_8S_{15}]^{6-}$	$P2_12_12_1$	P1 cluster	18.1936(24)	18.3672(25)	22.1072(28)	0.1018	S. D.

[a] $\beta = 91.159(2)^o$ for SCIF-2. S. G. = space group, S.B.U. = secondary building unit, S. D. = single diamond, D. D. = double diamond, T. D. = triple diamond.

7.2.2 Structure Determination

Single-crystal X-ray analysis was performed on a Bruker Smart APEX II CCD area diffractometer with nitrogen-flow temperature controller using graphite-monochromated $Mo_{K\alpha}$ radiation (λ = 0.71073 Å), operating in the ω and φ scan mode with a scan width of 0.5°. Raw data collection and refinement were done using SMART at 150K for obtaining good diffraction data. Data reduction was performed using $SAINT^{+}$ and corrected for Lorentz and polarization effects. The SADABS program was used for absorption correction. The structure was solved by direct methods and the structure refinements were based on $|F^2|$ with anisotropic displacement using SHELX-97. Most of non-hydrogen atoms in the framework were refined with anisotropic displacement parameters. Some organic amine template molecules can be pointed out, but some can not be located owing to serious disorder. Part of hydrogen atoms were placed in calculated positions. All crystallographic calculations were conducted with the SHELXTL software suites. The crystal 795458-795467 contain the supplementary crystallographic data, which can be obtained free of charge at www.ccdc.cam.ac.uk/conts/retrieving.html (or from the Cambridge Crystallographic Data Center, 12, Union Road, Cambridge CB21EZ, U.K.; fax: (+44) 1223-336-033; or deposit@ccdc.cam.ac.uk).

7.2.3 Powder X-ray Diffraction

Room temperature X-ray powder diffraction experiments were performed on a Bruker D8 Advance powder diffractometer, equipped with a Sol-X detector using Cu

$K\alpha_1$ radiation (λ = 1.5406 Å). The simulated XRD pattern was calculated from the structure data using the Mercury 2.4 software.

7.2.4 Optical Property

The band gaps were determined through the UV/vis/near-IR diffuse reflectance spectra measured on a Shimadzu UV-3101PC double-beam, double-monochromator spectrophotometer. $BaSO_4$ powder was used as both reference (100% reflectance) and sometimes base material for the coating of samples. Absorption (α/S) data were calculated from the reflectance data by using the Kubelka-Munk function: $\alpha/S = (1-R)^2/R$, where R is the reflectance at a given wavelength, α is the absorption coefficient, and S is the scattering coefficient.

7.2.5 Thermal Analysis

The simultaneous DSC-TGA thermal analysis was performed on TA instruments SDT Q600. All samples was prepared by grinding single crystals into fine powder and heated between room temperature and 1200 ^oC at a heating rate of 5 ^oC/min under N_2 gas or air flow (100 ml/min).

7.2.6 Gas Adsorption

CO_2 gas sorption experiments were carried out on a Micromeritics ASAP 2010 surface area and pore size analyzer. Prior to the measurement, the raw sample was was dried under vacuum at ambient temperature for 10 hours to yield an activated sample for gas adsorption measurements. Before the measurement, the sample was dried again by using the "degas" function of the surface area analyzer for 15 hours at 100^oC. The CO_2 adsorption measurement was performed at 273.15K with ice water bath.

7.2.7 Quantum Chemical Calculations for Frontier Orbital of the Fragment of the Crystal Lattice

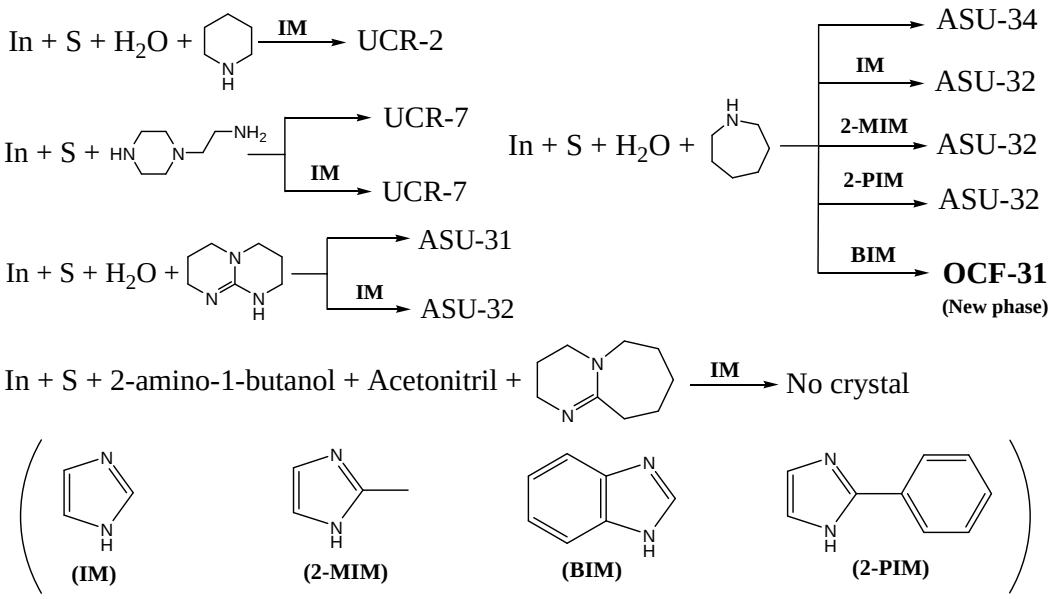
The DFT calculations were performed on B3LYP functional with LANL2DZ basis set using G09 package. The model systems were built based on original crystal structures however with small change on the distortion angle between the clusters and imidazolate ligands. A fragment with two clusters linked with seven imidazolate ligands ($[(In_{10}S_{16})_2(CH_3C_3N_2H_2)_7]$) was chosen to alternatively represent the feature of the whole crystal in order to reduce the calculation cost. The designed system holds one negative charge since the linkage imidazolate ligand is deprotonated, and the rest negative charge carried by the cluster building units were passivated by protons attached to the surface sulfur atoms. Hence in the data analysis the frontier orbitals which are responsible for the optical gap were picked as HOMO-1 and HOMO-2 since the none-passivated system carries 5 negative charges. Presented in here are the cases without distortion and with 30 degree distortion; and the 2-ethylimidazole was simplified as 2-methylimidazole for easier calculation.

7.3 Results and Discussion

7.3.1 Synthesis

Prior to this work, inorganic supertetrahedral frameworks are generally prepared by redox reactions between metal and non-metal elements in the presence of different amines.[10] Under such conditions, we have found that the addition of imidazole (or its derivatives) provides some control over the assembly processes, leading to various 3-D inorganic framework materials such as UCR-2,[16] UCR-7,[10b] ASU-31,[5c] ASU-32,[5c] ASU-

34,[5b] and a previously unknown phase called OCF-31 (Scheme 7.2 and Figure 7.1). Thus, when starting from elemental forms, clusters tend to self-assemble with themselves, instead of co-assembling with imidazolate.



Scheme 7.2. Comparison on synthetic procedure of several chalcogenide superlattices with or without adding imidazole or its derivatives.

7.3.2 Structure

By choosing both soluble metal and sulfide sources as precursor, a series of **SCIF-*n*** (n=1-9) with T3 or T4 clusters have been made with the use of 1, 8-diazabicyclo[5.4.0]-7-undecene (DBU) as template and their structures determined by single-crystal X-ray diffraction. These SCIFs are constructed from T3 or T4 clusters interlinked by various imidazolate ligands (Figure 7.2a and 7.2b), and their negatively charged frameworks are balanced by lithium cations and protonated amine ($HDBU^+$). These SCIFs adopt interpenetrating diamond-type topology (by treating an entire cluster as a single tetrahedral node, Figure 7.2e, 7.2g, 7.2i, 7.2k). The degree of interpenetration

(i.e., 2-fold vs. 3-fold) is related to the size of both clusters and imidazolate ligands. All SCIFs with T3 clusters exhibit two-fold interpenetration (Figure 7.2f, 7.2j, Figure 7.3). With larger T4 clusters, three-fold interpenetration which has never before been observed in chalcogenides superlattices can also be realized as in SCIF-8 (Figure 7.2h). However, two-fold interpenetration can be restored with T4 clusters by using a more bulky imidazolate ligand as in SCIF-9 (Figure 7.2l). SCIF-8 and SCIF-9 are the first example that demonstrates the covalent assembly of T4 clusters by an organic ligand. Prior to this work, T4 clusters have not been assembled into any dimension by an organic ligand. Even though these SCIFs exhibit the same diamond-type framework topology, they have quite different space group symmetries and various channel geometries. The highest symmetry occurs when 2-ethylimidazolate is used.

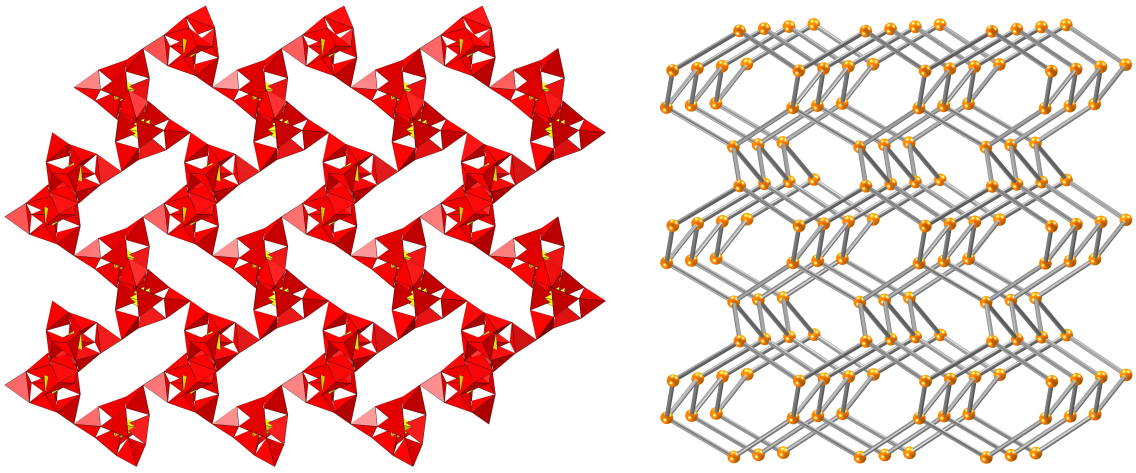
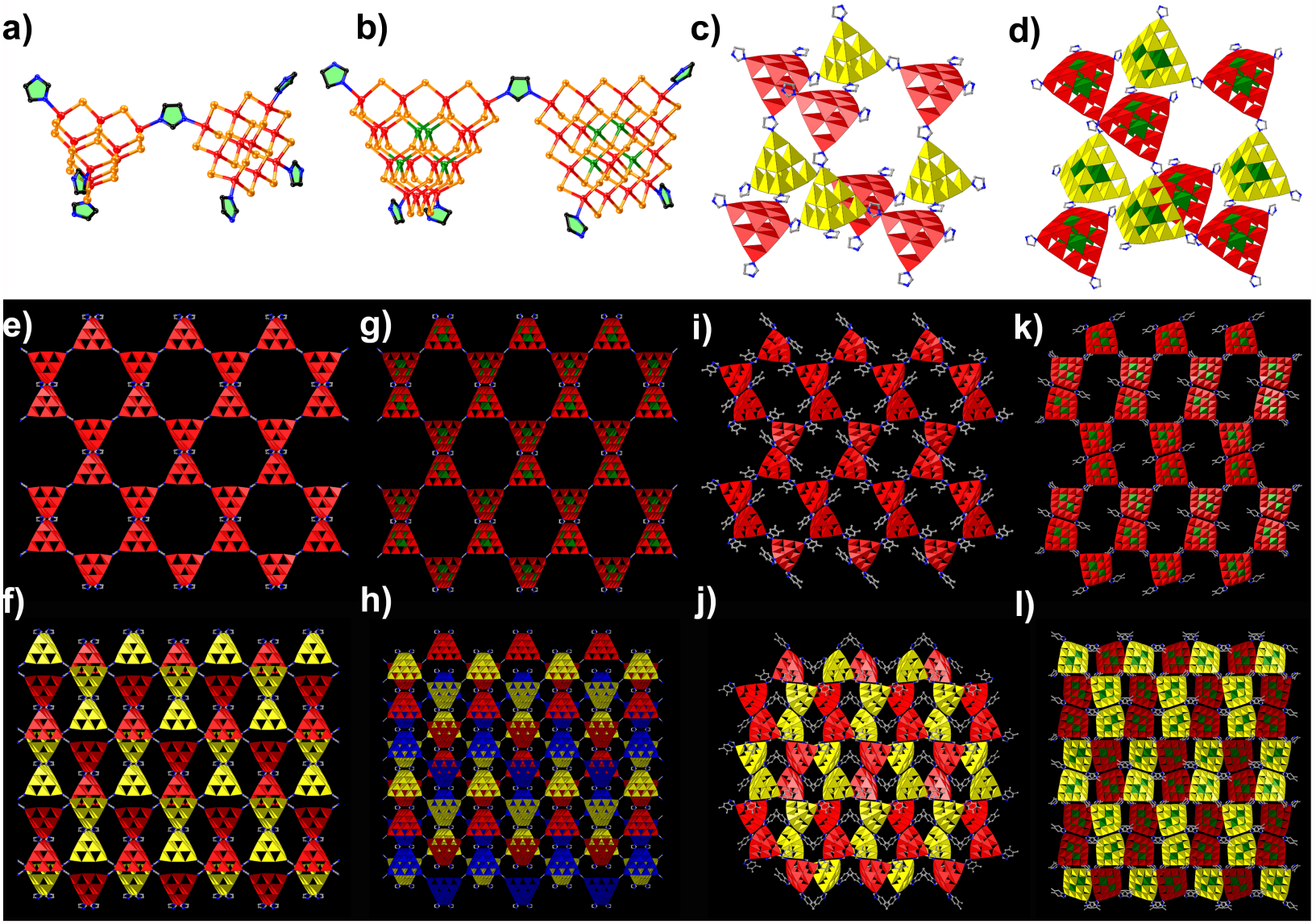


Figure 7.1. Single network (left) with diamond topology (right) when P1 clusters in OCF-31 are treated as tetrahedral nodes. Tetrahedron in yellow is the sulfur atom in central anti-T1.

Figure 7.2. Connectivity of supertetrahedral chalcogenide cluster T3 (a) and T4 (b) crosslinked by imidazolate. Classical adamantane-like unit based on T3 cluster (c) and T4 cluster (d) in SCIFs. 3-D single net and two-fold interpenetrated frameworks with diamond topology in SCIF-3 (e, f); single net and three-fold interpenetrated frameworks with diamond topology in SCIF-8 (g, h) viewed down the *b* axis, with ethyl group omitted for clarity. 3-D single and two-fold interpenetrated frameworks with diamond topology in SCIF-7 (i, j) and SCIF-9 (k, l), viewed down the *b* axis.


a)
b)
c)
d)
e)
g)
i)
k)
f)
h)
j)
l)

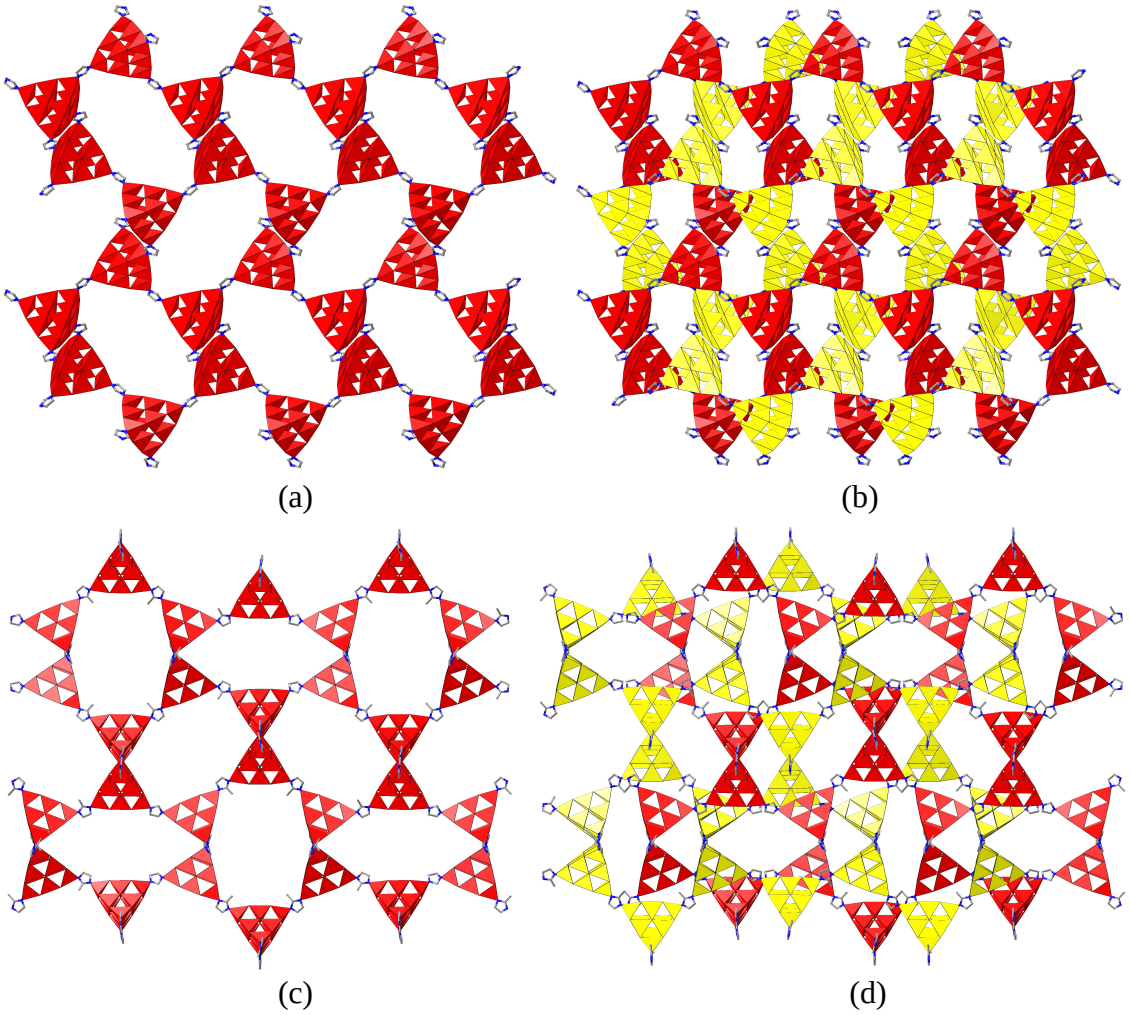


Figure 7.3. 3-D single (a, c) and two-fold interpenetrated (b, d) frameworks with diamond topology in SCIF-1 and SCIF-2, respectively, viewed through *b* axis.

The synthesis of SCIFs represents a significant advance in several aspects. For the first time, supertetrahedral chalcogenide clusters have been crosslinked with anionic organic ligands (imidazolates in this case). SCIFs also represent the first 3-D covalent inorganic-organic superlattices with chalcogenide tetrahedral clusters as one of the building blocks. While 3-D frameworks comprising only supertetrahedral clusters are well known,[5, 9, 11] all previous efforts aimed at crosslinking tetrahedral chalcogenide

clusters of any composition (e.g., organic-capped Cd-S-SPh system or inorganic Ga-S system) using organic ligands have only resulted in the formation of low-dimensional structures (up to 2-D). [13]

The formation of SCIFs depends on achieving a suitable balance among a number of factors. The complexity of the assembly can be seen from T4-containing SCIF-8 and SCIF-9 which require the assembly of a number of individual solution species (In^{3+}, Cd^{2+}, S^{2-}, , Im^{-}, plus extra-framework charge balancing and pore filling species such as $HDBU^{+}$), each of which plays a unique role. From such initial solubilized species, a much higher structural hierarchy (i.e., large T4 clusters templated by cations and crosslinked by organic anions) is established. It is worth noting that the chemistry of DBU is highly unique because among many amines used for the synthesis, it is so far the only one that has been found to template the formation of SCIFs.

Given the aforementioned complex multi-component chemical system, it is not unreasonable to expect that multiple competing pathways for the assembly into 3-D (or lower-dimensional) frameworks should exist. For example, Tn clusters can self-assemble into purely inorganic frameworks while Cd-imidazolate can form ZIF-type porous MOFs.[17] It is clear that the chemistry and bonding of the SCIF system lies at the interface between inorganic chalcogenide frameworks and ZIFs materials. The benefit of the co-assembly between chalcogenide clusters and imidazolates is the potential of such composite system for incorporating new structural patterns and properties (e.g., semiconductivity).

7.3.3 Optical Properties

Solid-state diffuse reflectance UV-Vis spectra were studied by using samples of SCIF-3, -7, -8, and -9 (Figure 7.4). The effect of the cluster size is obvious by comparing band gaps of T3-containing SCIF-3 (3.35eV) and SCIF-7 (3.43eV) with T4-containing SCIF-8 (3.12eV) and SCIF-9 (3.22eV). The difference in band gaps between materials with the same cluster size is less prominent and can result from the effect of imidazolate ligands and the related change in the lattice symmetry. The trend seems to be that the compound with a higher symmetry (e.g., tetragonal SCIF-3 vs. orthorhombic SCIF-7) has a lower band gap. In fact, a similar trend is also observed in solid TiO_2 semiconductors (3.03 eV for rutile and 3.18eV for anatase), in which the symmetry of TiO_6 pseudo-octahedron in rutile is higher than that in anatase.

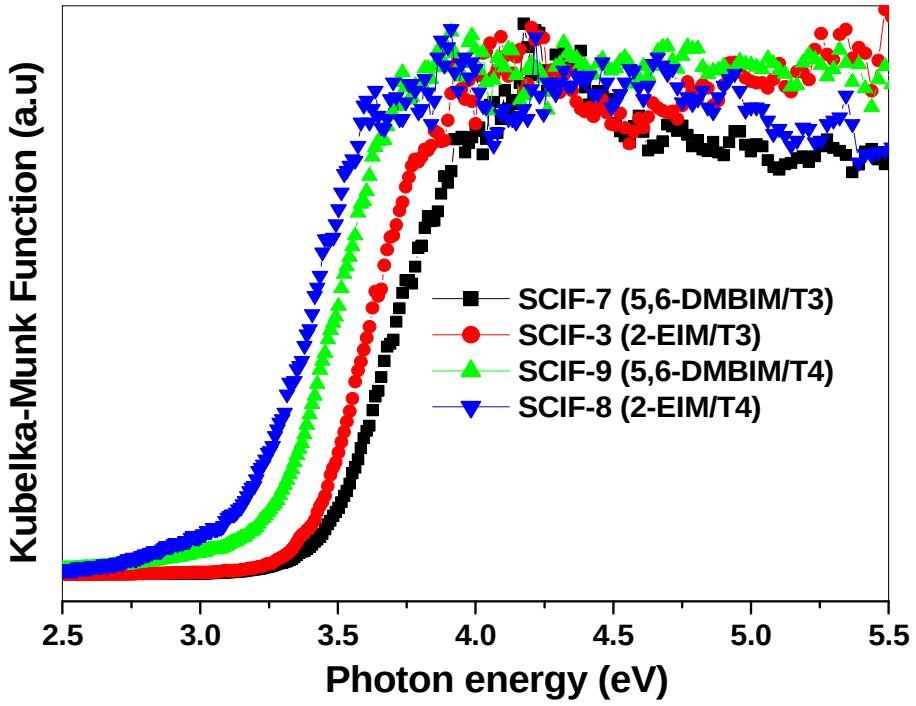
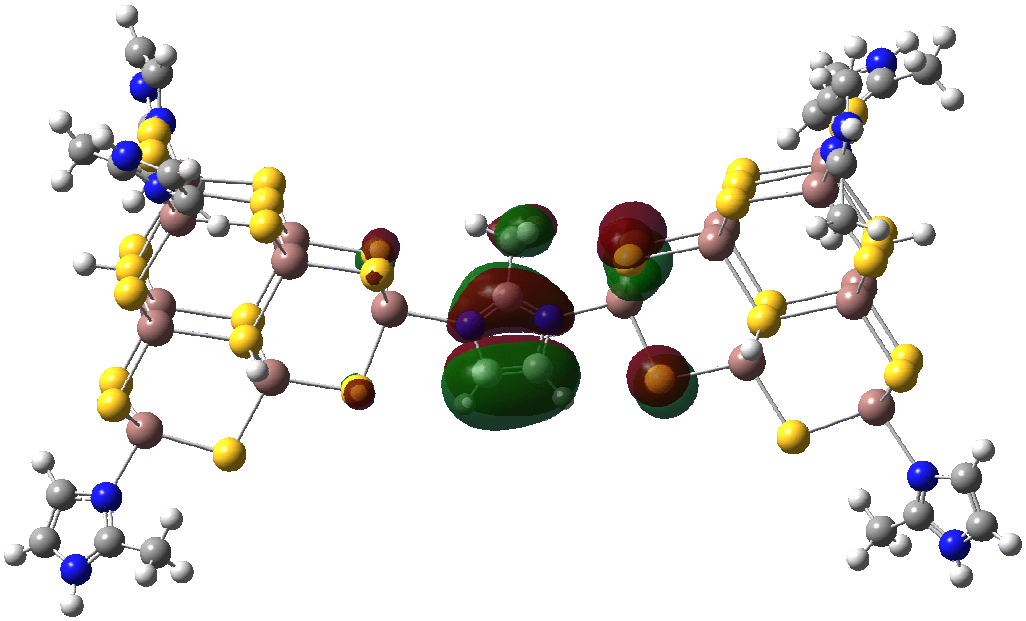
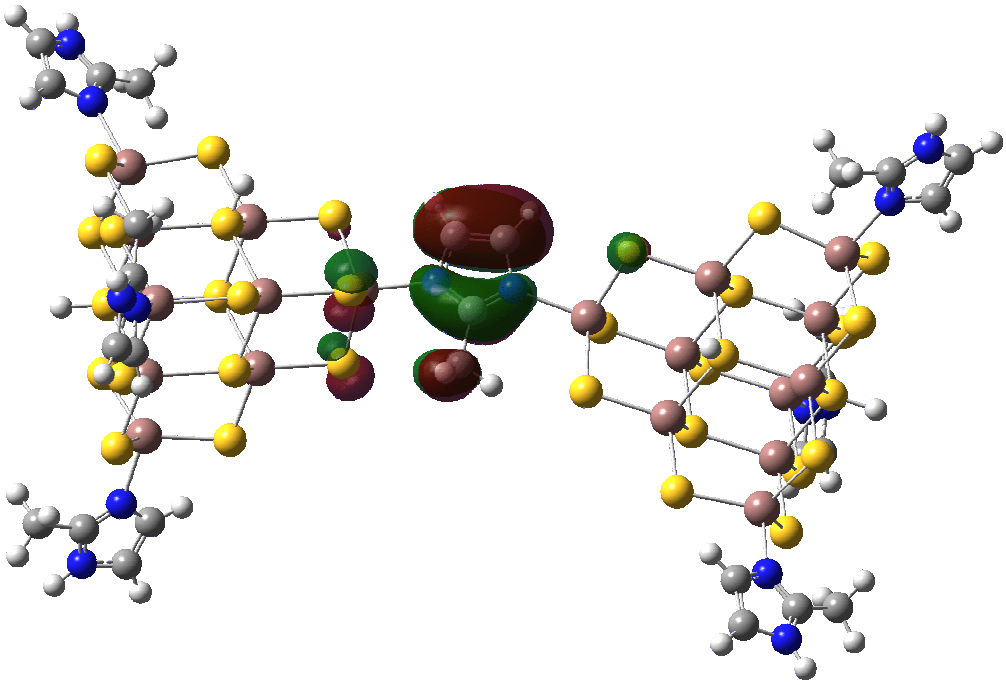


Figure 7.4. The normalized solid-state Uv-Vis absorption spectra of SCIF-3, -7, -8, -9.



(a)



(b)

Figure 7.5. The HOMO of T3-EIM-T3 molecular moiety in the perfect aligned (a, 0 degree distortion) and most distorted (b, 30 degree distortion) orientation, showing the p-π conjugation system between cluster and imidazolate.

7.3.4 Quantum Chemical Calculations

The above observed variation of band gaps with the crystal symmetry is likely determined by the p-π interactions between the sulfur atoms (near the corners of the supertetrahedra) and imidzolate π rings. Such interaction is strongly affected by the relative orientation of these two building blocks (i.e., cluster and imidazolate). A more parallel aligned p-π system gives a smaller band gap, and a more distorted alignment results in a wider band gap. To further support this, we performed quantum chemical calculations based on their crystal structures. Because of the relatively weak long-range interactions between clusters, we only focus on a molecular moiety as shown in Figure 7.5. The DFT calculations were performed on B3LYP functional with LANL2DZ basis set using G09 package.[18] The modeling systems were built to simulate two extreme cases of the perfect aligned and most distorted p-π systems. Figure 7.5 depicts the p-π conjugation in the T3-ethylimidazol-T3 moiety. The results show that in the perfectly aligned system, electrons are delocalized through imidazolate ring onto both sides. However, such delocalization is dramatically decreased when the distortion is introduced. While this preliminary simulation does not capture the whole picture of the crystal lattice, the results do help to better understand experimental data and support the use of ligand-cluster interactions to control local orientations of framework building units as a means in band gap engineering.

7.3.5 Gas Adsorption

The permanent porosity of SCIF-3 was confirmed by CO_2 gas sorption measurement performed on Micromeritics ASAP 2020 surface area and pore size

analyzer. Compared to the bridging S^{2-} anions in T3 and T4 inorganic frameworks (such as UCR-5 and UCR-7), imidazolate ligands are longer and less negative (-1 vs. -2), which contribute to the porosity because fewer protonated template molecules are required to balance the less negative charge of SCIF framework. However, the framework distortion as well as bulky substituents on the imidazolate ring and multi-fold interpenetration tends to reduce the porosity. Considering all these factors, SCIF-3 is chosen as a promising candidate for gas sorption analysis, because of its high symmetry and small substituent and lower degree of interpenetration. A sample of SCIF-3 was degassed at 100^{o}C prior to the measurement, and its stability upon degassing was confirmed by TGA and PXRD (Figure 7.6 and Figure 7.7). The initial gradual weight loss of 2.61% between 30-150ºC could be attributed to loss of solvent molecules trapped in the pore or adsorbed on the surface (acetonitril and water). An abrupt weight loss of 30.71% between 200-450^{o}C is attributed to the carbonization of template amine, which results in complete collapse of framework. While no obvious N_2 adsorption was observed, a significant CO_2 uptake capacity (18.6cm^3/g at 1 atm and 273.15K, Figure 7.8) occurred. Such a CO_2 uptake capacity is comparable to some quite porous metal-organic framework materials such as BIF-3.[19] The difference between N_2 and CO_2 adsorption is likely caused by the smaller dynamic diameter of CO_2 (0.33nm) (c.f. N_2 0.36nm) and the stronger interaction between CO_2 and charged porous environment.[20]

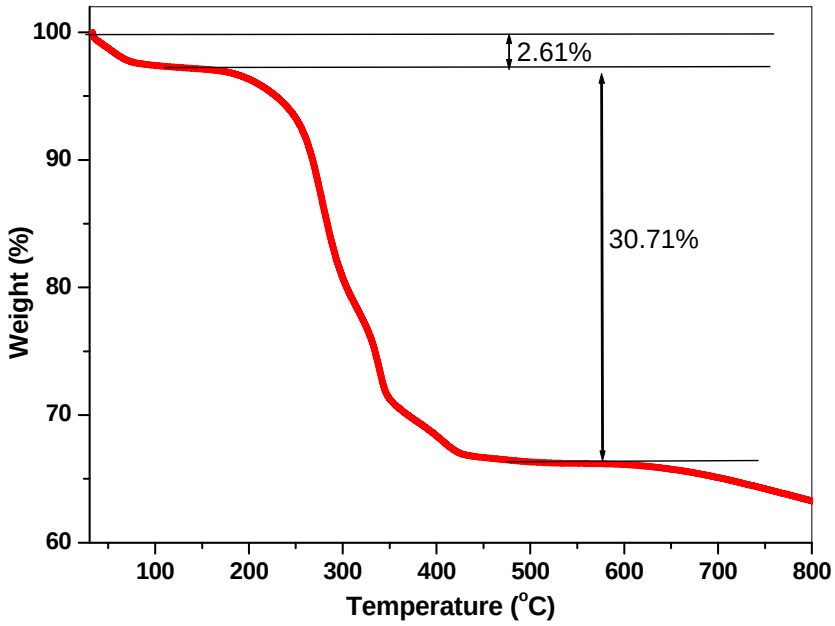


Figure 7.6. Thermogravimetric analysis (TGA) for complex SCIF-3 under nitrogen atmosphere.

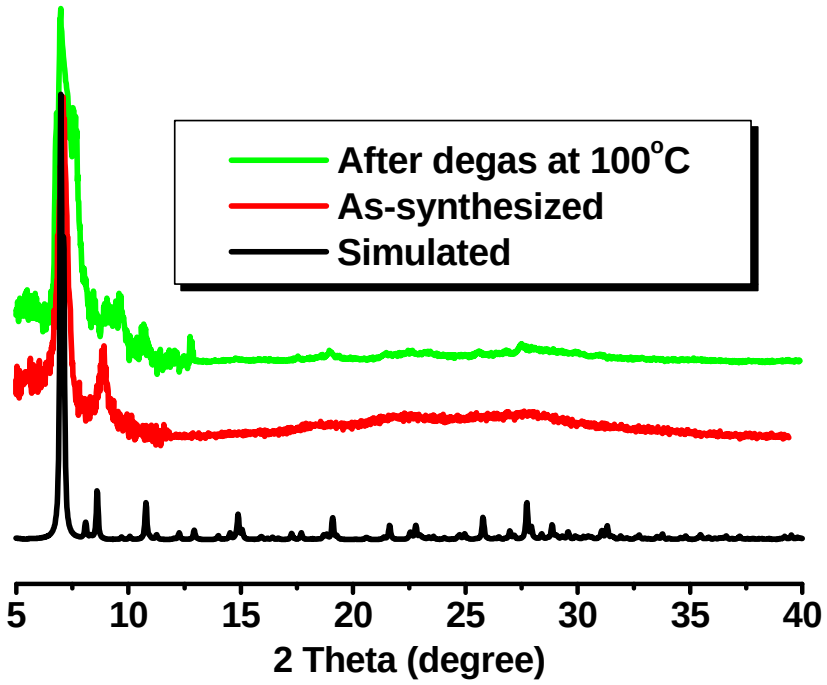


Figure 7.7. Powder X-ray diffraction patterns of SCIF-3.

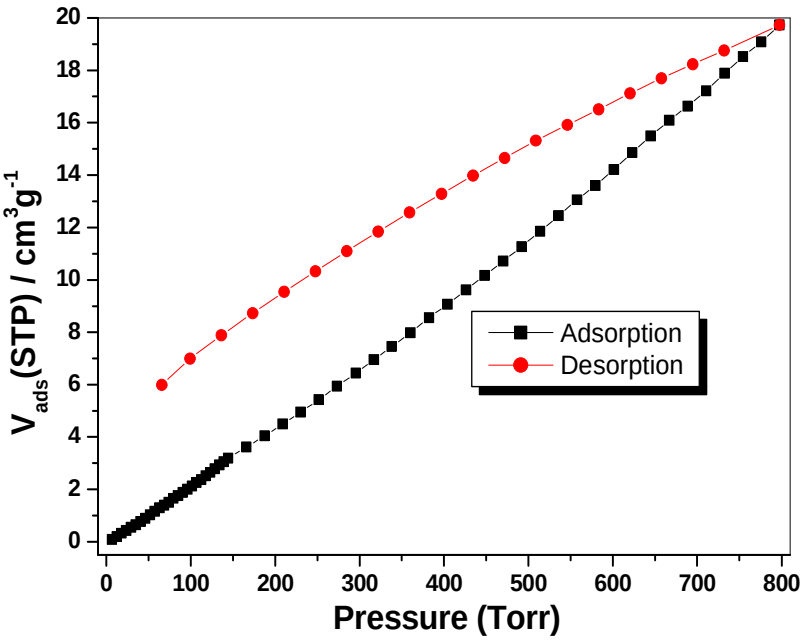


Figure 7.8. CO_2 gas sorption isotherms of SCIF-3 at 273.15K.

7.4 Conclusion

A family of 3-D covalent arrays of supertetrahedral chalcogenide clusters and imidazolate ligands has been synthesized and their unique structure, porosity, and semiconducting properties characterized. These are the first examples of supertetrahedral clusters being assembled with anionic ligands and are beautiful demonstration of integrative chemistry between metal chalcogenides and zeolitic imidazolates. Because of the wide availability of various anionic ligands including carboxylates, the use of negative ligands as a general strategy in the co-assembly between chalcogenide clusters and organic ligands could lead to a new generation of hybrid multi-functional porous materials. The work also represents a significant step forward for the metal chalcogenide chemistry because of the demonstrated feasibility to use organic ligands to covalently assemble *larger* supertetrahedral clusters into even *higher* dimensions (3-D).

7.5 References

(1) a) G. Férey, *Angew. Chem. Int. Ed.* **2003**, *42*, 2576-2579; b) C. L. Bowes, G. A. Ozin, *Adv. Mater.* **1996**, *8*, 13-28; c) J. F. Corrigan, O. Fuhr, D. Fenske, *Adv. Mater.* **2009**, *21*, 1867-1871.

(2) a) S. Dehnen, M. Melullis, *Coord. Chem. Re*v. **2007**, *251*, 1259-1280; b) P. Feng, X. Bu, N. Zheng, *Acc. Chem. Res.* **2005**, *38*, 293-303; c) X. Bu, N. Zheng, P. Feng, *Chem. Eur. J.* **2004**, *10*, 3356-3362; d) N. Zheng, X. Bu, B. Wang, P. Feng, *Science* **2002**, *298*, 2366-2369.

(3) A. P. Alivisatos, *J. Phys. Chem.* **1996**, *100*, 13226-13239.

(4) P. Vaqueiro, *Dalton Trans.* **2010**, *39*, 5965-5972.

(5) a) O. M. Yaghi, Z. Sun, D. A. Richardson, T. L. Groy, *J. Am. Chem. Soc.* **1994**, *116*, 807-808; b) H. Li, A. Laine, M. O'Keeffe, O. M. Yaghi, *Science* **1999**, *283*, 1145-1147; c) H. Li, M. Eddaoudi, A. Laine, M. O'Keeffe, O. M. Yaghi, *J. Am. Chem. Soc.* **1999**, *121*, 6096-6097; d) H. Li, J. Kim, T. L. Groy, M. O'Keeffe, O. M. Yaghi, *J. Am. Chem. Soc.* **2001**, *123*, 4867-4868; e) H. Li, J. Kim, M. O'Keeffe, O. M. Yaghi, *Angew. Chem. Int. Ed.* **2003**, *42*, 1819-1821.

(6) a) S. Dehnen, M. K. Brandmayer, *J. Am. Chem. Soc.* **2003**, *125*, 6618-6619; b) C. Zimmermann, M. Melullis, S. Dehnen, *Angew. Chem. Int. Ed.* **2002**, *41*, 4269-4272; c) C. Zimmermann, C. E. Anson, F. Weigend, R. Clérac, S. Dehnen, *Inorg. Chem.* **2005**, *44*, 5686-5695; d) M. Melullis, R. Clérac, S. Dehnen, *Chem. Commun.* **2005**, 6008-6010; e) E. Ruzin, A. Fuchs, S. Dehnen, *Chem. Commun.* **2006**, 4796-4798; f) Z. Hassanzadeh Fard, R. Clérac. S. Dehnen, *Chem. Eur. J.* **2010**, *16*, 2050-2053; g) S. Haddadpour, M. Melullis, H. Staesche, C. R. Mariappan, B. Roling, R. Clérac, S. Dehnen, *Inorg. Chem.* **2009**, *48*, 1689-1698.

(7) N. Zheng, X. Bu, H. Vu, P. Feng, *Angew. Chem. Int. Ed.* **2005**, *44*, 5299-5303.

(8) N. Zheng, X. Bu, P. Feng, *Nature* **2003**, *426*, 428-432.

(9) a) W. Su, X. Huang, J. Li, H. Fu, *J. Am. Chem. Soc.* **2002**, *124*, 12944-12945; b) P. Vaqueiro, M. L. Romero, *J. Phys. Chem. Solids* **2007**, *68*, 1239-1243.

(10) a) C. Wang, Y. Li, X. Bu, N. Zheng, O. Zivkovic, C.-S. Yang, P. Feng, *J. Am. Chem. Soc.* **2001**, *123*, 11506-11507; b) C. Wang, X. Bu, N. Zheng, P. Feng, *Chem.Commun.* **2002**, 1344-1345; c) X. Bu, N. Zheng, Y. Li, P.

Feng, P. *J. Am. Chem. Soc.* **2002**, *124*, 12646-12647; d) L. Wang, T. Wu, F. Zuo, X. Zhao, X. Bu, J. Wu, P. Feng, P. *J. Am. Chem. Soc.* **2010**, *132*, 3283-3285; e) T. Wu, X. Wang, X. Bu, X. Zhao, L. Wang, P. Feng, *Angew. Chem. Int. Ed.* **2009**, *48*, 7204-7207; f) T. Wu, L. Wang, X. Bu, V. Chau, P. Feng, *J. Am. Chem. Soc.* **2010**, *132*, 10823-10831.

(11) N. Zheng, J. Zhang, X. Bu, P. Feng, *Cryst. Growth Des.* **2007**, *7*, 2576-2581.

(12) a) J. Xie, X. Bu, N. Zheng, P. Feng, *Chem. Commun.* **2005**, 4916-4918; b) N. Zheng, X. Bu, H. Lu, L. Chen, P. Feng, *J. Am. Chem. Soc.* **2005**, *127*, 14990-14991; c) N. Zheng, X. Bu, J. Lauda, P. Feng, *Chem. Mater.* **2006**, *18*, 4307-4311.

(13) a) P. Vaqueiro, M. L. Romero, *J. Am. Chem. Soc.* **2008**, *130*, 9630-9631; b) P. Vaqueiro, M. L. Romero, B. C. Rowan, B. S. Richards, *Chem. Eur. J.* **2010**, *16*, 4462-4465.

(14) a) Y.-Q. Tian, Y.-M. Zhao, Z.-X. Chen, G.-N. Zhang, L.-H. Weng, D.-Y. Zhao, *Chem. Eur. J.* **2007**, *13*, 4146-4154; b) X.-C. Huang, Y.-Y. Lin, J. P. Zhang, X.-M. Chen, *Angew. Chem. Int. Ed.* **2006**, *45*, 1557-1559; c) K. S. Park, Z. Ni, A. P. Côté, J. Y. Choi, R. Huang, F. J. Uribe-Romo, H. K. Chae, M. O'Keeffe, O. M. Yaghi, *Proc. Natl Acad. Sci. USA* **2006**, *103*, 10186-10191; d) T. Wu, X. Bu, R. Liu, Z. E. Lin, J. Zhang, P. Feng, *Chem. Eur. J.* **2008**, *14*, 7771-7773.

(15) S. Zheng, T. Wu, J. Zhang, M. Chow, R. A. Nieto, P. Feng, X. Bu, *Angew. Chem. Int. Ed.* **2010**, *49*, 5362-5366.

(16) C. Wang, X. Bu, N. Zheng, P. Feng, *Angew. Chem. Int. Ed.* **2002**, *41*, 1959-1961.

(17) Y.-Q. Tian, S.-Y. Yao, D. Gu, K.-H. Cui, D.-W. Guo, G. Zhang, Z.-X. Chen, D.-Y. Zhao, *Chem. Eur. J.* **2010**, *16*, 1137-1141.

(18) C. Lee, W. Yang, R. G. Parr, Phys. Rev. B 1988, 37, 785-789.

(19) J. Zhang, T. Wu, C. Zhou, S. Chen, P. Feng, X. Bu, *Angew. Chem. Int. Ed.* **2009**, *48*, 2542-2545.

(20) S. Bag, M. G. Kanatzidis, *J. Am. Chem. Soc.* **2010**, *132*, 14951-14959.